PROBING THE CELLULAR UPTAKE OF DNA FUNCTIONALIZED GOLD
NANOPARTICLES

By

Alexis Camille Wong

Dissertation

Submitted to the Faculty of the

Graduate School of Vanderbilt University

in partial fulfillment of the requirements

for the degree of

DOCTOR OF PHILOSOPHY

in

Chemistry

August 11, 2017

Nashville, Tennessee

Approved:

David W. Wright, Ph.D.

John A. McLean, Ph.D.

Sandra J. Rosenthal, Ph.D.

C. David Weaver, Ph.D.

To my family and friends, for their constant love and support.

ACKNOWLEDGEMENTS

Joining the Wright lab is one of the best decisions I've made here – they made graduate school fun and taught me so much tangible and intangible knowledge. Stephen Jackson was my first mentor and taught me (almost) everything I know about gold nanoparticles. Thanks for giving me a solid scientific foundation to build on. Keersten Davis – I enjoyed working with you and learning from you. Thanks for being the lab mom/manager and helping us hold things together. Chris Gulka taught me everything else I know about gold nanoparticles. Thanks for all your scientific advice and for reminding me not to be too hard on myself. I'm so glad we met and very grateful for you. This Ph.D. would have been a lot more difficult without you. Anna Bitting – thanks for listening to me complain. A lot. Kim Fong – you were a great resource about all things biology, especially when the rest of the lab was clueless. Adam Travis always has the best gossip. I will miss cell room story time. To Lauren Gibson – thanks for taking a chance on me five years ago and becoming my roommate. I'm so excited for your future life as a professor at Elizabethtown College and I can't wait to see where life takes you. Wes Bauer – the worst best friend a person can have – or is it best worst friend? Anyway, I have really enjoyed my time with you. I'll miss our long talks at the end of the day. To the rest of the former and current Wright lab members – Dr. Nick Adams, Dr. Tom Scherr, Dr. Joseph Conrad, Dr. Danielle Kimmel, Dr. Lwiindi Mudenda, Dr. Jenny Nesbitt, Dr. Mindy Leelawong, Christine Markwalter, Andrew Kantor, Matthew Park, Kelly Richardson, Megan van der Horst, Carson Moore, Armin Nourani – thanks for everything.

To my first friends in Nashville – Bryson Howard (even though we already knew each other. Go Dins!), Brad Durbin, Allison Galassie, and Lauren Gibson – our friend circle was so important to me. I'm glad we bonded over the shared experience of re-living acid/base titrations during orientation. I loved having people to celebrate milestones with and remind me that there is

a life outside of lab. Drew Kellum – Dude! I have so enjoyed our almost weekly lunches and the deep conversations that we get into. You have helped keep me sane these past few years. Never change. Metal. I have to give a shout out to our custodian. Greg – the work we do would be impossible without you. On top of that, you're always around with an encouraging word or thoughtful conversation when things aren't going so well. Thank you for taking care of us.

I would not be in this program if it weren't for my AP chemistry teacher, Kristin Baksa. She inspired my love for chemistry and is the reason I studied it in college. Because of her, I was first introduced to research as a high school senior. At Furman, I had the privilege of being mentored by Drs. John and Sandy Wheeler, who further encouraged my love of research. I am also grateful to Drs. Jim Maher and Nicole Becker at the Mayo Clinic for choosing me as a summer research fellow and giving me knowledge that I continue to use today.

To my best friends, Rachel Clyborne, Joya Cooley, Amanda Sodergren, and Caitlin Sylvester – I can't believe how lucky I got living next to you all 9 (!) years ago on Haynesworth 200. Until we met, I didn't know it was possible to feel so close to four people, even when you are so far away from one another. You have made me laugh, cry, and everything in between. I wouldn't trade it for anything.

Finally, none of this would have been possible without my family. My parents are an endless supply of encouragement, ideas, and solutions even when they have no idea what I'm talking about. They have supported me in everything throughout this crazy journey – including hauling my stuff all over the country numerous times! I have learned so much about life from them. Thank you. To my sister – I am so proud of you and I can't wait to see what you do with your life. I am confident you will be successful in everything you do.

TABLE OF CONTENTS

LIST OF TABLES

LIST OF FIGURES

CHAPTER I

INTRODUCTION

Gold Nanoparticles in Biomedicine

Nanoscale gold possesses unique properties that are distinct from those of bulk gold. The bright red color of gold nanoparticle solutions arises from the phenomenon of localized surface plasmon resonance (LSPR).[1] LSPR occurs when free electrons on the nanoparticle surface collectively oscillate at the frequency of incident light. This causes the nanoparticles to scatter and absorb light, and generates strong electric fields on the particle surface. The position of the LSPR peak is related to the size, shape, structure, and surface environment of the nanomaterial. Gold nanoparticles can be synthesized in different sizes and shapes, which exhibit different optical properties. Post-synthesis modification with biologically relevant molecules such as small molecules, peptides, DNA, proteins, and polymers improves colloidal stability in biological media. Surface modification also provides functionality for biomedical applications like sensing, imaging, targeting, delivery, or diagnostics.[1–3] Nanoscale gold has been used in biomedicine mainly because of its low acute toxicity *in vivo* and unique optical properties conferred by LSPR.[1–3] Gold nanoparticles are strong fluorescence resonance energy transfer quenchers and can be combined with fluorescent reporter molecules to detect biological targets by changes in fluorescence intensity. LSPR makes gold nanoparticles useful for visualization of target molecules by optical imaging, signal readout in diagnostic lateral flow and aggregation assays, and enhancement of Raman scattering signal. Finally, gold nanoparticles can be used for drug delivery or as therapeutic agents themselves (*e.g.* photothermal and photodynamic therapy).

DNA Functionalized Gold Nanoparticles

Functionalization of gold nanoparticles with short sequences of thiolated DNA results in a material with its own distinctive properties. Since its introduction in 1996, DNA functionalized gold nanoparticle (DNA-AuNP) chemistry has become a unique platform for nucleic acid sensing strategies that range from diagnostic to therapeutic.[4–9] "Nano-flares" were the first intracellular nucleic acid sensing DNA-AuNPs.[10] In this construct, a 13 nm gold nanoparticle is conjugated to a DNA capture sequence that is designed to bind target mRNA. The flare, a short fluorescently labeled DNA strand, is complementary to a portion of the capture sequence, and the fluorescence is quenched by the gold surface. Hybridization of target mRNA to the capture sequence releases the flare and mRNA expression is detected as an increase in fluorescence. In this design, important spatial information is lost because the signal-generating strand is not bound to the mRNA target.

The Wright laboratory has developed hairpin DNA functionalized gold nanoparticles (hAuNPs) as intracellular mRNA sensors for live cell imaging.[6,7,11] A 15 nm gold nanoparticle is conjugated to i) a thymine spacer ligand and ii) a sensing DNA strand designed to assume a hairpin or stem-loop configuration (Figure 1.1). Both types of DNA are attached to the gold surface by a 5' hexane thiol modification. The hairpin DNA sequence is designed to have a ten-thymine spacer region, five base-pair stem formation sequence, recognition loop, and a 3' cyanine dye (Cy5) modification. The recognition loop sequence is complementary to an mRNA of interest. The self-complementary stem formation sequence forces the DNA to adopt a hairpin configuration, which holds the dye proximal to the gold surface, quenching the fluorescent signal. Upon hybridization of a complementary sequence to the recognition loop, the formation of a more thermodynamically stable mRNA-recognition loop double helix causes the stem to
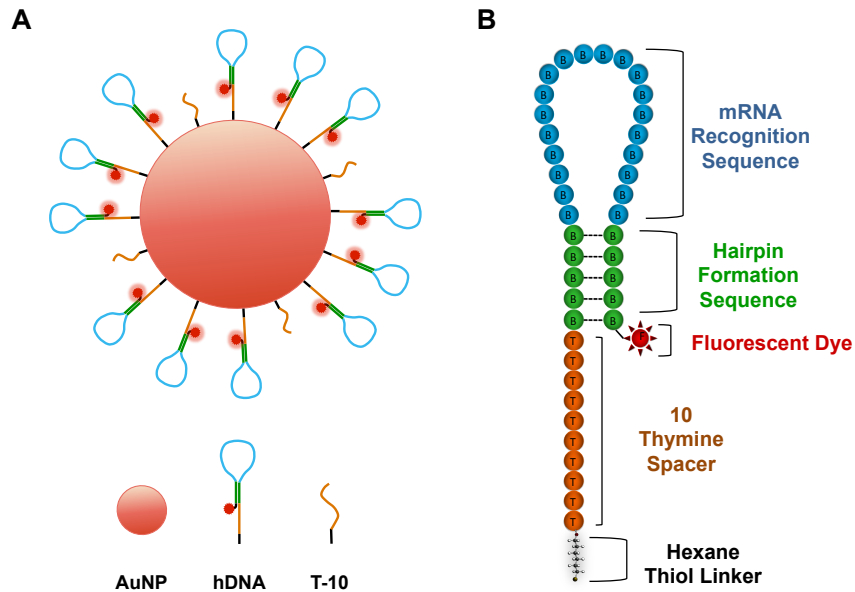
Figure 1.1. hAuNP design. (A) hAuNP structure (B) hairpin DNA design.

unwind and physically forces the fluorophore away from the gold surface. The presence of a

target mRNA is then detected as an increase in fluorescence (Figure 1.2). In this design, the

fluorescent reporter is hybridized to the mRNA target, meaning these probes can report on both

expression and the spatial localization of mRNA within the cell. hAuNPs are effective live cell

probes because they are efficiently internalized without transfection agents, are resistant to

nuclease degradation, and have low fluorescence background.[6,7]
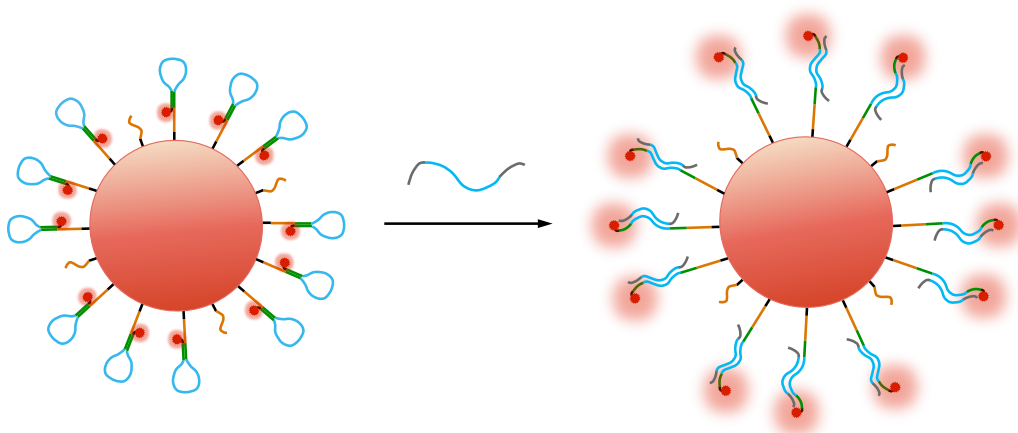
Figure 1.2. hAuNP sensor function. Binding of a complementary nucleic acid moves the fluorophore
away from the gold surface, and an increase in fluorescence is used as the signal readout.

3

Cellular Uptake of Gold Nanoparticles

In order to design effective nanomaterials that are successful in *in vivo* applications, the interactions between cells and gold nanoparticles must be understood at the *in vitro* level. A number of nanoparticle properties influence cell entry, including size, shape, composition, surface charge, aggregation state, and surface chemistry.[12–15] Cellular uptake is also influenced by biological variables, including cell type, cell age, surface proteins, culturing conditions, and the presence of a protein corona on the particle.[13,15] Nanomaterials are often transported across the membrane via multiple pathways, although one or more may be primary for a particular nanoparticle system. Most nanomaterials are internalized by active uptake mechanisms, including phagocytosis, pinocytosis, macropinocytosis, clathrin- and caveolae-mediated endocytosis (receptor-mediated), and non-specific endocytosis.[12,13,15] Of these, clathrin- and caveolae-mediated endocytosis are the most commonly reported mechanisms of nanoparticle uptake. During endocytosis, the cell encloses the nanoparticle into a plasma membrane derived vesicle and transports the material into the intracellular space. Typically, the mechanism of uptake is established using pharmacological compounds to systematically inhibit different target pathways and identify conditions that reduce nanoparticle accumulation.

The physicochemical properties of nanomaterials – size, shape, surface charge, and surface chemistry – are important determinants of cellular uptake kinetics and mechanism.[13,14,16] Because this dissertation only encompasses spherical gold nanoparticles, the effects of shape will not be discussed here. Nanoparticle surface chemistry is determined by the nature of the stabilizing ligands, which can confer enhanced cellular uptake properties, as is the case for nanoparticles modified with cell penetrating peptides or DNA.[7,10,13] There are conflicting reports on the size and surface charge that result in the highest cellular accumulation. Different results

are likely the consequence of the interplay of additional variables like nanoparticle material or chemistry of the surface ligands. As a result, it is difficult to choose one or two properties that universally predict cellular uptake. Rather, predictive factors must be determined for each nanoparticle system individually.

DNA-AuNPs are readily taken up by cells without requiring additional transfection reagents.[6,7,11,17,18] The dense 3D architecture of the DNA monolayer, rather than the nanoparticle core material, is responsible for cell entry. Efficient internalization has been demonstrated for gold nanoparticles, block copolymer nanoparticles, and even enzymes by coating these materials with a dense layer of DNA.[19,20] Crosslinking the DNA strands of a DNA-AuNP before dissolving the gold nanoparticle with KCN results in "hollow" DNA-AuNPs that retain the ability to traverse the cell membrane, further supporting the importance of the 3D structure.[17,21]

Mechanistic studies by the Mirkin laboratory indicate that endocytosis of DNA-AuNPs is mediated by scavenger receptor proteins located on the cell membrane.[17,22] Sodium azide treatment reduced nanoparticle association by about 55%, suggesting an energy-dependent mechanism.[17] Significant decreases in cellular uptake were achieved by pharmacological inhibitors that deplete or sequester cholesterol and by silencing the expression of caveolin-1 and a class A scavenger receptor (SR-A). Combined with immunofluorescence and TEM imaging showing that DNA-AuNPs localized to lipid-raft microdomains, this suggested that lipid-raft/caveolae-mediated endocytosis is a dominant mechanism. Expression of caveolin-1 and SR-A by four cell lines was positively correlated to the degree of nanoparticle accumulation, further confirming the importance of these proteins.[17] Additional investigations explored binding of DNA-AuNPs to SR-A. A protein pull down assay revealed enrichment of lipid-raft proteins and SR-A in the DNA-AuNP bound fraction, while a modified ELISA measured high affinity

binding between the SR-A and DNA-AuNPs. Treating cells with known SR ligands decreased accumulation of nanoparticles due to competition for binding to the receptor.[22] It was hypothesized that SR proteins mediate DNA-AuNP uptake because the dense DNA monolayer mimics the 3D structure of known SR ligands, such as poly I and poly G nucleic acids.

Mechanistic studies of hAuNP internalization from our laboratory suggested that cell membrane fluidity could play an important role.[6] Pharmacological compounds were used to inhibit different modes of endocytosis, and changes to hAuNP uptake were observed under three conditions. Inhibition of caveolae-mediated endocytosis by cholesterol depletion increased hAuNP uptake. Incubation of the cells at 4°C and addition of fetal bovine serum (FBS) to the culture medium reduced uptake. Depletion of cellular energy by sodium azide and 2-deoxy-D-glucose did not alter hAuNP internalization, suggesting that cell entry could occur through an energy independent mechanism. In addition to inhibiting endocytic pathways, depletion of cholesterol and incubation at 4°C both modulate membrane fluidity, leading to the conclusion that hAuNP – lipid membrane interactions could be involved in intracellular accumulation.

Scope of Dissertation

Understanding cellular uptake allows for the development of more effective nanomaterials that possess enhanced diagnostic and therapeutic performance. Furthermore, the safe application of such materials in biomedicine necessitates a rigorous understanding of how nanoparticles are transported into cells. The processes and variables that underlie cellular uptake are complex and interrelated, and a comprehensive explanation is still lacking. This dissertation explores the role of biological and physicochemical properties at the nano-bio interface to advance our knowledge of the cellular uptake of DNA-AuNPs. Chapter II attempts to elucidate the role of cell membrane lipids in the transport of hAuNPs into the cytoplasm, which has not

6

been previously explored. Giant unilamellar vesicles (GUVs) are chosen as a protein-free cell model to study the passive transport of hAuNPs. The inclusion of FBS, a common cell culture additive and known modulator of cellular uptake, causes the nanoparticles to concentrate in the vesicle membrane. In contrast, cultured cell lines fully internalize the nanoparticles without significant membrane adsorption. As a result, we conclude that while the existence of hAuNP-lipid interactions cannot be ruled out, GUVs are not an appropriate model of cellular uptake. Chapter III is based on the observation that gold nanoparticles conjugated to double stranded DNA are less efficiently internalized than nanoparticles attached to hairpin or single stranded DNA. This led to a systematic study of the physicochemical properties that influence the accumulation of DNA-AuNPs in cultured cells. The hydrodynamic diameter is found to be the most predictive property of how much nanomaterial a cell will accumulate. In comparison, surface charge and density of the DNA ligands are minor contributors. These results outline design considerations that will enhance cellular uptake and nanomaterial performance. Chapter IV quantifies the cellular accumulation of hAuNPs by human, insect, and bacterial cells to determine if differences in uptake are related to organism-specific membrane compositions. Three human cell lines and a *Drosophila melanogaster* cell line exhibit robust internalization of hAuNPs. This is hypothesized to be the result of scavenger receptor mediated endocytosis. In contrast, *Bacillus subtilis* and *Escherichia coli* and their protoplasts (cell wall deficient bacteria) accumulate lower amounts of nanoparticles. Addition of FBS alters the amount of bacteria- or protoplast-associated nanoparticles. Further investigations with electron microscope imaging are necessary to determine whether the nanoparticles are truly internalized or simply embedded in the cell wall or membrane. Finally, Chapter V outlines the importance of studying the nano-bio interface and offers future directions for studying the cellular uptake of hAuNPs.

CHAPTER II

GIANT UNILAMELLAR VESICLES AS MODEL SYSTEMS TO EXPLORE THE PASSIVE

TRANSPORT OF HAIRPIN DNA FUNCTIONALIZED GOLD NANOPARTICLES INTO

CELLS

Introduction

Nanomaterials are increasingly used for a number of environmental, biomedical, and

personal care applications and products.[13] The success of nanoparticles as biomedical

technologies often rests on the ability of these particles to enter the intracellular space or interact

with the external membrane, raising concerns about safety and potential toxic effects. Thus it is

important to understand the interaction between cells, as a fundamental biological unit, and

nanoparticles, in order to fully characterize the fate and downstream effects of the particles on a

biological system. This chapter aims to explore the cellular uptake mechanisms of hairpin DNA

functionalized gold nanoparticles (hAuNPs) using a simplified model membrane system.

Existing knowledge on DNA functionalized gold nanoparticles has focused on endocytic

mechanisms mediated by membrane proteins, without a complete exploration of the

contributions the phospholipid bilayer could be making towards nanoparticle internalization.[17,23]

The major function of the cell membrane is to form a protective barrier that controls the

flow of molecules into and out of the intracellular space.[13,24] Extracellular substances are brought

into the cell through two broad mechanisms: endocytosis, an active transport mechanism

requiring energy expenditure, and passive diffusion, which is energy independent. Endocytosis is

an overarching term that encompasses several subcategories, including phagocytosis,

pinocytosis, macropinocytosis, caveolae-dependent endocytosis, and clathrin-mediated endocytosis. Substances are transported from the exterior to the interior of the cell by enclosing them in vesicles derived from the plasma membrane. This mechanism is thought to be the primary pathway for nanomaterial uptake into the cell, and is typically explored by using pharmacological inhibitors to reduce or eradicate a target endocytic pathway.

In contrast to endocytosis, passive transport involves the diffusion of molecules through the lipids of the plasma membrane and is driven by concentration gradients.[13] Passive transport is difficult to study in cells, because the dominant mechanism of endocytosis makes it problematic to detect.[25] Because passive diffusion cannot be completely isolated from endocytosis, simplified membrane systems have been explored as models to understand the passive transport of nanoparticles.[26-30] Red blood cell models are useful, because these cells lack the ability to perform endocytosis; however, the fixed membrane composition of red blood cells does not allow for an exploration of membrane composition as a variable in nanoparticle internalization.

Giant unilamellar vesicles (GUVs) were chosen to model passive transport of nanoparticles. A GUV consists of a single phospholipid bilayer that encloses an aqueous buffer to form a sphere. The vesicles are similar in size to cells (tens of microns in diameter), can be prepared from a well-defined lipid blend, and mimic compartmentalization, a basic function of the plasma membrane.[24,31] Because no proteins are incorporated into the lipid bilayer, passive transport is the exclusive mode of translocation into GUVs. Other membrane systems – supported bilayers and liposomes – were initially explored (Appendix A), but GUVs were chosen for the ease of manipulating the lipid composition and the ability to visualize the vesicles by confocal microscopy.

Previous work suggested that cellular uptake of hAuNPs may be influenced by membrane fluidity. Jayagopal, et al. found that treating cells with nystatin/progesterone increased hAuNP uptake, while preincubating at 4°C and including fetal bovine serum (FBS) in the cell medium reduced hAuNP uptake.[6] Nystatin/progesterone and 4°C treatment both decrease endocytosis, by inhibiting caveolar endocytosis through cholesterol depletion and inhibiting cellular metabolism, respectively. These treatments also affect membrane fluidity, with pre-incubation at 4°C reducing fluidity and nystatin/progesterone increasing it. These results led to an interest in the role of cholesterol, temperature, and FBS in the passive transport of hAuNPs through a phospholipid bilayer. Cholesterol is a bidirectional regulator of membrane fluidity, keeping the membrane from becoming too stiff at cold temperatures, and keeping it ordered at high temperatures.[32] At a constant temperature, reducing the amount of cholesterol will make the membrane more fluid. Low temperatures are expected to increase membrane rigidity, while high temperatures should increase fluidity. The inclusion of FBS in cell culture medium is known to decrease uptake for many different types of nanoparticles,[6,22,33,34] although it sometimes increases uptake.[35,36] GUVs can easily be manipulated with respect to each of these variables – cholesterol content, temperature, FBS – to determine how nanoparticle transport across the model membrane is impacted. To explore this, GUVs were prepared from a custom blend of animal derived phospholipids intended to mimic the composition of an epithelial cell membrane. GUVs made with a range of cholesterol concentrations were exposed to hAuNPs at varying temperatures in the presence or absence of FBS. hAuNPs were found to strongly associate with the GUV membrane when FBS was present as demonstrated by confocal microscopy and flow cytometry. These results were compared to cellular uptake of hAuNPs by CaSki cells, a cervical cancer cell line, to evaluate the utility of GUVs as a model of nanoparticle uptake.

Materials and Methods

Materials

Citrate-stabilized gold nanoparticles (15 nm) were purchased from Ted Pella, Inc. All DNA was purchased from Integrated DNA Technologies. Amicon Ultra 3K MWCO filters were purchased from EMD Millipore. CaSki cells were purchased from ATCC. Egg phosphatidylcholine (PC), egg phosphatidylethanolamine (PE), liver phosphatidylinositol (PI), brain phosphatidylserine (PS), and egg sphingomyelin (SM) were purchased from Avanti Polar Lipids, Inc. The 8 well μslides were purchased from ibidi USA, Inc. Fetal bovine serum (FBS) was purchased from Atlanta Biologicals. $DiOC_{18}(3)$, penicillin/streptomycin, trypsin, and trypan blue were purchased from Thermo Fisher Scientific. HEPES was purchased from Research Products International, Corp. Molecular biology grade water, Tris-EDTA buffer, RPMI 1640 with L-glutamine, sodium pyruvate, and phosphate buffered saline (PBS), were purchased from Corning. All other chemicals and materials were purchased from Sigma-Aldrich or Fisher Scientific.

Cell Culture

CaSki cells were grown at 37°C in a humidified atmosphere with 5% CO_2. The culture medium was RPMI 1640 with L-glutamine supplemented with 10% FBS, 100 units/mL penicillin, 100 μg/mL streptomycin, 2.25 g/L D-glucose, 1 mM sodium pyruvate, and 10 mM HEPES. Upon reaching 80-90% confluence, the cells were subcultured and medium was replaced as needed.

DNA Preparation

All DNA was received as a lyophilized pellet. DNA containing a thiol modification was dissolved in a solution of 0.1 M dithiothreitol (DTT) in 0.1 M dibasic sodium phosphate, pH 8.3.

The DNA was vortexed to dissolve the pellet and reacted for 1 hour with rotation in the dark. The sample was desalted and washed with Tris-EDTA buffer in Amicon Ultra 3K molecular weight cutoff (MWCO) filters using the manufacturer's directions. The DNA was resuspended in Tris-EDTA buffer at an appropriate working concentration, which was determined by measuring the A_{260} using a Take3 Microvolume Plate and Biotek Synergy H4 microplate reader. Unmodified DNA sequences were reconstituted in Tris-EDTA buffer and the concentration determined as for thiolated sequences. All DNA was stored at -80°C until use.

hAuNP Synthesis

Citrate-stabilized AuNPs (15 nm) were diluted to 1 nM in molecular biology grade water and 1 mL of AuNPs containing 0.1% (v/v) Tween20 was dispensed into 1.5 mL centrifuge tubes. The T-10 diluent oligonucleotide was added at a final concentration of 0.1 µM. The tubes were incubated at room temperature overnight on a tube rotator and protected from light. Hairpin DNA was added at a final concentration of 0.3 µM and the samples were incubated overnight as before. The solutions were buffered to pH 7 with 100 mM phosphate buffer (10 mM final concentration) and the nanoparticles were adjusted to 0.1 M NaCl, followed by a ≥ 4 hour incubation. The nanoparticles were adjusted to 0.2 M NaCl, followed by a ≥ 4 hour incubation. Finally, the nanoparticles were adjusted to 0.3 M NaCl, followed by an overnight incubation. The hAuNPs were centrifuged at 21,100 *g* for 20 minutes to form a loose pellet. After removal of the supernatant, the pellet was resuspended in PBS. The process of centrifugation and resuspension was repeated two times to obtain a final, concentrated pellet. Individual tubes of hAuNPs were combined into a single batch of hAuNPs.

hAuNP Characterization

      The hAuNPs were characterized by fluorescence, dynamic light scattering, and oligonucleotide loading. hAuNP fluorescence was measured before and after the addition of a complementary oligonucleotide that binds to the loop region of the hDNA. The stock of concentrated hAuNPs was diluted to 1 nM in PBS with 0.1% Tween20. The hAuNPs were exposed to complementary and non-complementary DNA (3 uM) or no DNA for 1 hour at 37°C. The fluorescence of each solution was measured in triplicate in a black 96 well plate using a Biotek Synergy H4 microplate reader configured for Cy5 fluorescence (excitation: 650 nm; emission: 670 nm). Dynamic light scattering was used to obtain the hAuNP hydrodynamic diameter. A 1 nM solution of hAuNPs in PBS was filtered through a 0.22 μm PVDF syringe filter before analyzing with a Malvern ZetaSizer NanoZS. The zeta potential of the nanoparticles was measured on the same instrument. A 1 nM solution of hAuNPs in 10 mM NaCl was filtered through a 0.22 μm PVDF syringe filter before analyzing with a dip cell. To quantify the fluorescent hDNA loading on the nanoparticles, a 1 nM solution of hAuNPs diluted in 0.1 M DTT was reacted for 2 hours on a tube rotator. The samples were centrifuged at 21,100 g for 20 minutes and the supernatant was analyzed for Cy5 fluorescence in triplicate in a black 96 well plate. The resulting measurement was compared against the fluorescence from a calibration curve of free hDNA to find the concentration of fluorescent DNA in the hAuNP samples. The DNA concentration was divided by the AuNP concentration to arrive at the average number of hDNA ligands per nanoparticle. Reported values represent mean ± SD from three batches with three technical replicates each.

Preparation of Giant Unilamellar Vesicles

GUVs were prepared by the gentle swelling method as described by S. Manley and V. Gordon.[37] The lipids PC, PE, PI, PS, SM, and cholesterol were mixed together in a 50 mL round bottom flask in the desired ratios (Table 2.1). If needed, DiO dye (0.5 mg/mL ≈ 0.5 mM stock solution in DMF) was added at 0.1 mole%. The total amount of membrane components was 1 μmole. Chloroform (300 μL) was added and the solution was thoroughly mixed. The chloroform was removed with a rotary evaporator to form a thin lipid film, which was subjected to vacuum for 2 hours to remove trace solvent. The film was pre-hydrated for 30 minutes with warm (42 – 45°C) water saturated nitrogen. The flask was gently filled with 2 mL of 100 mM sucrose in PBS, sealed with parafilm, and incubated at 37°C for 24 – 48 hours. When the GUVs could be visualized as a cloudy suspension, they were transferred to a microcentrifuge tube and stored at 4°C for up to one week. Each batch of GUVs was checked for successful vesicle formation using confocal microscopy.

	Mole % of Membrane			
Lipid	0% Cholesterol	5% Cholesterol	10% Cholesterol	15% Cholesterol
PC	47	44.7	42.3	40
PE	17.6	16.7	15.8	15
PI	10.6	10.1	9.5	9
PS	8	7.6	7.2	7
SM	16.5	15.7	14.9	14
Cholesterol	0	5	10	15

Table 2.1. GUV membrane compositions

Confocal Microscopy – GUVs

Samples were composed of GUVs (1:10 dilution of GUV suspension) and hAuNPs (10 nM) diluted in 200 mM glucose in PBS with and without FBS (10% v/v). Each sample was mixed by inversion and incubated at 37, 25, or 4°C for 4 hours. Images were taken with a Zeiss

LSM 510 Meta Confocal Microscope using a 63x plan-apochromat 1.4 oil DIC objective and a 1.6 µm optical slice. Excitation of the DiO and Cy5 fluorophores was done with 488 nm and 633 nm lasers, respectively. Emission was collected with BP 505-550 and LP 650 filters. Optical slices were taken through the entire volume of the vesicle.

Flow Cytometry – GUVs

Single color controls were prepared from unstained and DiO stained GUVs. hAuNP only stained controls were prepared with unstained GUVs, supplemented with 10% FBS and incubated at 4°C for 4 hours. Samples were prepared by diluting a DiO stained GUV suspension 1:5 in 200 mM glucose in PBS. The GUVs were incubated with 10 nM hAuNPs with and without FBS (10% v/v) at 37, 25, or 4°C for 4 hours. The tubes were centrifuged at 1500 g for 10 minutes. The supernatant was removed and the GUVs were washed in 100 mM glucose in PBS three times to remove excess hAuNPs. A BD LSRII flow cytometer with excitation at 488 nm and 633 nm was used to collect 1,500 – 5,000 single GUV events from each sample. Using microbeads (Spherotech Ultra Rainbow Calibration beads, 6 peaks) of known size (5 – 5.4 µm) GUVs greater than 5 µm in diameter were collected. FlowJo analysis software was used to visualize the data. The unstained and DiO stained cells were used to set gates that identified the double positive population (GUVs positive for DiO and hAuNP fluorescence). Reported values represent mean ± SD from two replicates.

Cellular Uptake

CaSki cells (1.5×10^5 cells per well) were seeded into a 12-well plate one day in advance. Before adding nanoparticles, half of the wells were washed with PBS three times to remove trace FBS. hAuNPs were added to the cells at 1 nM final concentration in 0.5 mL of serum-free or serum-supplemented medium (10% v/v FBS). The cells were incubated at 37°C or

4°C for 4 hours. The hAuNP-containing media was removed. The cells were washed three times with PBS, trypsinized, and collected for flow cytometry or ICP-MS.

Flow Cytometry – CaSki Cells

A BD LSRII flow cytometer with excitation at 633 nm was used to collect 10,000 single cell events from each sample. Serum-supplemented and serum-free cells that were not exposed to hAuNPs were analyzed as a negative control. FlowJo analysis software was used to visualize the data. Reported values represent mean ± SD from three biological replicates.

ICP-MS – CaSki Cells

The cells were stained with trypan blue and counted on a Countess II automated cell counter. The samples were centrifuged at 500 g for 5 minutes to form a pellet, which was stored at -40°C until analysis, at which time the samples were digested overnight in 800 µL aqua regia (3:1 HCl : HNO$_3$). (*Warning: Aqua regia is extremely corrosive, handle with caution*). The next day, deionized H$_2$O was added to each tube to achieve a volume of 6 mL. The [197]Au content of the samples was measured on a Thermo Element 2 high resolution inductively coupled plasma mass spectrometer (ICP-MS) equipped with an electrospray ionization (ESI) auto sampler at medium resolution ($R = 4300$). Samples were uptaken by self-aspiration via a 0.50 mm ID sample probe and capillary to the spray chamber. The number of AuNPs per cell was calculated from the gold concentration and the number of cells counted, as described in Appendix E. Reported values represent mean ± SD from three biological replicates.

Confocal Microscopy of CaSki Cells

CaSki cells (5×10^4 cells/mL) were seeded into an 8-well µslide two days in advance. Before adding nanoparticles, half of the wells were washed with PBS three times to remove traces of FBS. hAuNPs were added to the cells at 1 nM final concentration in 200 µL of serum-

free or serum-supplemented (10% v/v FBS) medium. The cells were incubated at 37°C or 4°C for 4 hours. A working stock of DiO (10 nM) was prepared in serum-supplemented medium. The hAuNPs were removed and the cells washed three times with PBS, before being stained with DiO for 10 minutes at room temperature, protected from light. Excess stain was removed and the cells were washed three times with phenol-red free medium for one-minute intervals. A final volume of 100 μL of phenol-red free medium was added for imaging. Images were taken with a Zeiss LSM 510 Meta Confocal Microscope using a 63x plan-apochromat 1.4 oil DIC objective and a 1.4 μm optical slice. Excitation of the DiO and Cy5 fluorophores was done with 488 nm and 633 nm lasers, respectively. Emission was collected with BP 505-550 and LP 650 filters.

Results and Discussion

hAuNP Characterization

hAuNPs were synthesized using the hairpin DNA (hDNA) sequence given in Table 2.2. The recognition loop sequence was chosen to be non-targeting so as to focus only on cellular uptake. hAuNPs were characterized by fluorescence spectrophotometry, dynamic light scattering (DLS), zeta potential, and amount of hDNA per nanoparticle (Figure 2.1). Complementary and non-complementary DNA sequences were added to hAuNPs to demonstrate hDNA function. An increase in fluorescence only occurs with the addition of complementary DNA. Adding non-complementary DNA results in the same amount of fluorescence as untreated hAuNPs. The hydrodynamic diameter of the hAuNPs is 29.2 ± 0.5 nm, an increase of 10.8 nm compared to citrate-capped AuNPs. The increase in size arises from the conjugation of DNA to the gold surface. These nanoparticles have a negative zeta potential, as expected due to the negatively charged phosphate backbone of DNA. Each nanoparticle has an average of 76 ± 7 strands of hDNA attached to the surface, which was measured by using DTT to release the DNA ligands.

	Sequence (5' – 3')
hDNA	TTTTTTTTTT<u>CGACG</u>**GTTTCTCTACGTGTTCTTG**<u>CGTCG</u>
Complementary DNA	TTCAAGAACACGTAGAGAAACTT

Table 2.2. hDNA and complementary DNA sequences. Underline indicates stem formation sequence. Bold indicates recognition loop.

A

B

C
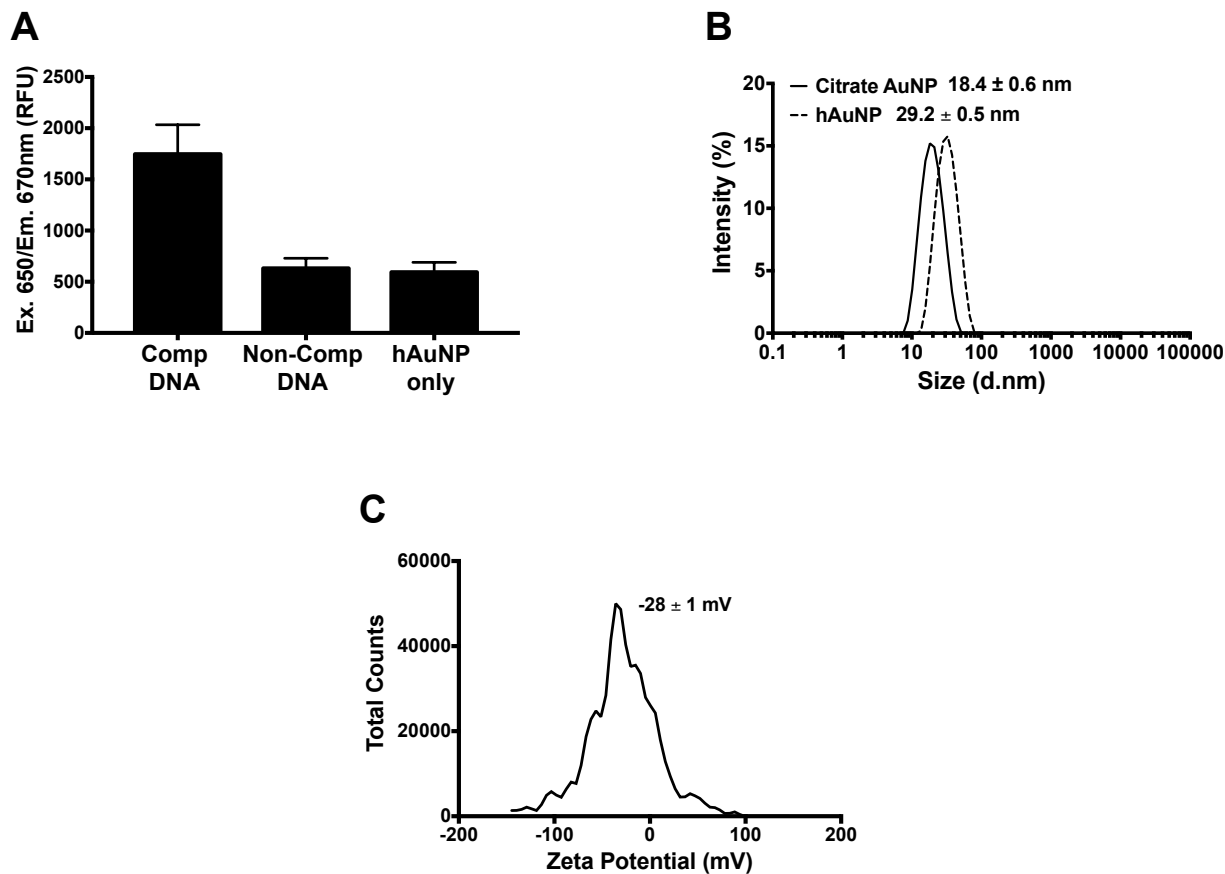
Figure 2.1. hAuNP Characterization. (A) The fluorescence of hAuNPs treated with complementary (comp) and non-complementary (non-comp) DNA demonstrated that the hairpin functions as expected. Complementary DNA caused an increase in fluorescence due to opening of the hairpin, but nonspecific DNA did not. (B) Conjugating DNA to create hAuNPs causes an increase in the hydrodynamic diameter of the gold nanoparticle. (C) The negative zeta potential of hAuNPs results from the negatively charged phosphate backbone of DNA.

hAuNP Interaction with GUVs

GUVs are useful models of cell membranes because they are cell-sized (10 – 30 μm in

diameter), easily prepared from custom lipid blends, and can be visualized using confocal

microscopy. A blend of phosphatidylcholine (PC), phosphatidylethanolamine (PE), phosphatidylinositol (PI), phosphatidylserine (PS), sphingomyelin (SM), and cholesterol was chosen to mimic the major lipid populations and composition found in an epithelial cell membrane (Figure 2.2A).[38–42] The initial composition (15% cholesterol) was then adjusted to create GUVs where the cholesterol content was decreased, while keeping the other lipids in the same ratios to one another (Table 2.1). The vesicles were prepared via the gentle hydration method, and visualized by confocal microscopy using a green fluorescent lipophilic dye (Figure 2.2B). Typical preparations consisted of GUVs with a range of sizes, with some vesicles appearing unilamellar and others appearing multilamellar. For clarity, unilamellar vesicles were chosen for all imaging experiments.
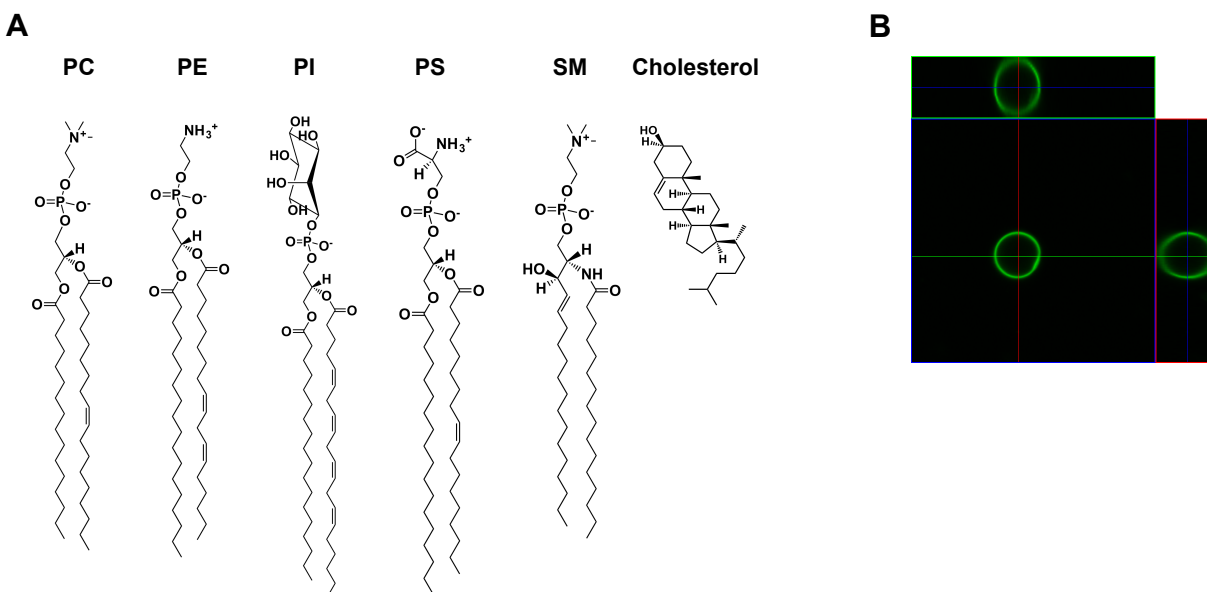
Figure 2.2. GUV lipid composition and visualization. (A) Structures of the lipids that comprise the GUV membrane. (B) The XY, XZ, and YZ images of a GUV. GUVs are spherical with uniform fluorescent staining throughout the membrane and an unstained lumen filled with aqueous medium.

To evaluate whether hAuNPs passively diffuse through the phospholipid bilayer, GUVs were treated with 10 nM hAuNPs for 4 hours at varying temperatures in the presence and

19

absence of FBS (10% v/v). Confocal microscope imaging reveals that in the presence of FBS,

hAuNPs localize and concentrate in the membrane of the GUV, as demonstrated by the

overlapping hAuNP fluorescence (red) and the DiO membrane fluorescence (green) (Figure 2.3,

Supplemental Figure D.1, Appendix D). Without FBS, hAuNP fluorescence is only observed

outside the vesicle, and hAuNP fluorescence is not detectable inside the vesicle lumen under any
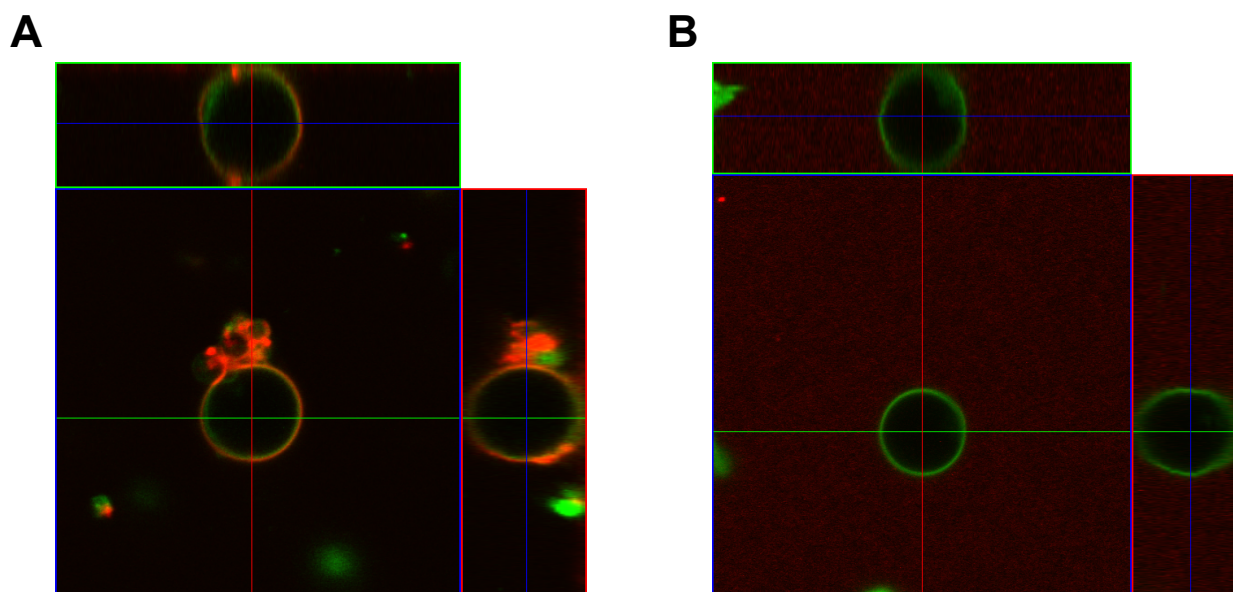
Figure 2.3. Representative images of 15% cholesterol GUVs exposed to hAuNPs in (A) 10% FBS and (B) 0% FBS. hAuNPs only associate with the GUV membrane when FBS is added. Green: DiO (membrane dye). Red: hAuNP

condition. All cholesterol concentrations and temperatures gave similar results (Supplemental

Figures D.2 – D.5, Appendix D). FBS facilitates the association and concentration of hAuNPs

within the phospholipid bilayer, but complete uptake into the vesicle is not observed in this

particular model. It is possible that hAuNPs are diffusing across the membrane, but are present in

the lumen in such a low concentration that the fluorescence is below the detection limit of the

instrument. Another explanation is that hAuNPs do not diffuse through pure lipid bilayers, and

membrane proteins drive the cellular uptake of nanoparticles. Several other reports exploring the

passive uptake of nanoparticles have shown that particles concentrate in the lipid bilayer, but do not pass through the membrane. Silica coated nanoparticles were found to adsorb or accumulate at phospholipid bilayers using GUVs and water-in-oil droplets.[27,30] GUVs were also used to demonstrate that polymer and gold nanoparticles accumulate in a densely packed layer at the vesicle membrane, although in each of these cases, the nanoparticle layer was heterogeneous and appeared aggregated, which was not observed with hAuNPs.[28,29] Wang, et al. showed that quantum dots become trapped in the membrane of red blood cells, without much internalization.[26] Although there was no FBS added to these systems, it is interesting that the nanoparticles adsorb to the membrane, but are not transported beyond the bilayer. For hAuNPs, it is possible that FBS is a mediator in this interaction, allowing more nanoparticles to adhere to the membrane. These data suggest that nanoparticles can strongly adsorb to the lipid membrane, but cannot complete the process of uptake without membrane proteins.

The hAuNP-GUV interaction was further explored by using flow cytometry to quantitate nanoparticle association with the membrane. Flow cytometry allows for analysis of thousands of vesicles from a sample, whereas confocal microscopy is limited in the number of images that can be collected per sample without requiring a significant amount of time. Calibration beads (5 μm) were used to set a FSC gate to collect GUVs larger than 5 μm. Events that were larger than 5 μm and double positive for DiO and Cy5 fluorescence (Q2 in Figure 2.4) were considered "hAuNP positive GUVs." GUVs were treated with hAuNPs as before, but several centrifugation steps were included to remove excess nanoparticles. Centrifugation and washing steps were necessary to reduce the coincident events that occurred during flow cytometry analysis due to the high concentration of nanoparticles in the samples. With no washing, 85% of the GUVs are classified as hAuNP positive in conditions (0% FBS) that do not result in detectable membrane association

by confocal microscopy (Figure 2.4A). After washing, the majority of GUVs are hAuNP

negative, which is more consistent with the imaging results (Figure 2.4C). This additional step

does not affect the vesicle morphology or alter the hAuNP behavior with respect to the GUV

membrane, as demonstrated by confocal microscopy (Figure 2.5). Under conditions where no

nanoparticle association with the membrane was expected, adding centrifugation steps does not

cause hAuNPs to become membrane-associated. FBS does not alter the scattering properties or

fluorescence of DiO labeled GUVs (Supplemental Figure D.6, Appendix D).
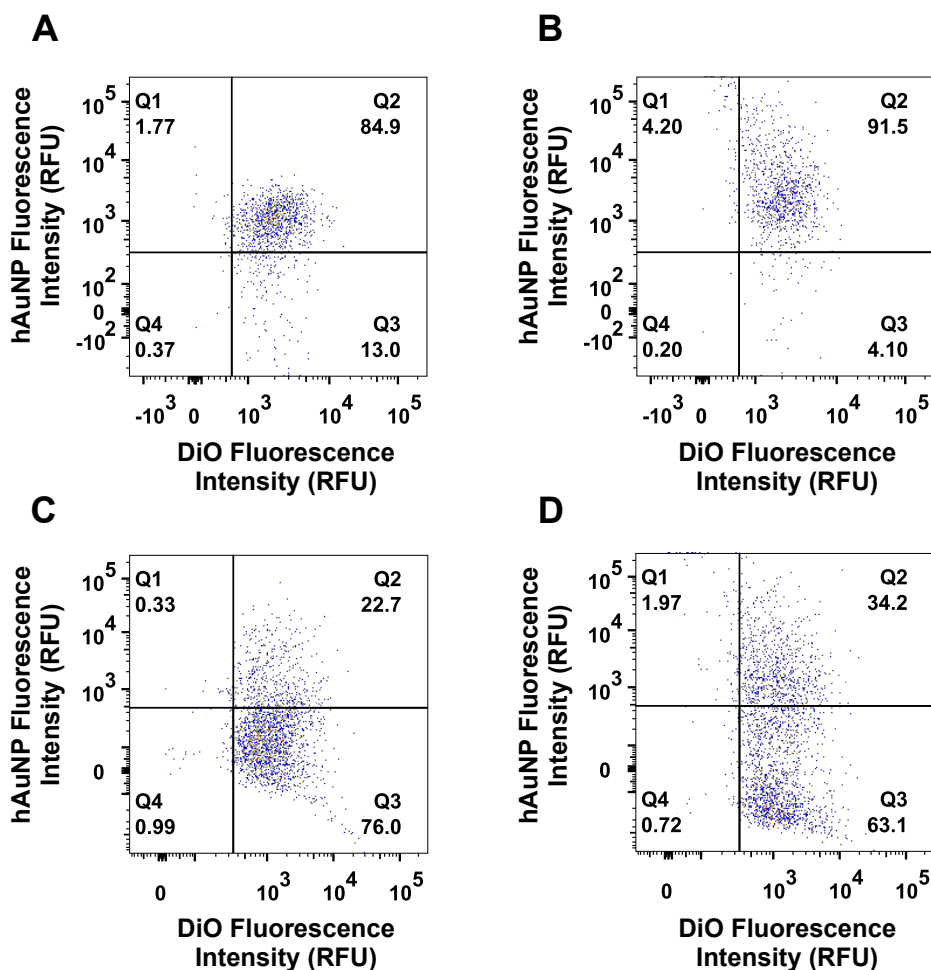
Figure 2.4. Flow cytometry dot plots of hAuNP fluorescence vs. DiO fluorescence for unwashed and washed GUVs. Unwashed GUVs were treated with hAuNPs at 4°C in (A) 0% FBS and (B) 10% FBS. Washed GUVs were treated with hAuNPs at 4°C in (C) 0% FBS and (D) 10% FBS. The centrifugation and washing steps are necessary to remove excess hAuNPs that cause coincident events that make the GUVs appear hAuNP positive. Q2 events are doubly positive for hAuNP and DiO fluorescence.
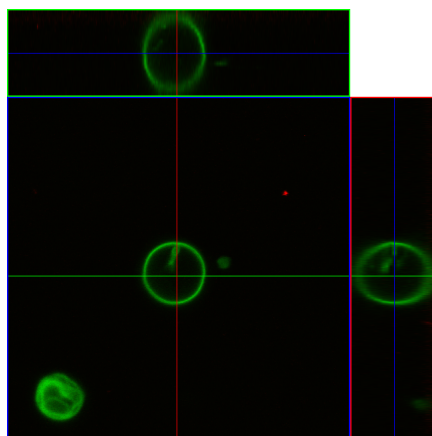
Figure 2.5. Effect of centrifugation on GUVs (15% cholesterol) exposed to hAuNPs at 4°C without FBS. After three centrifugation and washing steps, no significant changes in morphology occur. There is no detectable hAuNP fluorescence in the membrane, as is expected for these conditions. Therefore, it was concluded that centrifugation did not significantly alter how hAuNPs interact with the GUV membrane.

Figure 2.6 shows representative dot plots for 5% cholesterol GUVs treated with nanoparticles in 0% and 10% FBS. Each dot plot was divided into quadrants based on an unstained GUV sample in order to distinguish between singly and doubly positive GUV populations. The percentage of hAuNP positive GUVs was obtained from the Q2 gate and plotted against cholesterol content to determine how cholesterol, temperature, and FBS affect hAuNP association with the vesicle membrane (Figure 2.7). Varying the cholesterol concentration from 0 – 15 mol% does not impact the percentage of hAuNP positive GUVs, regardless of FBS content. Without FBS, the amount of hAuNP positive GUVs remains approximately the same over all temperatures. Adding FBS increases the amount of nanoparticle association with vesicle membranes, consistent with the confocal microscopy data. Flow cytometry provides an additional level of information by revealing that decreasing the temperature from 37°C to 4°C increases the number of GUVs that exhibit nanoparticle fluorescence. FBS demonstrates that temperature and the inclusion of FBS have the greatest influence on hAuNP association to the phospholipid bilayer, but the data are not consistent with
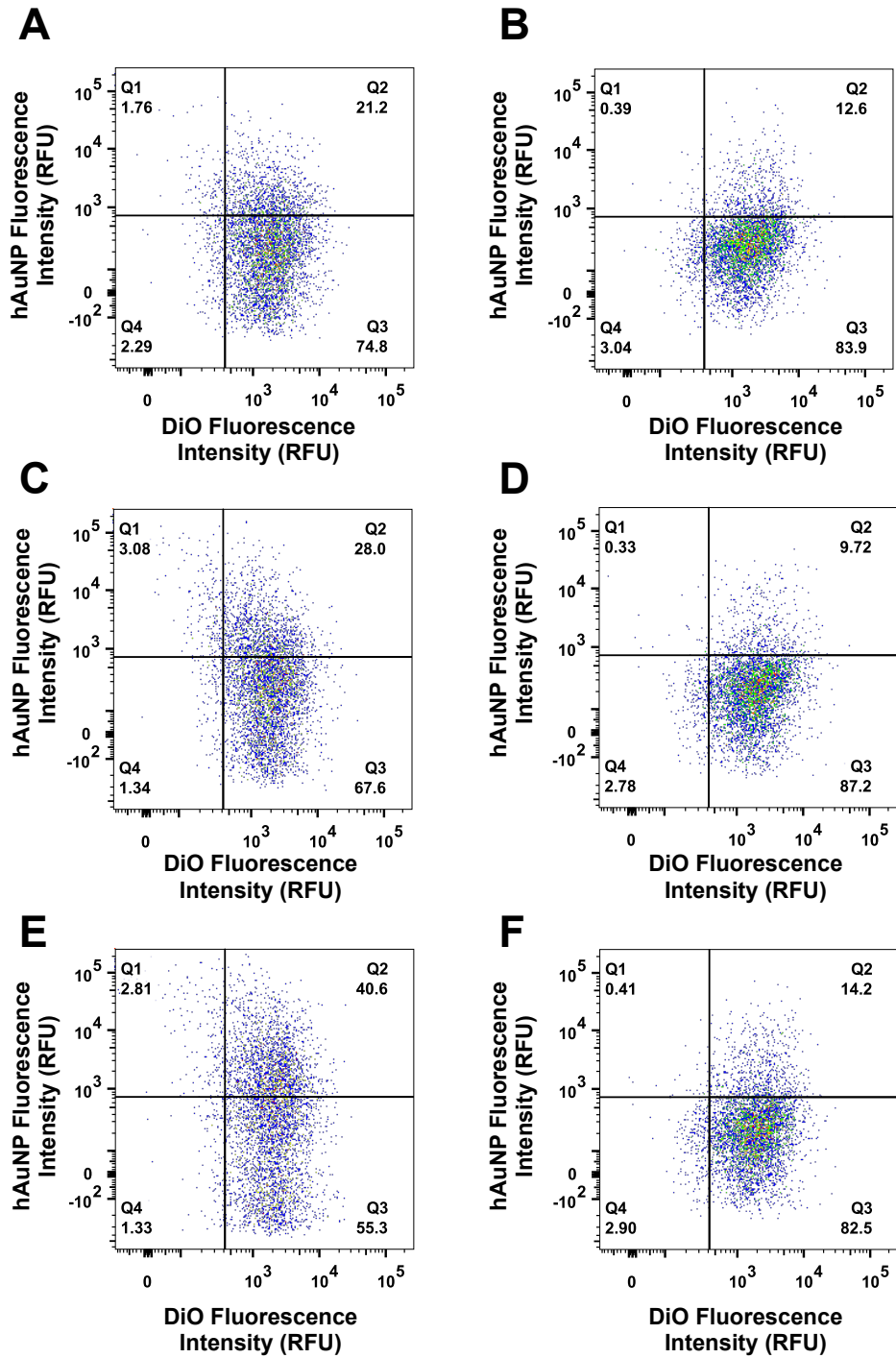
Figure 2.6. Flow cytometry results for 5% cholesterol GUVs after treatment at (A – B) 37°C (C – D) 25°C and (E – F) 4°C. (A, C, E) In the presence of 10% FBS, up to 40% of GUVs are hAuNP positive and the hAuNP fluorescence intensity shifts to higher values. (B, D, F) When no FBS is added, 10 – 15% of GUVs are hAuNP positive.

hypotheses based on *in vitro* cellular uptake data. It was expected that i) low temperatures would increase membrane stiffness, thus decreasing hAuNP uptake and ii) adding FBS would decrease uptake. In order to fully understand these results in the context of cellular uptake, the above experiments were recapitulated in a cervical cancer cell line.
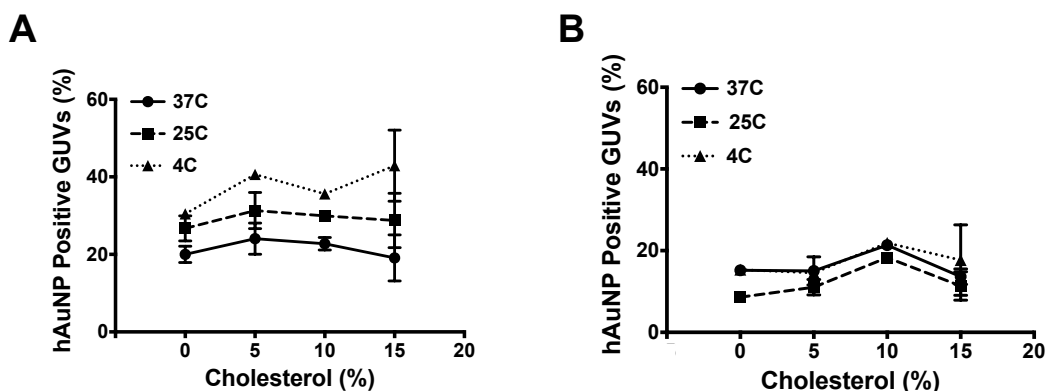
Figure 2.7. The percentage of hAuNP positive GUVs plotted as a function of cholesterol content (mol%) and temperature for (A) a 10% FBS matrix and (B) a 0% FBS matrix.

Comparing GUVs to a Human Cell Line

CaSki cells, a human cervical cancer cell line, were exposed to hAuNPs for 4 hours at 37°C and 4°C in 0% and 10% FBS supplemented cell medium. The cell membrane was labeled with DiO and the cells were imaged using confocal microscopy (Figure 2.8). There is no overlap between DiO fluorescence and hAuNP fluorescence, and nanoparticle fluorescence is only observed within the boundaries of the membrane dye. This indicates that hAuNPs are fully internalized without concentrating in the cell membrane, unlike hAuNP-treated GUVs. Temperature significantly affects nanoparticle uptake in cells. At 4°C, nanoparticle fluorescence is not detectable, but FBS does not cause a discernable change to hAuNP fluorescence. These results suggest that GUVs are not a good model for cellular uptake studies, because hAuNPs do not accumulate in the cell membrane and are not significantly internalized at low temperatures.

Cellular internalization of hAuNPs was also characterized by flow cytometry and ICP-

MS to measure hAuNP fluorescence and cellular gold content, respectively (Figure 2.9).

Consistent with the confocal microscopy images in Figure 2.8, cells treated at 37°C exhibit

higher fluorescence than cells treated at 4°C, but no difference is found between cells in 0% or

10% FBS supplemented medium. The mean fluorescence values are given in Supplemental
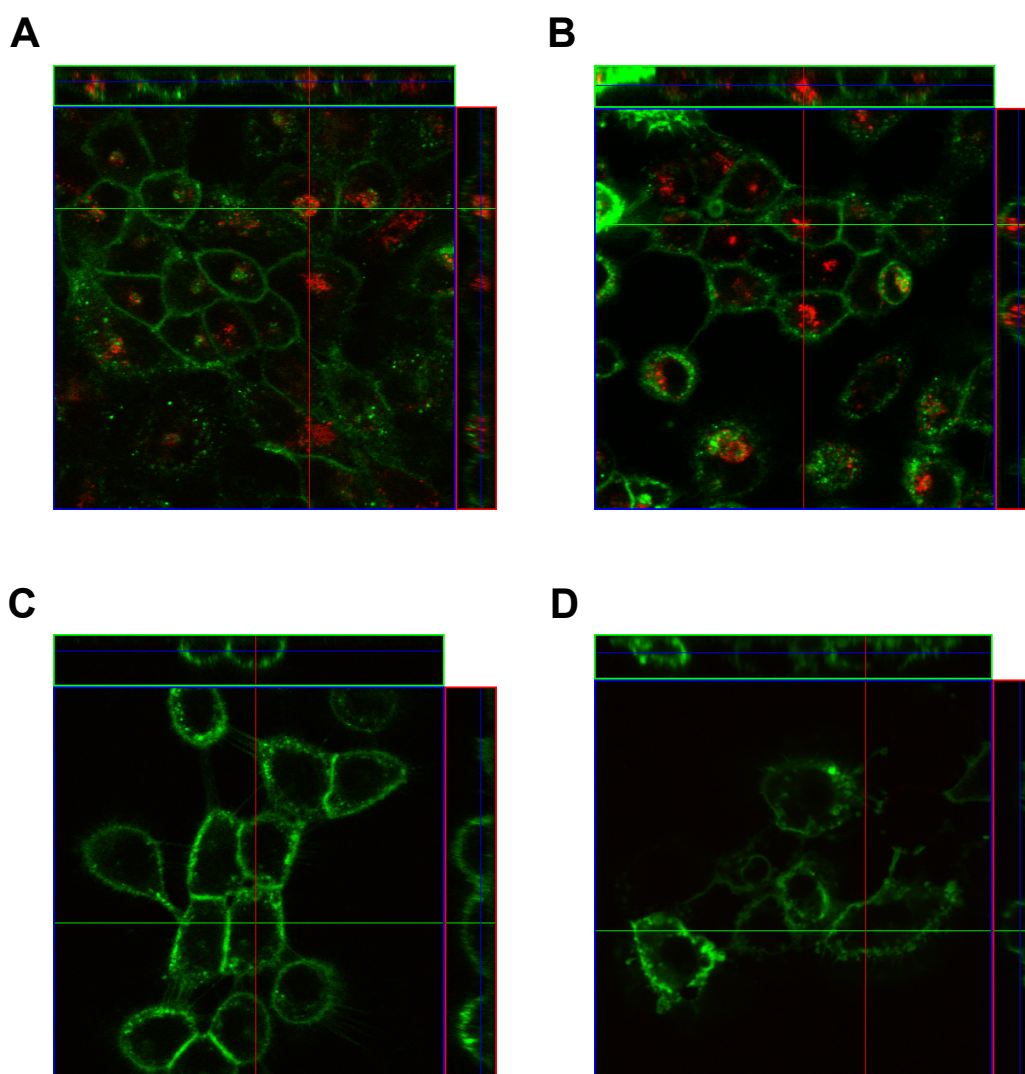
Figure 2.8. hAuNPs do not localize to the cell membrane, but are found in the cytoplasm, within the confines of the plasma membrane. At 37°C, hAuNP fluorescence is detected intracellularly in both (A) 10% FBS and (B) 0% FBS supplemented medium. At 4°C, hAuNP fluorescence for cells in (C) 10% FBS and (D) 0% FBS supplemented medium is not detectable.

Figure D.7, Appendix D. Here, fluorescence is a proxy for nanoparticle uptake, indicating that

cells internalize greater amounts of hAuNPs at 37°C than at 4°C. ICP-MS analysis confirms this

conclusion and reveals that including FBS reduces the amount of internalized gold nanoparticles.

It is unclear why the cellular gold content differs significantly based on the inclusion of FBS, but

mean cell fluorescence does not. The fluorescence of hAuNPs in PBS exhibits some temperature

dependence, but this does not completely explain the reduction in mean cell fluorescence

(Supplemental Figure D.8, Appendix D). At 4°C in PBS, a 34.6% reduction in fluorescence is

observed, whereas in cells at 4°C, a 93% reduction in mean cell fluorescence is measured. It is

possible that a portion of the cell fluorescence at 37°C arises from enzymatic degradation of the

DNA by nucleases, but further experiments would be required to confirm this hypothesis.
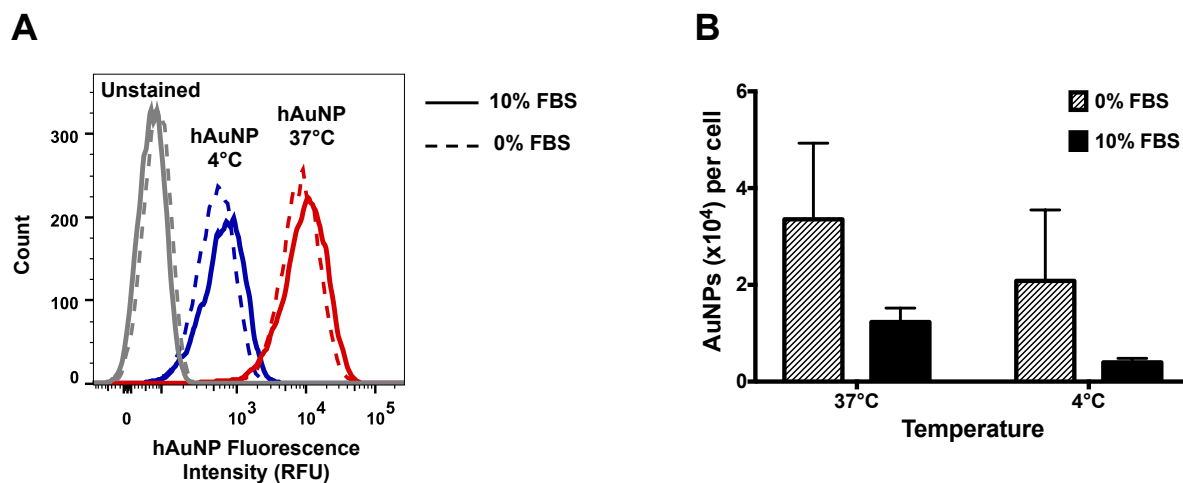
Figure 2.9. CaSki cell uptake of hAuNPs measured by flow cytometry and ICP-MS. (A) Flow cytometry reveals that cells treated with hAuNPs at 37°C have increased fluorescence over cells treated at 4°C. FBS does not affect the fluorescence. (B) ICP-MS demonstrates that the gold content of the cells depends on temperature and also on FBS, with cells internalizing greater amounts of nanoparticles in culture medium not supplemented with FBS.

Literature reports agree with these data and have also demonstrated that low temperatures

reduce the cellular uptake of nanoparticles. Decreased nanoparticle accumulation was typically

attributed to the down-regulation of energy dependent processes, including endocytosis, in

reaction to the cold temperature.[6,43,44] Also consistent with the literature, FBS supplemented medium has a clear effect on gold nanoparticle content, suppressing cellular uptake by about 5,000 nanoparticles per cell (Figure 2.9B). In cell culture medium containing FBS, decreased nanoparticle uptake has been attributed to the formation of a protein corona, which alters the nanoparticle-membrane interaction.[6,22,33,34]

The cell-based data suggests that GUVs are not an appropriate model of cellular uptake for these nanoparticles. hAuNP association with the GUV membrane is highest for low temperatures (4°C) and matrices containing 10% FBS, whereas cells have decreased uptake of nanoparticles under these conditions. Additionally, in order to detect fluorescent signal, GUVs require a hAuNP concentration ten times higher than that normally used in cells. Under typical conditions (37°C, 10% FBS), cells are highly fluorescent when 1 nM hAuNPs are introduced into the culture medium (Figure 2.9A), but hAuNP fluorescence is not detectable in GUVs until hAuNP concentrations of at least 5 nM are used (Figure 2.10). Additionally, in cells the entire population experiences a fluorescence shift, indicating that complete transfection occurs;
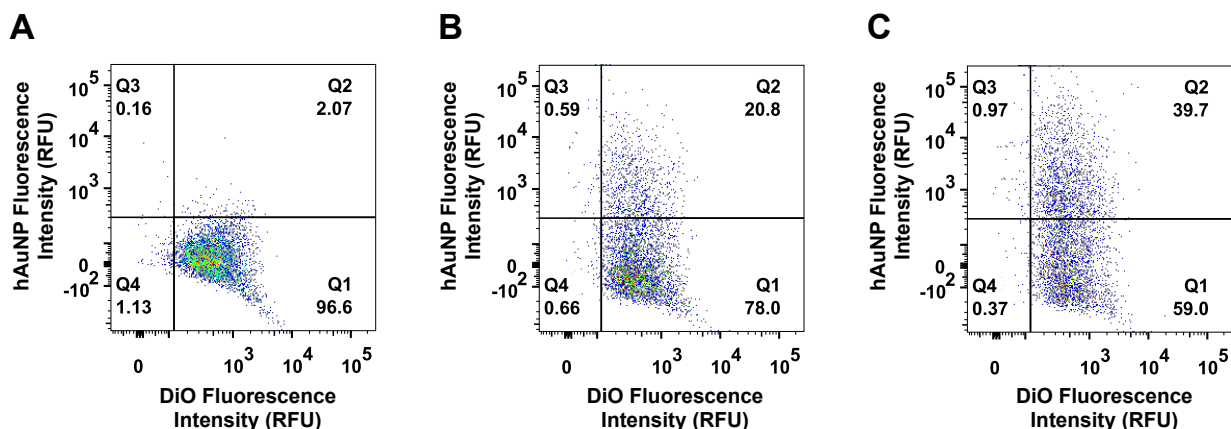
Figure 2.10. Detection of hAuNP positive GUVs is dependent on hAuNP concentration. (A) At 1 nM hAuNPs, no GUVs are positive for hAuNPs. Increasing amounts of hAuNP positive GUVs are present when vesicles are treated with (B) 5 nM and (C) 10 nM hAuNPs.

however, only ~40% of GUVs are hAuNP positive under the conditions explored here, and no evidence of transport into the GUV lumen could be obtained. The observation that cells are able to completely internalize large amounts of hAuNPs at low concentrations suggests that an active uptake mechanism is the dominant mode of transport into the cell. Although GUVs have been reported as useful models of the phospholipid bilayer, they do not recapitulate enough of the relevant characteristics of hAuNP cellular uptake to be useful in this context.

Conclusion

Although GUVs may provide a few hints about the role of the phospholipid bilayer in the cellular uptake of nanoparticles, they are not a good representation of the true interaction with the plasma membrane. Even at high concentrations, hAuNPs are never visualized inside the vesicle lumen, as would be expected if the nanoparticles could passively diffuse through a phospholipid membrane. Although the hAuNPs could be present inside the GUVs at concentrations below the detection limit of the microscope, this result remains in conflict with cell-based results. Cells do have detectable hAuNP fluorescence in the cytoplasm within a few hours of introducing hAuNPs at a 1 nM concentration in the cell medium. Additionally, FBS causes nanoparticles to localize and concentrate in the GUV membrane, a phenomenon that is not consistent with cell lines, which fully internalize the nanoparticles. hAuNP association with the GUV membrane increases at low temperatures and in 10% FBS, but cells have low uptake under those conditions. These results support the hypothesis that surface proteins are facilitating cellular uptake via endocytosis. An active mode of transport would account for the high accumulation of nanoparticles inside the cell when low concentrations of hAuNPs are introduced into the cell culture medium. In summary, although hAuNPs clearly interact with a pure phospholipid bilayer in the presence of FBS, the results do not support passive transport of the

nanoparticles through the bilayer. The GUV model membrane system does not accurately recapitulate the necessary characteristics of the cell membrane-nanoparticle interaction, leading to the conclusion that endocytic mechanisms are probably the dominant pathway for uptake.

Acknowledgements

CHAPTER III

SIZE-DEPENDENT CELLULAR UPTAKE OF DNA FUNCTIONALIZED GOLD

NANOPARTICLES

Introduction

Gold nanoparticles (AuNPs) have become increasingly popular in diagnostic and

therapeutic applications due to the biocompatibility, unique optical properties, small size, and

ease of molecular functionalization of nanostructured gold.[1,3,45,46] Such biomedical applications

require the introduction of AuNPs to biological fluids and tissues, and frequently depend on the

internalization of these nanoparticles by mammalian cells. Optical imaging of overexpressed

cancer-associated mRNA in live, intact cells has been accomplished with AuNPs conjugated to

fluorescent DNA that is complementary to the target mRNA sequence.[6,19,47,48] These molecular

probes are internalized by cells with high efficiency and do not require external transfection

agents. Fundamental investigations into the cellular uptake of these DNA functionalized AuNPs

(DNA-AuNPs) inform our understanding of their biological fate and assists in the ultimate

design and implementation of such functional AuNP systems for the molecular characterization

of diseased tissues.

The extent and efficiency of cellular uptake is dependent in part on the physicochemical

characteristics of the nanoparticle system,[13,14,49] including particle size,[18,44,50] shape,[44,51,52] surface

charge,[53–55] and surface chemistry.[34,56–62] Significant interplay between these factors is frequently

observed, making identification of the effect of individual components complex.[13,52,63,64]

Typically cells internalize positively charged nanoparticles in higher amounts than neutral or

31

negatively charged particles. However, DNA-AuNPs composed of highly dense, negatively charged DNA oligonucleotide strands have been shown to successfully enter cells in significant amounts such that intracellular mRNA imaging and delivery of therapeutic nucleic acids is achieved.[6,19,47,48,57] No consensus has been reached on how particle size affects the cellular accumulation of functionalized AuNPs. For example, Cho *et al.* observed maximum cellular uptake for small AuNPs (< 30 nm), while Chithrani and Chan found maximum uptake for larger AuNPs (50-70 nm).[44,52] These discrepancies are likely due to a complex relationship between the size, surface charge, and ligand chemistry of the individual functionalized AuNP systems. Although the surface functionality and chemistry of DNA-AuNPs has been explored,[56,58,60] a systematic investigation into the influence of nucleic acid conformation, particle size, and surface charge on cellular uptake has not been reported.

This chapter aims to understand which physicochemical properties affect the cellular accumulation of DNA-AuNPs. AuNPs are conjugated to hairpin DNA (hDNA) to form hAuNPs, single stranded DNA (ssDNA) to form ssAuNPs, and double stranded DNA (dsDNA) to form dsAuNPs (Figure 3.1). Inductively coupled plasma mass spectrometry (ICP-MS), flow cytometry, and confocal microscopy demonstrate that CaSki cells, a human cervical cancer cell line, accumulate these particles in different quantities. The results indicate that the greatest predictor of cellular accumulation is DNA-AuNP size. This chapter establishes that cellular internalization can be modulated through adjustment of nanoparticle size, which will allow for the design of DNA-AuNP diagnostic and therapeutic systems with optimal transfection efficiency and enhanced intracellular imaging or DNA delivery properties.
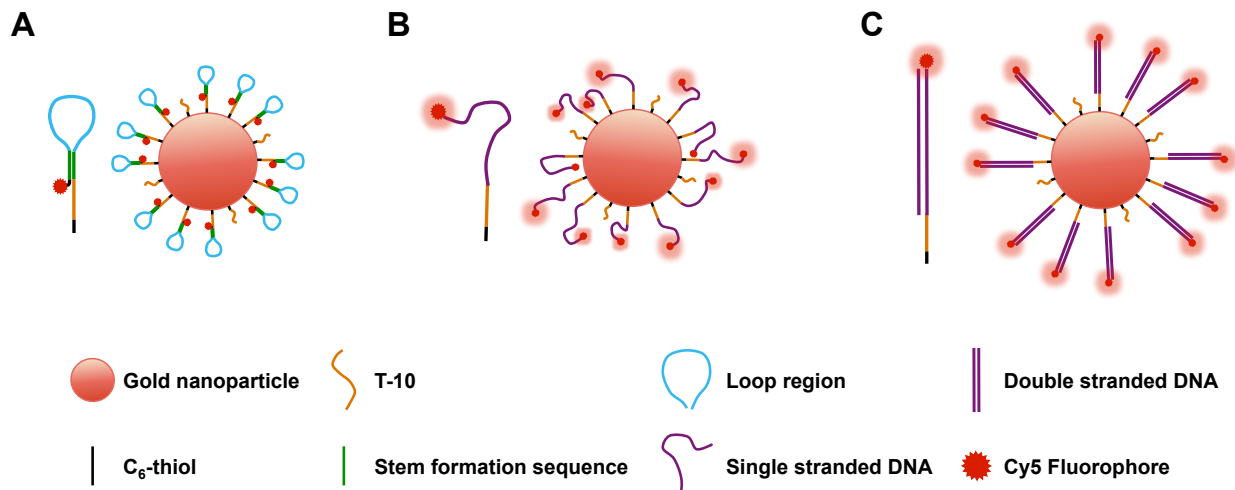
Figure 3.1. Representation of the DNA ligands and the DNA-AuNPs used in these experiments: (A) hDNA and hAuNPs, (B) ssDNA and ssAuNPs, and (C) dsDNA and dsAuNPs.

Materials and Methods

Cell Culture

CaSki cells (ATCC) were grown at 37°C in a humidified atmosphere with 5% CO_2. The cell culture medium was RPMI 1640 (with L-glutamine) supplemented with 10% fetal bovine serum (FBS), penicillin (100 units mL^{-1}), streptomycin (100 μg mL^{-1}), D-glucose (2.25 g L^{-1}), sodium pyruvate (1 mM), and HEPES (10 mM). Cells were subcultured upon reaching approximately 80% confluence and media was replaced as needed.

Preparation of DNA Oligonucleotides

Lyophilized thiolated DNA sequences (Integrated DNA Technologies) were reconstituted in dithiothreitol (0.1 M; DTT) in dibasic phosphate solution (0.1 M; pH 8.3) to reduce disulfide bonds. Following a one-hour incubation, the DNA was desalted and washed twice with Tris-EDTA (TE) buffer using the manufacturer's protocol for Amicon Ultra 3K MWCO Filters (EMD Millipore). The DNA was resuspended in TE buffer and the concentration was determined by UV absorbance at 260 nm using a BioTek Take3 Micro-Volume Plate and a BioTek Synergy H4 Hybrid microplate reader. All non-thiolated DNA sequences were resuspended in TE buffer

and the concentration was determined by UV absorbance. All sequences were adjusted to an appropriate working concentration using TE Buffer and stored at -80°C until use.

DNA-AuNP Synthesis

10, 15, 20, 40, and 50 nm AuNPs (Ted Pella) were adjusted to the same surface area (S.A.) per mL, 4.566×10^{14} nm^2/mL, using molecular biology grade water. Aliquots of 1 mL were supplemented with 0.1% (v/v) Tween 20. The thiolated ten thymine spacer ligand (T-10) was conjugated overnight at a final concentration of 0.1 µM. Fluorescent DNA was added at a final concentration of 0.3 µM and conjugated overnight. For dsAuNPs, the thiolated and complementary strands were added to the nanoparticles sequentially and allowed to conjugate and hybridize overnight. The solutions were buffered to pH 7.0 with phosphate buffer (10 mM), brought to a final concentration of 0.1 M NaCl, and allowed to incubate for ≥ 4 hours. The solutions were adjusted to 0.2 M NaCl and incubated for ≥ 4 hours. A final NaCl addition resulted in a concentration of 0.3 M NaCl and the solutions were incubated overnight. All conjugations and incubations were performed with rotation in the dark. The resulting DNA-AuNPs were purified and concentrated through three rounds of centrifugation and resuspension in phosphate buffered saline (PBS). Centrifugation was performed at 21,100g for 20 minutes for 15 and 20 nm AuNPs; 16,100g for 45 minutes for 10 nm AuNPs; and 5,000g for 30 minutes for 40 and 50 nm AuNPs. To prepare complemented DNA-AuNPs from ssAuNPs and hAuNPs, concentrated DNA-AuNPs were diluted to 1 nM in PBS and supplemented with 0.1% (v/v) Tween 20. Complementary strands were added at a final concentration of 3 µM and the solutions were incubated for five hours at room temperature before centrifuging and washing twice with PBS.

DNA-AuNP Characterization

Fluorescence measurements were performed in black 96-well plates using a BioTek Synergy H4 Hybrid microplate reader with excitation and emission settings configured for Cy5 (ex: 650 nm; em: 670 nm). Samples were diluted to the same S.A. mL^{-1} (4.6×10^{14} nm^2 mL^{-1}) in PBS. Hydrodynamic diameter and zeta potential measurements were performed by diluting the samples to the same absorbance value ($A_{520nm} = 0.369$) in either PBS (hydrodynamic diameter) or 10 mM NaCl dissolved in molecular biology grade water (zeta potential). Samples were passed through a 0.22 µm PVDF syringe filter (Fisher Scientific) before analysis. A dip cell was used to obtain zeta potential measurements. All measurements were recorded with a Malvern Zetasizer Nano ZS at 25°C. To quantify the average number of fluorescent DNA ligands per particle, concentrated DNA-AuNPs were resuspended in DTT (500 µL; 0.1 M) in dibasic phosphate solution (0.1 M; pH 8.3) to a final concentration of 1 nM (10, 15, 20 nm AuNPs), 0.15 nM (40 nm AuNP), or 0.096 nM (50 nm AuNP). The solutions were reacted for two hours before centrifuging at 21,100g for 20 minutes to pellet any remaining AuNPs. The fluorescence of the supernatant was measured and compared to a calibration curve of free DNA to determine the concentration of fluorescent DNA in the supernatant. Dividing the DNA concentration by the nanoparticle concentration gives the average number of fluorescent DNA strands per particle. Reported values represent the mean ± SD for three different preparations of nanoparticles.

Flow Cytometry

CaSki cells were seeded in 12 well plates, allowed to adhere, and treated with 1 nM (6×10^{11} nanoparticles/mL) DNA-AuNPs prepared in fresh cell media. Unless otherwise noted, cells were treated with DNA-AuNPs for 24 hours. To measure the cellular uptake over time, cells were treated for 2, 4, 6, 8, 10, and 24 hours. Following treatment, the AuNP solution was

removed and the cells were washed three times with PBS. The cells were detached using trypsin and 20,000 events were collected on a BD LSRII flow cytometer with excitation at 633 nm. Unstained cells that were not exposed to DNA-AuNPs were analyzed as a negative control. To study the uptake over time, cells were detached with trypsin, fixed in 2% paraformaldehyde for 15 minutes at 4°C, washed by centrifugation at 300g for five minutes, and resuspended in PBS before analysis. For all other experiments, cells were not fixed for analysis. Typically, reported values represent mean ± SD for three biological replicates with analytical triplicates. For experiments measuring cellular uptake over time, reported values represent mean ± SD for two biological replicates with analytical triplicates, and the sample size is sufficient to provide the necessary statistical rigor.

ICP-MS Analysis of Cellular Uptake

CaSki cells were seeded in 12 well plates and allowed to adhere. For all experiments, cells were treated with 1 nM (6×10^{11} nanoparticles/mL) DNA-AuNPs prepared in fresh cell media. To measure the cellular uptake over time, cells were treated for 2, 4, 6, 8, 10, and 24 hours. For all other uptake experiments, the incubation time was 24 hours. The AuNP solution was removed and the cells were washed three times with PBS. The cells were detached using trypsin, collected in 15 mL conical tubes, stained with Trypan blue to assess cell viability, and counted using a Countess II automated cell counter (Life Technologies). Centrifuging at 300g for 10 minutes pelleted the cells and the remaining media was completely removed. The cell pellet was digested overnight in 0.8 mL of *aqua regia* (*Warning: extremely corrosive, handle with caution*) followed by dilution to 6 mL with deionized water (18.2 MΩ•cm). A Thermo Element 2 high resolution inductively coupled plasma mass spectrometer (ICP-MS, Thermo Fisher Scientific, Bremen, Germany) equipped with an ESI auto sampler (Elemental Scientific, Omaha,

NE) was used to quantify the gold in the samples. Samples were uptaken by self-aspiration via a 0.50 mm ID sample probe and capillary to the spray chamber. Gold was quantified by measuring the ^{197}Au isotope at medium resolution (R=4300). The amount of AuNPs per cell was calculated as described in Appendix E. Typically, reported values represent mean ± SD for three biological replicates with analytical triplicates. For experiments measuring cellular uptake over time, reported values represent mean ± SD for two biological replicates with analytical triplicates, and the sample size is sufficient to provide the necessary statistical rigor.

ICP-MS Analysis of Cellular Excretion

CaSki cells were seeded in 12 well plates and treated for 16 hours with 1 nM (6×10^{11} nanoparticles/mL) DNA-AuNPs prepared in fresh cell media. The media containing excess AuNPs was removed and the cells were washed three times with PBS and incubated in fresh media containing no DNA-AuNPs for 2, 4, 6, and 8 hours. See the Supporting Information for the AuNP per cell calculations. The percent AuNP retention was calculated by dividing the AuNPs per cell at a given time point by the AuNPs per cell at 0 hours post-media replacement. Reported values represent mean ± SD for three biological replicates with analytical triplicates.

Confocal Microscopy

CaSki cells were seeded in the wells of an eight well μ-slide (ibidi USA, Inc). DNA-AuNPs were added at 1 nM (6×10^{11} nanoparticles/mL) final concentration in fresh media for four hours. The nucleic acid stain, STYO13, was added at a final concentration of 400 nM for one hour. The cells were washed three times with phenol-red free RPMI 1640 supplemented with 10% FBS and 10 mM HEPES. A final volume of 100 μL of phenol-red free media was used to image the cells on a Zeiss LSM 510 Meta inverted confocal microscope. Images were obtained using a 40X oil objective with excitation at 633 nm (Cy5 labeled DNA-AuNP) and 488 nm

(SYTO13 nucleic acid stain) and the pinhole was set to 84 μm. The emission wavelengths for Cy5 and SYTO13 are 670 nm and 509 nm, respectively.

Results and Discussion

Gold Nanoparticles Conjugated to Hairpin, Single Stranded, or Double Stranded DNA Enter Cells in Different Quantities

Two types of DNA ligands are conjugated to 15 nm citrate-stabilized AuNPs through a 5'-thiol group: i) a ten thymine spacer ligand (T-10) to prevent crowding of the longer oligonucleotides[65] and ii) a cyanine dye (Cy5) labeled oligonucleotide sequence with a hairpin, single stranded, or double stranded conformation (see Supplemental Table E.1, Appendix E for sequence information). All fluorophore labeled sequences are designed to have a total length of approximately 40 nucleotides. The hDNA has a 10 thymine spacer region, a stem formation sequence of five base pairs, and a loop sequence of 19 nucleotides.[65] The ss- and dsDNA sequences have a 10 thymine spacer region followed by an additional region of 30 nucleotides. The 19 base loop region of hDNA and 30 base region of ss- and dsDNA are randomized sequences of the four DNA nucleobases (A, C, G, and T) designed to have no known homology to human RNA so these studies would be focused purely on cellular uptake, rather than RNA sensing. GenScript Sequence Scramble[66] was used to randomize the sequences and NCBI Nucleotide BLAST[67] was used to minimize sequence homology to the human mRNA transcript database. Hairpin DNA, ssDNA, and dsDNA are attached to citrate-stabilized AuNPs via gold-thiol bonds to form hAuNPs, ssAuNPs, and dsAuNPs, respectively. To form dsAuNPs, the complementary oligonucleotide (30 bases in length) is added with the thiolated strand in equimolar amounts during synthesis.

In the absence of cells, the inherent fluorescence of the DNA-AuNPs varies, likely as a result of the conformation of the DNA on the particle surface (Supplemental Figure E.1A, Appendix E). The hAuNP is designed so that the fluorophore is held close to the gold surface by the stem-loop conformation of the DNA, resulting in the lowest observed fluorescence. The ssAuNP is formed from DNA of significant length, which can sample all energetically available random coil conformations. This could bring the 3'-fluorophore close to the gold surface, producing the observed quenching. The dsAuNP exhibits high fluorescence due to the double helical conformation that forces the fluorophore away from the gold surface, where the quenching efficiency is lower. Measurements of the hydrodynamic diameter reveal that hAuNPs and ssAuNPs have similar sizes of ~31 nm (Supplemental Figure E.1B, Appendix E). This small size is likely due to the folding of the DNA, whether forced by design (hAuNP) or sampled as the lowest energy conformation (ssAuNP). The dsAuNPs have a much larger hydrodynamic diameter of 66 nm due to the fully extended double helix. All three DNA-AuNPs have a similar zeta potential around -30 mV (Supplemental Figure E.1C, Appendix E).

Confocal microscopy demonstrates that all of the DNA-AuNPs readily enter and localize to the cytoplasm of CaSki cells, a human cervical carcinoma cell line, without the need for transfection agents and within a few hours of introduction to the cell media (Figure 3.2). Z-stack images reveal that DNA-AuNP fluorescence (red) is observed throughout the volume of the cytoplasm, rather than solely localizing at the surface of the external cell membrane. These images also show that internalization of DNA-AuNPs occurs heterogeneously (Supplemental Figure E.2, Appendix E), which is also supported by flow cytometry data, where the single cell population exhibits a distribution of fluorescence (see below). At the resolution and slice thickness of these images, we observe no DNA-AuNPs entering the nuclear compartment;

| hAuNP | ssAuNP | dsAuNP |
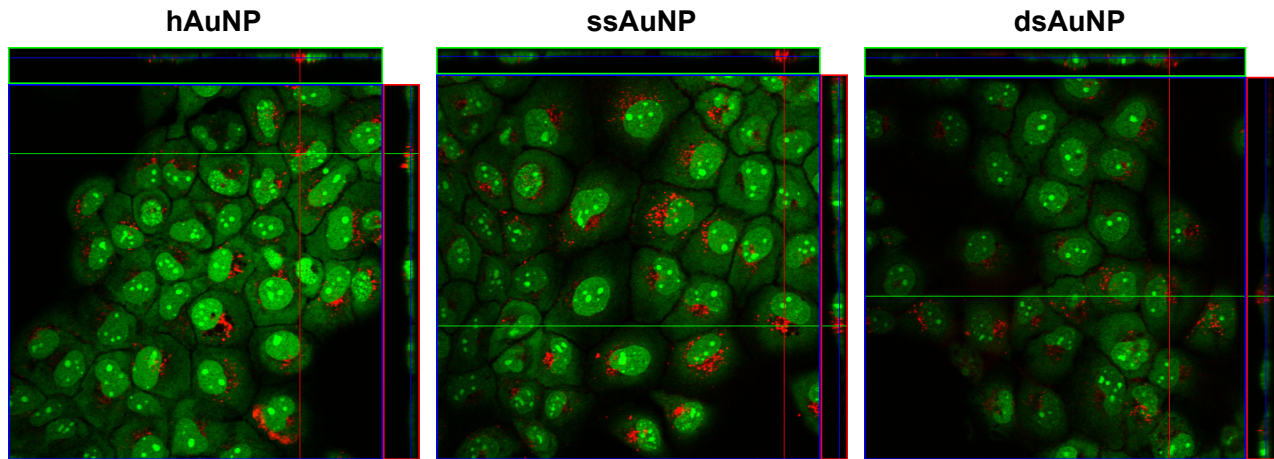
Figure 3.2. DNA-AuNPs localize within the cell. Confocal microscopy demonstrates that DNA-AuNPs are located in the cytosol of CaSki cells, rather than adsorbing to the cell membrane. Side and top views show the fluorescence in the XZ and YZ planes, which reveals that DNA-AuNPs are found throughout the entire volume of the cell. Red: Cy5 labeled DNA-AuNPs. Green: SYTO13 nucleic acid stain.

however, the particles do tend to collect in the perinuclear region of the cytoplasm. DNA-AuNPs are known to nonspecifically enter a number of cell lines, and a mechanism of DNA-AuNP binding to cell surface scavenger receptor proteins followed by lipid-raft/caveolae-mediated endocytosis has been proposed.[17] After entering the intracellular compartment, DNA-AuNPs are mainly localized within perinuclear endosomes, with a small portion escaping into the cytosol.[68] The mechanism of endosomal escape remains unknown, but Wu, *et al.* attributed the intracellular signaling and gene silencing properties of these particles to this small population of free DNA-AuNPs. Previously our laboratory utilized hAuNPs to fluorescently label viral mRNA in living cells.[6] Measurement of RSV-specific hAuNP fluorescence in cells infected with respiratory syncytial virus (RSV) indicated that at least a fraction of the nanoparticles are present in the cytoplasm and available to bind mRNA, rather than sequestered within endocytic vesicles.

Cells incubated with hAuNPs, ssAuNPs, or dsAuNPs were evaluated for fluorescence by flow cytometry (Figure 3.3). Cells treated with dsAuNPs have a histogram shifted to lower fluorescence values compared to cells treated with hAuNPs or ssAuNPs, suggesting lower

amounts of transfection. The mean fluorescence for each cell population is given in

Supplemental Figure E.3, Appendix E. Control cell viability studies were performed by the

Trypan blue exclusion method (Supplemental Figure E.4, Appendix E). The cells maintained $\geq$

95% viability, which is consistent with previous results that showed no cytotoxicity of hAuNP-

treated cells using fluorescent stains and flow cytometry.[6,48] ICP-MS provides aggregate data
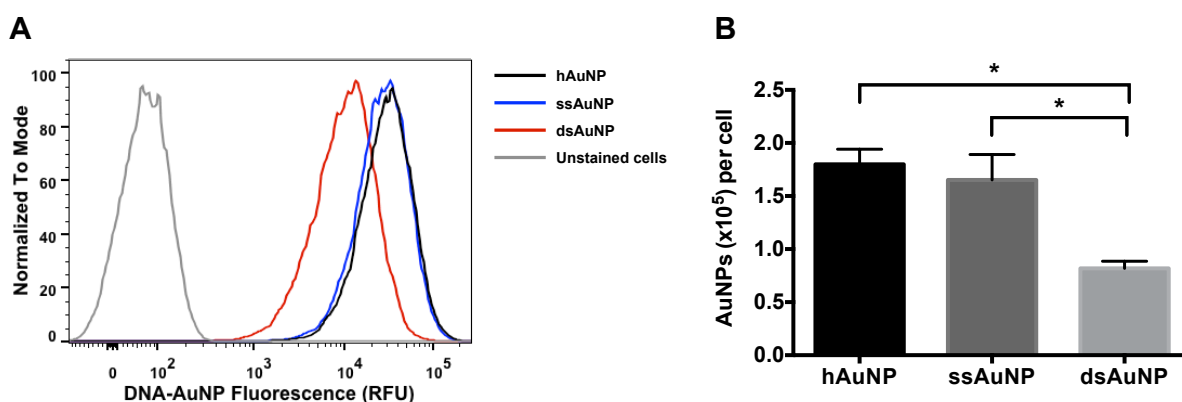
Figure 3.3. CaSki cells internalize DNA-AuNPs in different amounts. (A) Flow cytometry demonstrates that cells incubated with hAuNPs and ssAuNPs have populations shifted to higher fluorescence compared to cells incubated with dsAuNPs. These results suggest that cells internalize the three DNA-AuNPs differently. (B) ICP-MS analysis of the gold concentration confirms that cells internalize dsAuNPs in significantly lower quantities than hAuNPs and ssAuNPs. Error bars represent standard deviation from three biological replicates. *p < 0.05

about the average cellular uptake of DNA-AuNPs by measuring the amount of gold internalized

by the cells. To normalize across samples, the amount of internalized AuNPs was calculated on a

per cell basis (see Appendix E for detailed calculations). ICP-MS analysis confirms that cells

incubated with hAuNPs and ssAuNPs have significantly more (~ 2x) AuNPs per cell compared

to cells incubated with dsAuNPs (Figure 3.3B) (p < 0.05). Differences in the cellular uptake of

AuNPs functionalized with ssDNA and dsDNA have been observed previously, but to our

knowledge, no explanation has been proposed.[69] The levels of AuNPs per cell measured here

($\sim 1.8 \times 10^5$) is comparable to previous reports that employed higher concentrations of

nanoparticles and shorter incubation times.[60] Using low nM concentrations, the transfection of

DNA-AuNPs reaches the same order of magnitude as that of Narayan *et al.* by utilizing longer time scales, indicating that fine control over the accumulation of DNA-AuNPs in cells can be exerted by modifying the nanoparticle concentration and cell exposure time.
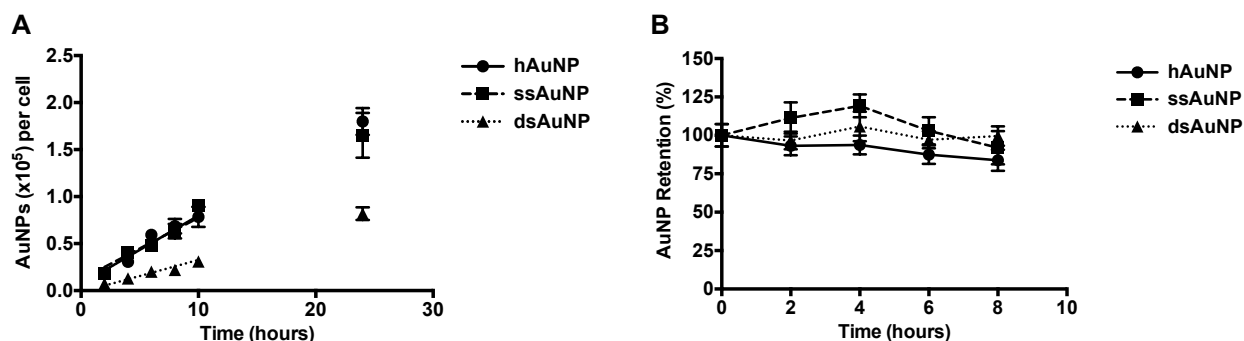
Figure 3.4. ICP-MS analysis of cellular uptake and excretion over time. (A) The average number of AuNPs per cell is monitored over 24 hours of DNA-AuNP exposure time. The cellular uptake of all DNA-AuNPs is linear with time, but dsAuNPs exhibit a reduced rate of uptake compared to hAuNPs and ssAuNPs, which results in a lower intracellular accumulation of dsAuNPs. Error bars denote standard deviation from two biological replicates. (B) Excretion of DNA-AuNPs was monitored for 8 hours after removing the nanoparticles from the cell media. DNA-AuNPs are not significantly excreted from cells. Compared to the 0 hour time point, the change in the percentage of AuNP retention over eight hours is not statistically significant for any DNA-AuNP ($p > 0.05$). Error bars denote standard deviation from three biological replicates.

The internalization of nanoparticles over time was explored by incubating cells with hAuNPs, ssAuNPs, or dsAuNPs for 2 – 24 hours. Cellular accumulation was measured by ICP-MS and flow cytometry (Figure 3.4A and Supplemental Figure E.5, Appendix E). The cells internalize increasing quantities of DNA-AuNPs over time and a line of best fit was calculated using a linear regression between 2 and 10 hours of incubation time. The slope of this line indicates that the DNA-AuNPs have different rates of uptake. hAuNPs and ssAuNPs possess the fastest rate of uptake at 8000 ± 1000 nanoparticles per cell per hour, followed by dsAuNPs at 2830 ± 260 DNA-AuNPs per cell per hour. The rate at which nanoparticles enter the cell directly determines the final amount of DNA-AuNPs found inside; therefore, the reduced rate of uptake of dsAuNPs contributes to the lower intracellular levels of these nanoparticles. Flow cytometry

shows that the mean fluorescence of the single cell population saturates between 10 and 24 hours of incubation time, which may be due to self-quenching of the fluorescent DNA upon reaching a critical intracellular nanoparticle concentration. It is also possible that DNase degradation occurs within the cell causing a separation of Cy5 from the AuNP that results in recycling of fluorescent fragments out of the cell, while the AuNP core remains internalized, as proposed by Wu, *et al.*[68] The saturation of fluorescence observed here may be due to equilibrium between the processes of DNA-AuNP uptake and expulsion of fluorescent degradation products. By ICP-MS analysis, the levels of AuNP per cell do not saturate over 24 hours, similar to previous reports that did not observe saturation in cells exposed to high concentrations of DNA-AuNPs over shorter time periods.[17] It is possible that saturation of cellular uptake would be observed with longer exposure times. However, this is difficult to assess because the nanoparticles are transferred to daughter cells during cell division if exposure periods longer than the cell doubling time are used.[70] Additionally, at 24 hours of incubation time, each cell has accumulated an average of almost two million hAuNPs or ssAuNPs, each of which has ~80 functional DNA strands attached, which should be sufficient for imaging or therapeutic applications, negating the need to achieve saturating conditions.

To determine if intracellular DNA-AuNPs exit cells, nanoparticles were loaded into the cells over a 16-hour incubation period. The cells were washed, fresh culture media was added, and the cells were incubated for an additional $2 - 8$ hours, which was followed by ICP-MS analysis. All three DNA-AuNPs have approximately 100% retention in cells after removal of the extracellular AuNP solution and are not excreted in significant amounts when each time point was compared to the initial AuNP accumulation at 0 hours (Figure 3.4B) ($p > 0.05$). These data correlate well with previous reports, which found that the quantities of functionalized AuNPs

that are exocytosed are often less than 20% of the internalized nanoparticles.[68,71,72] Wu *et al.*
proposed that the high retention of functionalized AuNPs within cells was due to loss of
stabilizing ligands, aggregation of the particles, and subsequent loss of biological recognition of
the AuNPs, which prevents them from being excreted.[68]

Addition of Complementary Oligonucleotide Strands to ssAuNPs and hAuNPs Reduces the
Cellular Uptake of These Particles

To determine the impact of DNA conformation on cellular internalization,
complementary strands were added to hAuNPs and ssAuNPs to form "complemented" versions
of these particles. It is hypothesized that complemented DNA-AuNPs will behave like dsAuNPs
when introduced to cells. ICP-MS shows that hAuNPs, ssAuNPs, and complemented hAuNPs
are internalized at higher levels than complemented ssAuNPs and dsAuNPs (Figure 3.5A).
Complemented ssAuNPs have similar cellular accumulation to dsAuNPs because these two
nanoparticles exhibit indistinguishable physicochemical properties (Supplemental Figure E.6,
Appendix E). When analyzed by flow cytometry, cells incubated with hAuNPs and ssAuNPs
attain higher fluorescence than cells incubated with complemented ssAuNPs and dsAuNPs,
which correlates to the ICP-MS results (Figure 3.5B and Supplemental Figure E.7, Appendix E).
Cells treated with complemented hAuNPs have an intermediate fluorescence but high AuNP per
cell content. This likely occurs because only a fraction of the hDNA on these particles have
hybridized to the complementary DNA, as suggested by the low inherent fluorescence of
complemented hAuNPs compared to dsAuNPs, as well as the high heterogeneity in
hydrodynamic diameter (Supplemental Figure E.6A and C, Appendix E).
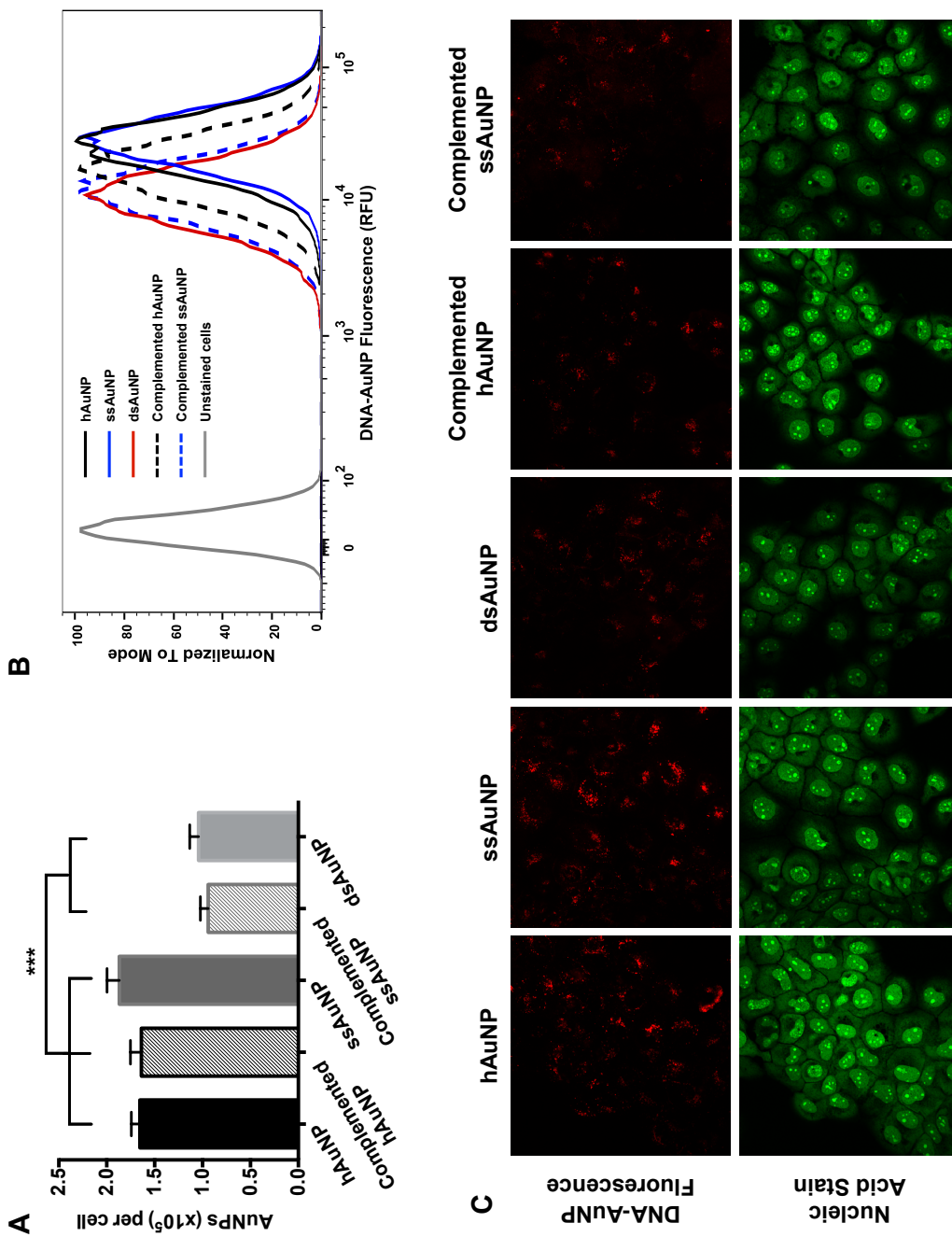
Figure 3.5. Addition of complementary DNA to hAuNPs and ssAuNPs reduces cellular uptake. (A) ICP-MS analysis shows that no significant difference in cell entry is observed for complemented hAuNPs, hAuNPs, and ssAuNPs. Cells incubated with complemented ssAuNPs and dsAuNPs exhibit no significant difference in DNA-AuNP accumulation. Error bars denote standard deviation from three biological replicates. ***p < 0.001 (B) When analyzed via flow cytometry, cells treated with complemented hAuNPs exhibit intermediate fluorescence between cells treated with hAuNPs or dsAuNPs. Cells treated with complemented ssAuNPs have similar fluorescence as cells treated with dsAuNPs. (C) Confocal microscopy qualitatively shows that cells incubated with hAuNPs and ssAuNPs exhibit brighter fluorescence than cells incubated with dsAuNPs, complemented hAuNPs, or complemented ssAuNPs. Red: Cy5 dye labeled DNA-AuNPs. Green: SYTO13 nucleic acid stain.

Confocal microscopy provides an additional method to evaluate the cellular uptake of hAuNPs, ssAuNPs, dsAuNPs, and their complemented versions. After four hours of incubation, cells treated with hAuNPs and ssAuNPs exhibit qualitatively brighter fluorescence than cells incubated with dsAuNPs, complemented hAuNPs, or complemented ssAuNPs (Figure 3.5C). Across the ICP-MS, flow cytometry, and confocal microscopy data, we generally observe agreement in the differences in DNA-AuNP cellular uptake measured by these three orthogonal techniques. Changing the DNA conformation on the nanoparticle surface affects the cellular uptake properties of these DNA-AuNPs. However, differences in cellular uptake cannot be definitively attributed to DNA conformation, because particle size has not been controlled for in this set of DNA-AuNPs.

DNA-AuNP Size Determines the Extent of Cellular Accumulation

Particle size plays a large role in the cellular uptake properties of a variety of nanoparticle systems.[13,14,18,44,49,50] To determine the influence of size, DNA-AuNPs are designed with i) increasing lengths of DNA conjugated to AuNPs of uniform diameter or ii) AuNP cores of increasing diameter conjugated to a single length of DNA.

Effect of Fluorescent DNA Length on the Cellular Uptake of DNA-AuNPs

These oligonucleotides are based on the design of the single stranded and double stranded DNA used previously. The original 40 base DNA strand was systematically shortened by eight bases to produce sequences of 16, 24, and 32 bases in length (see Supplemental Table E.2, Appendix E for sequence information). These ssAuNPs and dsAuNPs were synthesized analogously to previous DNA-AuNPs. An increase in the native fluorescence and hydrodynamic diameter of the dsAuNPs compared to their corresponding ssAuNPs of identical sequence length confirms that dsDNA was formed on the particle surface (Supplemental Figure E.8A and B

Appendix E). For the smaller DNA-AuNPs (ss16- and ss24-DNA), changes in fluorescence and hydrodynamic diameter are small, which we attribute to the inability of the short ssDNA to fold into a random coil, resulting in a strand that does not change in size with the addition of a complementary DNA strand. The extended length of the ss32 and ss40 strands of DNA allows for sampling of different conformations, which results in decreased fluorescence and size as the oligonucleotide folds. The larger size and higher fluorescence of ds32-AuNPs and ds40-AuNPs result from the adoption of a double helical conformation. All the DNA-AuNPs have statistically similar zeta potentials (~ -28 mV), regardless of DNA length or hybridization state (Supplemental Figure E.8C, Appendix E). We hypothesize that this uniformity in zeta potential occurs because the DNA phosphate backbone becomes saturated with sodium ions during synthesis so as to achieve a similar surface charge across all types of DNA-AuNPs.

The extent of internalization of these eight DNA-AuNPs is dependent on the hydrodynamic diameter of the particle construct (Figure 3.6). Due to the folding of the DNA, the DNA-AuNPs separated into two size groups centered around 30 nm and 60 nm in diameter. The smaller DNA-AuNPs had higher levels of uptake than the larger DNA-AuNPs ($p < 0.05$). Zeta potential measurements did not correlate with cellular uptake, as was expected from the uniform zeta potentials of this group of DNA-AuNPs (Supplemental Figure E.9A Appendix D,); therefore, surface charge does not influence the internalization of these DNA-AuNPs.

Oligonucleotide density of DNA-AuNPs has previously been shown to influence cellular uptake.[57] From our results, it is difficult to draw definitive conclusions about the role of DNA density in cellular uptake. However, we observe that i) for DNA-AuNPs with significantly different DNA loading densities, there is no significant difference in cellular uptake (Supplemental Figure E.10A, Appendix E) and ii) for DNA-AuNPs that have the same density of

DNA loading, significant differences in AuNP accumulation could be achieved, which we attribute to DNA-AuNP size since all other variables are held constant (Supplemental Figure E.10B, Appendix E). Because DNA density cannot reliably predict nanoparticle accumulation in cells, it is likely not a major determinant of cellular uptake properties.
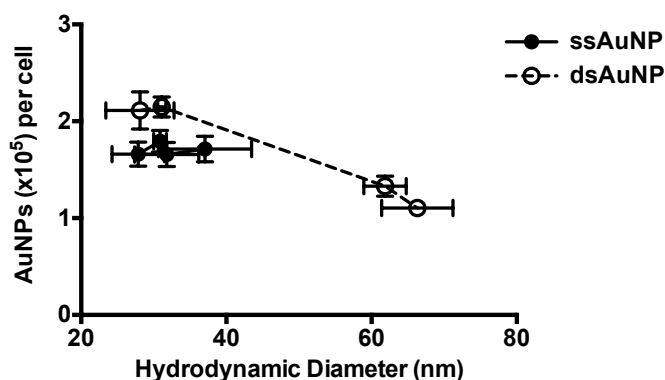
Figure 3.6. Varying the length of the DNA strand results in different sizes of DNA-AuNP, which are internalized by cells in different quantities. Single stranded or double stranded DNA of 16, 24, 32, or 40 nucleotides in length is conjugated to a 15 nm AuNP. ICP-MS reveals that an increase in hydrodynamic diameter of the DNA-AuNPs decreases the extent of nanoparticle internalization. Error bars denote standard deviation from three biological replicates.

For nanoparticles of identical hydrodynamic diameter and zeta potential, Massich *et al.* observed that ssAuNPs exhibited ~ 20 times higher accumulation in cells than dsAuNPs.[69] Here, it is observed that for DNA-AuNPs 30 nm in hydrodynamic diameter, ssAuNPs only exhibit 1.25 times higher cellular uptake than dsAuNPs, indicating that the conformation of DNA plays a minimal role in determining the amount of internalized particles.

Effect of AuNP Core Diameter on the Cellular Uptake of DNA-AuNPs

In order to further elucidate the roles of size and DNA conformation, the hydrodynamic diameter of the DNA-AuNPs was changed by varying the size of the AuNP core. Gold nanoparticles of increasing diameter were conjugated with a sequence of fluorescent DNA 24 nucleotides in length. This DNA length results in DNA-AuNPs large enough to cover the size range of interest. During synthesis, the citrate-stabilized AuNP solutions were adjusted to

concentrations with the same surface area (S.A.)/mL values, so that each reaction had the same amount of gold surface area available for binding thiolated DNA. The resulting DNA-AuNPs have a hydrodynamic diameter range of 23 – 62 nm, with a uniform size distribution (Supplemental Figure E.11, Appendix E). The fluorescence of these particles in PBS demonstrates that DNA is conjugated to the nanoparticle; however, comparisons cannot be made across the DNA-AuNPs due to variability in the quenching efficiency of differently sized cores. Zeta potential measurements of these DNA-AuNPs range from -25 mV to -35 mV. The surface charge is largely determined by the diameter of the AuNP core, as shown by zeta potential measurements of citrate-stabilized AuNPs with increasing diameters (Supplemental Figure E.11C, Appendix E).

The cellular uptake of DNA-AuNPs made with increasing sizes of gold cores is highly size dependent (Figure 3.7). DNA-AuNPs with 10 nm cores result in the highest cellular uptake, and internalization decreases as the hydrodynamic diameter of the DNA-AuNP construct increases. The level of AuNPs per cell plateaus at hydrodynamic diameters larger than 50 nm where the difference in AuNP internalization is no longer significant ($p > 0.05$). For these nanoparticles, DNA density is also shown to play a minimal role in cellular uptake (Supplemental Figure E.10C – D, Appendix E). Because surface charge trends with AuNP core diameter, the effects of size and surface charge cannot be completely disentangled, and surface charge may be involved in cellular uptake. However, it is worth noting that the DNA-AuNPs used in previous experiments have the same zeta potential (Supplemental Figure E.1C and E.8C, Appendix E), but exhibit different cellular uptake behavior, suggesting that the role of surface charge in cellular accumulation is probably minimal.
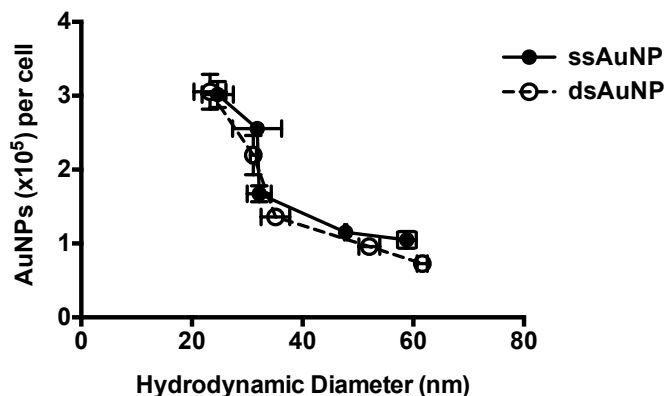
Figure 3.7. Increasing the size of DNA-AuNPs by changing the size of the AuNP core reduces cellular uptake. AuNPs (10, 15, 20, 40, or 50 nm diameter cores) were conjugated to single stranded and double stranded DNA of 24 nucleotides in length. ICP-MS analysis demonstrates that the hydrodynamic diameter of the DNA-AuNP is inversely related to cellular accumulation and further confirms that particle size is the major contributor to cellular uptake for this system. Error bars denote standard deviation from four biological replicates.

Although DNA-AuNPs with 40 and 50 nm cores have lower internalization compared to smaller nanoparticles, the amount of AuNPs per cell is not insignificant and can be controlled by optimizing concentration and incubation time. At transfections of ~100,000 large DNA-AuNPs per cell and 350-750 fluorescent DNA per nanoparticle, there are 35-75 million functional DNA inside each cell. Therefore, even for applications that require nanoparticle constructs ≥50 nm in hydrodynamic diameter, cellular imaging or drug delivery should be feasible.

These results correlate with independent studies that show that cellular uptake of functionalized AuNPs varies inversely with particle size. Cho *et al.* reported that 15 nm gold nanospheres and 33 nm gold nanocages exhibited higher cellular internalization than 45 nm nanospheres and 55 nm nanocages, regardless of the functional group on the gold surface.[52] Elbakry *et al.* demonstrated that the amount of AuNPs per cell decreased dramatically as the hydrodynamic diameter of coated AuNPs increased from 32 to 85 nm.[18] These data, along with the results shown here, conflict with some reports, which state that for particles less than 100 nm, AuNPs around 50 nm in size are internalized by cells in higher amounts than smaller AuNPs.[44,64]

It is difficult to explain these differences in reports of optimal size, but these varying results may be due to the use of different ligands or preparation methods.

Conclusion

Careful isolation and elimination of the effects of nanoparticle characteristics on cellular internalization allow us to determine that the overall size of a DNA-AuNP construct is the primary characteristic that dictates the cellular uptake properties of this nanoparticle system. ICP-MS analysis of cells incubated with varying sizes of DNA-AuNPs supports this conclusion, as the average amount of AuNPs internalized per cell is highly dependent on the hydrodynamic diameter of the functionalized nanoparticle. The size of the DNA-AuNPs also determines the rate of cellular uptake with small nanoparticles exhibiting a rate of uptake almost three times that of larger nanoparticles. Confocal microscopy shows that DNA-AuNPs are truly internalized, rather than adhering only to the external cell membrane. Cells do not distinguish DNA-AuNPs by the conformation of DNA, as evidenced by data showing that ssAuNPs and dsAuNPs of similar size are internalized in similar quantities. Although it is difficult to completely disentangle the effects of nanoparticle size, DNA density, and surface charge, cells are shown to accumulate nanoparticles with the same surface charge or DNA density in significantly different amounts. This indicates that another factor is driving internalization, supporting our hypothesis that compared to nanoparticle size, surface charge and DNA density play a minor role in determining cellular uptake properties. These results contribute to our understanding of how DNA-AuNPs interact with the cell and what properties of the nanoparticle system are most important in the cellular internalization process. We demonstrate that we can exert control over the rate of uptake and the final accumulation of functionalized AuNPs in cells by adjusting the nanoparticle size, particle concentration, and cell exposure time, although it may be difficult to generalize these

results to other ligand types or nanoparticle systems. Due to the ease of modulating nanoparticle size, these studies will inform the rational design of intracellular AuNP probes that possess optimal cellular transfection efficiencies, enhancing the ability to perform imaging or therapeutic applications on faster time scales with lower concentrations of DNA-AuNPs.

Acknowledgements

CHAPTER IV

UPTAKE OF HAIRPIN DNA FUNCTIONALIZED GOLD NANOPARTICLES BY HUMAN,

INSECT, AND BACTERIAL CELL LINES

Introduction

While Chapter III undertook a systematic investigation of the nanoparticle properties responsible for internalization, this chapter attempts to elucidate the biological properties that affect cellular uptake by characterizing the interaction of hairpin DNA functionalized gold nanoparticles (hAuNPs) with cells from four different organisms. For most cells, the plasma membrane is the initial point of contact with nanoparticles, and therefore plays an important role in mediating cellular uptake. Because the cell membranes of various organisms are intrinsically different, I hypothesized that this inherent diversity would be reflected in the extent of nanoparticle uptake by different cell types. Three human cell lines, one *Drosophila melanogaster* cell line, and the bacteria *Bacillus subtilis* and *Escherichia coli* are chosen to encompass the diversity of membranes found across species. It has been established that different mammalian cell lines exhibit variation in the amount of DNA functionalized gold nanoparticles (DNA-AuNPs) transported into the cell.[17,57] It is hypothesized that these nanoparticles are internalized via protein-mediated endocytosis, and differences in the degree of uptake could be the result of the differential expression of cell surface proteins.[17,22] To our knowledge, no uptake studies have been reported for insect cells or bacteria, and it is unknown how these cells interact with hAuNPs.

The basic structure of the cell membrane is conserved across species. It is composed of amphipathic lipids that spontaneously form self-sealing bilayers (Figure 4.1).[41] Proteins are embedded in the lipid bilayer or attached to the internal or external surface. The plasma membrane is integral to many functions, including movement of ions and molecules into and out of the cell. The hydrophobic portion of the bilayer creates an essentially impermeable barrier to the free movement of hydrophilic molecules.[38] Some nonpolar compounds can diffuse through the lipid bilayer, but in general, membrane proteins facilitate the transport of polar compounds.
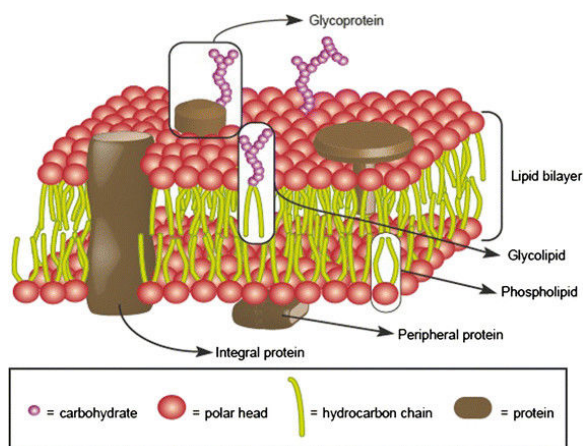
Figure 4.1. A schematic view of the plasma membrane structure. Amphipathic lipids form a bilayer through self-association of the hydrophobic tails. Proteins are embedded in the bilayer or attached to the surface. Carbohydrates decorate both lipids and proteins on the extracellular surface. (Reprinted with permission from: Lombard J. Once upon a time the cell membranes: 175 years of cell boundary research. *Biology Direct*. **2014**, *9* (32), doi:10.1186/s13062-014-0032-7. Copyright Lombard; licensee BioMed Central. 2014)

For human and insect cells, the first interaction with hAuNPs is through the plasma membrane, and the nature of this interaction determines if and how much nanomaterial the cell will internalize. With bacteria, the cell is protected by a peptidoglycan cell wall, and in the case of gram-negative bacteria, an additional outer membrane, that surround the cell membrane and may prevent hAuNPs from interacting directly with the underlying plasma membrane (Figure 4.2). Because the cell wall could be a significant barrier to hAuNP uptake, the internalization of

hAuNPs by cell wall deficient bacteria, or protoplasts, is also explored. Cell wall deficient bacteria are readily prepared by enzymatic treatment, which cleaves the peptidoglycan layer without affecting the internal biochemistry of the resulting protoplast.[73–77] The cell wall of gram-positive bacteria is completely removed, leaving the cytoplasmic membrane fully exposed.[73,77] Although gram-negative bacteria often do not undergo complete cell wall removal, large regions of the cytoplasmic membrane are exposed upon enzymatic treatment.[74–76] The term "protoplast" generally refers to cell wall deficient gram-positive bacteria, while "spheroplast" refers to cell wall deficient gram-negative bacteria. For clarity, the term "protoplasts" will refer to cell wall deficient *B. subtilis* and *E. coli* throughout this Chapter.
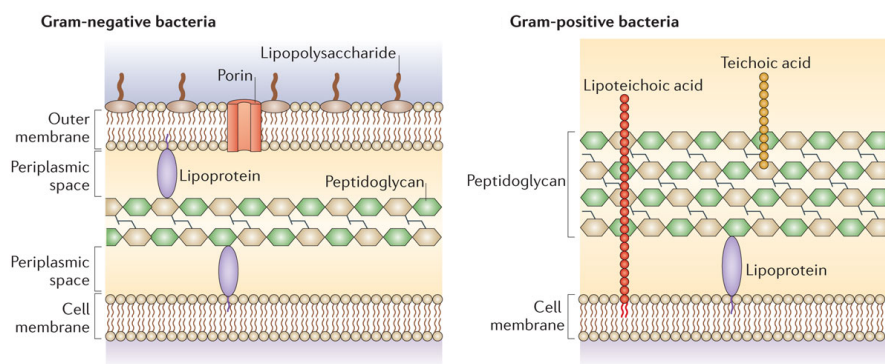
Figure 4.2. A schematic view of the cell wall of gram-negative and gram-positive bacteria. The cell membrane of gram-negative bacteria is protected by a thin layer of peptidoglycan attached to the outer membrane, which is decorated with lipopolysaccharides. Gram-positive cells have a much thicker peptidoglycan layer interspersed with teichoic acids. Adapted by permission from Macmillan Publishers Ltd: Nature Reviews Microbiology. Brown, L.; Wolf, J. M.; Prados-Rosales, R.; Casadevall, A. Through the wall: extracellular vesicles in Gram-positive bacteria, mycobacteria and fungi. *Nat. Rev. Microbiol.* **2015**, *13* (10), 620–630. Copyright 2015.

The uptake of hAuNPs by human cells, insect cells, bacteria, and protoplasts is evaluated by flow cytometry, confocal microscopy, and inductively coupled plasma – mass spectrometry (ICP-MS). Human and insect cells internalize hAuNPs in large amounts, while intact *B. subtilis* and *E. coli* exhibit almost no cellular association. Removing the cell wall increases the amount of nanoparticles associated with the protoplasts, but hAuNP accumulation does not reach the same

level as that of human and insect cells. The low accumulation of nanoparticles precludes the use of hAuNPs in bacterial imaging or gene expression studies, because the single cell fluorescence intensities are not significant enough to perform these applications. Examining the cellular uptake kinetics reveals that the human and insect cell lines exhibit different uptake profiles. Because hAuNP uptake varies by cell type, I hypothesized that the degree of accumulation is controlled by a biological characteristic that differs between the cells. Based on previous evidence, this is most likely a consequence of the expression of scavenger receptors, proteins that bind a broad range of polyanionic ligands.[17,58] Both human and insect cells express members of the scavenger receptor family on the cell surface, and the role of these proteins in cellular uptake is explored using the known scavenger receptor ligands, polyinosinic acid (polyI) and dextran sulfate. Competition studies show that hAuNP accumulation in human and insect cells is significantly reduced in the presence of these molecules, but not with control compounds that do not bind scavenger receptors. This evidence supports a scavenger receptor mediated uptake mechanism for hAuNPs, as has been reported previously for DNA-AuNPs and mammalian cells.[17,58] Further mechanistic studies into the interaction between hAuNPs and the human and insect cell membrane will be required to fully characterize the uptake process. These results enhance our knowledge about the processes involved in the internalization of hAuNPs, which enables the design and evaluation of functional gold nanoparticles with optimal cellular uptake properties for imaging and therapeutic applications.

Materials and Methods

Materials

Citrate-stabilized gold nanoparticles (15 nm) were purchased from Ted Pella, Inc. DNA was purchased from Integrated DNA Technologies. Amicon Ultra 3K MWCO filters were

purchased from EMD Millipore. CaSki cells were purchased from ATCC, HEp3 cells were a gift from the Andries Zijlstra laboratory, HEK-293 and S2R+ cells were a gift from the David Weaver laboratory, and *Bacillus subtilis* and *Escherichia coli* (ATCC 10536) were gifts from the Brian Bachmann laboratory. The 8 well μslides were purchased from ibidi USA, Inc. Fetal bovine serum (FBS) was purchased from Atlanta Biologicals. Propidium iodide, SYTO13, CountBright Absolute Counting Beads, penicillin/streptomycin, trypsin, DMEM, and trypan blue were purchased from Thermo Fisher Scientific. HEPES was purchased from Research Products International, Corp. Molecular biology grade water, Tris-EDTA buffer, RPMI 1640 with L-glutamine, sodium pyruvate, and phosphate buffered saline (PBS), were purchased from Corning. All other materials were purchased from Sigma-Aldrich or Fisher Scientific.

DNA Preparation

Pellets of lyophilized DNA containing a thiol modification were rehydrated in 0.1 M dithiothreitol (DTT) dissolved in 0.1 M dibasic phosphate solution, pH 8.3. The solution was vortexed until the pellet dissolved and allowed to react for 1 hour with rotation in the dark. The DNA was desalted and washed with Tris-EDTA buffer using the manufacturer's directions for Amicon Ultra 3K molecular weight cutoff (MWCO) filters. The DNA was resuspended in Tris-EDTA buffer at an appropriate working concentration, which was determined by measuring the A_{260} using a Take3 Microvolume Plate and Biotek Synergy H4 microplate reader. Unmodified DNA sequences were reconstituted in Tris-EDTA buffer. All DNA was stored at -80°C until use.

hAuNP Synthesis

A stock solution of 15 nm citrate-stabilized AuNPs was diluted to 1 nM in molecular biology grade water and Tween20 (0.1% v/v) was added to 1 mL aliquots of AuNPs. The T-10 diluent oligonucleotide was added at a final concentration of 0.1 μM. The tubes were incubated

at room temperature overnight on a tube rotator and protected from light. The hDNA oligonucleotide was added at a final concentration of 0.3 μM and the samples were incubated overnight as before. Phosphate buffer (100 mM, pH 7) was added at a final concentration of 10 mM and the nanoparticles were adjusted to 0.1 M NaCl, followed by a ≥ 4 hour incubation. The nanoparticles were adjusted to 0.2 M NaCl, followed by a ≥ 4 hour incubation. The nanoparticles were adjusted to 0.3 M NaCl, followed by a final overnight incubation. The resulting hAuNPs were centrifuged at 21,100 g for 20 minutes to form a loose pellet. The supernatant was removed and discarded, and the pellet was resuspended in PBS. The process of centrifugation and resuspension was repeated twice more to obtain a final, concentrated pellet. The individual tubes of AuNPs were combined into a single batch of hAuNPs.

hAuNP Characterization

The hAuNPs were characterized by fluorescence, dynamic light scattering, and oligonucleotide loading as described previously. Briefly, to characterize the hairpin DNA on the nanoparticle surface, hAuNP fluorescence was measured before and after the addition of an oligonucleotide complementary to the loop region of the hDNA. The hAuNP stock was diluted to 1 nM in PBS with 0.1% Tween20. This sample was aliquoted and exposed to complementary and non-complementary DNA at 3 uM or no DNA for 1 hour at 37°C. The fluorescence of each solution was measured in triplicate in a black 96 well plate using a Biotek Synergy H4 microplate reader configured for Cy5 fluorescence (excitation: 650 nm; emission: 670 nm). Dynamic light scattering was used to measure the hydrodynamic diameter of the hAuNPs. A 1 nM solution of hAuNPs in PBS was filtered through a 0.22 μm PVDF syringe filter before analyzing with a Malvern ZetaSizer NanoZS. For zeta potential measurements, a 1 nM solution of hAuNPs in 10 mM NaCl was filtered through a 0.22 μm PVDF syringe filter before analyzing

with a dip cell and Malvern ZetaSizer NanoZS. To quantify the fluorescent hDNA loading on the nanoparticles, a 1 nM solution of hAuNPs in 0.1 M DTT was incubated for 2 hours on a tube rotator. The samples were centrifuged at 21,100 *g* for 20 minutes and analyzed for Cy5 fluorescence in triplicate in a black 96 well plate. The resulting measurement was compared against the fluorescence from a calibration curve of free hDNA to find the concentration of fluorescent DNA in the hAuNP samples. The DNA concentration was divided by the AuNP concentration to arrive at the average number of hDNA ligands per nanoparticle. Reported values represent mean ± SD from three batches with three technical replicates each.

Mammalian and Insect Cell Culture

CaSki, HEp3, HEK-293 cells were grown at 37°C in a humidified atmosphere with 5% CO_2. CaSki cells were cultured in RPMI 1640 with L-glutamine supplemented with 10% fetal bovine serum (FBS), 100 units/mL penicillin, 100 μg/mL streptomycin, 2.25 g/L D-glucose, 1 mM sodium pyruvate, and 10 mM HEPES. HEp3 cells were cultured in DMEM with L-glutamine and sodium pyruvate supplemented with 10% FBS, 100 units/mL penicillin, 100 μg/mL streptomycin, 10 mM HEPES, and 1x MEM non-essential amino acids. HEK-293 cells were cultured in DMEM with L-glutamine supplemented with 10% FBS, 100 units/mL penicillin, 100 μg/mL streptomycin. S2R+ cells were grown at 25°C in a humidified atmosphere. The cells were maintained in M3 medium with 5 mM $NaHCO_3$ (pH 6.6) supplemented with 1 g/L yeast extract, 2.5 g/L bactopeptone, 10% FBS, 100 units/mL penicillin, and 100 μg/mL streptomycin. Cells were subcultured upon reaching 80-90% confluence.

Bacterial Culture

B. subtilis was maintained in ISP2 broth (pH 7.2), which consisted of 10 mg/mL malt extract, 4 mg/mL dextrose, and 4 mg/mL yeast extract. A 30 μL aliquot of *B. subtilis* glycerol

stock was streaked onto an ISP2 agar plate and allowed to grow overnight at 30°C. Liquid cultures were inoculated from a single colony and allowed to grow overnight at 30°C and 190 rpm. The cells were subcultured into fresh medium at OD_{600} = 0.05 and grown for subsequent use in cellular uptake studies. Overnight cultures of *E. coli* were grown in LB broth at 37°C and 180 rpm. The next day, 1% of the overnight culture was inoculated into fresh LB and grown for subsequent use in cellular uptake studies.

Protoplast Preparation

B. subtilis (OD_{600} = 1.0) was pelleted at 4425 *g* for 5 minutes at 4°C. The pellet was resuspended in *B. subtilis* protoplast buffer (1:1 ratio of 2x ISP2 and 2x SMM). The composition of 2x SMM (pH 6.5) was 1 M sucrose, 0.04 M maleic acid, and 0.04 M $MgCl_2$. Lysozyme (1 mg/mL in 1x SMM) was added to the cells at a final concentration of 0.2 mg/mL for 35 minutes at 30°C and 170 rpm. Protoplast formation was confirmed by observing the change from rod to spherical morphology under a light microscope. The protoplasts were pelleted at 2000 *g* for 5 minutes at 4°C and washed in protoplast buffer once before a final resuspension in either protoplast buffer or protoplast buffer with 10% FBS for cellular uptake experiments.

E. coli (OD_{600} = 0.9) was pelleted at 4425 *g* for 5 minutes at 4°C. The pellet was washed one time with 10 mM Tris-HCl, pH 8.0 and resuspended in 0.5 M sucrose, 0.03 M Tris-HCl (pH 8.0), 100 μg/mL lysozyme, and 10 mM EDTA for 45 minutes at 37°C and 180 rpm. The protoplasts were pelleted at 2000 *g* for 5 minutes at 4°C and washed in *E. coli* protoplast buffer (0.5 M sucrose, 0.03 M Tris-HCl, pH 8.0) once before a final resuspension in either protoplast buffer or protoplast buffer with 10% FBS for cellular uptake experiments.

Human and Insect Cellular Uptake Kinetics

CaSki, HEp3, and HEK-293 cells (2×10^5 cells per well) were seeded into a 12-well plate one day in advance. hAuNPs were added to the cells at 1 nM final concentration in 0.5 mL of the appropriate medium and incubated at 37°C and 5% CO_2 for 2 – 8 hours. At different time points, the hAuNP-containing medium was removed and the cells were washed with PBS to remove excess uninternalized nanoparticles. The cells were trypsinized for counting with a Countess II automated cell counter, and centrifuged at 500 *g* for 5 minutes to form a pellet. The supernatant was removed and the pellets were frozen at -40°C until subsequent analysis by inductively coupled plasma – mass spectrometry (ICP-MS).

S2R+ cells (6×10^5 cells per well) were seeded into a 12-well plate one day in advance. hAuNPs were added to the cells at 1 nM final concentration in 0.5 mL of the appropriate medium and incubated at 25°C for 2 – 8 hours. At different time points, the loosely adherent cells were washed off the well plate by repeated pipetting of the existing medium. The cell suspension was transferred to a 1.5 mL centrifuge tube and an aliquot was saved for counting. The cells were pelleted by centrifugation at 1500 *g* for 5 minutes. The supernatant was removed and the cells were resuspended in an equal volume of fresh medium. This process was repeated once and the cells were transferred to a 15 mL conical tube and centrifuged again to produce the final pellet. After removal of the supernatant, the pellets were frozen at -40°C until ICP-MS analysis.

The S2R+ supernatants were analyzed for gold content by inductively coupled plasma – optical emission spectroscopy (ICP-OES) to ensure that loosely bound and uninternalized nanoparticles were removed. The supernatants were digested overnight in 800 µL aqua regia (3:1 HCl : HNO_3). (*Warning: Aqua regia is extremely corrosive, handle with caution*). Deionized H_2O was added to each tube to achieve a total volume of 6 mL. Gold was quantified by

measuring the integrated area of the emission peak at 267.595 nm on a Perkin Elmer Optima 7000 DV instrument. The reported concentration was in µg/L, which was converted to molarity as described in Appendix F. Reported values represent mean ± SD from three replicates.

Bacteria and Protoplast Cellular Uptake

hAuNP stability in the bacterial growth medium and protoplast buffers was evaluated by collecting gold nanoparticle absorbance spectra in each matrix using a microplate reader. To measure the cellular uptake of intact bacteria, fresh cultures of *B. subtilis* and *E. coli* were grown for 1.5 hours. The bacteria were suspended in their respective broth or broth + 10% FBS and distributed into 0.5 mL aliquots. hAuNPs were added at 1 nM final concentration for 2 hours at 30°C (*B. subtilis*) or 37°C (*E. coli*) and 180 rpm. Untreated controls were also prepared under the same conditions. The cells were centrifuged at 1500 *g* for 10 minutes at 4°C and washed twice with 0.85% NaCl. The final suspension was in 0.85% NaCl. A portion of the bacterial suspension was transferred to a 15 mL conical tube and stored at -40°C until subsequent ICP-MS analysis. Samples were also prepared for analysis by flow cytometry. A 1:100 dilution of bacteria was prepared in a solution of 5 µM SYTO13 and 30 µM propidium iodide (PI) in 0.85% NaCl and incubated at room temperature for 15 minutes before adding 50 uL of CountBright beads. The samples were analyzed by collecting 5000 bead events on a BD LSRII flow cytometer equipped with excitation at 488 nm, 535 nm, and 633 nm. Unstained and single color controls were also analyzed. FlowJo analysis software was used to visualize the data. Reported values represent mean ± SD from three biological replicates.

Protoplasts suspended in their respective protoplast buffer or protoplast buffer + 10% FBS were treated and processed as above for 30 minutes and 2 hours, except that protoplast

buffer was used as the wash and dilution buffer instead of 0.85% NaCl. Reported values represent mean ± SD from three biological replicates.

ICP-MS

Samples were thawed and digested overnight in 800 µL of aqua regia. Deionized H_2O was added to each tube to achieve a volume of 6 mL. The ^{197}Au content of the samples was measured at medium resolution ($R = 4300$) on a Thermo Element 2 high resolution inductively coupled plasma mass spectrometer (ICP-MS) equipped with an electrospray ionization (ESI) auto sampler. Samples were uptaken by self-aspiration via a 0.50 mm ID sample probe and capillary to the spray chamber. The number of AuNPs per cell was calculated from the gold concentration measured by ICP-MS and the number of cells counted in the sample, as described in Appendix E. Reported values represent mean ± SD from three biological replicates.

Flow Cytometry

CaSki, HEp3, and HEK-293 cells (2×10^5 cells per well) were seeded into a 12-well plate one day in advance. hAuNPs (1 nM) were added to the cells in 0.5 mL of culture medium and incubated at 37°C and 5% CO_2 for 2 or 8 hours. The hAuNP-containing medium was removed and the cells were washed three times with PBS. The cells were dissociated by trypsin and 10,000 events were collected on a BD LSRII flow cytometer with excitation at 633 nm. Untreated cells were analyzed as a negative control. FlowJo analysis software was used to visualize the data. To obtain mean cell fluorescence, the geometric mean of the hAuNP fluorescence of each sample was calculated in FlowJo. Reported values represent mean ± SD from three biological replicates.

S2R+ cells (6×10^5 cells per well) were seeded into a 12-well plate one day in advance. hAuNPs (1 nM) were added to the cells in 0.5 mL of culture medium and incubated at 25°C.

After 2 and 8 hours, the loosely adherent cells were washed off the well plate by repeated pipetting of the existing medium. The cell suspension was transferred to a 1.5 mL centrifuge tube and the cells were pelleted by centrifugation at 1500 g for 5 minutes. The supernatant was removed and the cells resuspended in an equal volume of fresh medium. This process was repeated twice before analyzing the cells by flow cytometry as described above.

Confocal Microscopy

CaSki cells (5×10^4 cells/mL), HEp3 cells (5×10^4 cells/mL), and HEK-293 cells (1.1×10^5 cells/mL) were seeded into an 8-well μslide one day in advance. S2R+ cells (7.5×10^5 cells/mL) were seeded into an 8-well μslide two days in advance. The cells were exposed to 1 nM hAuNPs in culture medium for 8 hours at 37°C and 5% CO_2. The cells were stained with SYTO13 nucleic acid stain (400 nM for CaSki, 1 μM for HEp3, HEK-293, and S2R+) for 1 hour prior to imaging. Excess hAuNPs and SYTO13 was removed and the cells were washed with their respective medium before adding a final volume of 100 μL of phenol-red free medium for imaging. S2R+ cells were imaged in M3 medium. Images were taken with a Zeiss LSM 510 Meta Confocal Microscope using a 63x plan-apochromat 1.4 oil DIC objective and a 1.5 μm optical slice. Excitation of the SYTO13 and Cy5 fluorophores was done with 488 nm and 633 nm lasers, respectively. Emission was collected with BP 505-550 and LP 650 filters.

Competitive Inhibition Assay

Stock solutions of polyI and polyadenylic acid (polyA) were prepared in Tris-EDTA buffer at 3.47 mg/mL, and stored at -20°C. Stock solutions of dextran sulfate and galactose were prepared fresh in PBS at 4 mg/mL. CaSki, HEp3, and HEK-293 cells (1.5×10^5 cells per well) and S2R+ cells (6×10^5 cells per well) were seeded into 12 well plates one day in advance. PolyI and polyA were thawed and heated at 50°C for 10 minutes until fully dissolved. The culture

medium was replaced with fresh medium and polyI, polyA, dextran sulfate, or galactose at 50, 250, and 500 µg/mL for 30 minutes at 37°C (CaSki, HEp3, and HEK-293) or 25°C (S2R+). hAuNPs were added directly to the medium at 1 nM for four hours. Controls included untreated cells and cells treated with hAuNPs only. After treatment the culture medium was removed, and CaSki, HEp3, and HEK-293 cells were washed three times with PBS before being dissociated with trypsin and collected for flow cytometry. To collect the loosely adherent S2R+ cells, the existing culture medium was repeatedly pipetted against the surface of the well, and the cell suspension was collected into 1.5 mL centrifuge tubes. The S2R+ cells were pelleted by centrifuging at 500g for 5 minutes. The supernatant was removed and the cells were resuspended in fresh culture medium. This was repeated two times before collecting the cells for flow cytometry. Using a BD LSRII flow cytometer with excitation at 633 nm, 10,000 single cell events were collected for each sample. Untreated cells were analyzed as a negative control. FlowJo analysis software was used to visualize the data and calculate the geometric mean of the Cy5 fluorescence. The data is represented as percent of control, where the geometric mean of each sample was normalized by the value calculated for hAuNP only samples and converted to a percent. Reported values represent mean ± SD from three biological replicates.

Statistical Analysis

Statistical analysis was performed using an unpaired t-test.

Results and Discussion

Human and Drosophila Cell Lines Accumulate Large Quantities of hAuNPs

As in the previous chapters, the hAuNPs were designed to be non-targeting to focus solely on cellular uptake. The nanoparticles were characterized by fluorescence, hydrodynamic diameter, zeta potential, and amount of hDNA per nanoparticle (Supplemental Figure F.1,

Appendix F). The results were comparable with those from Chapters II and III. Cellular uptake was evaluated for the human cell lines, CaSki, HEp3, and HEK-293, and the insect cell line, S2R+. These cell lines were chosen to represent a range of cultured cell and tissue types. CaSki cells are derived from an epidermoid carcinoma of the cervix that metastasized to the small intestine.[78] The HEp3 cell line is derived from a rapidly growing metastatic epidermoid carcinoma thought to have originated in the buccal mucosa.[79] HEK-293 cells are derived from human embryonic kidney cells transformed by sheared adenoviral DNA.[80] The S2R+ cell line is a *Drosophila melanogaster* derived cell and an isolate of Schneider's line 2 (S2), which came from the late stage of embryonic development.[81] Exposure to hAuNPs does not compromise cell viability compared to an untreated control, as measured by the trypan blue exclusion assay (Supplemental Figure F.2, Appendix F).

hAuNP internalization was initially characterized by flow cytometry and confocal microscopy (Figure 4.3). Flow cytometry provides information about the fluorescence intensity of the cell population, as well as the transfection efficiency, or the amount of cells in the population that are positive for hAuNP fluorescence, and therefore contain nanoparticles. To quantify transfection efficiency, a hAuNP positive gate is set based on the background fluorescence of unstained cells so that only 1% of negative cells are included (Supplemental Figure F.3, Appendix F). This gate is then applied to the remaining samples and events falling within the gate are identified as positive for hAuNP fluorescence. Two hours after exposure to hAuNPs, 98% of the cells have measurable nanoparticle fluorescence (Figure 4.3A). An examination of time points shorter than two hours reveals that the percentage of hAuNP positive CaSki cells increases quickly within the first hour of exposure, reaching 67% only 15 minutes after adding nanoparticles to the culture medium (Supplemental Figure F.4, Appendix F).

Nanoparticle association and uptake occurs quickly and uniformly for the cells, which behave as

a single population. Longer hAuNP exposure times result in an increase in mean cell
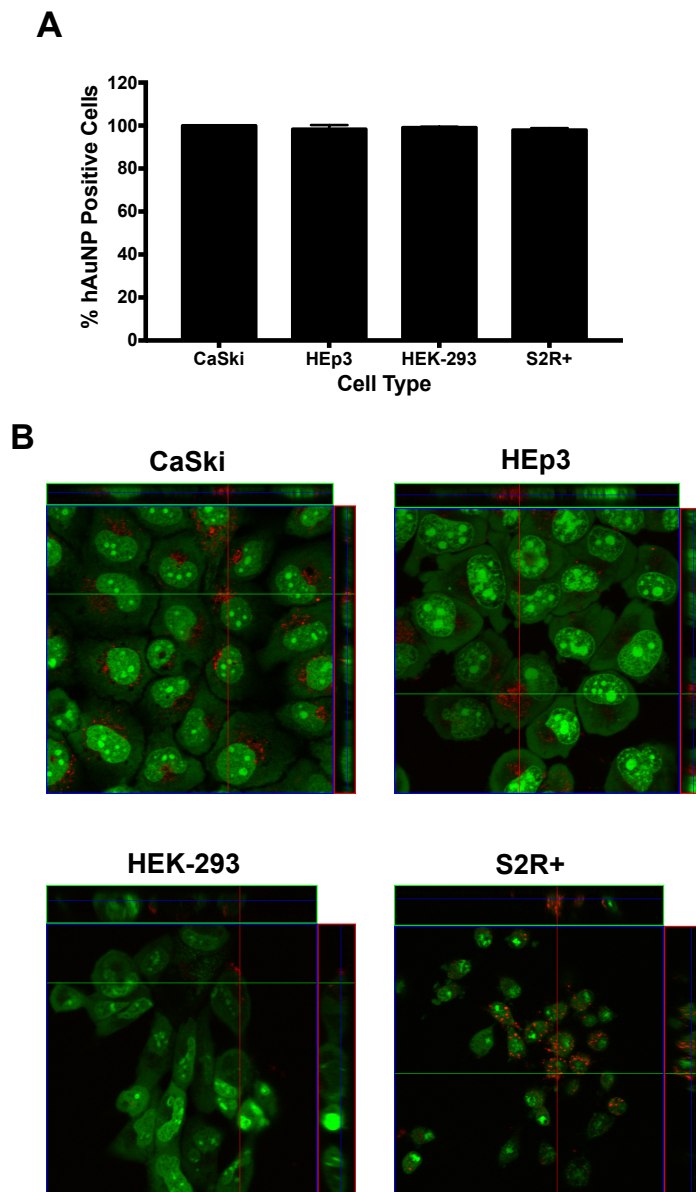
Figure 4.3. Transfection efficiency and confocal microscope images of CaSki, HEp3, HEK-293, and S2R+ cells. (A) After 2 hours of nanoparticle exposure, 98% of the cells exhibit hAuNP fluorescence, indicating that the cells behave as a single population. (B) Imaging along the z-axis of the cells with confocal microscopy reveals that hAuNPs enter the cell and localize to the cytoplasm and perinuclear space. HEK-293 cells have almost undetectable fluorescence compared the other cells. Green: nucleic acid stain. Red: hAuNPs.

fluorescence intensity, consistent with increased accumulation of nanoparticles over time

(Supplemental Figures F.5 – F.6, Appendix F). Variations in fluorescence suggest that the

different cell lines take up different amounts of nanoparticles. CaSki and HEp3 cells have the highest amount of fluorescence, followed by S2R+. HEK-293 cells exhibit low fluorescence intensities regardless of hAuNP exposure time.

The cells were imaged by confocal microscopy after an 8 hour hAuNP treatment (Figure 4.3B). Imaging through the z-axis demonstrates that cells internalize hAuNPs, which are localized throughout the cytoplasm, but not in the nucleus, consistent with data from Chapter III. As with flow cytometry, CaSki, HEp3, and S2R+ have high levels of fluorescence, but HEK-293 cells have nearly undetectable fluorescence. Imaging reveals a distribution of nanoparticle fluorescence across the individual cells, with some cells having larger regions of fluorescence than others. This is also reflected by the flow cytometry histograms showing that a population of cells exhibits a distribution of fluorescence intensities (Supplemental Figure F.5, Appendix F).

Flow cytometry demonstrates that all of the cells in the population take up hAuNPs, and confocal microscopy confirms that the nanoparticles are truly internalized by the cell. However, these techniques do not provide quantitative data about the amount of nanoparticles in the cells. ICP-MS is an aggregate measurement of the cellular gold content, which can be converted to an average number of gold nanoparticles per cell. To obtain kinetic measurements, hAuNPs were added directly to the cell culture medium for $2 - 8$ hours, and the cellular gold content was determined by ICP-MS (see Appendix F for calculations). CaSki and HEp3 cells internalize hAuNPs at much higher rates of uptake than HEK-293 cells (Figure 4.4A). The rate of HEK-293 nanoparticle uptake was determined from the slope of the linear regression, and is not significantly different from zero ($p > 0.05$), indicating that these cells take up almost no hAuNPs in the time period explored here. The hAuNP content of HEp3 cells begins to saturate at $3.9 \times$

10^4 hAuNPs per cell between 6 and 8 hours of exposure. By 8 hours, CaSki cells achieve

approximately the same amount of nanoparticles per cell without reaching saturation. This is
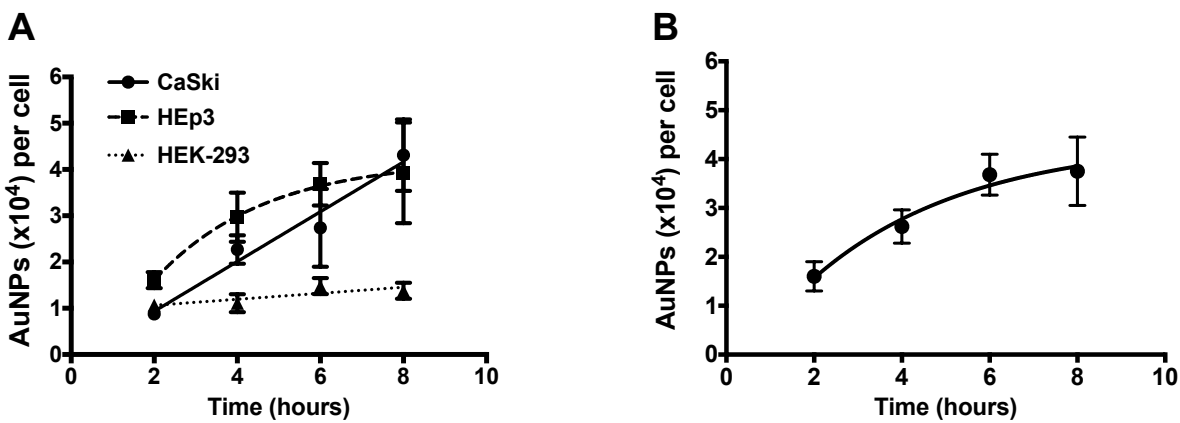
Figure 4.4. Cellular uptake of hAuNPs by human and insect cell lines. (A) CaSki and HEp3 cells exhibit robust uptake of hAuNPs, but HEK-293 cells have a static uptake of hAuNPs in this 8 hour time period. (B) S2R+ cells exhibit robust uptake of hAuNPs as determined by ICP-MS and accumulate similar amounts of gold nanoparticles per cell as human cell lines.

consistent with data from Chapter III, which shows that the nanoparticle content of CaSki cells

does not saturate over a 24 hour time period. The S2R+ *Drosophila* cell line also exhibits robust

nanoparticle uptake, ultimately reaching similar amounts of hAuNPs per cell as the human cell

lines, CaSki and HEp3 (Figure 4.4B). Like HEp3 cells, S2R+ cells approach saturation between

6 and 8 hours of hAuNP exposure time. Previously, Giljohann et al. also demonstrated that

different cell types internalize different amounts of nanoparticles.[57] HeLa (human), C166

(mouse), and A549 (human) cells internalized high, medium, and low amounts of DNA-AuNPs,

respectively. In a later report, differences in uptake were hypothesized to be the result of varying

expression levels of caveolin-1 and class A scavenger receptor proteins on the cell surface.[17] The

expression level of these two proteins was positively correlated with the gold content of four

different cell types.

Scavenger Receptor Ligands Inhibit hAuNP Uptake

The evidence from Chapter II and previous reports suggests that hAuNPs enter cells via a protein-mediated mechanism. Scavenger receptors are a family of cell surface proteins that bind and remove unwanted foreign material from the exterior of the cell by endocytosis.[82] Scavenger receptor proteins are primarily expressed by immune cells such as macrophages and dendritic cells, but also by fibroblasts, microglia, astrocytes, endothelial, and epithelial cells.[83] Proteins in this family are involved in innate immunity and bind both self and non-self molecules, including lipoproteins, proteins, apoptotic cells, lipopolysaccharide, lipoteichoic acid, bacterial CpG DNA, and whole pathogens.[82] Scavenger receptor ligands are often polyanionic molecules, and this binding is probably driven by electrostatic attraction to large cationic regions of the proteins. In both human and insect cell lines, scavenger receptors have been implicated in the binding and internalization of free nucleic acids and of nanoparticles with and without DNA attached.[17,35,83–87] In human cells, class A scavenger receptors (SR-A) have been proposed as putative receptors for free DNA and DNA-AuNPs.[17,22,60,84,86,87] Choi et al. characterized the binding of SR-A to DNA-AuNPs, identified SR-A as a primary mediator of DNA-AuNP uptake, and attributed differences in internalization by four cell lines to differences in SR-A expression.[17] Cells deficient in class B scavenger receptors were found to have a 25% reduction in DNA-AuNP uptake, indicating the potential for other scavenger receptor families to be involved in cell entry. Additional support for this idea comes from Zhu et al.[84] In this work, spleen cells from SR-A$^{-/-}$ mice retained the ability to internalize nucleic acids, suggesting that other cell surface proteins are involved in the uptake process, and could be compensating for the loss of SR-A.

Interestingly, HEK-293 cells are considered non-phagocytic and do not express SR-A, which may account for the low levels of hAuNP uptake into these cells compared to CaSki,

HEp3, or S2R+.[88] Orr et al. used flow cytometry to show that increased uptake of fluorescent silica nanoparticles occurred in HEK-293 cells engineered to overexpress SR-A but not in unmodified cells. Unmodified cells did exhibit low levels of nanoparticle-associated fluorescence, demonstrating that HEK-293 cells are capable of taking up nanoparticles, probably via non-SR-A mediated mechanisms. The expression of scavenger receptors in CaSki and HEp3 cells has not been reported in the literature at this time. Some of the cell lines explored previously by our laboratory have been reported to express scavenger receptor proteins.[6,11] HEp-2, a laryngeal carcinoma, is known to express class B scavenger receptors, while the epithelial breast cancer cell lines MCF7 and MDA-MB-231 are known to express class A and B scavenger receptors.[89–91] In addition to these cell types, Choi et al. found that mouse endothelial cells (C166), human lung adenocarcinoma epithelial cells (A549), mouse fibroblasts (3T3), and human keratinocytes (HaCaT) express SR-A.[17] *Drosophila* cells express a number of scavenger receptors.[85,92] Among these, class C scavenger receptors have been demonstrated to internalize free dsRNA in cultured *Drosophila* S2 cells.[85] Using RNA interference to reduce the expression of two scavenger receptor proteins significantly decreased the cellular uptake of dsRNA. Pearson, et al. reported that *Drosophila* S2 cells express a class C scavenger receptor that has activity and polyanionic ligand-binding properties resembling that of SR-A.[93] A number of known SR-A ligands inhibited the uptake of ^{125}I-labeled acetylated low-density lipoprotein by greater than 85% in this insect cell line.

I hypothesized that the differential expression of scavenger receptors could explain the observed differences in cellular uptake, and that treatment with SR-A ligands should abolish hAuNP uptake. To explore this, CaSki, HEp3, and HEK-293, and S2R+ cells were pre-treated with ligands known to bind class A and class C scavenger receptors,[58,93,94] and evaluated for

hAuNP fluorescence by flow cytometry. The human cell lines were exposed to polyI and polyA as an inhibitor and negative control, respectively. polyI and polyA were not soluble in the insect cell culture medium; therefore, the compounds dextran sulfate and galactose were explored as inhibitor and negative control for the S2R+ cells. Upon treatment with polyI or dextran sulfate, hAuNP uptake is considerably reduced for each cell line (Figure 4.5). At the highest concentration, polyI results in up to 90% inhibition of hAuNP uptake. At 50 μg/mL, dextran sulfate actually increases hAuNP uptake in S2R+ cells, which may be due to activation of a different protein receptor. However, the higher concentrations of this compound do inhibit the internalization of nanoparticles as expected. At the highest concentration of dextran sulfate, hAuNP uptake into insect cells is reduced by about 70%. Treatment with control compounds does not significantly affect hAuNP uptake for any cell type (Supplemental Figure F.7, Appendix F). When represented as percent of control, polyA appears to alter hAuNP uptake, but there is no concentration dependent shift in the fluorescence histogram, which indicates that polyA does not have a significant effect on uptake (Supplemental Figure F.8, Appendix F). In contrast, treatment with polyI or dextran sulfate causes significant, concentration dependent
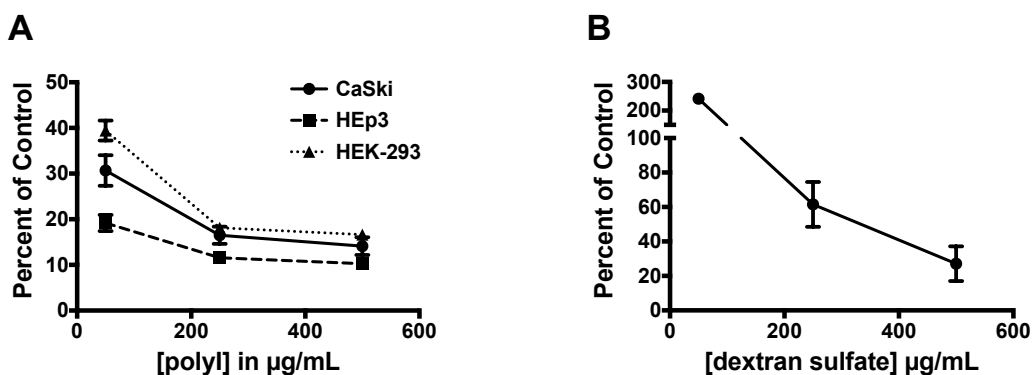
Figure 4.5. Scavenger receptor ligands inhibit hAuNP uptake in a concentration dependent manner. (A) PolyI results in up to 90% inhibition in the human cell lines. (B) Dextran sulfate inhibits hAuNP uptake by up to 70% in the insect cell line S2R+.

shifts in the fluorescence intensity of the cells. Cell viability is not affected by treatment with any of these compounds (Supplemental Figure F.9 Appendix F). hAuNP stability is maintained in the presence of each compound (Supplemental Figure F.10, Appendix F).

The scavenger receptor ligands, polyI and dextran sulfate, are able to competitively bind to this cell surface protein and prevent the cellular uptake of hAuNPs, supporting the hypothesis that internalization is a scavenger receptor mediated mechanism. Despite reports that HEK-293 cells do not express SR-A, Figure 4.4 shows that the cells internalize a significant amount of gold nanoparticles that is similar in scale to the other cell types (10^4 AuNPs per cell). In addition, polyI decreases hAuNP uptake similarly for the different cell types, which indicates that either the HEK-293 cells express very low levels of SR-A or the cells express a protein with similar activity that also binds polyI. Further mechanistic studies will be required to explore this hypothesis, and could include knockdown of scavenger receptor expression and over-expression of the protein in scavenger receptor negative cell lines.

hAuNPs Do Not Associate Significantly with Intact Bacteria

E. coli and *B. subtilis* were chosen as model organisms of gram-negative and gram-positive bacteria, respectively. Cells in the exponential growth phase were treated with hAuNPs in growth medium supplemented with 0% or 10% FBS. After 2 hours, excess hAuNPs were removed by centrifugation, and the cells were analyzed by flow cytometry and ICP-MS. During flow cytometry, cell viability was obtained using a combination of SYTO13 and PI fluorescent dyes, and cell counts were obtained using CountBright absolute counting beads. hAuNPs are stable in the bacterial media and no aggregation is detected by UV-vis spectrophotometry (Supplemental Figure F.11, Appendix F). Flow cytometry reveals that *B. subtilis* and *E. coli* have no significant hAuNP fluorescence, whether treated under normal growth conditions or with

10% FBS added to the growth medium (Supplemental Figure F.12, Appendix F). hAuNPs do not affect cell viability, but adding 10% FBS to *B. subtilis* cultures results in a slight decrease in the number of live cells (Supplemental Figure F.13, Appendix F). As measured by ICP-MS, association of hAuNPs with *B. subtilis* and *E. coli* is low compared to human or insect cells, but significantly different from untreated controls (Figure 4.6). In the absence of hAuNPs, no gold is detected in bacterial cells (data not shown). FBS alters the amount of associated hAuNPs, although the reason for this is not clear.
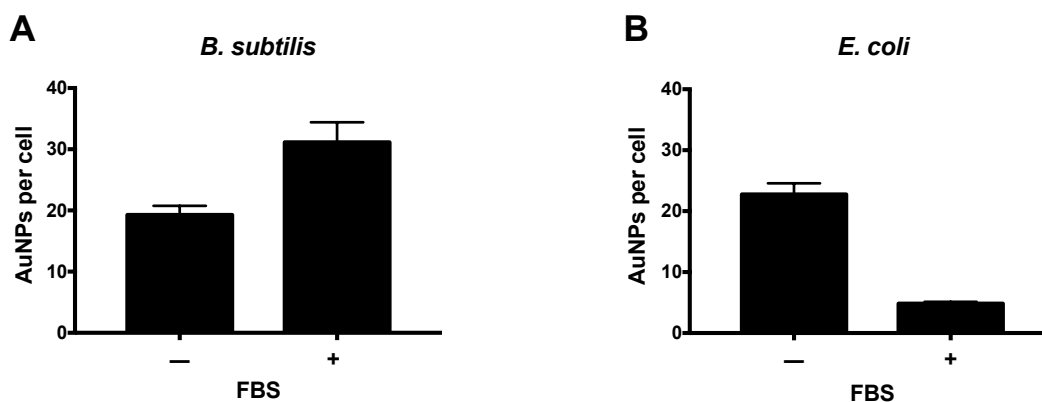
Figure 4.6. Quantification of hAuNP association with bacteria. ICP-MS analysis reveals that (A) *B. subtilis* and (B) *E. coli* accumulate low amounts of nanoparticles compared to human or insect cells.

Low hAuNP accumulation in bacteria could indicate an inability to transport hAuNPs through the cell wall components, possibly because there is no evidence of the expression of scavenger receptors or homologous proteins in bacteria. The low gold content explains the absence of hAuNP fluorescence in intact cells. At 5 – 30 hAuNPs per cell, there are not enough fluorophores associated with the cell to detect fluorescence from a single bacterium. Because no fluorescence can be detected, the use of DNA-AuNPs for imaging or gene expression applications with bacteria is not feasible. Furthermore, the location of the hAuNPs with respect to the bacterial cell is currently unknown, because ICP-MS and flow cytometry cannot distinguish nanoparticles located in the cellular interior from those on the exterior surface. To

fully understand the interaction of hAuNPs with bacteria, localization studies would be required to determine whether the nanoparticles are embedded in the cell wall or truly internalized.

Removing the Bacterial Cell Wall Increases hAuNP Association

The cell wall of bacteria prevents hAuNPs from interacting directly with the underlying plasma membrane, which is the primary point of interaction with human and insect cells. Enzymatic degradation by lysozyme removes the cell wall, exposing the membrane. The resulting cell bodies, known as protoplasts, are sensitive to cell lysis. Only a small amount of each protoplast preparation was identified as live (*i.e.* with intact membranes), probably due to the stress induced by treatment with lysozyme (Supplemental Figure F.14, Appendix F). Even 30 minutes after ending the enzymatic reaction, less than 30% of *B. subtilis* and *E. coli* protoplasts are stained as live. Adding hAuNPs to the protoplasts does not affect the viability.

B. subtilis and *E. coli* protoplasts were exposed to hAuNPs for 30 minutes and 2 hours and analyzed by flow cytometry and ICP-MS. Each cell type and time point represents a separate experiment. For *B. subtilis* protoplasts, hAuNP fluorescence is only measurable in the absence of FBS (Figure 4.7). In the presence of FBS, no hAuNP positive cells are detected. It is unclear why the amount of hAuNP positive cells decreases with time, even though the amount of gold nanoparticles per cell slightly increases, but may be a result of the low viability of these protoplasts at two hours (Figure 4.9). ICP-MS analysis demonstrates that the protoplasts accumulate greater amounts of hAuNPs when FBS is not present, consistent with the flow cytometry data. Up to 1000 hAuNPs per cell are detected after a two-hour exposure period, which is much greater than the gold content of intact *B. subtilis* cells. In FBS supplemented protoplast buffer, the protoplasts accumulate approximately the same amount of gold nanoparticles as intact cells.

In contrast to the *B. subtilis* protoplasts, large quantities of hAuNPs are taken up by *E. coli* protoplasts when the protoplast buffer is supplemented with 10% FBS, as demonstrated by
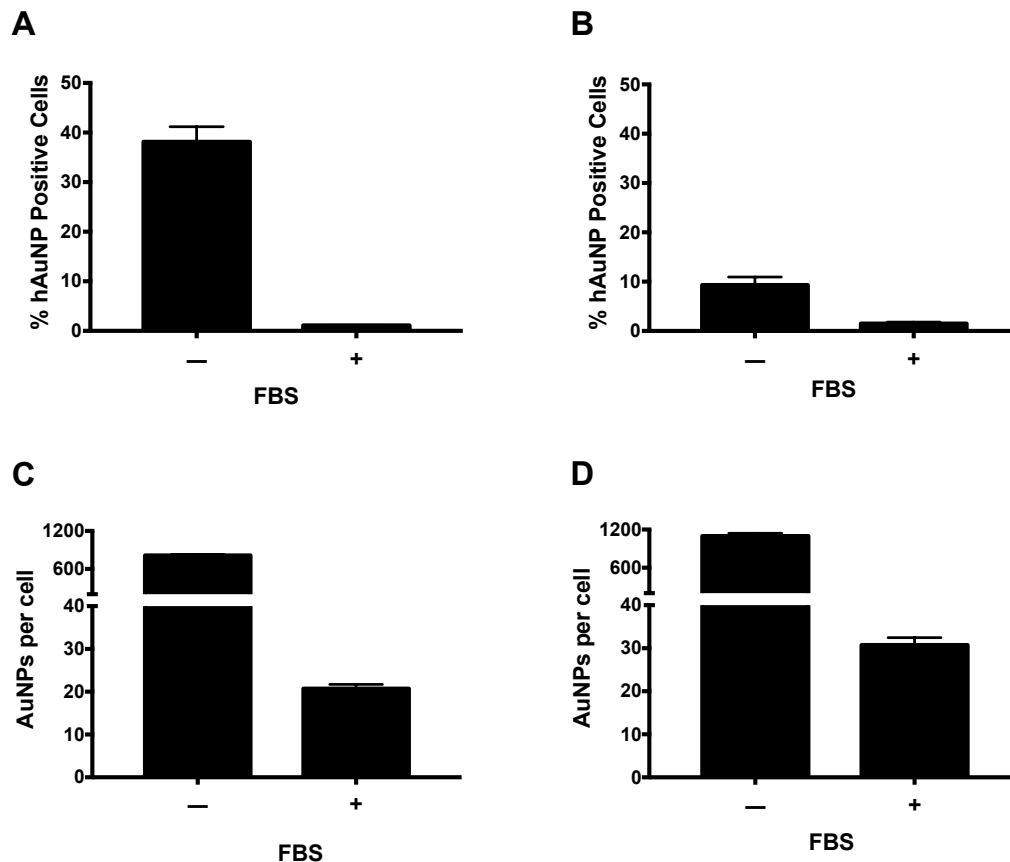
Figure 4.7. hAuNP association with *B. subtilis* protoplasts is higher in the absence of FBS. Using flow cytometry, hAuNP fluorescence is detectable in protoplasts exposed for (A) 30 minutes and (B) 2 hours only when the protoplast buffer is not supplemented with FBS. ICP-MS demonstrates that more hAuNPs are associated with protoplasts in the absence of FBS after (C) 30 minutes and (D) 2 hours. Under all conditions, there is a significant difference in nanoparticle association when FBS is included.

measurable hAuNP fluorescence and high gold nanoparticle per cell values (Figure 4.8). When

no FBS was added, the protoplasts have approximately the same gold content as intact *E. coli*

and no detectable fluorescence. There are many interacting and overlapping factors that

contribute to these results, including the efficiency of cell wall removal, the particular

composition of the exposed membrane, the presence of FBS, and the stability of each type of

protoplast. As these components interact, it could lead to results that do not have a clear pattern

between the species or conditions examined. Removing the cell wall clearly increases the amount

of hAuNPs accumulated by *B. subtilis* and *E. coli* protoplasts, in a manner dependent on the

inclusion or exclusion of FBS in the protoplast buffer. The dependence on FBS could be a result

of the particular cytoplasmic membrane of each species, and the mechanism by which the

hAuNPs are associating with the protoplast.
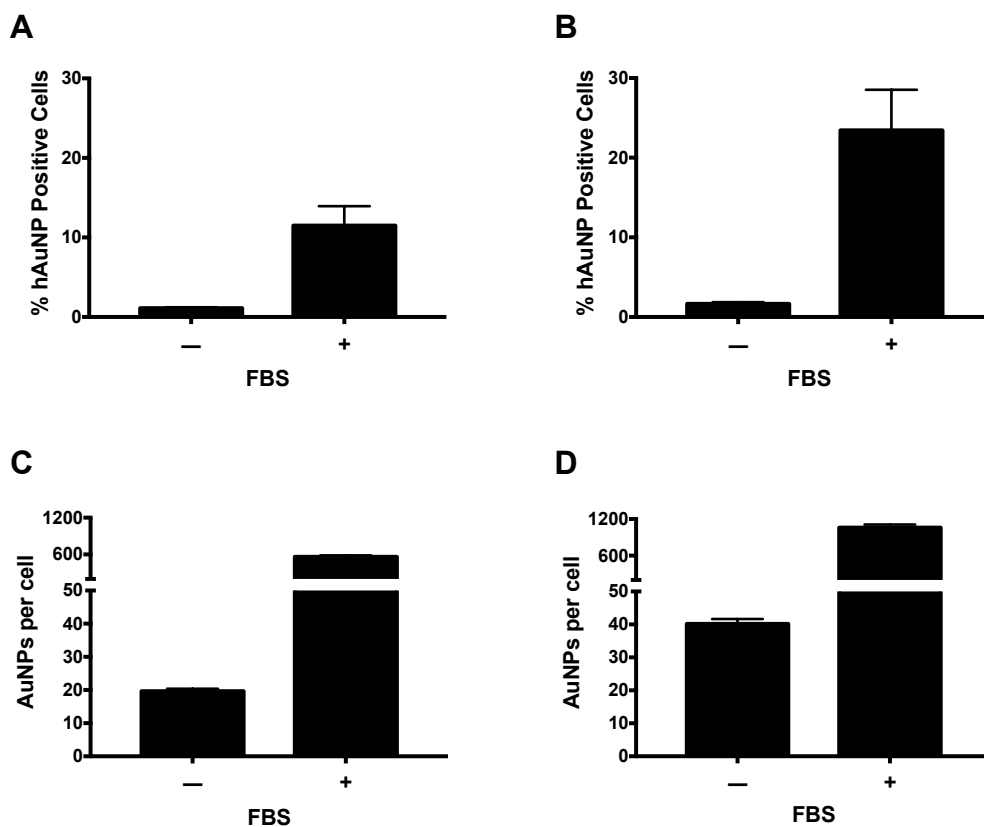
Figure 4.8. hAuNP association with *E. coli* protoplasts is higher in the presence of FBS. Using flow cytometry, hAuNP fluorescence is detectable in protoplasts exposed for (A) 30 minutes and (B) 2 hours only when the protoplast buffer is supplemented with FBS. ICP-MS demonstrates that more hAuNPs are associated with protoplasts in the presence of FBS after (C) 30 minutes and (D) 2 hours. Under all conditions, there is a significant difference in nanoparticle association when FBS is included.

hAuNP positive *B. subtilis* and *E. coli* protoplasts were analyzed for SYTO13 and

propidium iodide (PI) staining. In most cases, 25-30% of hAuNP positive protoplasts were

designated as live, *i.e.* they had excluded PI (Figure 4.9). It is uncertain whether the protoplasts

marked dead accumulated hAuNPs before or after cell death. PI is a membrane impermeant cell

stain that identifies bacteria as dead only if the membrane is compromised and becomes

permeable to the dye. The existence of a hAuNP positive protoplast population that excludes PI

demonstrates that protoplasts with intact membranes are able to accumulate hAuNPs. As with the

intact bacteria, these accumulated nanoparticles may be embedded in the cytoplasmic membrane

or internalized into the protoplast. Further imaging studies would be required to determine the

nature of the interaction between hAuNPs and bacterial protoplasts.
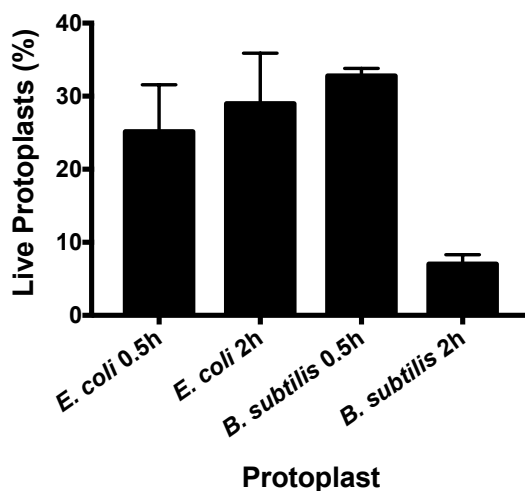
Figure 4.9. Percentage of hAuNP positive protoplasts that are also live. Protoplasts that stain with STYO13, but not PI are designated as live.

Comparing the *E. coli* and *B. subtilis* protoplasts to their respective intact cells

demonstrates that the outer membrane and peptidoglycan layers have a significant effect on how

hAuNPs interact with bacterial cells. It is clear that removing the cell wall increases nanoparticle

accumulation, but compared to human and insect cells, protoplasts do not accumulate enough

nanoparticles to produce a sufficient signal for use in imaging or gene expression applications.

Even though protoplasts accumulate more gold nanoparticles than intact bacteria, at most only

38% of the protoplasts have detectable hAuNP fluorescence. It is possible that a population of

protoplasts exists that does not associate with hAuNPs. Another explanation is that all of the

78

protoplasts interact with hAuNPs, but fluorescence is only detectable in those protoplasts that have accumulated the highest amount of nanoparticles. The flow cytometry histograms generally support this hypothesis and show a single population that shifts to higher fluorescence intensities, with a large portion of the cells overlapping with untreated controls (Supplemental Figures F.16 and F.17, Appendix F).

The study of how nanoparticles interact with bacterial cells is a relatively small field, mainly confined to the context of the antibacterial activity or environmental impacts of nanomaterials.[95–103] Most research has focused on understanding the mechanism of silver nanoparticle cytotoxicity to microbes or on whether bacteria are an appropriate model to assess the genotoxicity of nanomaterials. Few rigorous studies are solely focused on nanoparticle uptake into bacteria, and almost none quantify the amount of nanoparticle association or uptake. To evaluate nanoparticle uptake, Kumar et al. and Butler et al. use flow cytometry, which provides a semi-quantitative measurement of how many nanoparticles associate to single bacterial cells.[97,100] Such studies are often supplemented by transmission electron microscopy,[95–97,100,103] probably the most definitive method to support or disprove bacterial internalization of nanoparticles, although the images can be difficult to interpret objectively. Using a wide range of nanoparticle types, both true uptake and only surface association to bacteria have each been reported using these methods. To date, no mechanistic explanations of bacterial uptake have been proposed. If bacteria do internalize nanoparticles, it is unclear how this occurs.

Conclusion

By exploring the interaction between hAuNPs and cells originating from multiple species, we demonstrate that hAuNP association and uptake is not limited to mammalian cells. Human and *Drosophila* cell lines accumulate large quantities of nanoparticles intracellularly, as

demonstrated by flow cytometry, ICP-MS, and confocal microscopy. Based on the results of the competitive binding assay with known scavenger receptor ligands and on literature evidence, we hypothesize that scavenger receptor mediated endocytosis is a dominant pathway for hAuNP entry into human and insect cells. More detailed mechanistic studies are necessary to fully identify the pathway of uptake and determine the biological properties important to hAuNP-cell interactions. hAuNP association is very low in *E. coli* and *B. subtilis*, probably because there is no machinery to transport the nanoparticles across the cell wall. Exposing the plasma membrane of *E. coli* and *B. subtilis* increases the amount of accumulated hAuNPs, but not to sufficient levels to enable the detection of RNA, a common application of these types of functionalized nanoparticles. To our knowledge, this represents the first time that the amount of nanoparticle association with bacteria and protoplasts has been quantified.

Most likely there are multiple pathways by which cells internalize nanoparticles. The particular mechanism for hAuNP uptake and association depends on a number of biological parameters, including cell type (*e.g.* macrophage, epithelial) and species, expression of cell surface proteins, and environmental conditions (*e.g.* serum proteins). A complete understanding of how hAuNPs are internalized by or associated with cells remains elusive. However, these results expand our understanding of the interface between hAuNPs and cells and form a foundation for future mechanistic investigations. Such knowledge will inform nanoparticle design, safety, and efficacy considerations in biomedical applications.

Acknowledgements

CHAPTER V

OUTLOOK: TOWARDS A COMPLETE PICTURE OF NANOPARTICLE

INTERNALIZATION MECHANISMS

Importance of Studying the Nano-Bio Interface

Biology occurs on the nanoscale, and nanoparticles are uniquely positioned to interface with biological systems in ways that are unlike traditional macroscale medical devices. Like molecular drugs, nanoparticles can act at a subcellular level, while also leveraging the advantages of unique properties derived from their size. Nanomaterials hold much promise for providing tools to diagnose and treat disease or to study the underlying biology of normal and aberrant processes. As nanoparticles are increasingly used in medicine, personal care products, environmental and agriculture applications and more, it is vital that we fully understand the ways that nanoparticles affect the human body.

The fundamental unit of life is the cell, and all investigations of biological interactions, mechanisms of uptake, or cytotoxicity must begin in cell culture. In order to design effective sensors, therapeutics, and diagnostics, we must understand the processes that underlie the transport of nanoparticles into the cell: who are the binding partners, what machinery is involved, how is uptake initiated, what occurs after the particles enter the cell, what properties enhance or reduce uptake? Understanding cellular uptake will allow us to design sensors and therapeutics with more accurate delivery mechanisms, that require less material to be effective, and have fewer negative outcomes.

Nanotechnology has the potential to revolutionize aspects of human health, including disease treatment, disease diagnosis, and the generation of biological knowledge. It is important not only for the nano community to develop efficient, safe, and paradigm shifting technology, but also to effectively communicate the benefits and risks with the general public. To do so requires a deep and fundamental understanding of how nanomaterials interact with and alter biological systems. Thus, we must design systematic, stringent experiments in order to answer these fundamentally important questions and clearly understand the capability of nanotechnology to fulfill unmet biomedical needs.

Contribution to Biomedical Applications

Gold nanoparticles can be used in numerous biomedical applications, largely due to their unique optical properties and ease of functionalization. In this dissertation, I have identified several nanoparticle and biological properties that control DNA functionalized gold nanoparticle (DNA-AuNP) uptake into cultured cells through a systematic investigation of individual variables. The most important physicochemical property of the nanoparticle is size, or hydrodynamic diameter, and size is inversely related to cellular uptake. The expression of scavenger receptor proteins on the cell surface is an critical biological factor that determines the amount of DNA-AuNP uptake. These findings have important implications for the design of DNA-AuNPs for various biomedical applications, including drug delivery, diagnostic imaging, and targeted therapy.

RNA interference (RNAi) through delivery of silencing RNA to a cell is a method of inhibiting gene expression that can be used to treat disease. DNA-AuNPs can be designed as siRNA delivery vehicles whose cellular accumulation is controlled by DNA-AuNP size, concentration, and cell exposure time. To maximize accumulation over short time periods, small

DNA-AuNPs at high concentration would be used, as per the parameters determined in Chapter III. The size of the gold nanoparticle core also controls the amount of siRNA delivered, because more siRNA can be attached to a larger particle. Therefore, tuning of the nanoparticle size controls siRNA delivery in two ways: through the amount of siRNA loaded onto each particle and through the efficiency of cellular uptake.

These ideas can be extended to drug delivery and diagnostic imaging applications, where fine control of nanoparticle delivery to particular tissues is achieved through nanoparticle concentration, exposure time, and nanoparticle size, which affects both cellular uptake efficiency of the nanoparticle and the amount of drug or imaging agent loaded onto each nanoparticle. Because most cell types indiscriminately internalize DNA-AuNPs, it may be desirable to add a targeting ligand to direct the nanoparticles to a particular cell population, although this could alter the cellular uptake properties. Targeted photothermal therapy is a potential application of dually functionalized gold nanoparticles. The ligands could include i) an antibody or protein that specifically binds to a diseased cell and ii) DNA to facilitate cellular uptake. High concentrations of smaller functionalized AuNPs have been demonstrated to produce greater temperature changes than larger AuNPs after exposure to radiofrequency electric fields.[104] Larger temperature changes correspond to greater cell death, which is desirable for treatment of diseased tissues. Chapter III reports that cells preferentially internalize smaller DNA-AuNPs in large amounts; therefore, these smaller particles would be ideal for use in RF hyperthermia to treat cancers.

Finally, Chapter IV proposes the hypothesis that an interaction with scavenger receptor proteins on the cell surface is at least partially responsible for the translocation of DNA-AuNPs across the cell membrane. Therefore, it is expected that when these particles are exposed to a

whole organism, cells with high scavenger receptor expression will preferentially internalize DNA-AuNPs. The ability to perform imaging and therapeutic applications would then be enhanced in these cell populations, including macrophages, vascular smooth muscle, and endothelial tissues.

Future Work

Much progress has been made to understand the mechanism by which cells internalize DNA-AuNPs, but this dissertation underscores that questions remain to be answered. Evidence from Chapter II suggests that protein mediated cellular uptake is the primary mechanism by which nanoparticles accumulate inside cells, but also provided evidence for an interaction between membrane lipids and hAuNPs. Considering the role of serum proteins and the protein corona in the nano-bio interface, it is interesting that FBS causes hAuNPs to concentrate in a pure lipid membrane. This phenomenon was not reproducible in typical human cell culture. However, future confocal microscope studies could examine the localization of hAuNPs in red blood cells, which lack the capability to perform endocytosis. Like giant unilamellar vesicles, it is expected that hAuNPs will be found in one of three locations: outside the cell, adsorbed on or in the cell membrane, or fully internalized by the cell. If nanoparticles were found inside the cell, this would indicate that a non-endocytic process was occurring, and further mechanistic studies could explore how hAuNPs are taken up by red blood cells, possibly by performing single nanoparticle imaging and tracking with confocal microscopy or dark-field imaging, or by transmission electron microscope (TEM) imaging.

The intracellular fate of DNA-AuNPs is still not fully understood. Wu, *et al*. found that over 24 hours after exposure, the particles are trafficked through the endocytic pathway, and the DNA is detached from the nanoparticle core, possibly by DNase II enzymes that are highly

active at the low pH found in late endosomes.[68] Fluorophore labeled DNA is recycled out of the cell, but the nanoparticle core remains trapped within the cell. There are many examples of using DNA-AuNPs to image intracellular RNA or to silence RNA expression; therefore, some portion of the particles must exit the endosomal pathway in order to exert these functions. Endocytic trafficking could be further studied by using pH sensitive fluorophores, such as the pHrodo dyes, which are highly fluorescent in acidic environments, but not at neutral pH. The pHrodo dyes can be purchased with a number of different attachment chemistries, and DNA-AuNPs could be synthesized with the pHrodo dye to provide a way to measure the pH of the local environment surrounding the particle. After cellular uptake of the particles, fluorescent signal specific to the pHrodo dye would support a hypothesis of endocytic uptake, which could be further explored using fluorescent proteins that specifically label the different stages of endocytosis. Colocalization of DNA-AuNP fluorescence with the fluorescent protein markers would indicate that the nanoparticles are being trafficked through the endocytic pathway. If this were the case, it would be interesting to design and synthesize new DNA-AuNP constructs with enhanced capabilities to escape the endosome and enter the cytosol, where they can exert their intended function.

In addition to dissecting the particular intracellular pathways that act upon DNA-AuNPs, it is also important to determine the fate of the gold nanoparticle core. As demonstrated in Chapter III, and in the literature, AuNPs are not exocytosed by cells. If these particles are to be used in whole organisms for diagnostic and therapeutic applications, we must understand what ultimately happens to the nanoparticle. Therefore, long-term studies are necessary to determine whether the nanoparticle remains intact within the cell or is degraded, whether the gold is ever recycled out of the cell, and what the long-term impacts on cell viability and cell biology are.

The presence of DNA-AuNPs in cells could be monitored by TEM, confocal microscopy, and ICP-MS over multiple days of cell growth. In these experiments, the cells would have to be treated as a population rather than individually in order to account for cell division, which will artificially decrease AuNP per cell measurements. ICP-MS provides quantitative data about the amount of gold in the cells, while TEM imaging provides information about the state of the AuNPs (aggregated, dispersed, dissociated). Combining the data from these two techniques show whether the AuNPs are broken down, and if the resulting gold fragments or gold atoms are removed from the cell. Cell biology could be monitored through a variety of cell-based assays, and some examples include the MTT assay (metabolic activity), the resazurin assay (cellular reduction potential), and the protease viability assay.

The process of cellular uptake is complex and involves a number of different variables, as demonstrated in this dissertation. Different pathways have been proposed, but further investigation is required to confirm the mechanism by which cells internalize DNA-AuNPs. A time course of TEM starting from initial nanoparticle exposure ($\leq$ 15 minutes) will demonstrate how the DNA-AuNPs interact with the cell surface. The presence of particles inside invaginations in the membrane and in vesicles within the cell would support an endocytic mechanism, whereas large amounts of free nanoparticles inside the cell would support a non-endocytic mechanism. Additionally, a wide range of endocytic inhibitors should be explored, and the results analyzed by ICP-MS to quantify the amount of gold nanoparticles per cell. ICP-MS provides a more accurate representation of cellular uptake than fluorescence, which can be difficult to interpret. Pharmacological compounds examined by Jayagopal, *et al*. can be revisited, in addition to compounds used by Patel, *et al*. and Choi, *et al*.[17,22]

Chapter III indicates that cellular uptake is negatively correlated with the hydrodynamic diameter, or size, of DNA-AuNPs and that cells preferentially take up smaller DNA-AuNPs. The reason for this is unknown. A time course of TEM images could help explain the biology behind this observation. The preferential uptake of nanoparticles of a particular size has been postulated to be a function of membrane wrapping during endocytosis, where nanoparticles with the fastest wrapping time were internalized in the highest amounts.[44] Time course TEM images for DNA-AuNPs of varying hydrodynamic diameters could provide information about the kinetics of membrane wrapping and endocytosis, although at a static level. Dynamic information about the kinetics of membrane translocation could be gained from a combination of dark-field microscopy, to image light scattered by the gold nanoparticle core, and single nanoparticle fluorescence microscopy, to image fluorescently labeled cells and the DNA-AuNPs interacting with the cell.[105]

Chapter III also raises the question of the distribution of gold nanoparticle core sizes found within a stock solution of particles of nominal size. It is possible that within the population of DNA-AuNPs that are introduced to cells, the cells preferentially internalize the particles on the small end of the size distribution. This hypothesis could be explored using TEM to quantify the size distribution of the DNA-AuNPs prior to cell exposure. If there were a significant breadth to this size distribution, subsequent TEM imaging of cells exposed to DNA-AuNPs would demonstrate whether the smaller particles within the population are internalized in greater amounts. Sufficient statistical sampling protocols would be required to obtain enough data and images to determine whether the results are significant. Additionally, flow cytometry clearly demonstrates that a population of cells exposed to DNA-AuNPs contains a distribution of fluorescence intensity, ranging from low to high. With the current ICP-MS protocols, we can

only calculate an average number of gold nanoparticles per cell. Mass cytometry can quantify the distribution of gold nanoparticles across an entire cell population, and would be an interesting technique to explore. This could demonstrate whether the gold nanoparticle content of individual cells correlates with the fluorescence content.

In Chapter IV, nanoparticle association and uptake were demonstrated for cells originating from diverse organisms. Extending this investigation to other types of cells like plant or yeast cells would provide more insight into how hAuNP uptake varies by biological system and membrane composition. It could also determine whether DNA-AuNPs are internalized through a mechanism that is conserved across species. Previous reports from the literature suggest that the scavenger receptor family of proteins is primarily responsible for cellular uptake of DNA-AuNPs. These proteins have been identified in both human and *Drosophila* cells. Competitive binding studies in Chapter IV between DNA-AuNPs and known scavenger receptor inhibitors establish the importance of these proteins in the cellular uptake mechanism. Further exploration into the expression of class A and class C scavenger receptors could provide a biological explanation for the differences in kinetics of gold nanoparticle accumulation. Proteomics studies using Western blotting and mass spectrometry can be done to quantify the expression of these receptors in any cell line of interest. Knockdown (RNA interference) or knockout cell lines that have reduced or no scavenger receptor expression could be explored for effects on DNA-AuNP internalization. Additionally, expression of class A scavenger receptor in HEK-293 cells should result in dramatic increases in cellular uptake over time, as was observed for the CaSki, HEp3, and S2R+ cell lines. HEK-293 cells are reported to not express SR-A, which is thought to explain the static cellular uptake profile observed in Chapter IV; however, the cells do accumulate significant amounts of hAuNPs (10^4 AuNPs per cell); therefore, one or

more additional mechanisms must also be involved in the membrane transport of these particles. Further studies should investigate the cell surface binding partners and pathways that are involved in uptake for HEK-293 cells. These mechanisms may be occurring in other cell lines as well, because it is likely that each cell type has multiple modes of nanoparticle translocation.

Chapter IV quantifies hAuNP association with bacteria and protoplasts for the first time, and found that the cell wall significantly reduces the amount of nanoparticles accumulated by bacteria. Per cell volume, protoplasts accumulate incredibly large amounts of hAuNPs (hundreds of nanoparticles per μm^3 compared to tens of nanopaticles per μm^3 for human cells), but neither ICP-MS nor flow cytometry can distinguish the location of the particles. To fully understand this interaction, future studies with TEM imaging are needed to determine the location of associated nanoparticles in bacteria and protoplasts and establish whether the cytoplasmic membrane of bacteria is capable of mediating hAuNP endocytosis. Mechanistic studies on hAuNP internalization by bacterial protoplasts could then identify proteins or other membrane structures involved in cellular uptake.

APPENDIX A

Alternative Model Membrane Systems to Investigate Cellular Uptake Mechanisms of Hairpin

DNA Functionalized Gold Nanoparticles

In addition to the giant unilamellar vesicles described in Chapter II, two other models

were explored as potential systems to study the passive transport of hairpin DNA functionalized

gold nanoparticles (hAuNPs) across cell membranes. Our goal was to design a protein-free

model system in which the influence of membrane lipids on cellular uptake could be explored.

Ideally, the influence of multiple variables could be examined, including cholesterol

concentration, temperature, and fetal bovine serum (FBS). To this end, parallel artificial

membrane permeability assay and liposomes were explored as model membrane systems.

Parallel artificial membrane permeability assay (PAMPA)

Introduction to PAMPA

In medicinal chemistry, the parallel artificial membrane permeability assay (PAMPA) is a

commonly used tool for predicting the *in vivo* permeability of drug candidates.[106,107] A porous

membrane filter, typically made of polyvinylidene fluoride (PVDF), is coated with a solution of

phospholipids and sandwiched between a donor and acceptor plate. Drug compounds are placed

in the donor plate and the transfer of these compounds through the phospholipid layer into the

acceptor plate is measured by UV-Vis spectrophotometry or LC/MS after a defined time period

(Supplemental Figure A.1). The results of this assay are used in drug discovery programs to rank

candidate compounds based on high or low permeability. We hypothesized that PAMPA could

be adapted to examine the potential of hAuNPs to passively diffuse through lipid membranes.
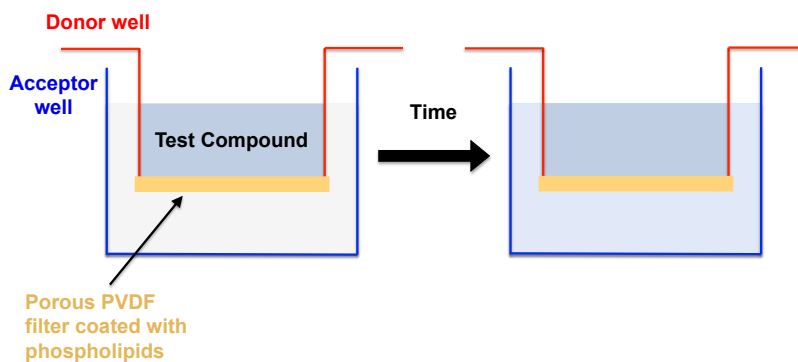
Supplemental Figure A.1. Schematic of PAMPA. A porous filter separating the donor and acceptor wells is covered with a layer of phospholipids. Over time, compounds diffuse from the donor to the acceptor well according to their permeability.

Unless otherwise specified, reagents were purchased from Sigma Aldrich or Fisher Scientific. Two types of assay formats were explored. In one format, custom mixtures of lipids are prepared in dodecane and applied to a PVDF filter plate by the user.[107,108] Initially, we used a phospholipid bilayer of 5% (w/v) lecithin in dodecane. Lecithin, primarily composed of phosphatidylcholine, is often used in PAMPA and was recommended by the filter plate manufacturer (Millipore). The second assay format used the Gentest pre-coated PAMPA plate system (Corning, Inc.), which is pre-coated with a lipid-oil-lipid tri-layer structure that shortens the pathlength of the phospholipid bilayer and reduces the amount of organic solvents required.[108]

Lecithin PAMPA

Caffeine and amiloride have been established as high and low permeability compounds, respectively, and were employed as controls to confirm that the assay was functioning as expected.[109,110] Solutions of 500 µM caffeine and amiloride were prepared separately in phosphate buffered saline (PBS). hAuNP and citrate AuNP test solutions were prepared at 10, 15, and 20 nM in PBS or water, respectively. Citrate-capped AuNPs were used as a control nanoparticle. The hDNA sequences used to prepare these hAuNPs are identical to the hDNA

used in Chapters II – IV (Supplemental Table A.1). A probe sonicator set to 5% amplitude for

four 10 second intervals was used to achieve complete dissolution of lecithin (5% w/v) in

dodecane. The lecithin solution (5 µL) was applied to the wells of a Millipore multiscreen filter

plate immediately prior to filling the donor plate wells with 150 µL of caffeine, amiloride,

hAuNPs or citrate-capped AuNPs. The acceptor wells were filled with 300 µL of PBS and the

two plates were assembled so that the lecithin coated filter was sandwiched between the donor

	Sequence (5' – 3')
hDNA	TTTTTTTTTT<u>CGACG</u>**GTTTCTCTACGTGTTCTTG**<u>CGTCG</u>
Complementary DNA	TT**CAAGAACACGTAGAGAAAC**TT

Supplemental Table A.1. hDNA and complementary DNA sequences. The hDNA sequence is modified with a 5' hexane thiol and a 3' Cy5. Underlined portions indicate the stem formation sequence and bold portions indicate complementary bases.
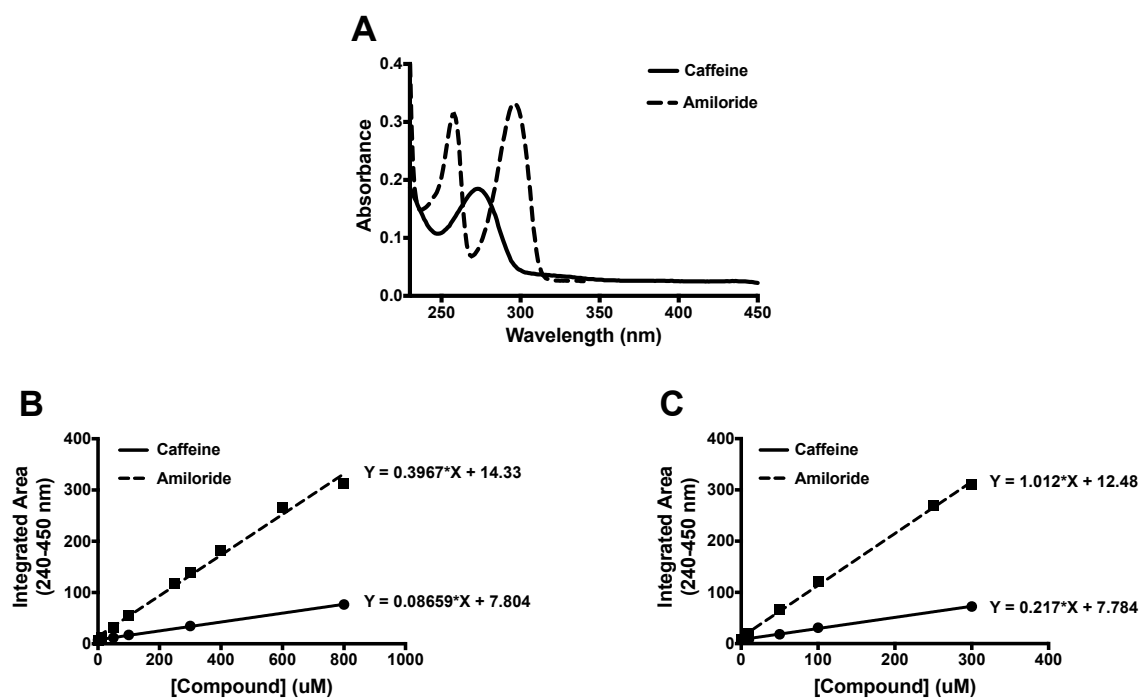
Supplemental Figure A.2. Quantification strategy for caffeine and amiloride. (A) Representative UV absorbance spectra for caffeine and amiloride. Standard curves of caffeine and amiloride at (B) 100 µL and (C) 250 µL volumes, which used to determine the concentration of each compound.

and acceptor wells, while ensuring that the membrane was fully contacted with buffer on both

sides. The assembly was placed in a humidified 25°C incubator for 16 hours.

Upon completion of the assay, the UV absorbance of the caffeine and amiloride solutions

was collected using a BioTek Synergy H4 Hybrid microplate reader. UV spectra (230 – 450 nm,

2 nm step) were collected from 100 µL of donor well solution and 250 µL of the acceptor well

solution in a 96-well UV transparent plate (Costar). The spectra were integrated from 240 – 450

nm and compared to a standard curve to determine the concentrations of caffeine and amiloride

(Supplemental Figure A.2). The effective permeability (P_e) was calculated as follows:

$$P_e = \frac{-\ln[1 - \frac{C_A(t)}{C_{equilibrium}}]}{A * \left(\frac{1}{V_D} + \frac{1}{V_A}\right) * t} \tag{1}$$

where $C_{equilibrium} = \frac{[C_D(t) * V_D + C_A(t) * V_A]}{V_D + V_A}$

$C_A(t)$ = concentration of compound in acceptor well at time t
$C_D(t)$ = concentration of compound in donor well at time t
V_D = volume in donor well
V_A = volume in acceptor well
A = filter area (cm^2)
t = incubation time (s)

Caffeine was found to have a log P_e of -5.50 ± 0.11, while a log P_e could not be calculated for

amiloride because no amiloride was detected in the acceptor wells. These results correlated with

previous reports that measured a high permeability for caffeine and low permeability for

amiloride, confirming that the assay performed as expected.

Nanoparticles could not be detected in the acceptor wells by UV-Vis spectrophotometry;

therefore, 5 µL from the donor wells and 250 µL from the acceptor wells were collected in 15

mL conical tubes for elemental analysis by inductively coupled plasma – optical emission

spectroscopy (ICP-OES). The PVDF membrane filters from a hAuNP and a citrate-capped

AuNP well were cut out of the plate and also analyzed. Each sample was acid digested in aqua

regia (3:1 ratio of hydrochloric acid : nitric acid) overnight, before diluting with deionized water

to the desired volume. *Warning: aqua regia is highly corrosive, handle with caution.* The

membranes were removed before ICP-OES analysis. Gold was quantified by measuring the

integrated area of the 267.595 nm emission peak on a Perkin Elmer Optima 7000 DV instrument.

The reported concentration was in µg/L, which was converted to give the concentration of

AuNPs in molarity (Equation 2). Equation 3 explains the derivation of the value 1.04×10^5 gold

atoms per nanoparticle for 15 nm diameter gold nanoparticles, where ρ is the density of fcc gold

(19.3 g cm^{-3}), D is the average diameter of the gold nanoparticle core (in cm), M is the atomic

mass of gold (196.97 g/mol), and N_A is Avogadro's number (6.022×10^{23} nanoparticles/mol).

$$\frac{\mu g}{L} \times \frac{g}{10^6 \ \mu g} \times \frac{mol}{196.97g} \times \frac{6.022 \times 10^{23} \ atoms}{mol} \times \frac{NP}{1.04 \times 10^5 \ atoms} \times \frac{\text{Volume of ICP-OES sample}}{\text{Volume taken from well} * 6.022 \times 10^{23}} \quad (2)$$

$$N_{Au/NP} = \frac{\pi}{6} \frac{\rho D^3}{M} N_A \quad (3)$$
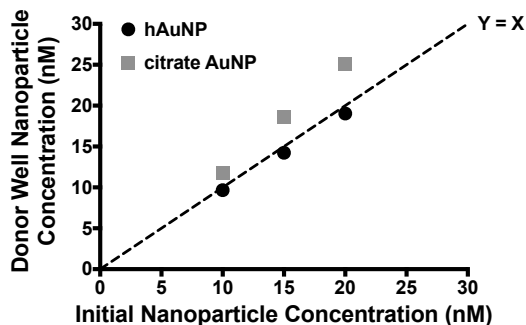
Supplemental Figure A.3. Donor well concentrations of hAuNPs and citrate AuNPs measured by ICP-OES. The results corresponded to the amount of nanoparticles added to each donor well, as demonstrated by the data points falling along the line of identity. Gold was not detected in any acceptor well.

The calculated donor well concentration of hAuNPs and citrate AuNPs corresponded to the

initial nanoparticle concentration (10, 15, and 20 nM) added to the donor plate (Supplemental

Figure A.3). No gold was detected in the acceptor solutions or the filters, indicating that hAuNPs had not been significantly transported across the lipid-coated filter. We hypothesized that the nanoparticles could not interact with the phospholipid bilayer due to an excess of highly nonpolar dodecane also present at the filter, which was visible as a greasy spot on the membrane.

Gentest Pre-coated PAMPA Plate System

A second assay format was evaluated, in which the filter plates were pre-coated with a thin layer of lipids by the manufacturer. These were intended to be a better mimic of biological membranes. Caffeine and amiloride were prepared as before. hAuNPs were prepared at 10 nM in PBS or complete cell medium (RPMI 1640 with L-glutamine, supplemented with 10% FBS, 100 units/mL penicillin, 100 µg/mL streptomycin, 2.25 g/L D-glucose, 1 mM sodium pyruvate, and 10 mM HEPES). Cell culture medium was used to mimic the matrix that nanoparticle uptake normally occurs in. The acceptor plate was filled with complete medium or PBS with and without complementary DNA. The assay was performed as before, with the same controls, incubation time, incubation temperature, and analysis. Effective permeability values (log P_e) were calculated for caffeine and amiloride at -4.62 ± 0.14 and -6.49 ± 0.15, respectively, which
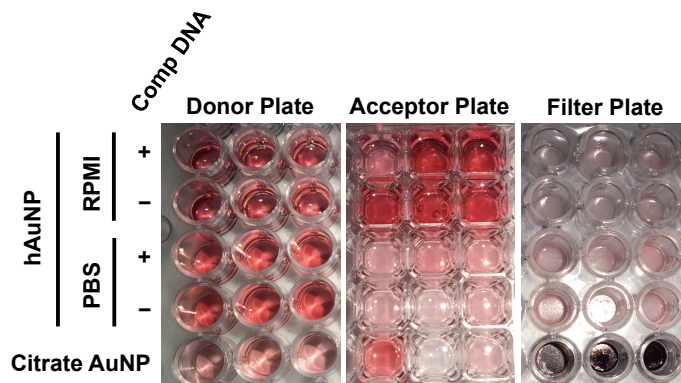
Supplemental Figure A.4. Images of the donor, acceptor and filter plates. hAuNPs and citrate AuNPs were transferred to the acceptor plate, either through the phospholipid bilayer or by direct solution transfer. The transfer was not consistent across all replicate wells. hAuNPs and citrate AuNPs embedded in the membrane filters, with citrate AuNPs appearing to aggregate based on the dark purple color.

indicates that caffeine has a higher permeability than amiloride, as expected.

After the 16 hour incubation, some hAuNPs and citrate AuNPs are visible in the acceptor plate (Supplemental Figure A.4). In cell medium, this may be primarily due to leaking of the donor solution into the acceptor well, rather than transport through the phospholipid bilayer. For these wells, the donor wells contain less volume than expected, while the acceptor wells contain more volume than expected. No significant changes in donor or acceptor well volume are found for the other samples, suggesting hAuNPs could have been transferred through the phospholipid membrane. The nanoparticle interaction with the pre-coated membrane filters is evident from the light pink hue of the filter that persists through multiple rinses, suggesting that hAuNPs are embedded in the filter. The dark purple-black hue of membrane filters in the citrate AuNP wells indicates that large amounts of nanoparticles aggregated in the filter. Using ICP-OES, high hAuNP concentrations are found in the complete medium acceptor wells and membrane filters, while lower concentrations are measured in PBS wells (Supplemental Figure A.5).
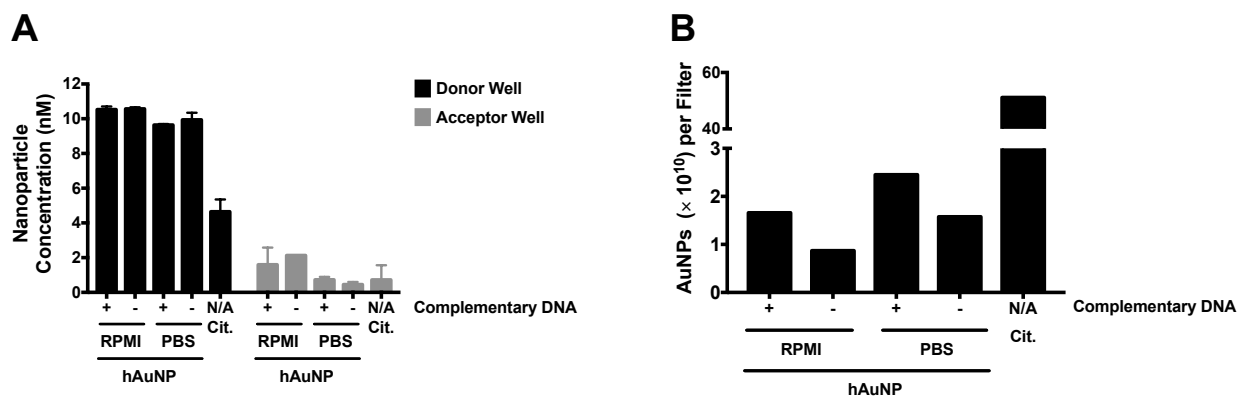
Supplemental Figure A.5. Distribution of hAuNPs in the donor and acceptor wells and the filter. (A) Donor and acceptor well nanoparticle concentrations as determined by ICP-OES. Gold was detected in all acceptor wells, with higher concentrations detected when RPMI was used as a matrix. However, this may be due to leaking of the solutions rather than transport through the phospholipid bilayer. Complementary DNA did not affect the amount of nanoparticles that were measured in the acceptor well (B) One filter from each condition was evaluated for its gold nanoparticle content. Citrate AuNP filters retained high amounts of nanoparticles, explaining the dark purple color of the filter.

Complementary DNA does not affect the amount of hAuNPs transported across the membrane.

A second assay using the pre-coated plates was also performed for 1, 2, 5, and 10 nM hAuNPs over 5 – 16 hours of incubation time. No complementary DNA was added and the matrix was PBS for all samples. The acceptor wells did contain some hAuNPs after 9 and 16 hours, but nanoparticle transport was inconsistent between replicates (Supplemental Figure A.6). Only at 10 nM hAuNPs and 16 hours of incubation did all the replicate wells contain detectable gold. The nanoparticle concentration in the acceptor wells (~0.1 nM) is approximately the same as the concentration in the corresponding wells of the previous experiment, which is ~0.45 nM.
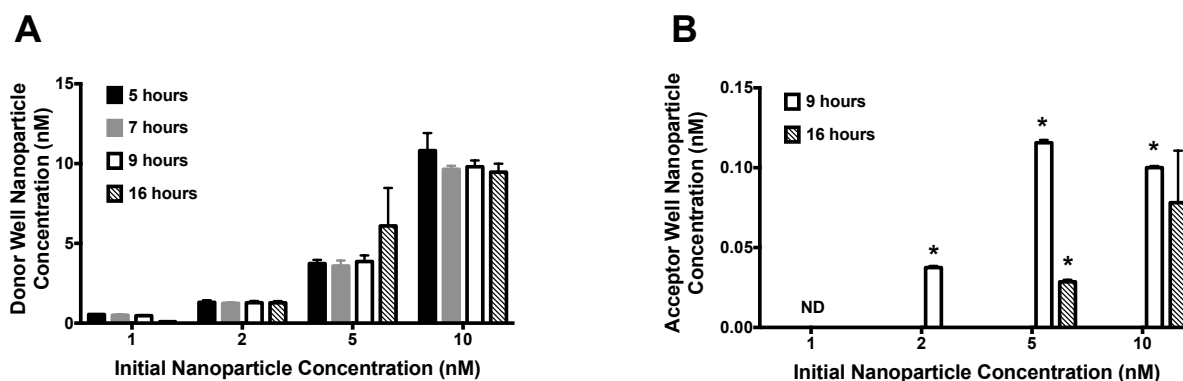
Supplemental Figure A.6. Distribution of hAuNP in the donor and acceptor wells over time. (A) Donor well nanoparticle concentration determined by ICP-OES (B) Acceptor well nanoparticle concentration determined by ICP-OES. *Gold was detectable in a few wells, but not consistently across replicate wells.

Ultimately PAMPA was abandoned as a strategy to explore the passive transport of hAuNPs across cell membranes. The Gentest pre-coated plate system was inconsistent and did not allow for customization of the lipid bilayer, which was a necessary goal of this work. Although customizable, the lecithin PAMPA it is not suitable for analysis of hAuNPs due to the extreme hydrophobicity of the solvent required to form the lipid bilayer.

Liposomes as Model Cell Membranes

Liposomes in a PBS Matrix

Due to the limitations of PAMPA, liposomes were chosen as an alternate strategy to explore the passive transport of hAuNPs. Liposomes were made from a custom blend of animal lipids and cholesterol designed to mimic the composition of an epithelial cell membrane.[38–42] The component lipids (1 μmole total in chloroform) were mixed in glass test tubes in the percentages given in Supplemental Table A.2. The mixture was dried into a thin film under a stream of N_2 gas and lyophilized overnight to remove trace amounts of chloroform.

| Lipid	Mole % of Membrane
Phosphatidylcholine	40
Phosphatidylethanolamine	15
Phosphatidylinositol	9
Phosphatidylserine	7
Sphingomyelin	14
Cholesterol	15

Supplemental Table A.2. Liposome membrane composition

The lipid film was rehydrated with PBS or PBS with 30 μM complementary DNA to achieve a final concentration of 1 mM lipids. The suspension was maintained at 42 – 45°C for one hour with intermittent mixing to form multilamellar vesicles (MLVs). MLVs were subjected to five freeze-thaw cycles in a dry ice/acetone bath before passing the suspension through a 0.2 μm polycarbonate membrane 11 times using the Avanti Mini Extruder (Avanti Polar Lipids). Unencapsulated complementary DNA was removed using 50K MWCO filters and multiple PBS washes. The filtrates were collected, stained with 50 nM SYTO13 (DNA binding dye), and the fluorescence recorded on a microplate reader configured for SYTO13 (Ex. 499 nm/9.0 nm ; Em. 509 nm/9.0 nm ; Gain 100). Four PBS washes were required to remove excess DNA (Supplemental Figure A.7). The filtrate fluorescence after four PBS washes corresponds to ~15

nM DNA, and could be either free DNA or DNA from liposomes that have broken open. A

Malvern Zetasizer NanoZS instrument was used to measure the liposome diameter. Unpurified

and MWCO filter purified liposomes (RI = 1.35) were diluted to 50 uM lipid in PBS and

analyzed at 25°C in a glass cuvette with a square aperture. Purification in the MWCO filter

results in a slight increase in the size distribution of the liposomes (Supplemental Figure A.8).
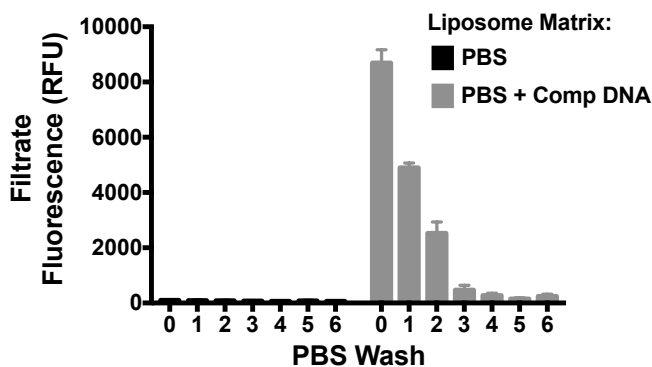
Supplemental Figure A.7. Fluorescence of filtrates from unmodified (PBS) and DNA-encapsulating liposomes (PBS + Comp DNA). After four PBS washes, the fluorescence reaches a minimum level.

In the presence and absence of 10% FBS, hAuNPs (1 nM) were introduced to

suspensions of liposomes and DNA-encapsulating liposomes used as is after purification. As a

control, samples of hAuNPs with and without complementary DNA (3 µM) were also prepared
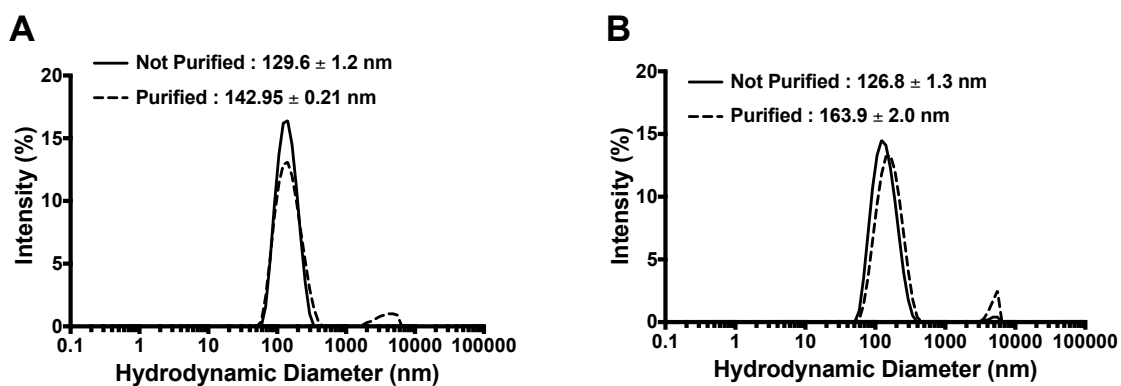
Supplemental Figure A.8. DLS results for (A) unmodified liposomes and (B) DNA-encapsulating liposomes before and after MWCO filter purification.
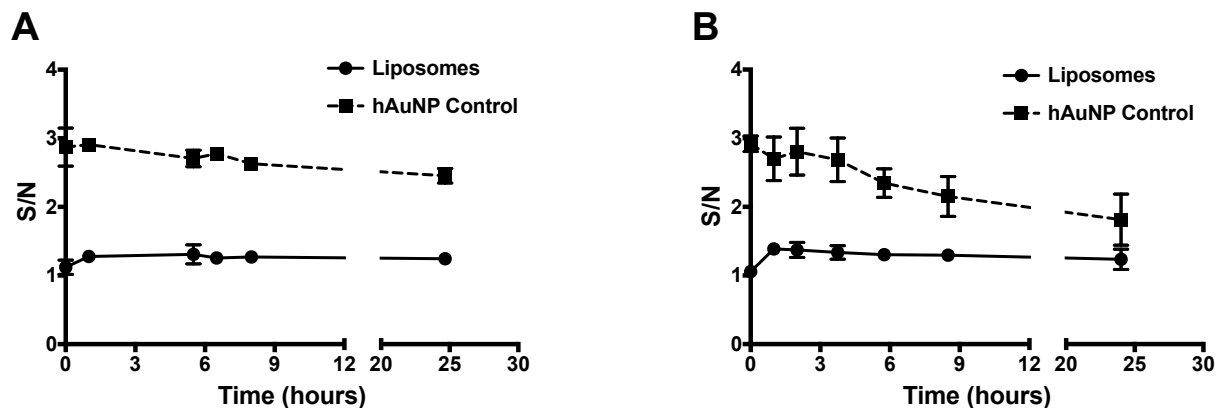
**Supplemental Figure A.9.** S/N of hAuNP treated liposomes with (A) 10% FBS and (B) no FBS. A hAuNP control of hAuNPs alone and hAuNPs with complementary DNA in PBS was also included.

in PBS. The hAuNP fluorescence was monitored over 24 hours on a microplate reader configured with settings for Cy5 (Ex. 650 nm/9.0 nm ; Em. 670 nm/9.0 nm ; Gain 100). The data are reported as signal to noise (S/N), which is the ratio of the hAuNP fluorescence of DNA-encapsulating liposomes to the hAuNP fluorescence of unmodified liposomes (Supplemental Figure A.9). The S/N of the control is the ratio of hAuNP fluorescence with complementary DNA to that of hAuNPs alone. No hAuNP signal is observed for DNA-encapsulating liposomes compared to unmodified liposomes in either 10% or 0% FBS (S/N ≈ 1.3). This could indicate that hAuNPs do not cross the liposome membrane to interact with the encapsulated DNA or that there is not a significant amount of encapsulated complementary DNA for the hAuNPs to interact with. The hAuNPs treated with excess complementary DNA produced the expected S/N of 3, indicating that the hAuNPs were functioning properly. FBS appears to stabilize the fluorescence, as indicated by minimal change in the S/N for 10% FBS samples, but a decrease in S/N of samples without FBS over time. This was primarily due to a loss in the fluorescence signal, rather than an increase in background fluorescence (data not shown).

Liposomes in a Tris-EDTA Buffer Matrix

In the literature, reports indicate that using low concentrations of sodium chloride during

rehydration of the lipid film may increase the DNA encapsulation efficiency.[111] Tris-EDTA (TE) buffer was chosen as an alternative to PBS, which contains up to 150 mM sodium chloride, in an effort to increase the amount of liposome encapsulated DNA. Liposomes were made analogously to the above procedure, but TE buffer was used as the rehydration medium. Removal of excess complementary DNA was achieved after three PBS washes (data not shown). DLS revealed that these liposomes were more stable to purification, with minimal changes to the hydrodynamic diameter (Supplemental Figure A.10).
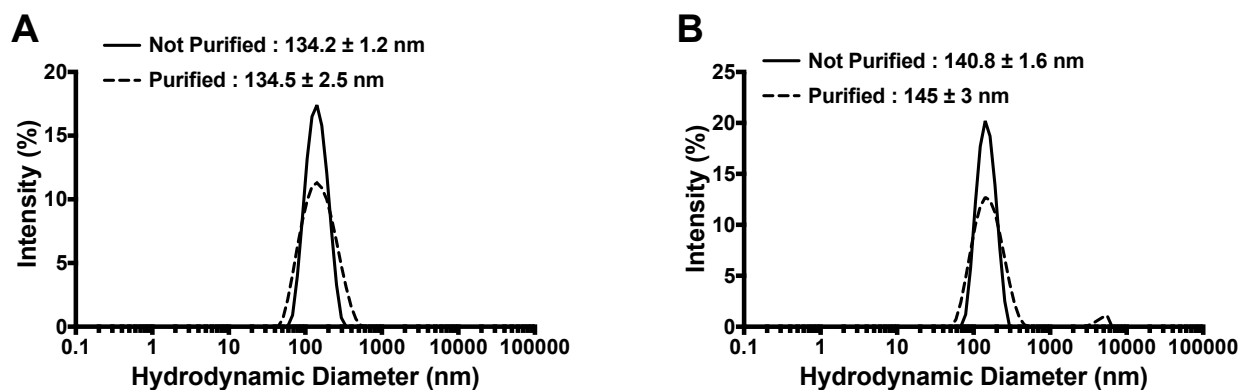

Supplemental Figure A.10. DLS results for (A) liposomes and (B) DNA encapsulating liposomes before and after MWCO filter purification.

hAuNP fluorescence of DNA-encapsulating liposomes was measured using the same method as above, but no FBS was added. The hAuNP S/N increases quickly until about 1 hour after introducing the hAuNPs to the liposomes, when it increases more slowly (Supplemental Figure A.11). A maximum S/N of 2.4 is achieved after 3 hours. It is unclear whether this signal is due to hAuNPs passing through the liposomal membrane and binding encapsulated complementary DNA or whether this signal is from free DNA outside of the liposomes. Of note, hAuNPs treated with complementary DNA exhibit an immediate fluorescence increase. The delay in fluorescence signal with liposomes suggests that hAuNPs might need to enter the

liposomal compartment before hybridizing with the complementary DNA; however, more

evidence is required to support this conclusion.

Ultimately the liposome approach does not provide easily interpretable data that confirms

that hAuNPs passively diffuse through the membrane into the lumen. The best method to

differentiate between hAuNPs outside and hAuNPs inside the liposome is a visual technique like

confocal microscopy. Due to their size, liposomes are difficult to visualize by confocal

microscopy; therefore, giant unilamellar vesicles (10 – 30 µm in diameter) were employed as

cell-sized membrane model systems that could easily be analyzed via confocal microscopy and

flow cytometry (see Chapter II).
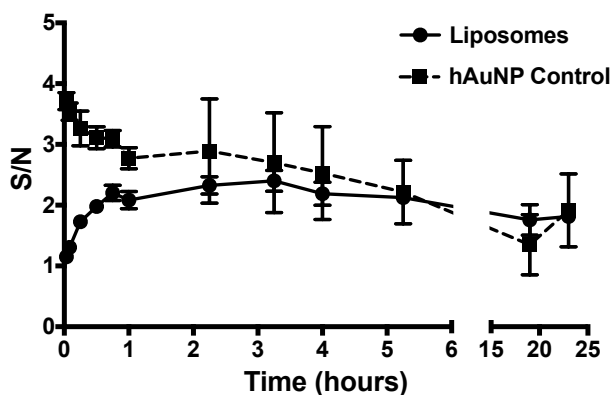
Supplemental Figure A.11. S/N of hAuNP treated DNA-encapsulating liposomes vs. unmodified liposomes in TE Buffer.

APPENDIX B

Efforts Towards Hairpin DNA Functionalized Gold Nanoparticles with Enhanced Signal

The current generation of hairpin DNA functionalized gold nanoparticles (hAuNPs) has been successfully employed for the detection of overexpressed mRNA in live cells, but achieves a signal-to-noise (S/N) of 3 – 5 at best.[6,7,11] Three strategies were explored to improve hAuNP S/N through modification of the hairpin DNA (hDNA): titration of hDNA density, multiple recognition loop sequences, and increasing the length of the stem formation sequence (Supplemental Figure B.1). If successful, these changes would improve the sensitivity of hAuNPs, thus enhancing their ability to image small changes in mRNA expression.

Rationale for Signal Enhancement Strategies

A ~1000 nt mRNA occupies a spherical area of ~40 – 60 nm in diameter.[112] The size of mRNA combined with the bulkiness of the hDNA, likely results in only a fraction of the hDNA strands binding to target mRNA. Therefore, some hairpins are adding unnecessary background fluorescence instead of contributing to productive signal. Decreasing the density of the hairpin ligand on the gold surface should result in a probe with increased S/N in cells, because there will be fewer extraneous hDNA contributing to nonproductive background. Fewer hDNA should also reduce crowding on the nanoparticle surface and increase availability of the recognition loop for hybridization. A second enhancement strategy involves functionalizing a nanoparticle with multiple hDNA strands that target different regions within the same mRNA. With this approach, instead of binding one particle per mRNA, up to three nanoparticles could bind per mRNA. This should yield a higher fluorescent signal per mRNA copy without increasing background fluorescence. Finally, it is hypothesized that the background fluorescence of these probes is
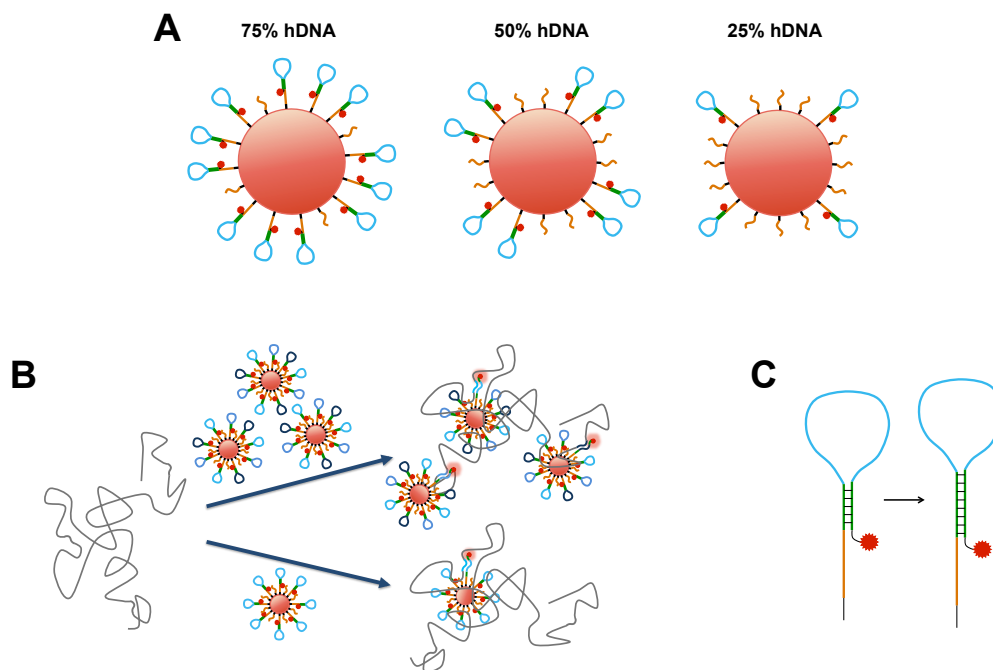
Supplemental Figure B.1. Strategies to enhance hAuNP signal to noise. (A) Reducing the amount of hDNA on the nanoparticle. (B) hAuNPs that bind multiple distinct regions of an mRNA (top) compared to only one nanoparticle binding (bottom). (C) Increasing the length of the stem formation sequence.

partially due to DNA "breathing." This occurs when a region of double stranded DNA transiently opens.[113,114] Breathing could increase the distance between the fluorophore and the gold surface, thus reducing quenching efficiency. Adding base pairs to the stem formation sequence should stabilize the hairpin, and reduce breathing and background fluorescence.

Titration of hDNA Density

For these experiments, the recognition loops are designed to target E6 mRNA expressed by HPV type 16 transformed cells, either through selection of PCR primers from the literature or by selection of a sequence calculated to have optimal binding using RNAstructure software from the Mathews Lab at the University of Rochester Medical Center (Supplemental Table B.1).[115,116] Negative control (scramble) hAuNPs are designed to be non-targeting and represent background fluorescence. To generate scramble sequences, the E6 recognition loop sequence was submitted

to GenScript Sequence Scramble, and the output is a scrambled sequence that contains the same

nucleotide content as the original sequence, with minimal homology to known mRNA

transcripts. All oligos were screened for overlap with non-target HPV-16 or human transcripts in

Nucleotide BLAST and had ≤ 68% overlap with off-target transcripts.

Name	Sequence (5' - 3')
E6	TTTTTTTTTTCGACG**GTTTCTCTACGTGTTCTTG**CGTCG
E6 comp	TT**CAAGAACACGTAGAGAAAC**TT
E6_2	TTTTTTTTTTGCAGC**GGTAACTTTCTGGGTCGCTCCTGTG**GCTGC
E6_2 comp	TT**CACAGGAGCGACCCAGAAAGTTACC**TT
E6_3	TTTTTTTTTTGCAGC**CATCTCTATATACTATGCATAAATC**GCTGC
E6_3 comp	TT**GATTTATGCATAGTATATAGAGATG**TT
E6scram	TTTTTTTTTTGCAGC**GCTTCGTCGTTATTGTTCT**GCTGC
E6scram comp	TT**AGAACAATAACGACGAAGC**TT

Sequences incorporate a 5' C6 thiol and 3' Cy5
Underline indicates stem formation sequence
Bold indicates recognition loop sequence

Supplemental Table B.1. hDNA sequences used to explore how decreased hDNA density and multiple recognition loops affect probe performance.

To synthesize hAuNPs with decreasing amounts of hDNA ligand, the typical synthesis

procedure (see Chapter II) was modified by systematically varying the ratio of hDNA to T-10

ligands (Supplemental Table B.2). The resulting hAuNPs were characterized by their interaction

with short complementary and non-complementary synthetic DNA sequences. The stock of

hAuNPs was diluted to 1 nM in phosphate buffered saline (PBS) and complementary or non-

complementary DNA was added at 3 µM. Fluorescence spectrophotometry demonstrates the

specificity of hAuNPs for their intended target sequences (Supplemental Figure B.2). Only

hAuNPs exposed to complementary DNA exhibit increased fluorescence signal over

%hDNA	Concentration of T-10 (µM)	Concentration of hDNA (µM)
75	0.1	0.3
50	0.2	0.2
25	0.3	0.1

Supplemental Table B.2. Synthesis conditions for hAuNPs with decreasing amounts of hDNA ligand.

background. The amount of fluorescence is dependent on the concentration of hDNA added during synthesis, but the S/N (ratio between fluorescence with complementary and non-complementary DNA) is constant for all three probes at ~5.
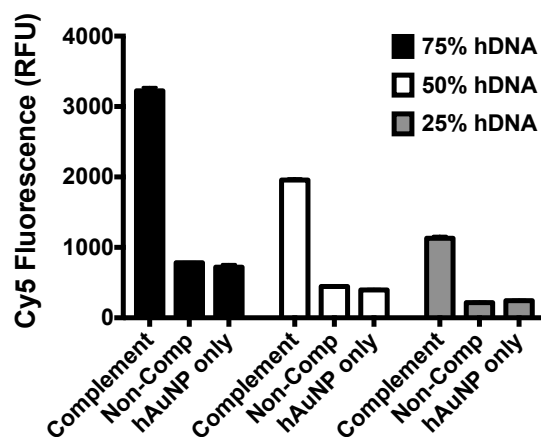
Supplemental Figure B.2. Fluorescence spectrophotometry of hAuNPs with complementary and non-complementary DNA. Complementary DNA causes an increased fluorescence signal from hAuNPs that is dependent on how much hDNA was added during synthesis.

hAuNPs were also characterized by quantifying the number of hDNA ligands attached per AuNP. hAuNPs (1 nM) were resuspended in dithiothreitol (0.1 M in 0.1 M disbasic sodium phosphate, pH 8.3) to reduce gold-thiol bonds and release the oligonucleotides from the nanoparticle. The fluorescence of the resulting solution was compared to a standard curve of hDNA to find the concentration of fluorescent DNA in the hAuNP samples. The concentration of hDNA strands was divided by the concentration of AuNPs to calculate the number of hDNA strands attached to each nanoparticle. The calculated quantities of hDNA per AuNP correspond to the amount of hDNA input for synthesis (Supplemental Figure B.3).

Initially 75% hDNA hAuNPs were evaluated in total RNA extracts from two cervical cancer cell lines – CaSki, which contains HPV16 sequences, and HeLa, a negative control. hAuNPs (0.5 nM) were incubated with increasing concentrations of CaSki or HeLa total RNA
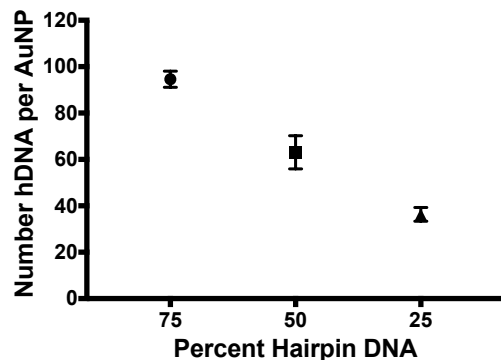
Supplemental Figure B.3. Amount of hDNA strands per gold nanoparticle.

for 1 hour at 37°C. Fluorescence was evaluated on a microplate reader using settings configured for Cy5 (Ex. 650nm/9.0nm ; Em. 670nm/9.0nm ; Gain 100). There was no significant difference in hAuNP fluorescence with CaSki or HeLa RNA (Supplemental Figure B.4). Next, flow cytometry was used to measure the fluorescence of E6 and negative control hAuNPs in CaSki cells. Cells were seeded in a 24 well plate (2×10^5 cells/well) and allowed to adhere overnight. The medium was replaced with 0.5, 1, or 2 nM E6 or negative control hAuNPs in fresh medium. After 4 hours at 37°C, the cells were washed three times with PBS, dissociated using trypsin, and analyzed by flow cytometry. E6 hAuNPs have a slight increase in fluorescence compared to negative control hAuNPs, corresponding to a S/N of ~1.27 for all hAuNP concentrations (Supplemental Figure B.5). Histograms of the fluorescence intensity reveal that the cell populations are almost completely overlapping and that there is no significant E6 signal. Such
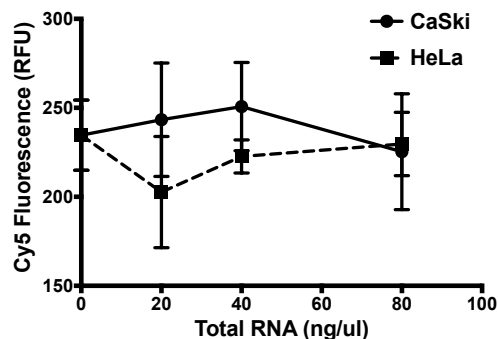
Supplemental Figure B.4. Fluorescence of E6 hAuNPs (75% hDNA) in CaSki and HeLa total RNA. No significant difference in hAuNP signal was found for any RNA concentration ($p > 0.05$).

108

low signal precluded the full evaluation of this strategy in cells, because the probes could not be validated. It is possible that the nanoparticles are not binding to the target mRNA or that the target mRNA is not present in high levels.
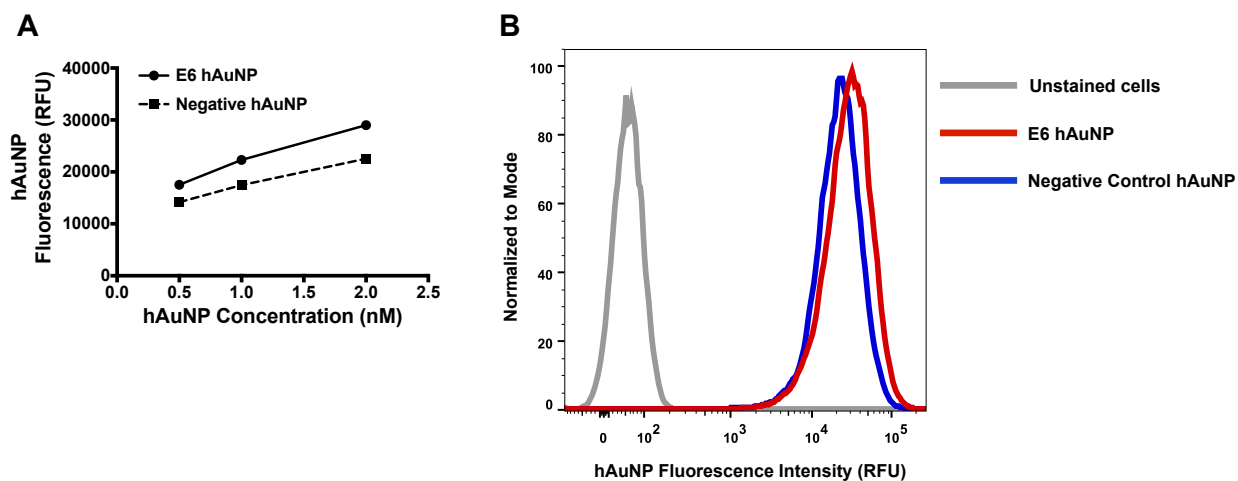
Supplemental Figure B.5. Flow cytometry results for E6 and scramble hAuNP treated CaSki cells. (A) Mean hAuNP fluorescence intensity for E6 and negative control hAuNPs in CaSki cells. (B) The histograms show that both cell populations are nearly overlapping.

hAuNPs That Bind Multiple Regions of a Single mRNA

Three recognition loops were designed to bind to E6 mRNA in regions separated by greater than 100 nucleotides (Supplemental Table B.1). During synthesis, the hDNA sequences were added in a 1:1:1 ratio. The resulting hAuNPs were characterized by fluorescence spectrophotometry. Complementary DNA oligos were added sequentially and simultaneously to demonstrate that three unique hairpin sequences were conjugated to one AuNP (Supplemental Figure B.6). Addition of individual complementary DNA sequences results in an approximately 1:1:1 ratio of fluorescence intensity, indicating that the amount of each hDNA conjugated to the nanoparticle is a direct result of the synthetic conditions.
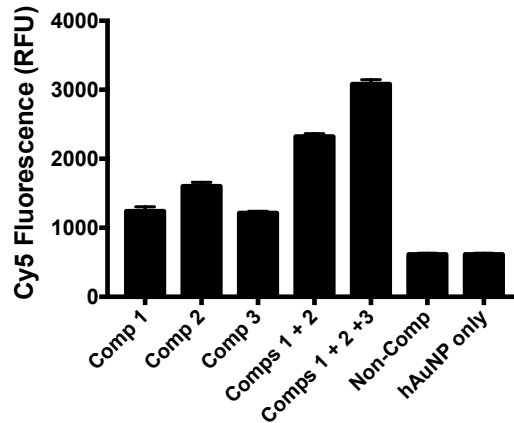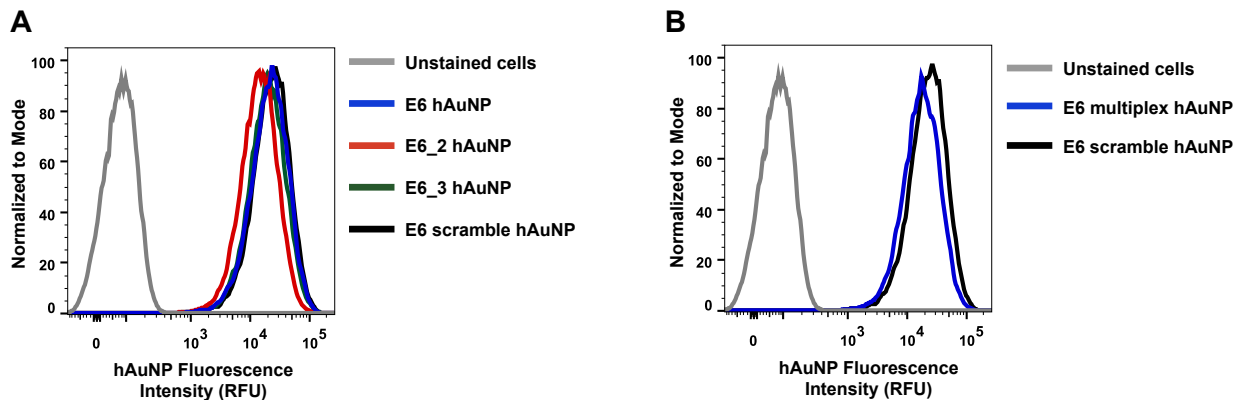
Supplemental Figure B.6. Fluorescence of hAuNPs targeting multiple regions of one mRNA. Each complement added separately produces approximately one third of the total possible fluorescence.

These hAuNPs were tested in CaSki cells for signal enhancement. hAuNPs were made with each E6 hDNA individually (E6, E6_2, and E6_3 hAuNPs), in combination (multiplex hAuNP), and with a negative control sequence (scramble hAuNP). CaSki cells were seeded into 12 well plates at 1×10^5 cells/well and allowed to adhere overnight. Fresh medium containing 0.5 nM hAuNPs was added for 4 hours at 37°C. The cells were washed three times with PBS, detached with trypsin, and analyzed by flow cytometry. No difference in fluorescence is found for E6 hAuNPs compared to scramble hAuNPs (Supplemental Figure B.7). As above, this could be due to the probes not functioning as expected or to low mRNA levels.

Increasing the Length of the Stem Formation Sequence

Longer stem formation sequences were designed by adding one or two G-C base pairs to the normal five base pair stem (Supplemental Table B.3). The recognition loop for these hDNA was designed to target matrix metalloproteinase-14 (MMP14) mRNA. Evaluation of the fluorescence with complementary and non-complementary DNA reveals no significant improvement in S/N (Supplemental Figure B.8). This suggests that DNA breathing does not have a meaningful effect on background fluorescence or stem-loop stability. Due to the difficulties of designing recognition loop sequences that could successfully produce detectable signal over

110

background hAuNPs in cells, these strategies were unable to be tested for their ability to improve

hAuNP signal in cells.

A **B**

Supplemental Figure B.7. Flow cytometry results for multiplexed E6 hAuNPs in CaSki cells. (A) Cells were treated with the individual E6 hAuNPs and a negative control scramble hAuNP. There are no differences in fluorescence between targeting hAuNPs and the negative control. (B) Cells were treated with a hAuNP attached to all three E6 hDNA sequences. There are no differences in fluorescence between the multiplex hAuNP and the negative control.

Name	Sequence (5' - 3')
hMMP14*	TTTTTTTTTT<u>GCAGC</u>**GCTCTTCTCCTCTTTTCCGGTTTT**<u>GCTGC</u>
MMP14_comp	TT**AAAACCGGAAAAGAGGAGAAGAGC**TT
hMMP14stem+1*	TTTTTTTTTT<u>CGCAGC</u>**GCTCTTCTCCTCTTTTCCGGTTTT**<u>GCTGCG</u>
hMMP14stem+2*	TTTTTTTTTT<u>CGCAGCG</u>**GCTCTTCTCCTCTTTTCCGGTTTT**<u>CGCTGCG</u>

*Sequences incorporate a 5' C6 thiol and 3' Cy5
Underline indicates stem formation sequence
Bold indicates recognition loop sequence

Supplemental Table B.3. DNA sequences with longer stem formation regions
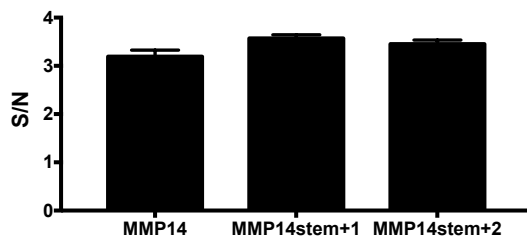
Supplemental Figure B.8. Signal to noise of longer stem formation sequences. Compared to a normal five base stem (MMP14), no large increase in S/N was found for hDNA with stems that were one (MMP14stem+1) and two (MMP14stem+2) base pairs longer.

111

APPENDIX C

Spontaneous Self-Assembly and Disassembly of Colloidal Gold Nanoparticles Induced by

Tetrakis(Hydroxymethyl) Phosphonium Chloride

Introduction

The hallmark of nanotechnology lies in the responsibility of adsorbed nanoparticle

capping ligands to prevent materials from returning to the bulk phase. Gold nanoparticles

(AuNPs) in particular have been synthesized with thiol, amine, and phosphorus capping ligands

in order to avoid aggregation.[117] The structural features of ligands on small AuNPs (< 5 nm)

have been extensively characterized, which is made possible by the formation of dense

monolayers and the high concentration of adsorbed ligands that transduce spectroscopic

signatures.[118] However, the characterization of capping ligands on larger colloids is often

performed empirically, rather than via direct spectroscopic methods due to the lower

concentration of adsorbed ligands. In this investigation, we take advantage of empirical evidence

provided by the optical properties of 15 nm AuNPs, followed by direct evidence from ^{31}P nuclear

magnetic resonance (NMR) to hypothesize a mechanism for self-assembly and subsequent

disassembly of AuNP chains induced by a well-known tetrakis(hydroxymethyl) phosphonium

chloride (THPC) capping ligand.

THPC has been extensively exploited as a strong reducing agent to synthesize aqueous 2–

4 nm AuNPs under basic conditions.[119,120] The rapid, reproducible synthesis of these small

particles has afforded electroless plating strategies of microparticle platforms, as the THPC

AuNPs serve as seed-mediated templates.[121–125] However, to our knowledge, THPC has never

been utilized to spontaneously assemble and disassemble colloidal suspensions of AuNPs. Previously, colloidal AuNPs have been shown to self-assemble into ordered one-dimensional and two-dimensional structures upon exposure to various stress-induced stimuli such as salt,[126] pressure,[127] temperature,[128,129] pH,[130] organic solvents,[126,131,132] DNA interactions,[4,133] and alkanethiol ligand exchange.[131,134,135] Many of these AuNPs employ phosphine capping ligands for stability due to strong, non-covalent interactions with the Au surface.[126–128] These noble metal particles form ordered linear assemblies similar to nanorods, transmitting tunable colors in solution that can be attributed to surface plasmon coupling.[136] The reversible assembly and disassembly of nanomaterials without salt or physical forces poses a significant challenge because the electrostatic repulsion afforded by the surrounding media must overcome the van der Waals interactions from the adsorbed capping ligands and the inherent dipole moment of the particles.[128,135] However, in this work, we observe assembly only utilizing a THPC capping ligand, and AuNP disassembly is achieved without physical forces or external additives. Notably, the use of ^{31}P NMR to understand THPC chemistry provides a means to further understand the role of phosphorus capping ligands in AuNP assembly and stability.

Materials and Methods

Materials and Reagents

Citrate-stabilized 15 nm gold nanoparticles (AuNPs) and citrate-stabilized 20 nm silver nanoparticles (AgNPs) stored in 2 mM citrate buffer were purchased from Ted Pella, Inc. Tetrakis(hydroxymethyl) phosphonium chloride (THPC) and tri(hydroxymethyl) phosphine (THP) were purchased from Sigma-Aldrich. Tri(hydroxypropyl) phosphine (THPP) was purchased from EMD Millipore. Copper TEM grids were purchased from Ted Pella, Inc. All other materials, reagents, and buffers were purchased from either Sigma-Aldrich or Fisher

Scientific and used without further modification. Deionized water used in this investigation was purified with a resistivity greater than or equal to 18.2 MΩ•cm.

Instrumentation

UV-vis spectra were collected on an Agilent 8453 spectrophotometer with a photodiode array detector or a Biotek Synergy H4 plate reader. Dynamic laser light scattering measurements were performed on a Malvern Zetasizer. Transmission electron microscopy (TEM) images were captured on a Tecnai Osiris instrument at an accelerating voltage of 20 kV. Inductively coupled plasma optical emission spectroscopy (ICP-OES) was performed on a Perkin Elmer Optima 7000 DV instrument. X-ray photoelectron spectroscopy (XPS) was performed on a PHI 5000 Versaprobe instrument. ^{31}P nuclear magnetic resonance (NMR) spectra were acquired on a Bruker 600 MHz spectrometer with a CPQCI probe. Color photographs of suspended particles were captured with a Nikon Coolpix 18.1 Megapixel digital camera.

ICP-OES Analysis of THPC Ligand Adsorbed to AuNPs

To an aqueous suspension of 15 nm citrate-stabilized AuNPs (2.3 nM, 4 mLs), 100 μM THPC was added and incubated for 2 days. The particles were then each split into 1 mL aliquots into 1.5 mL Eppendorf microcentrifuge tubes and washed by centrifuging for 45 minutes at 7400 rcf. The supernatant was removed and the THPC AuNPs were resuspended in 1 mL 0.1 M N-cyclohexyl-2-aminoethanesulfonic acid (CHES) buffer containing 0.025% v/v Tween 20 (pH 9.0). It should be noted that this buffer system contains an undetectable quantity of phosphorus. This centrifuge/wash procedure was repeated three additional times before finally suspending each aliquot in 1 mL deionized water. The particles were spun down a final time for 45 minutes at 7400 rcf and the supernatant was removed. The pellets from the 4 aliquots were then combined into a 15 mL conical tube, and 800 μLs of fresh aqua regia (3:1 v/v trace-metal grade

114

HCl:HNO$_3$) solution was added to dissolve the gold nanoparticles. This solution was finally diluted to a total volume of 4 mLs with deionized water. The phosphorus emission line at 213.618 nm was used to quantify the phosphorus concentration in each gold nanoparticle sample. Samples were calibrated with fresh phosphoric acid ICP standard solution.

XPS Analysis of Phosphorus

A 100 μM THPC solution was first incubated with an aqueous suspension of 15 nm citrate-stabilized AuNPs (2.3 nM). At 5 minute, 30 minute, 60 minute, and 48 hour time intervals, respectively, the particles were centrifuged at 21,100 g for 1 minute, the supernatant was removed, and the THPC AuNPs were resuspended in 250 μLs deionized water. Next, a 100 μL aliquot of the THPC particle suspension in water was immediately drop-cast on a B-doped silicon wafer and allowed to dry. Unmodified citrate-stabilized AuNPs were also drop-cast on a B-doped silicon wafer as a control. Survey scans and high resolution scans were performed with a monochromated Al Kα source (hν = 1486.6 eV) with a 100 μm beam diameter operating at 25 W. The analyzer was oriented 45° with respect to the normal. For survey scans, the samples were analyzed at a path energy of 187.85 eV, while high resolution scans were collected at 23.5 eV. Peak analysis was performed with CasaXPS software and fitted with Gaussian/Lorentzian lines with 30% Gauss character. The Shirley method was utilized to model the background of the spectra. Phosphorus P 2p and Au 4f peak binding energy positions were calibrated relative to the C 1s unsaturated hydrocarbon binding energy at 284.8 eV, while all P 2p and Au 4f peaks were normalized to the counts of the most intense peak.

^{31}P NMR on-particle

In order to perform ^{31}P NMR on 15 nm THPC-functionalized AuNPs, particles were quenched by centrifugation and resuspension in acidic buffer at 1 minute, 30 minute, 4 hour, and

48 hour intervals, respectively, after adding 100 μM THPC to citrate-stabilized AuNPs. First,

100 μM THPC was added to 10 1 mL aliquots of 2.3 nM citrate-stabilized AuNPs and allowed to

incubate for the aforementioned time intervals. Afterwards, the particles were centrifuged for 5

minutes at 16,100 rcf (aggregated particles) or 45 minutes at 7400 rcf (monodisperse particles).

The supernatant was then removed and each aliquot of particles was suspended in 100 μLs 0.1 M

2-(N-morpholino)ethanesulfonic acid (MES) with 0.025% v/v Tween 20 (pH 4.4). The 10

aliquots were next combined into one aliquot and centrifuged again. After removing the

supernatant, the particles were resuspended in 180 μLs 0.1 M MES with 0.025% Tween 20 (pH

4.4), effectively concentrating the AuNPs by a factor of 50 relative to their stock concentration.

This solution was added to a 3 mm NMR tube and run with a cold ^{31}P NMR channel. A

minimum of 30,000 scans was performed to acquire each spectrum of THPC functionalized to

the AuNPs. For analysis of free THPC in solution, a concentrated THPC sample was stored in

deionized water for 24 hours before acquiring spectra.

^{31}P NMR off-particle

Ten 1 mL aliquots of citrate-stabilized AuNPs (2.3 nM) were incubated with 100 μM

THPC for 30 minutes. The particles were centrifuged for 5 minutes at 16,100 rcf and the

supernatant was removed. Each aliquot was resuspended in 100 μLs of 0.1 M MES with 0.025%

v/v Tween 20 (pH 4.4). The 10 aliquots were combined and centrifuged again. The supernatant

was removed and the particles were resuspended in 180 μLs of 1 M potassium cyanide for 30

minutes with shaking. The solution was centrifuged briefly to pellet debris and the supernatant

was used for ^{31}P NMR analysis.

TEM Sample Preparation

For TEM sample preparation without HCl quenching (Supplemental Figure C.1), the

THPC AuNPs were centrifuged once at 21,100 *g* at the appropriate time intervals after THPC

addition. The supernatant was removed and the particles were resuspended in 250 μLs deionized

water, effectively concentrating them by a factor of four. Finally, a 5 μL samples was deposited

onto a copper grid and the solvent was wicked away using filter paper. For TEM sample

preparation with HCl quenching (Supplemental Figure C.2), 6.6 mM HCl was added to the

THPC AuNPs at the appropriate time intervals after THPC addition. Approximately 24 hours

after HCl addition, samples were prepared by depositing a 10 μL sample onto a copper grid and

wicking away the solvent with filter paper.

Results and Discussion

Upon incubating 15 nm citrate-stabilized AuNPs with 100 mM THPC, the particles instantly

undergo a red-to-blue color shift, which is reflective of the presence of an additional longitudinal

SPR band at 680 nm in the UV-vis spectrum (Supplemental Figure C.1a). THPC can promote the

rapid formation of linear assemblies in a similar manner to a short alkanethiol due to the rapid

displacement of citrate ions.[131] After approximately five minutes, the longitudinal band begins to

blueshift before ultimately disappearing, as the particles break apart into smaller assemblies over

the next 48 hours (Supplemental Figure C.1b–d). The assembly of the particles into linear chains

and subsequent disassembly into monodisperse spheres occurs spontaneously, requiring no

additives, pH changes, or temperature variability. THPC remains adsorbed to the particles, as

evident by quantitative ICP-OES and observations of particle stability after enduring multiple

centrifugation cycles (Supplemental Figure C.7 and C.8). Additionally, excess citrate does not

significantly displace the THPC on the particle surface, suggesting that THPC remains adsorbed

117

to the surface throughout the assembly/disassembly process. Due to the high ionic strength of the solution, significantly less ligand is required to initiate the reaction relative to the rather high mM salt concentrations previously reported.
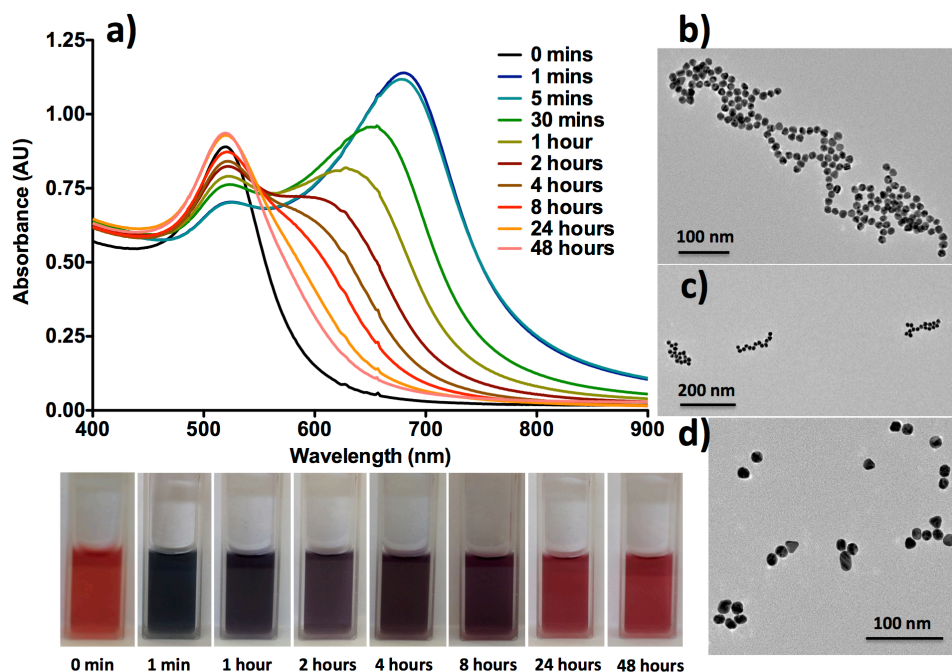
Supplemental Figure C.1. Spontaneous assembly and disassembly of 15 nm citrate-stabilized AuNPs (2.3 nM, pH 6.3, 2 mM sodium citrate buffer) induced by 100 µM THPC. a) UV-vis spectra and resulting color changes. TEM images captured b) 5 minutes, c) 30 minutes, and d) 48 hours after THPC addition to the particles.

To investigate the mechanism of THPC AuNP disassembly, the particles are reacted with salt, acid, and base (Supplemental Figure C.9). These particles can be manipulated via acid/base chemistry to finely tune the SPR band and control the number of particles per chain. It is observed that the particles rapidly disassemble in the presence of NaOH, whereas the disassembly process is quenched in the presence of HCl. At four time intervals following THPC addition, 6.6 mM HCl is added to quench disassembly and the stability is monitored (Supplemental Figure C.2). The particles are stable for 24 hours after HCl addition, as indicated by the negligible change in UV-vis absorbance spectra over time. Thus, quenching the THPC

disassembly reaction allows for precise manipulation of the size of the AuNP chains and the SPR band. We hypothesize that disassembly is initiated because the ligand undergoes a chemical change upon adsorption. Upon reacting THPC with NaOH in bulk solution, Hoffman first observed a THPC oxidation while Grayson elucidated the mechanism of conversion to tri(hydroxymethyl) phosphine oxide (THPO).[137–139] Because this aqueous chemistry is well characterized, we hypothesize that this reaction can also proceed on-particle. It is plausible that an oxidized THPC ligand adsorbed to the nanoparticle surface cannot maintain the van der Waals interactions necessary for particle assembly.
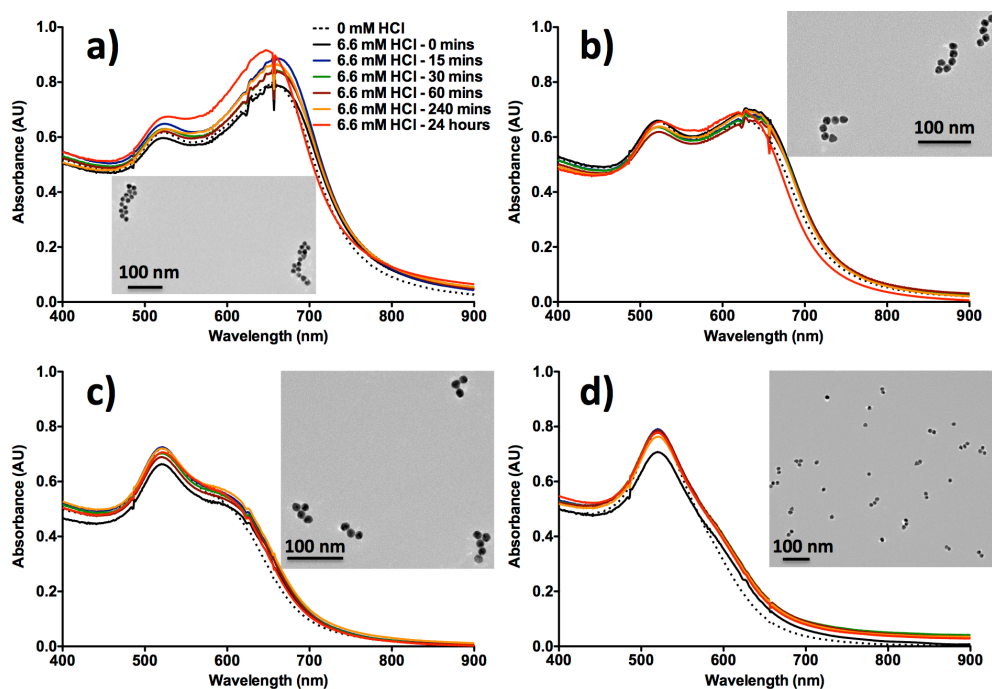
Supplemental Figure C.2. HCl quenching of THPC AuNP disassembly. To four separate aliquots of 2.3 nM suspensions of citrate-stabilized AuNPs, 100 μM THPC was added. Particle disassembly was quenched with 6.6 mM HCl at a) 30 minutes, b) 60 minutes, c) 4 hours, and d) 24 hours after THPC addition. The UV-vis spectra were monitored over 24 hours after HCl addition to determine particle stability, while TEM samples were prepared 24 hours after quenching with HCl.

As the pH of the citrate-stabilized AuNP suspension increases, the rate of THPC AuNP disassembly also increases (Supplemental Figure C.10). This rate of disassembly can be

monitored by measuring the particle absorbance ratio (A_{680nm}/A_{520nm}) after THPC addition. The rate of decay follows an exponential trend relative to pH, which suggests pseudo second-order order kinetics similar to the THPC oxidation mechanism elucidated by Grayson in bulk solution (Supplemental Figure C.11).[139] The decay constant observed at pH 9.6 ($k = 0.15$ M^{-1} min^{-1}) is consistent with that reported by Grayson ($k = 0.166$ M^{-1} min^{-1}), although at a reduced pH value compared to Grayson's system (pH 13).

The assembly/disassembly process was further confirmed by using dynamic light scattering and zeta potential to measure the hydrodynamic diameter and surface charge of the particle aggregates. Upon addition of THPC the particles immediately aggregate to assemblies of about 170 nm in diameter and begin to disassemble after about five minutes, which correlates to the time that the UV-vis spectra begin to blueshift (Supplemental Figure C.12). Following incubation with THPC, the zeta potential initially decreases to more negative values, followed by an increase to a final value of approximately −25 mV over a reaction period of two days (Supplemental Figure C.13). The initial decrease in zeta potential may be explained by the deviation from ideal conditions of monodispersity and the large size of the assembly, which slows the electrophoretic mobility of the particles, the property that is measured in order to calculate zeta potential.

In order to characterize the phosphorus species adsorbed to the particles, ^{31}P NMR spectroscopy is employed at different time intervals in the reaction. The ^{31}P NMR spectral profiles of THPC and its derivatives are well characterized in aqueous solutions.[140–143] Our ^{31}P NMR spectral profiles of pure ligand in deionized water reveal multiple peaks, as the oxidation reaction progresses above the ligand's pKa (5.5). However, under acidic conditions, a dominant THPC peak (δ, +26 ppm) and a smaller peak representing THPO (δ, +49 ppm) are elucidated,

consistent with previous reports (Supplemental Figure C.3a). Upon adsorption to the particles, a

dominant peak is observed at all time points after THPC addition (δ, +36 ppm) (Supplemental

Figure C.3b). Shao et al. identify this species as THPC hydroxide (THPOH). Grayson and

Hoffman recognize pentavalent THPOH as an intermediate in the conversion of THPC to THPO,

but we observe only THPOH throughout the on-particle reaction. The adsorbed pentavalent

phosphorane species is most likely sterically hindered by the Au surface, and the oxidation to
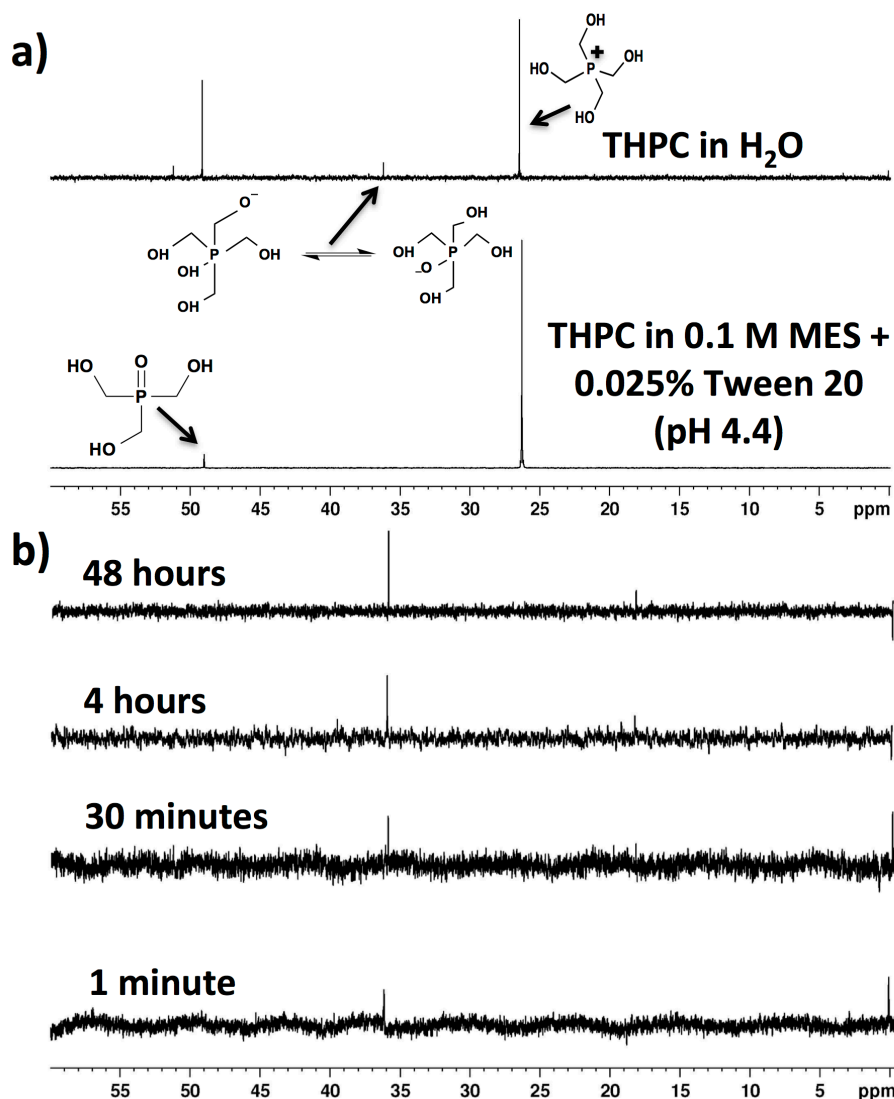
Supplemental Figure C.3. ^{31}P NMR spectra of THPC in a) free solution and b) adsorbed to AuNPs. Particles are stored in 0.1 M MES buffer containing 0.025% Tween 20 (pH 4.4).

THPO cannot reach completion (Supplemental Figure C.14). Additional off-particle evidence is

consistent with the proposed mechanism, with ^{31}P NMR revealing the expected THPOH peak (δ,

+36 ppm) after chemical degradation of THPC AuNPs by potassium cyanide (Supplemental

Figure C.15). The X-ray photoelectron spectroscopy (XPS) data also agrees with the presence of

an electronegative species that interacts with the phosphorus atom adsorbed to the particles

(Supplemental Figures C.16 – C.18). The P 2p binding energy (BE) is revealed to increase from

131.7 eV to 133.0 eV one hour after THPC incubation. As BE increases, the shielding

surrounding the phosphorus atom decreases due to the presence of an additional coordinated

electronegative substituent. It is also worth mentioning that P^V THPC derivatives possess

signature peaks above BE values of 132.5 eV.[144] The ^{31}P NMR data along with the XPS analysis

strongly suggests that the THPC is oxidized to a pentavalent THPOH species on-particle.
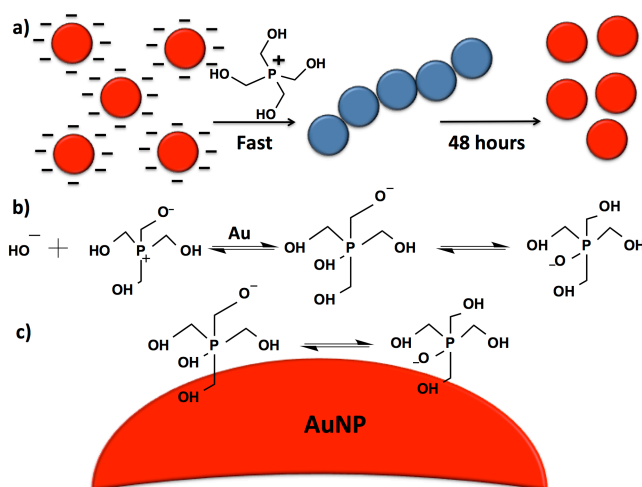
Supplemental Figure C.4. Hypothesized mechanism of THPC AuNP assembly and disassembly. a) Upon reacting the citrate AuNPs with THPC, the particles immediately assemble into linear chains and slowly disassemble over the course of 48 hours. The temporary dipole moment of each particle created by the rapid displacement of citrate promotes particle assembly, but disassembly is only observed when the pH is above the pKa of the ligand. b) When the pH is above the pKa of THPC, the ligand is catalytically converted to a pentavalent phosphorane. c) These pentavalent THPOH isomers remain adsorbed to the particles and the excess negative charge cannot maintain the assembly, which breaks apart into monodisperse components.

The hypothesized mechanism of spontaneous assembly and disassembly is depicted in Supplemental Figure C.4. Induced by the large dipole moment on each particle that results from rapid citrate displacement,[131,135] the particles first rapidly assemble, triggering a red-to-blue color change. Upon adsorption, the Au surface renders itself as a catalytic substrate to convert THPC into THPOH on-particle. Evidence that the metal surface acts as a catalyst is supported by the extremely rapid self-assembly and disassembly of 20 nm citrate-stabilized AgNPs (Supplemental Figure C.19). With AgNPs, the particles return to their yellow color approximately 5 minutes after THPC addition, but ultimately aggregate minutes later. The kinetics of AgNP disassembly is orders of magnitude faster than that of THPC AuNPs, which is interesting considering Ag often exhibits differing catalytic activity relative to Au.[145,146] AuNP disassembly only occurs when the pH is above the ligand pKa because the excess negative charge at the surface cannot hold the assembly together (Supplemental Figure C.4b and c). The chains are ultimately broken apart into their monodisperse components, transitioning from blue to purple to red colors.

To further investigate this mechanism, it is hypothesized that tertiary hydroxyalkyl phosphines possessing neutral pKa values can experience similar assembly/disassembly properties relative to THPC. Many phosphonium ligands retain pKa values above 15, and this environment is not suitable for aqueous nanoparticles. The tertiary phosphines, tri(hydroxymethyl) phosphine (THP) and tri(hydroxypropyl) phosphine (THPP), were chosen because of their aqueous solubility and pKa values amenable to aqueous AuNPs. THP displays nearly identical assembly/disassembly behavior relative to THPC because their chemical structures are so similar (Supplemental Figure C.5a). THPP possesses a slightly higher pKa value of 7.2[147] and the pH of the particle solution must be increased for the AuNPs to demonstrate disassembly characteristics similar to THPC (Supplemental Figure C.5b). At pH

6.3, complete THPP AuNP disassembly requires more than four days, whereas at pH 7.9, the particles approach monodispersity in no more than 24 hours (Supplemental Figure C.20). The ability to further support the hypothesis with tertiary hydroxyalkyl phosphines not only establishes versatility with this approach, but also provides opportunities to develop a range of nanomaterial assemblies.
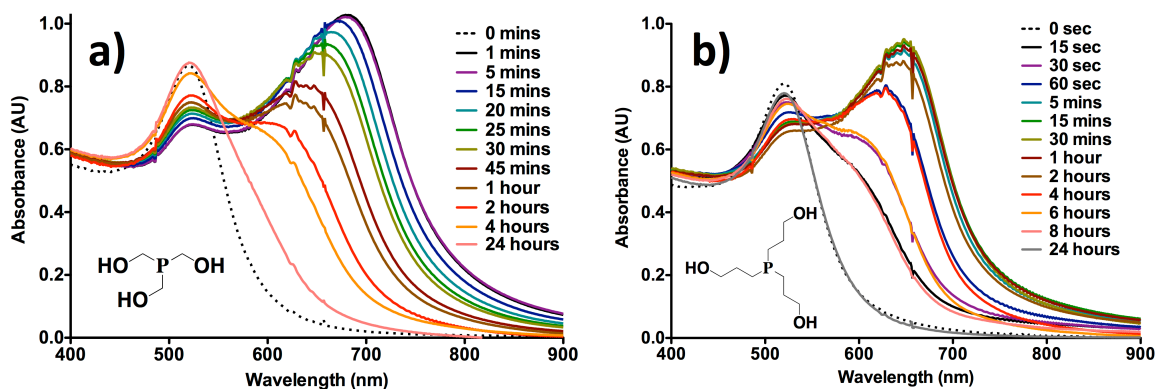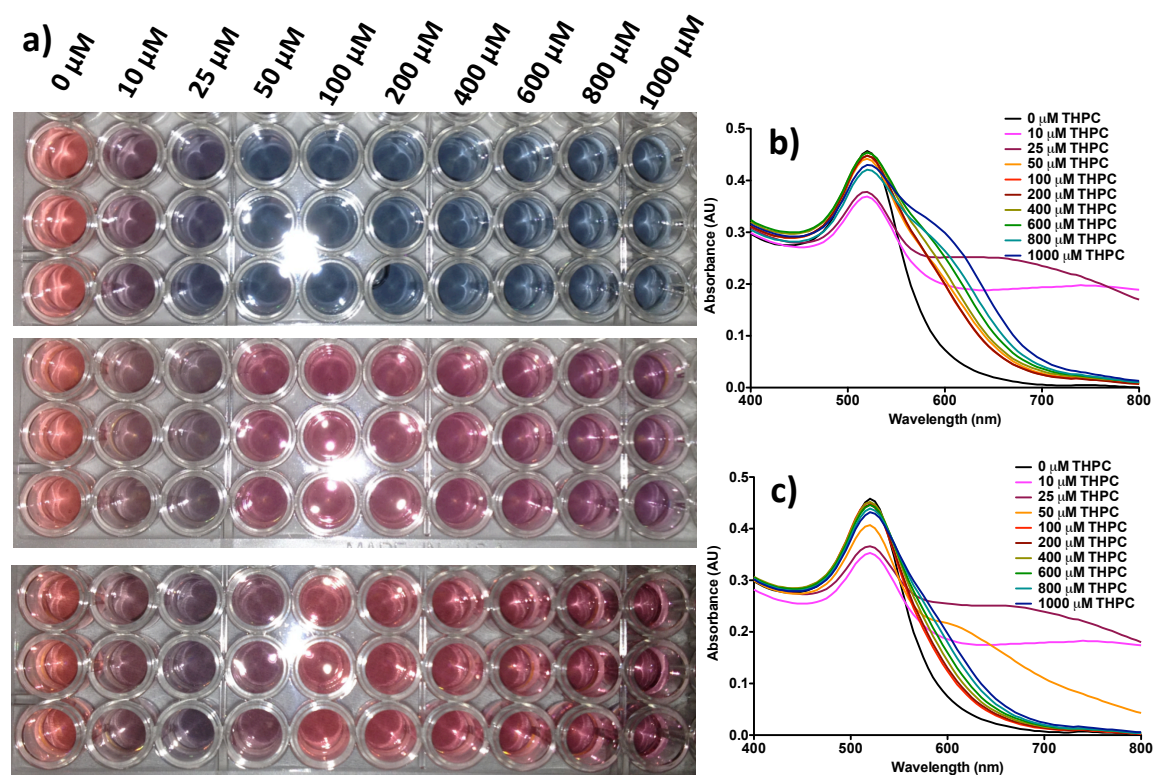

Supplemental Figure C.5. Spontaneous assembly and disassembly of AuNPs induced by tertiary hydroxyalkyl phosphine ligands. a) UV-vis absorbance spectra of 100 μM THP at pH 6.3 and b) 100 μM THPP at pH 7.9.

Conclusion

In this investigation, a spontaneous method for AuNP assembly and subsequent disassembly that requires no additives or stress-induced stimuli is demonstrated. Additionally, significantly less ligand is required to promote particle assembly and disassembly in comparison to high mM salt concentrations. The pKa of the hydroxyalkyl phosphine or phosphonium ligand plays an important role because the disassembly reaction is favored when the pH is above the ligand pKa. Manipulation of the THPC AuNP chains is accomplished by exploiting acid/base chemistry to finely tune the nature of the assembly, and this work provides a platform to develop advanced nanomaterial structures using various phosphine and/or phosphonium small molecules. Finally, the disassembly is most likely driven by the oxidation of the THPC ligand on-particle to

the pentavalent THPOH species, which was identified in the first example of on-particle ^{31}P NMR spectroscopy on 15 nm gold colloids. The application of ^{31}P NMR spectroscopy to analyze ligand signatures on particles of this size offers an invaluable tool for exploring and understanding the role of phosphorus capping ligands adsorbed to nanomaterial substrates.

Supporting Information

Supplemental Figure C.6. Concentration dependence of THPC AuNP assembly and disassembly. a) Color images of THPC AuNPs in a 96-well plate upon incubating 2.3 nM citrate-stabilized AuNPs (15 nm) with THPC between 0 and 1000 μM concentrations. Concentration dependent color changes are evident 5 minutes after THPC addition (top), 24 hours after THPC addition (middle), and 48 hours after THPC addition (bottom). Each nanoparticle reaction was performed in triplicate. Acquired UV-vis spectra b) 24 hours and c) 48 hours after THPC addition. A 100 μM THPC concentration was chosen because of the most rapid rates of gold nanoparticle assembly and disassembly.
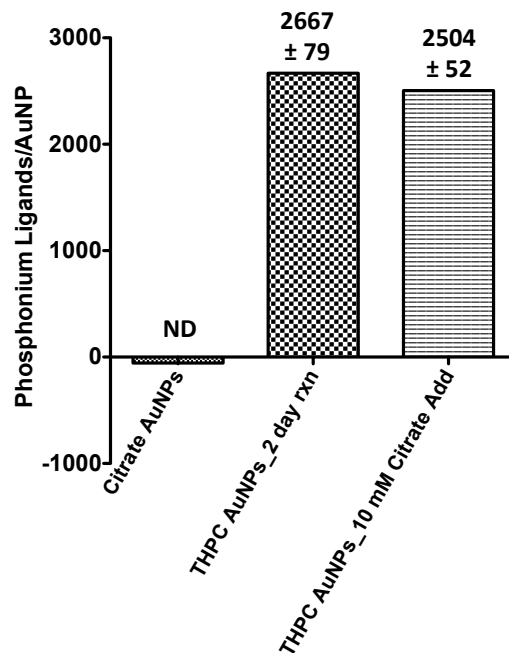
Supplemental Figure C.7. ICP-OES analysis to quantify the number of phosphonium ligands per gold nanoparticle. The 15 nm citrate-stabilized nanoparticles (left bar) possess an undetectable quantity of phosphorus, while the THPC AuNPs (middle bar) possess nearly 2700 ligands after a 2-day incubation. In order to determine if free citrate can displace the THPC ligand, 100 μM THPC was added to 15 nm citrate-stabilized AuNPs (2.3 nM) and allowed to incubate for five minutes, so that the particles transmitted a blue color. Next, 10 mM sodium citrate solution was added and the particles were subsequently washed five times by centrifugation. The similar ligand densities in the middle and right bars suggest that free citrate does not displace the strong-binding phosphorus ligands adsorbed to the gold surface. All of these measurements were performed in triplicate.
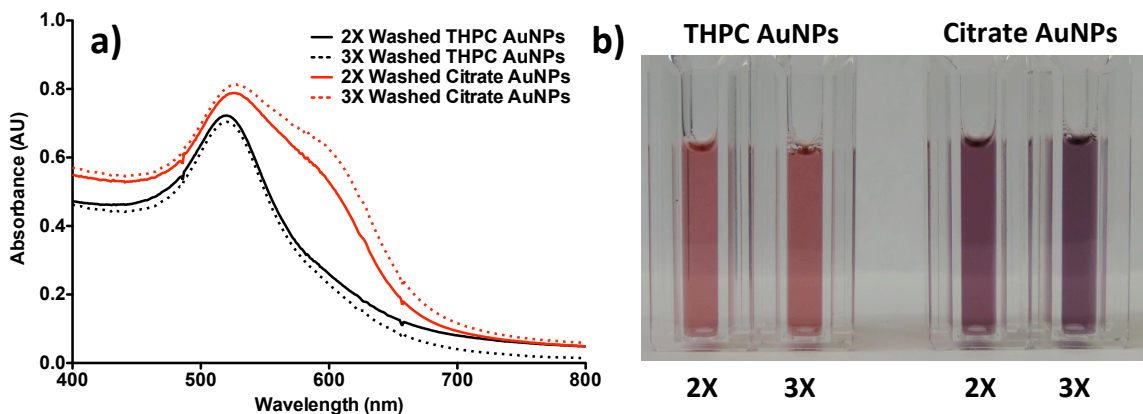
Supplemental Figure C.8. Qualitative determination of THPC adsorption to the AuNP surface. a) UV-vis spectra and b) color images of washed THPC AuNPs and washed citrate AuNPs, respectively, after resuspending in CHES buffer. Upon incubating 100 μM THPC for 2 days with 15 nm citrate-stabilized AuNPs (2.3 nM), the particles were centrifuged for 45 minutes at 7400 rcf and resuspended in 1 mL 0.1 M CHES buffer containing 0.025% v/v Tween 20 (pH 9.0). This process was repeated additional times in order to acquire UV-vis spectra and capture images of washed THPC AuNPs and citrate AuNPs, respectively. The citrate AuNPs begin to aggregate upon washing, which is evident from the formation of an additional peak in the UV-vis spectrum and a red-to-purple color change in solution. As citrate anions are weakly adsorbed to the AuNP surface, the physical forces imposed by centrifugation and resuspension desorb the species from the particle surface, reducing stability. On the contrary, the THPC ligand is more strongly adsorbed to the particle surface, so that the particles can endure wash cycles.
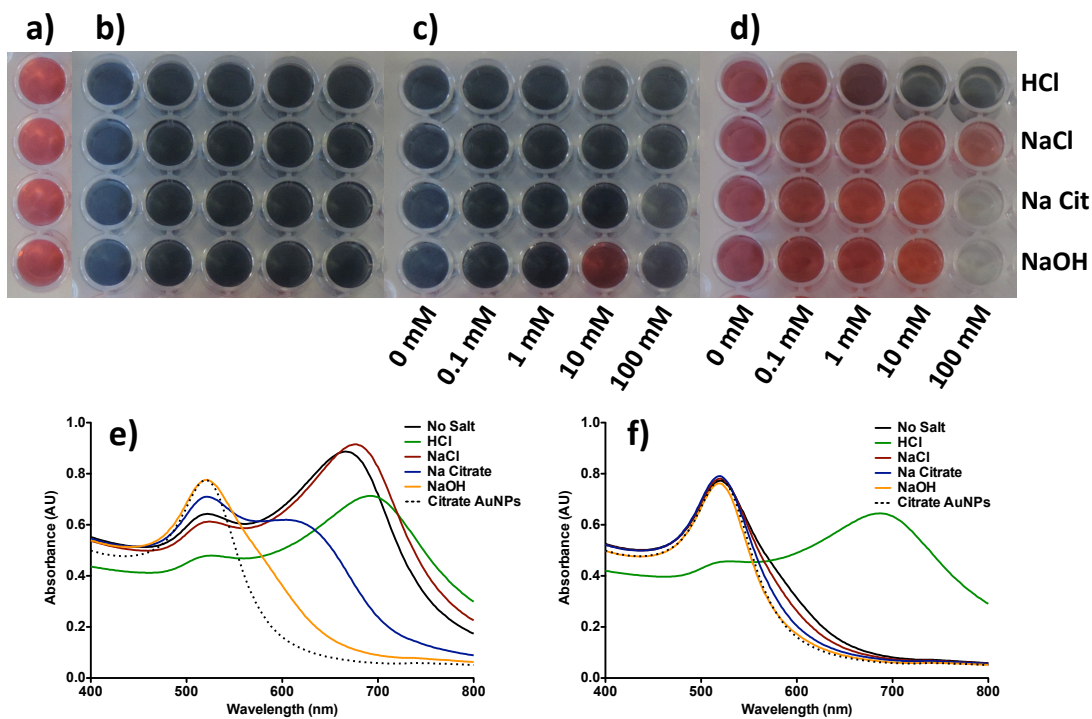
Supplemental Figure C.9. Self-assembly and disassembly of THPC AuNPs upon the addition of HCl, NaCl, sodium citrate (Na Cit), and NaOH. a) Images of 15 nm citrate-stabilized AuNPs (2.3 nM) captured in 96 well plates. b) Images of gold nanoparticles 5 minutes after a 100 μM THPC addition (all 20 wells contain 100 μM THPC). It should also be mentioned that although many nanoparticle reactions are inconsistent, these reactions are extremely reproducible, as indicated by the nearly identical shades of blue colors transmitted in all 20 wells. c) Images captured after serial titrations with HCl, NaCl, Na Cit, and NaOH, respectively. The images were captured 5 minutes after salt addition. d) Images captured 18 hours after salt addition. e) UV-vis spectra of THPC AuNPs 30 minutes after adding 10 mM salt. f) UV-vis spectra of THPC AuNPs 24 hours after adding salt. The addition of HCl to THPC AuNPs quenches disassembly, while NaOH expedites THPC AuNP disassembly. This experiment suggests that NaCl does not play a significant role in THPC AuNP disassembly, while sodium citrate disassembles the particles at a slower rate than NaOH, but still faster than NaCl.
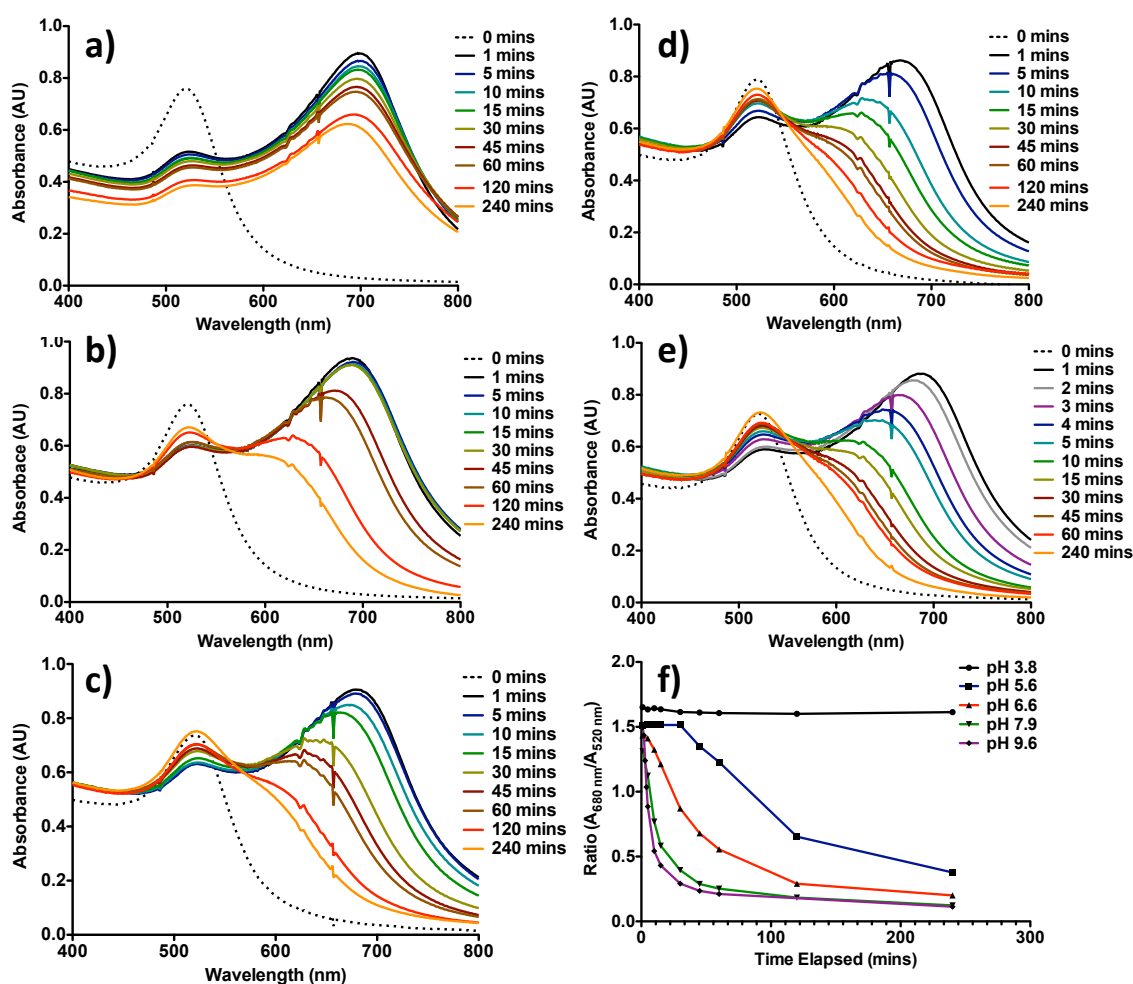
Supplemental Figure C.10. UV-vis spectra of THPC AuNPs suspended in 2 mM tribasic sodium citrate at a) pH 3.8, b) pH 5.6, c) pH 6.6, d) pH 7.9, and e) pH 9.6. f) Plot of the absorbance ratio ($A_{680\,nm}/A_{520\,nm}$) over a 4-hour time interval. Citrate-stabilized AuNPs were centrifuged one time at 7400 rcf for 45 minutes, and the supernatant was removed. The particles were next resuspended in 2 mM sodium citrate (tribasic) at different pH values to generate particle concentrations of 2.3 nM (1 mL aliquot). When 100 μM THPC is added to the particles suspended in more basic conditions, the rate of disassembly increases. However, at acidic pH values below the pKa of the phosphonium ligand, disassembly does not occur, and the particles ultimately aggregate.
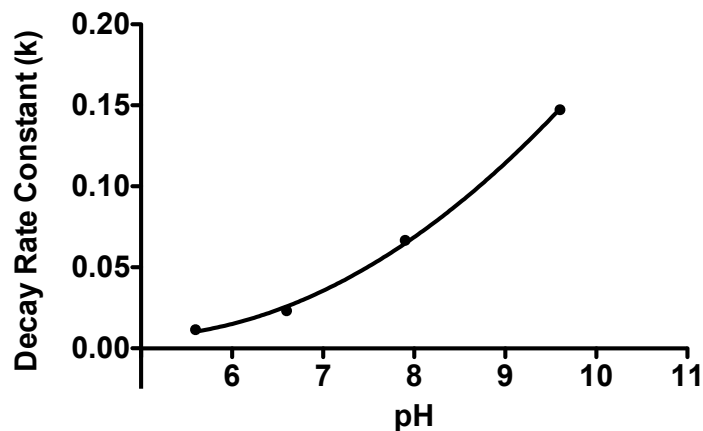
Supplemental Figure C.11. Plot of the decay rate constant as a function of the pH of solution. The rate of decay or dissociation was calculated using the plasmon shifts ($A_{680\ nm}/A_{520\ nm}$) provided from the data in Figure C.10. The rate of decay increases exponentially as the pH of the solution increases. When the particles are suspended in a solution possessing a pH value greater than 10, no color change is evident after THPC addition, and the particles remain red.
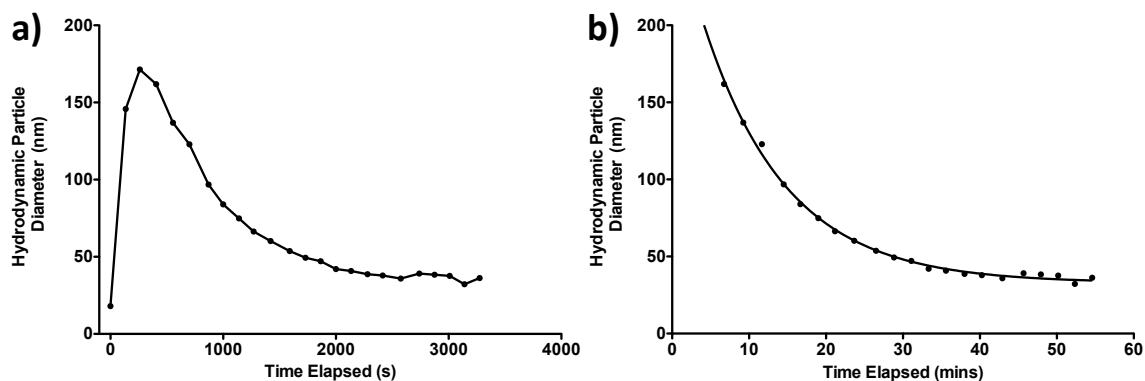

Supplemental Figure C.12. Dynamic light scattering (DLS) of 15 nm citrate AuNPs upon addition of THPC. In a glass cuvette with a square opening, 100 μM THPC was added to 1 mL of a 2.3 nM suspension of AuNPs. The hydrodynamic diameter of the particles was recorded at regular time intervals as the reaction progressed. a) Plot of hydrodynamic particle diameter upon exposure to THPC, highlighting that the particles immediately form assemblies. The particle chains begin dissociating minutes after addition of THPC, which correlates with the time required for the UV-vis spectra to begin to blueshift. b) The THPC AuNPs fit a decay curve, which is similar to the generated decay curves monitoring the plasmon bands in the UV-vis spectra.
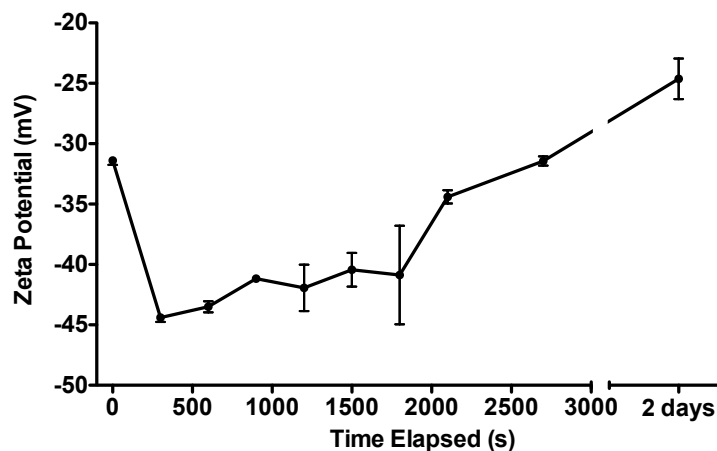
Supplemental Figure C.13. Zeta potential of 15 nm AuNPs upon incubation with THPC. In 10 separate 1.5 mL Eppendorf tubes, 100 μM THPC was added to a 2.3 nM suspension (1.0 mL) of 15 nm citrate AuNPs simultaneously. Each measurement was performed with a fresh particle suspension at different time points. The zeta potential at t = 0 is representative of 15 nm citrate AuNPs. The zeta potential increases as a function of incubation time, moving towards more positive values as the assemblies begin to dissociate. When the particles achieve monodispersity after two days, the final zeta potential value is slightly more positive than citrate AuNPs, which correlates with a negatively charged species adsorbed to the surface of the particle. Since citrate is more negative than THPOH, the final zeta potential after two days correlates with an adsorbed THPOH species.
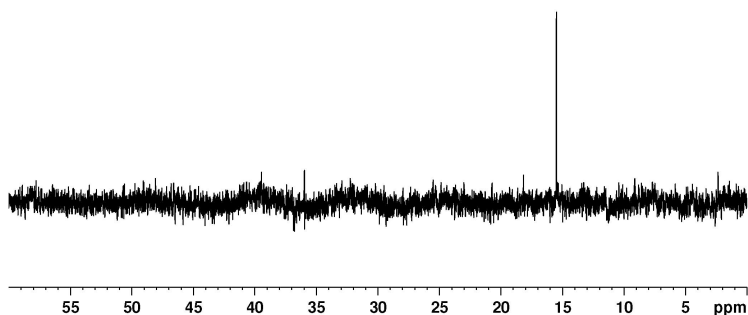

Supplemental Figure C.14. ^{31}P NMR spectrum of THPC AuNPs (100 nM) stored in basic buffer (pH 9.0). Citrate AuNPs (2.3 nM, 10 mLs) were first reacted with 100 μM THPC and allowed to incubate undisturbed for 48 hours. Afterwards, the particles were centrifuged at 7400 rcf for 45 minutes (10 1 mL aliquots) and the supernatant was removed. Next, each aliquot was resuspended in 100 μL 0.1 M CHES with 0.025% Tween 20 (pH 9.0). Afterwards, each aliquot was combined into one aliquot, and the centrifugation process was repeated. After removing the supernatant, particles were resuspended in 180 μLs CHES buffer, concentrating the particles by a factor of approximately 50. After storing at room temperature for 24 hours, this solution was added to a 3 mM NMR tube for ^{31}P spectral acquisition. No peak for THPO (δ, +49 ppm) is observed, suggesting that THPC cannot fully oxidize to THPO on-particle.
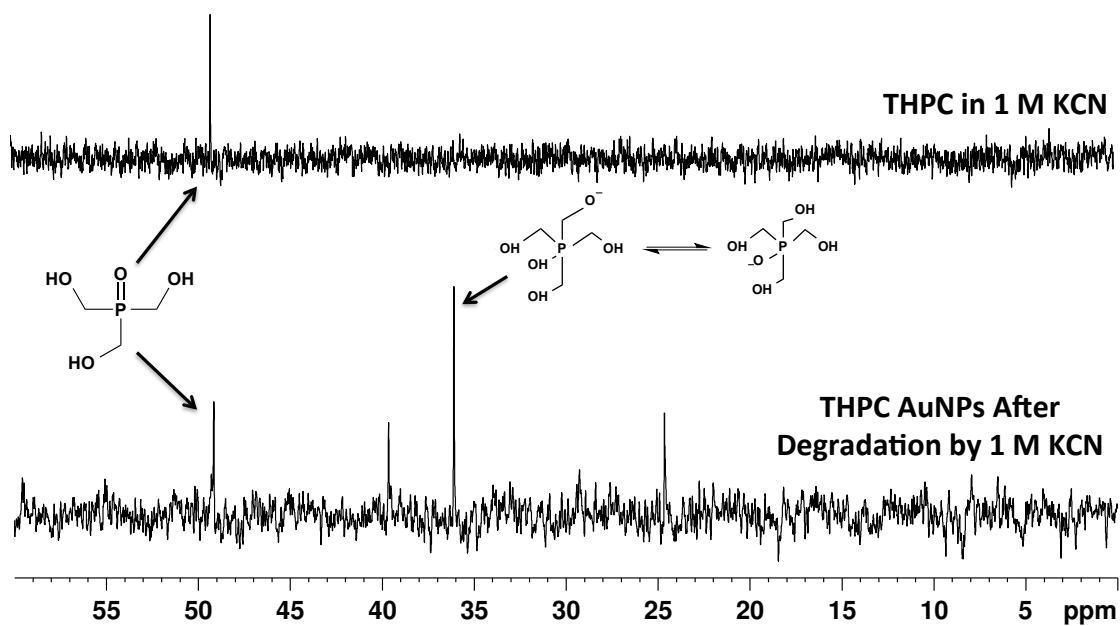
Supplemental Figure C.15. ^{31}P NMR spectra of concentrated THPC and THPC AuNPs after chemical degradation by 1 M potassium cyanide (KCN). The THPC ligand is converted entirely to THPO (δ, +49 ppm) upon exposure to KCN. Following chemical digestion of the THPC AuNPs, four peaks are observed: THPO (δ, +49 ppm), THPOH (δ, +36 ppm), and two unidentified peaks (δ, +39.6 ppm and +24.6 ppm) resulting from the chemical degradation process. These results are consistent with the proposed mechanism of the particle preventing complete oxidation of THPC to THPO, however chemical degradation introduces changes to the ^{31}P spectrum that are not observed in on-particle NMR.
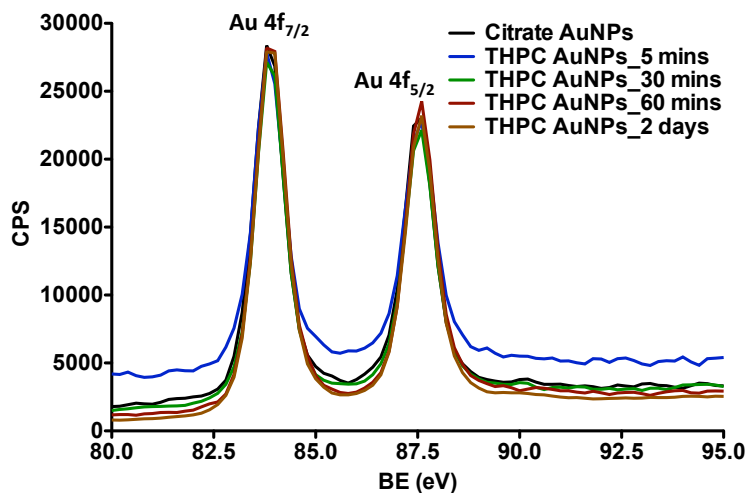
Supplemental Figure C.16. Raw XPS spectral data of the Au 4f peaks of THPC AuNPs after different reaction time intervals with THPC. The Au $4f_{7/2}$ peak for all samples possess binding energies of 83.8 eV, while the Au $4f_{5/2}$ peak for each sample possesses binding energies of 87.6 eV. These peaks are consistent with Au^0, and demonstrate that the instrument is calibrated. Additionally, the THPC does not induce chemical changes to the gold nanoparticle surface.
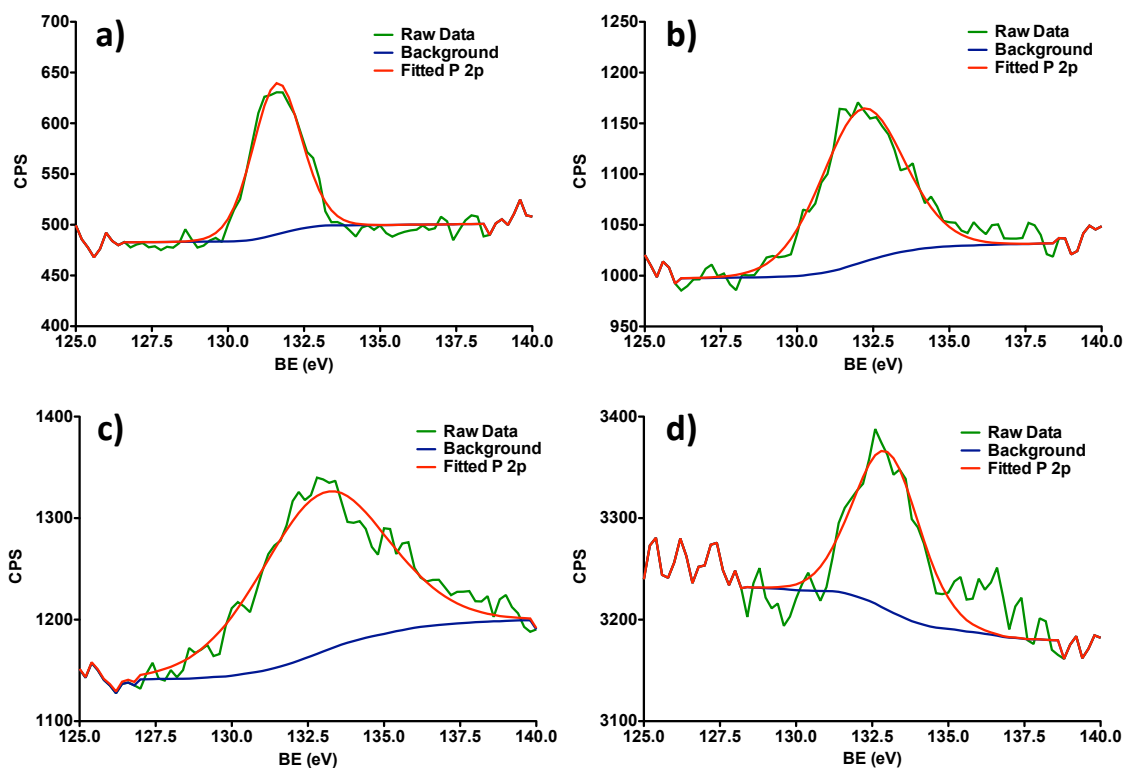

Supplemental Figure C.17. Raw data, background modeling, and fitted P 2p XPS spectra of THPC AuNPs after a) 5 minutes, b) 30 minutes, c) 60 minutes, and d) 48 hours of THPC incubation.
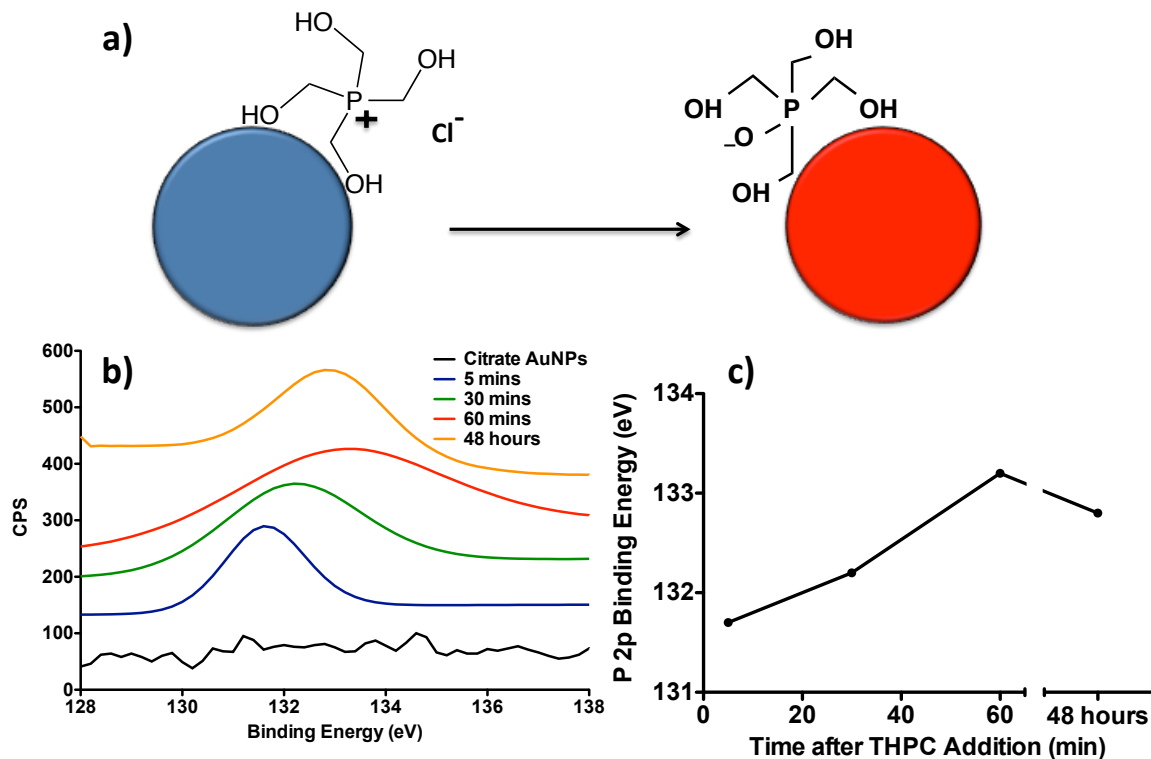
Supplemental Figure C.18. Evidence to support the THPC oxidation to pentavalent THPC hydroxide. a) Hypothesized schematic of AuNP disassembly. As THPC-functionalized particles assemble, they form linear chains and a blue color is observed. As the oxidation reaction occurs at the particle's surface, the particles disassemble into more monodisperse entities because there is too much negative surface charge to maintain the assembly. b) Fitted P 2p XPS spectra as a function of time elapsed after THPC addition. Since no significant phosphorus signal is observed for citrate AuNPs, no fit is necessary. c) The P 2p binding energy increases relative to THPC incubation time, suggesting the presence of a pentavalent phosphorus species adsorbed to the particles.
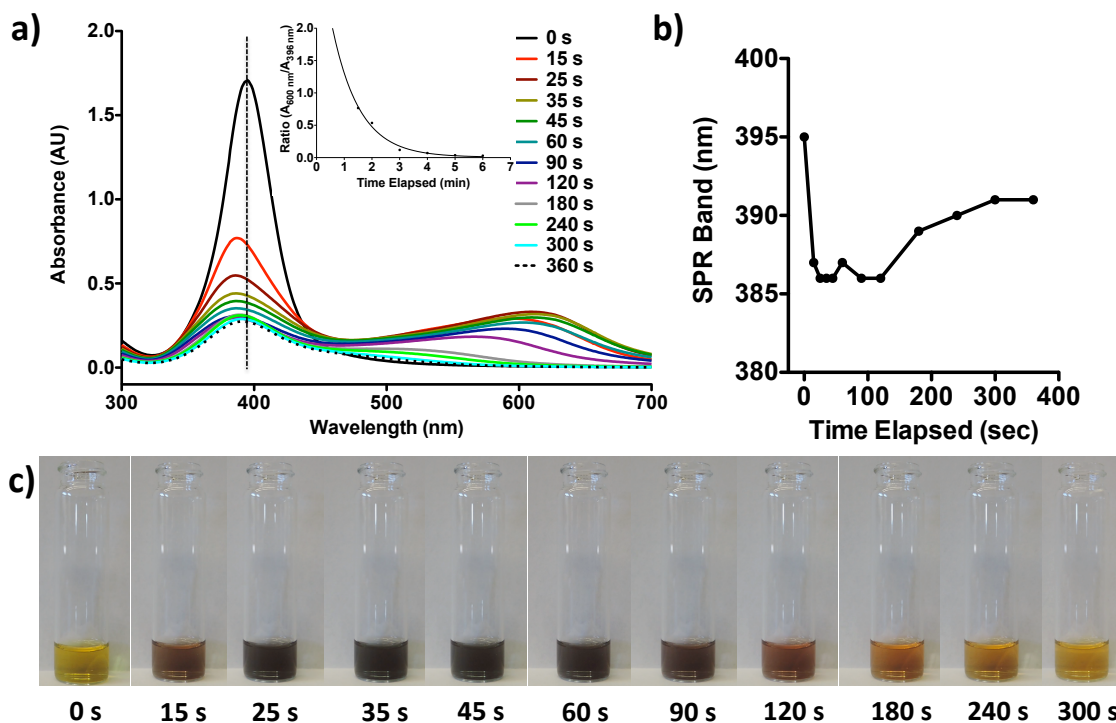
Supplemental Figure C.19. Rapid assembly and disassembly of THPC AgNPs. a) UV-vis of 1 mM THPC added to 20 nm citrate-stabilized AgNPs (400 pM). Note the dotted black line centered on the localized surface plasmon resonance band (SPR) of citrate-stabilized AgNPs, highlighting the blue shift after initial THPC addition. Inset is the rate of decay versus time by monitoring the ratio of plasmon bands ($A_{600\ nm}/A_{396\ nm}$). The rate constant (k = 1.015) for AgNPs is significantly greater than for AuNPs, suggesting in this application, Ag has greater catalytic activity. b) Plot of the primary silver localized SPR band over time and c) THPC AgNP color changes over a five-minute timespan. The initial blue shift of the localized SPR band at 395 nm can be attributed by the vast presence of charge carriers encompassing the nanoparticles, as the oxidation reaction progresses. After approximately two minutes, the primary localized SPR band of the THPC AgNPs begins to redshift. The UV-vis spectra and images of the THPC AgNPs after 6 minutes are not shown, as they begin to lose stability and crash out of solution.
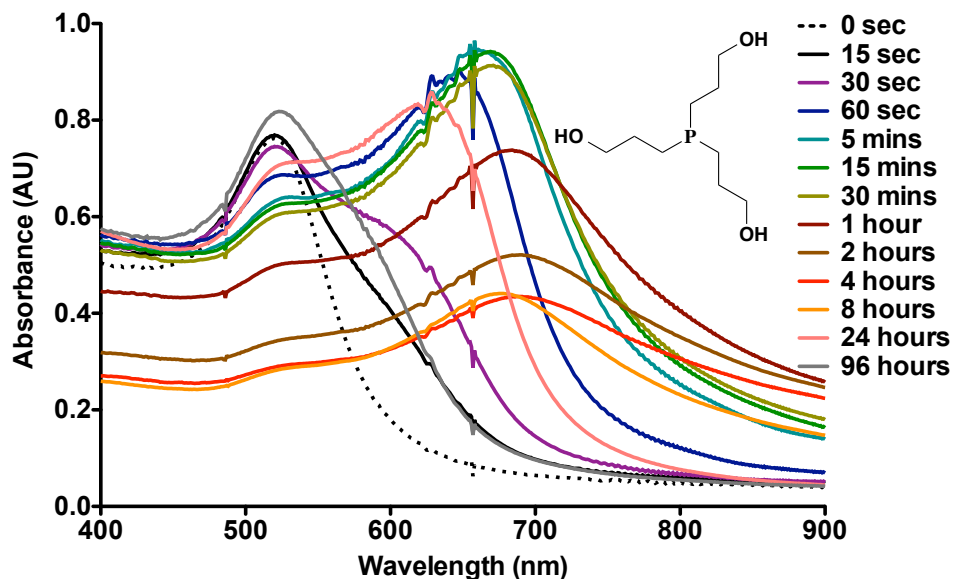
Supplemental Figure C.20. Slow reversible assembly and disassembly of THPP AuNPs at pH 6.3. To a 2.3 nM solution of 15 nm citrate-stabilized AuNPs (pH 6.3), a 100 μM solution of THPP was added and UV-vis spectral kinetics were monitored over 96 hours.
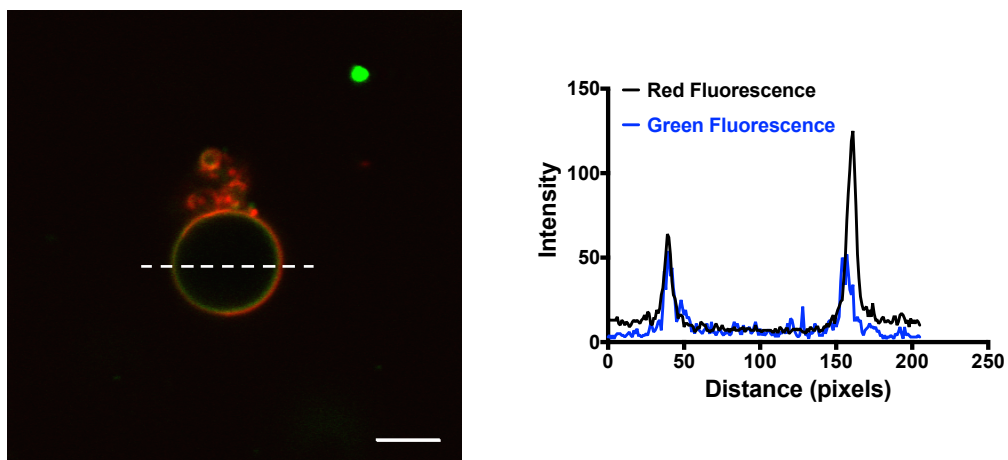
Supporting Information: Chapter II

Supplemental Figure D.1. Line plot of fluorescence intensity for hAuNP treated GUV. ImageJ was used to plot the red and green fluorescence intensity profiles for the dotted line marked in the GUV image. A clear overlap between the red and green fluorescence is observed when the two profiles are overlaid, supporting the conclusion that hAuNPs localize and concentrate in the GUV membrane. Scale bar: 10 µm.

10% FBS — **0% FBS**
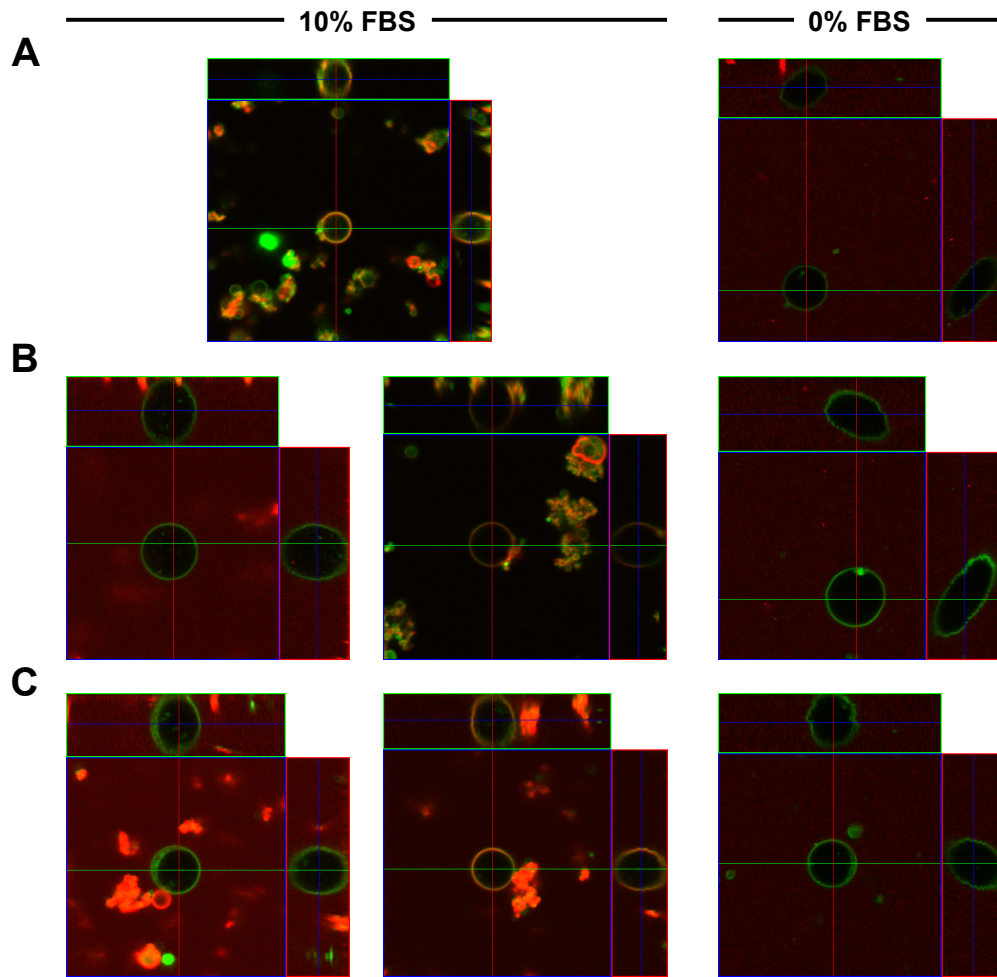
Supplemental Figure D.2. Representative confocal microscope images of 0% cholesterol GUVs. (A) 4°C (B) 25°C (C) 37°C
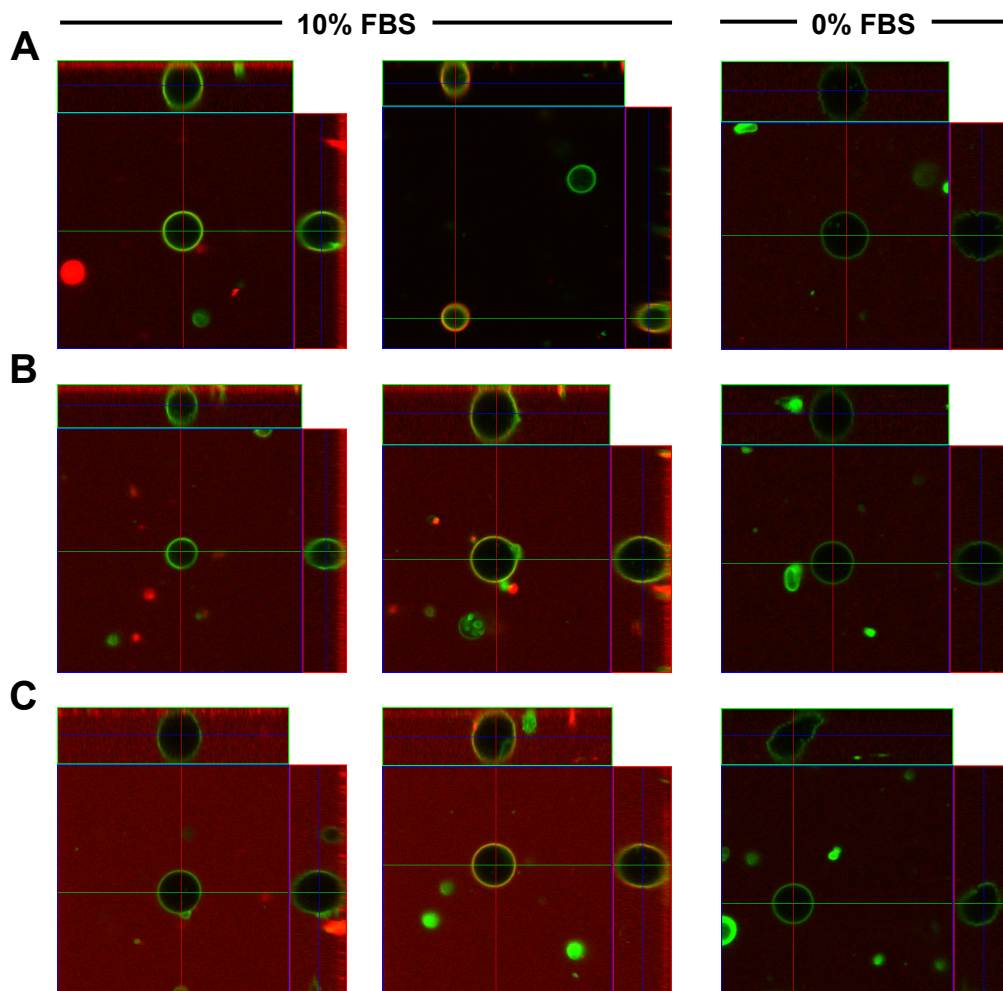
Supplemental Figure D.3. Representative confocal microscope images of 5% cholesterol GUVs. (A) 4°C (B) 25°C (C) 37°C
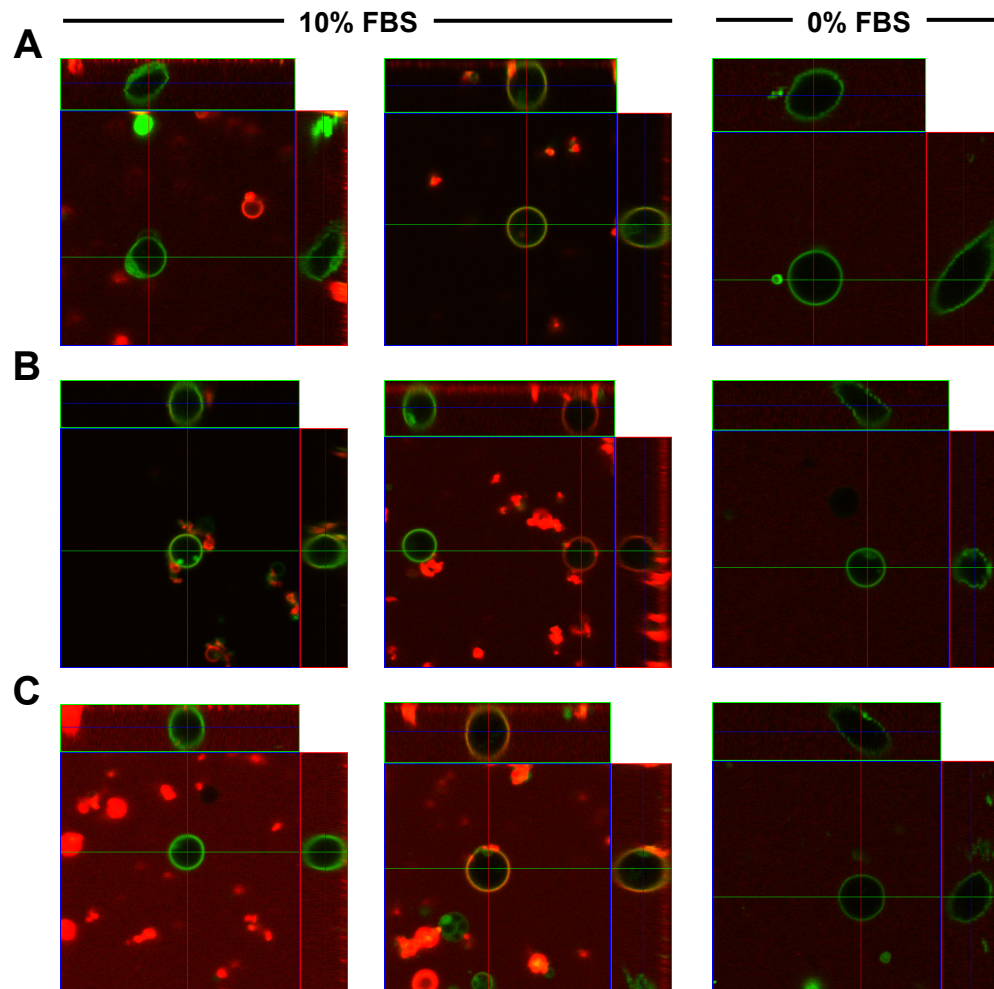
Supplemental Figure D.4. Representative confocal microscope images of 10% cholesterol GUVs. (A) 4°C (B) 25°C (C) 37°C
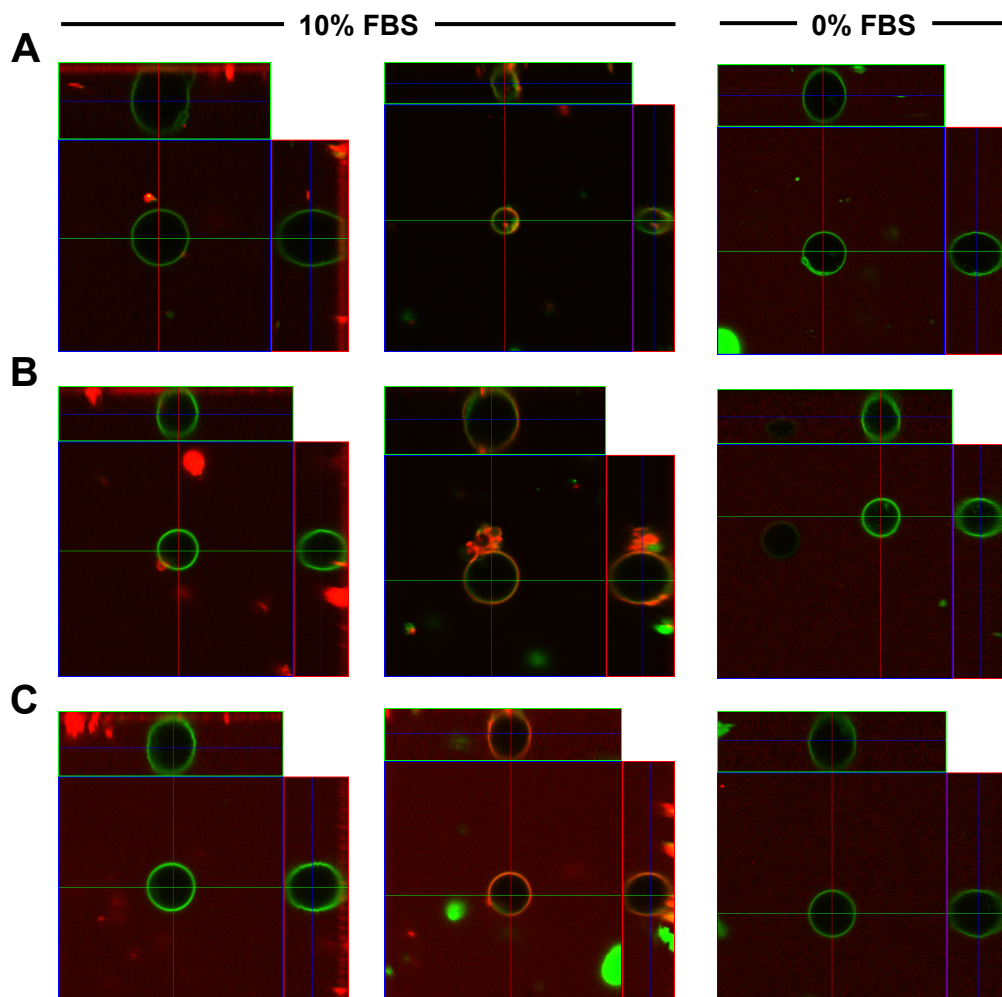
Supplemental Figure D.5. Representative confocal microscope images of 15% cholesterol GUVs. (A) 4°C (B) 25°C (C) 37°C

A Ungated

SSC-A vs FSC-A

GUVs

B Single GUVs

hAuNP Fluorescence Intensity (RFU) vs DiO Fluorescence Intensity (RFU)

Q1   Q2

Q4   Q3

GUV

GUV + 10% FBS
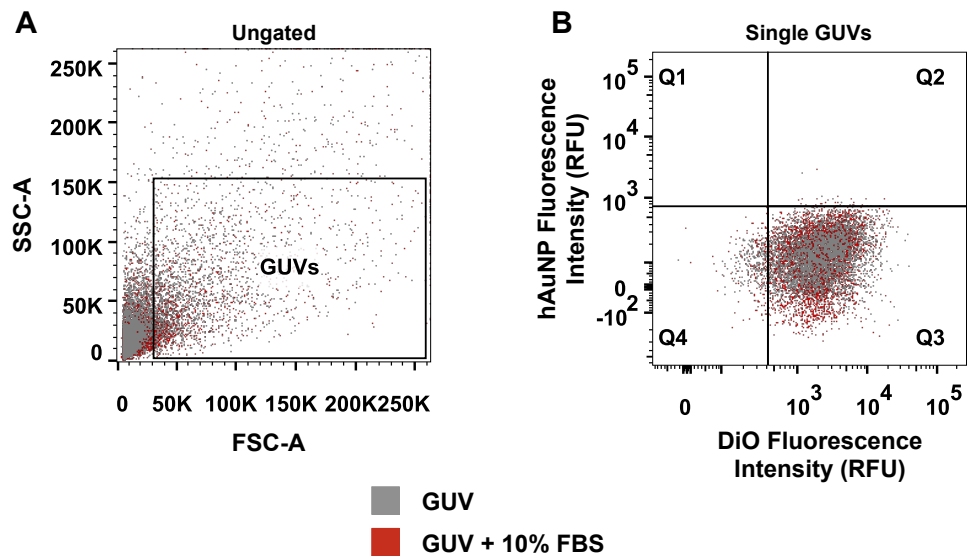
Supplemental Figure D.6. Adding FBS does not change the (A) scattering or (B) fluorescence properties of GUVs, as demonstrated by flow cytometry.

Mean Cell Fluorescence vs Temperature

0% FBS
10% FBS

37°C   4°C
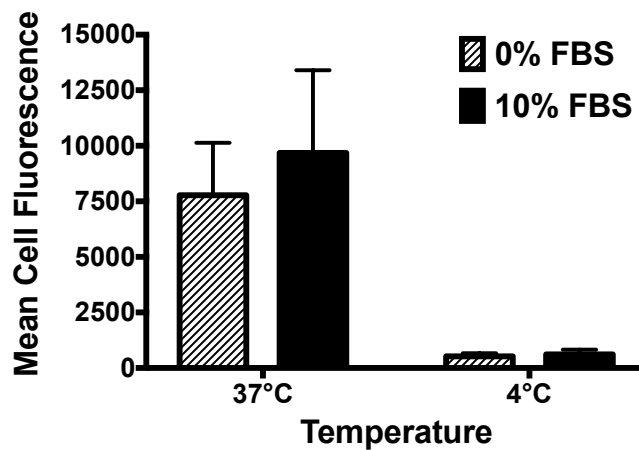
Supplemental Figure D.7. Mean fluorescence values for cells treated with hAuNPs at 37°C and 4°C in the presence and absence of FBS.
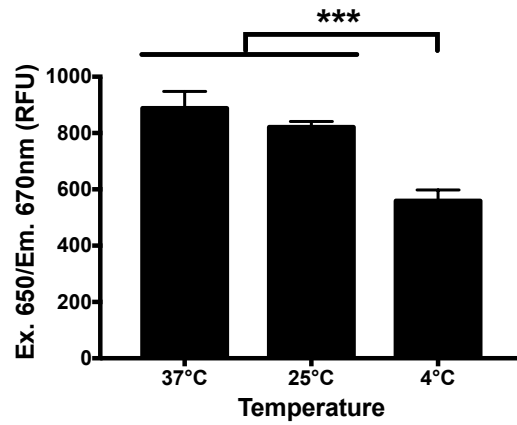
Supplemental Figure D.8. Temperature dependence of hAuNP fluorescence in PBS. hAuNPs were diluted to 1 nM in PBS and incubated at the given temperatures for 4 hours before quantifying the fluorescence of Cy5. At 4°C, hAuNPs have a 34.6% reduction in fluorescence compared to 25°C or 37°C, but this does not account for the dramatically reduced fluorescence observed with hAuNP treated cells at 4°C. ***p = 0.0002.

Appendix E

Supporting Information: Chapter III

ICP-MS Calculations

ICP-MS analysis provides gold concentration in µg/L. To convert this to a AuNPs per

cell result, the following conversion scheme was used to arrive at the amount of AuNPs/L:

$$\frac{\mu g}{L} \times \frac{g}{10^6 \mu g} \times \frac{mol}{196.97g} \times \frac{6.022 \times 10^{23}\, atoms}{mol} \times \frac{NP}{N_{Au/NP}}$$

where $N_{Au/NP} = \frac{\pi}{6} \frac{\rho D^3}{M} N_A$.

In the equation for $N_{Au/NP}$, ρ is the density of fcc gold (19.3 g/cm), D is the average

diameter of the gold nanoparticle core (in cm) as measured using transmission electron

microscopy (TEM) images and ImageJ software (data not shown), M is the atomic mass of gold

(196.97 g/mol), and N_A is Avogadro's number (6.022×10^{23} nanoparticles/mol).

Next, the AuNPs/L value is multiplied by the volume of analysis (6 mL) to arrive at the

total number of AuNPs in the sample. To get the average amount of AuNPs per cell, the total

AuNPs is divided by the average number of cells. These values are used directly to compare

cellular uptake across different samples and are also used to calculate the percent of AuNP

retention.

Name	Sequence (5'-3')
T-10	TTTTTTTTTT
hDNA*	TTTTTTTTTT<u>GCAGC</u>**GCTTCGTCGTTATTGTTCT**<u>GCTGC</u>
hDNA complement	TT**AGAACAATAACGACGAAGC**TT
ssDNA*	TTTTTTTTTT**ATCAACCTTGGTTATACGATGACCGGTGCG**
ssDNA complement	**CGCACCGGTCATCGTATAACCAAGGTTGAT**
dsDNA*	TTTTTTTTTT**ATCAACCTTGGTTATACGATGACCGGTGCG**
dsDNA complement	**CGCACCGGTCATCGTATAACCAAGGTTGAT**

*Sequences incorporate a 5' hexane thiol and 3' Cy5
T-10 incorporates a 5' hexane thiol
Underline represents stem formation sequence
Bold represents portions that are complementary between the pairs

Supplemental Table E.1. List of DNA sequences conjugated to AuNPs

DNA-AuNPs are prepared from the DNA sequences listed in Supplemental Table E.1 to characterize the cellular uptake of AuNPs functionalized with different conformations of DNA. The cellular uptake and excretion are also examined using flow cytometry and ICP-MS. The cellular uptake of complemented versions of hAuNPs and ssAuNPs is determined by ICP-MS, flow cytometry, and confocal microscopy.
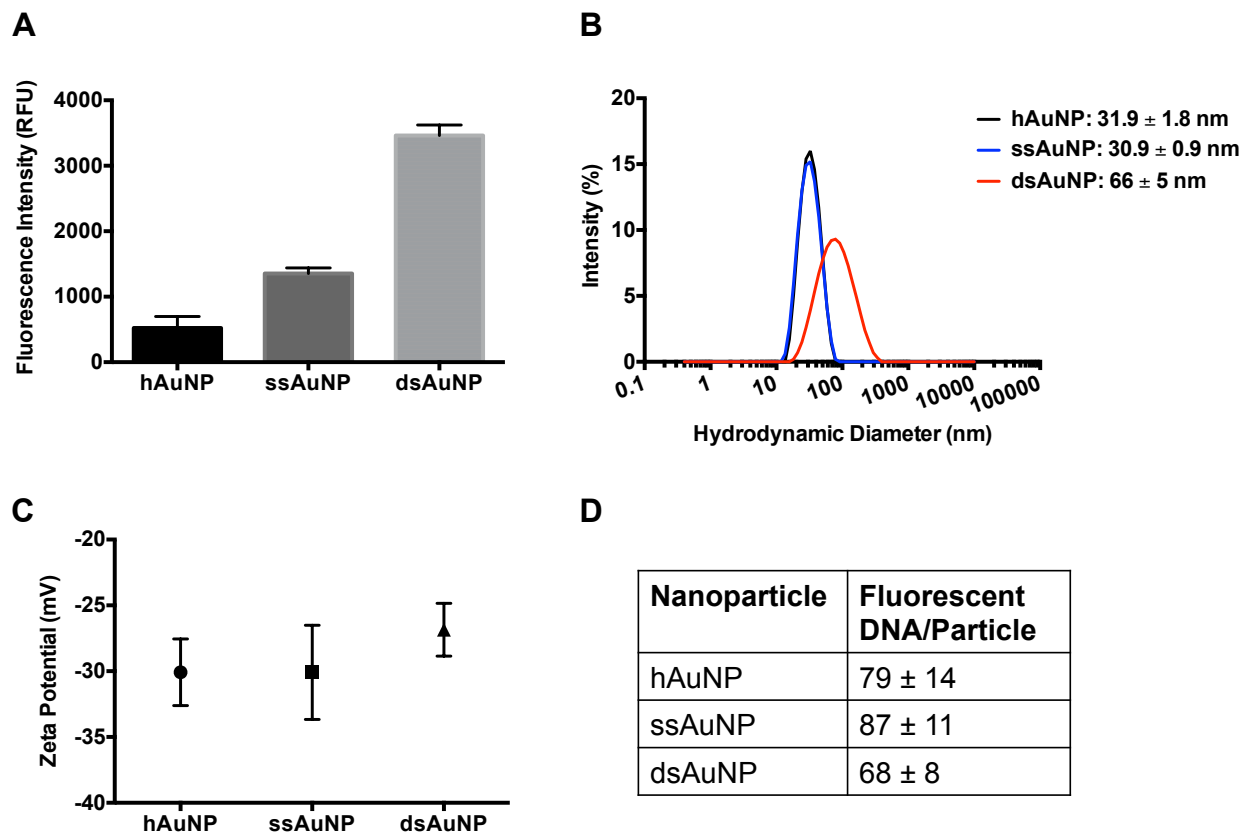
Supplemental Figure E.1. Characterization of DNA functionalized gold nanoparticles. (A) The fluorescence of DNA-AuNPs in PBS (*i.e.* in the absence of cells) is reflective of how their expected DNA conformation (hairpin, random coil, or double helix) affects the placement of the Cy5 fluorophore relative to the gold surface. Hairpin DNA has the lowest fluorescence because the fluorophore is held close to the AuNP by the self-complementary stem. Single stranded DNA has an intermediate fluorescence that we attribute to the flexibility of the sequence as it samples all available conformations. Double stranded DNA has the highest fluorescence due to the rigidity of the double helix, which forces the fluorophore away from the AuNP. (B) Representative histograms of the hydrodynamic diameter of hAuNPs, ssAuNPs, and dsAuNPs. Measurement of the hydrodynamic diameter of DNA-AuNPs reveals that dsAuNPs are much larger than the similarly sized hAuNPs and dsAuNPs. These DNA-AuNPs have approximately the same (C) zeta potential and (D) average number of fluorescent DNA strands conjugated per particle. Error bars denote standard deviation from at least three preparations of particles.
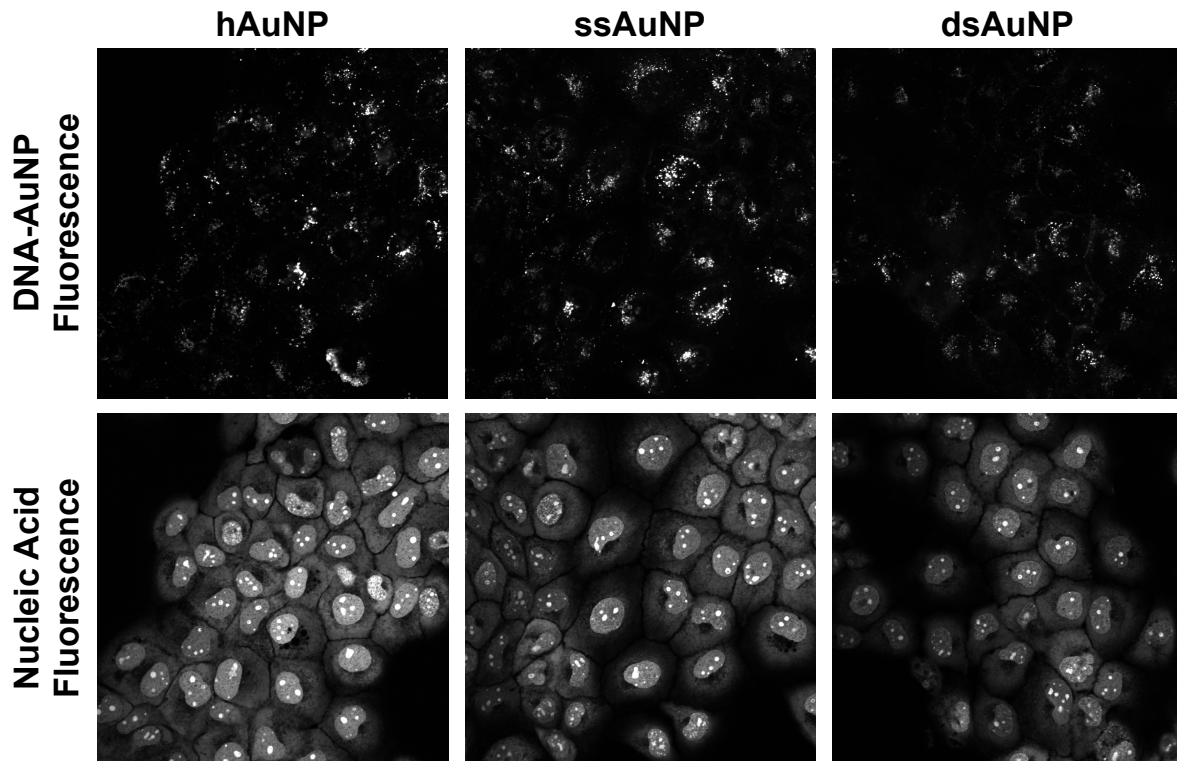
Supplemental Figure E.2. Cells exhibit a heterogeneous distribution of internalized DNA-AuNPs. Each cell exposed to DNA-AuNPs accumulates nanoparticles intracellularly, although in different amounts. This is most evident without the use of false color in the images, and can be seen by comparing the DNA-AuNP fluorescence to the nucleic acid fluorescence, which provides the location of the cells. The heterogeneous distribution of fluorescence observed by confocal microscopy is also observed in flow cytometry, where the cell population has a distribution of fluorescence centered around a mean value.
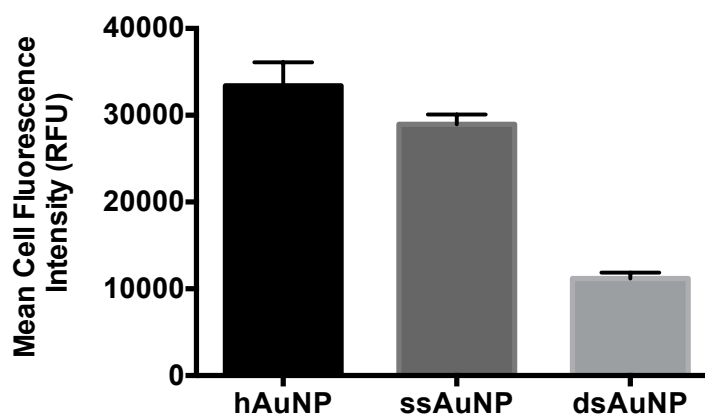
Supplemental Figure E.3. Mean cell fluorescence of cells incubated with DNA-AuNPs. CaSki cells are incubated with DNA-AuNPs and evaluated for fluorescence by flow cytometry. The values shown here are obtained by calculating the geometric mean of the fluorescence histogram of the single cell population. Cells incubated with hAuNPs and ssAuNPs have similar fluorescence levels, while cells incubated with dsAuNPs have lower fluorescence. Error bars denote the standard deviation in the geometric mean of three biological replicates.
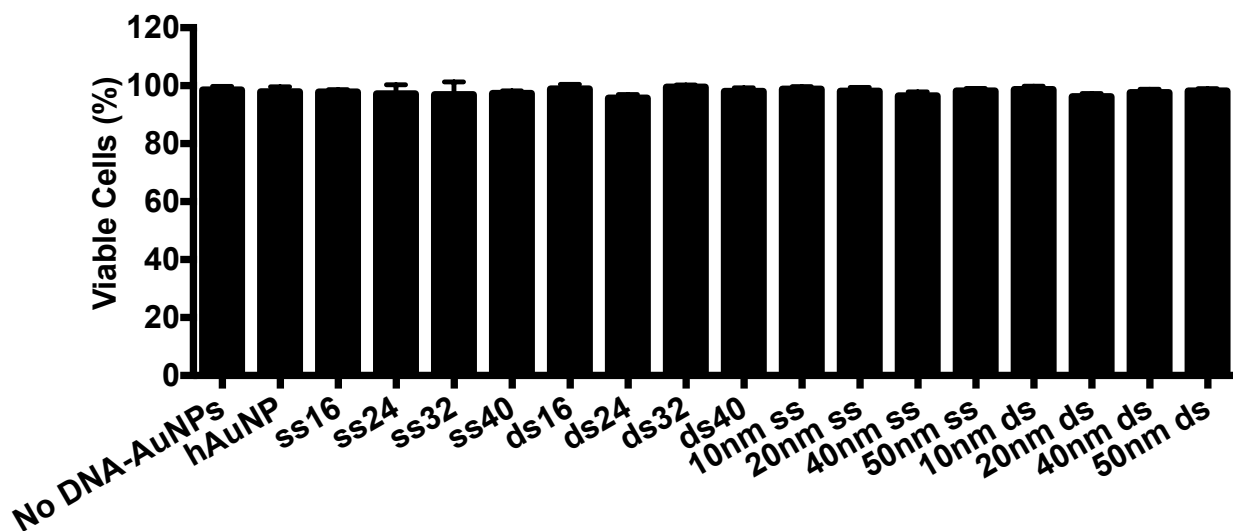
Supplemental Figure E.4. Cell viability after DNA-AuNP treatment. After 24 hours of exposure to DNA-AuNPs, the viability of cells was evaluated using the Trypan blue exclusion assay. Regardless of the type of DNA-AuNP, cells exhibited $\geq$ 95% viability after incubation with the nanoparticles. Note: In the naming schemes used throughout the paper, ssAuNPs and dsAuNPs are identical to ss40-AuNPs and ds40-AuNPs; ss24 and ds24 are identical to 15nm ss and 15nm ds.
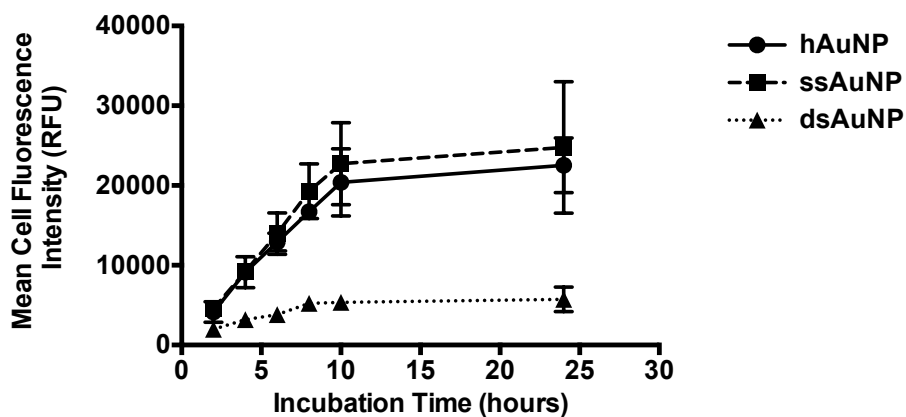
Supplemental Figure E.5. Cellular uptake over time analyzed by flow cytometry. CaSki cells are incubated with DNA-AuNPs for 2 – 24 hours and evaluated for fluorescence by flow cytometry. The values shown here are obtained by calculating the geometric mean of the fluorescence histogram of the single cell population. These values represent the central tendency of the fluorescence of each cell population analyzed. Similar to the ICP-MS results, hAuNPs and ssAuNPs exhibit identical behavior, and have high cellular fluorescence, while dsAuNPs result in much lower cellular fluorescence. Error bars denote the standard deviation in the geometric mean of two biological replicates.
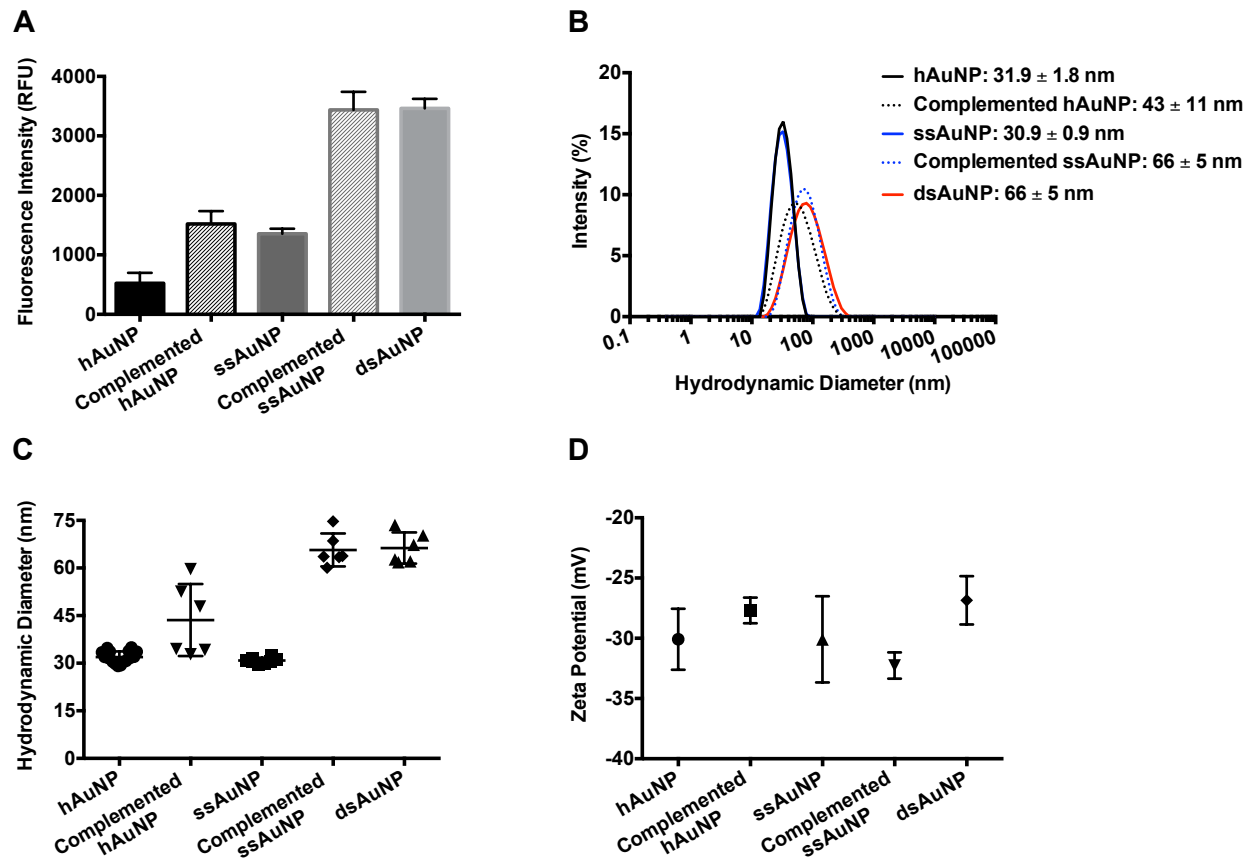
**Supplemental Figure E.6.** Characterization of complemented DNA-AuNPs. (A) Compared to their hAuNP and ssAuNP counterparts, the fluorescence of complemented hAuNPs and complemented ssAuNPs in PBS is increased, indicating that the AuNP-conjugated DNA strand is extended upon hybridizing to the complementary strand. (B) Representative histograms of the hydrodynamic diameter of complemented DNA-AuNPs. An increase in the hydrodynamic diameter of complemented hAuNPs and complemented ssAuNPs also shows the successful hybridization of the complementary strand to the AuNP-conjugated strand. (C) The hydrodynamic diameter data displays large spread over multiple batches of complemented hAuNPs, possibly contributing to the conflicting ICP-MS and flow cytometry results obtained for cellular uptake of complemented hAuNPs. All other DNA-AuNP size measurements are tightly grouped with a standard deviation of ≤ 5 nm. (D) The zeta potential of complemented DNA-AuNPs is similar to other DNA-AuNPs, with values between -25 mV and -30 mV.
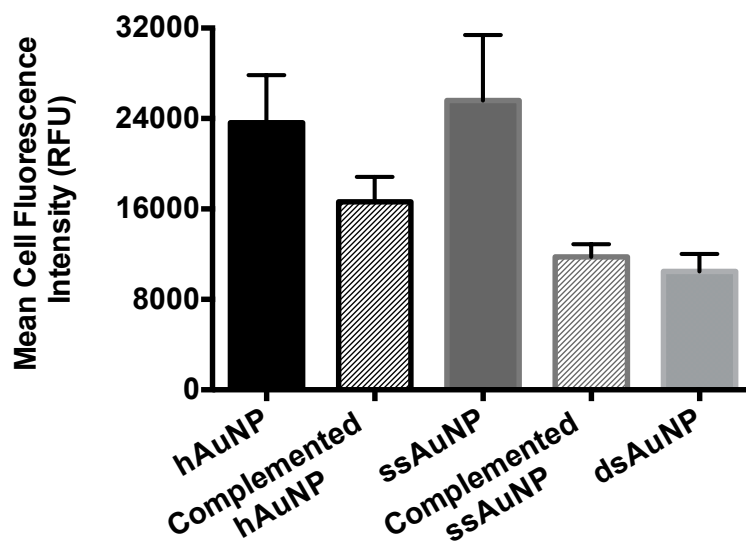
Supplemental Figure E.7. Fluorescence of cells incubated with complemented DNA-AuNPs. CaSki cells were incubated with DNA-AuNPs and complemented DNA-AuNPs and evaluated for fluorescence by flow cytometry. The values shown here are obtained by calculating the geometric mean of the fluorescence histogram of the single cell population. These values represent the central tendency of the fluorescence of each cell population analyzed. Cells incubated with complemented ssAuNPs have fluorescence similar to cells incubated with dsAuNPs. CaSki cells incubated with complemented hAuNPs have intermediate fluorescence behavior. Error bars denote the standard deviation in the geometric mean of three biological replicates.

Name	Sequence (5'-3')
ds40DNA*	TTTTTTTTTT**ATCAACCTTGGTTATACGATGACCGGTGCG**
ds40DNA complement	**CGCACCGGTCATCGTATAACCAAGGTTGAT**
ds32 DNA*	TTTTTTTTTT**ATCAACCTTGGTTATACGATGA**
ds32 DNA complement	**TCATCGTATAACCAAGGTTGAT**
ds24 DNA*	TTTTTTTTTT**ATCAACCTTGGTTA**
ds24 DNA complement	**TAACCAAGGTTGAT**
ds16 DNA*	TTTTTTTTTT**ATCAAC**
ds16 DNA complement	**GTTGAT**
ss40 DNA*	TTTTTTTTTTATCAACCTTGGTTATACGATGACCGGTGCG
ss32 DNA*	TTTTTTTTTTATCAACCTTGGTTATACGATGA
ss24 DNA*	TTTTTTTTTTATCAACCTTGGTTA
ss16 DNA*	TTTTTTTTTTATCAAC

*Sequences incorporate a 5' hexane thiol and 3' Cy5
Bold represents portions that are complementary between the pairs

Supplemental Table E.2. List of DNA sequences used to prepare ssAuNPs and dsAuNPs

One set of DNA-AuNPs was prepared using 15 nm AuNPs and the sequences listed in Supplemental Table E.2. The effect of the different sizes of these nanoparticles on cellular uptake was determined by ICP-MS. A second set of DNA-AuNPs was prepared from 10, 15, 20, 40, and 50 nm diameter AuNPs conjugated to ss24- and ds24-DNA and the cellular uptake of these nanoparticles was studied by ICP-MS.
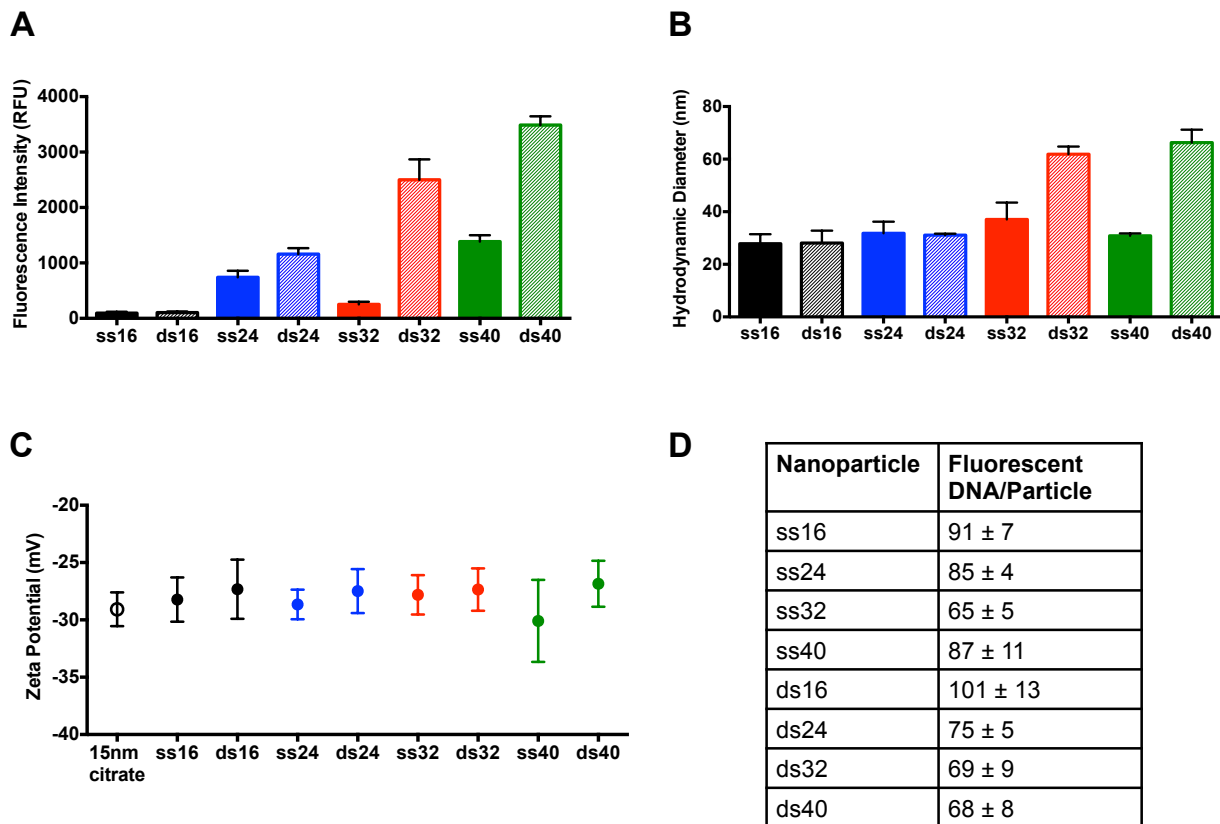
Supplemental Figure E.8. Characterization of 15 nm AuNPs conjugated to Cy5 labeled single stranded and double stranded DNA that is 16, 24, 32, or 40 nucleotides in length. In PBS, the (A) fluorescence and (B) hydrodynamic diameter measurements of these DNA-AuNPs show that nanoparticles with single stranded DNA can be distinguished from those with double stranded DNA. (C) Zeta potential measurements for these DNA-AuNPs and for citrate-stabilized AuNPs result in similar values around -28 mV for all the nanoparticles. (D) The DNA-AuNPs are also characterized by the average number of fluorescent DNA bound per particle, which ranges from 65 to 101 DNA per particle. Error bars denote standard deviation from three or more preparations of particles.
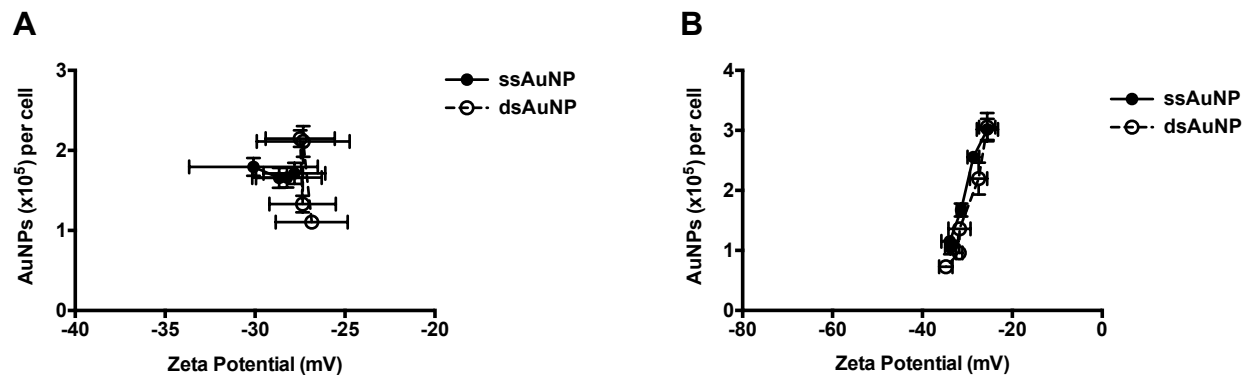
Supplemental Figure E.9. Zeta potential does not significantly influence the cellular uptake of ssAuNPs or dsAuNPs. (A) Varying lengths of ss- and dsDNA are conjugated to 15 nm AuNPs and the cellular uptake of these DNA-AuNPs is evaluated by ICP-MS. Plotting the average number of AuNPs per cell against zeta potential reveals no trend in cellular uptake, which is expected considering that all of these DNA-AuNPs had the same zeta potential. (B) ss- and dsDNA of a uniform length are conjugated to 10, 15, 20, 40, or 50 nm AuNPs and the cellular uptake of these DNA-AuNPs is evaluated by ICP-MS. A small trend in cellular uptake versus zeta potential is observed; however, differences in zeta potential between these DNA-AuNPs are likely due to differences in size of the AuNP core (see Supplemental Figure E.11), and probably play a minimal role in determining internalization. Error bars denote standard deviation from three biological replicates.
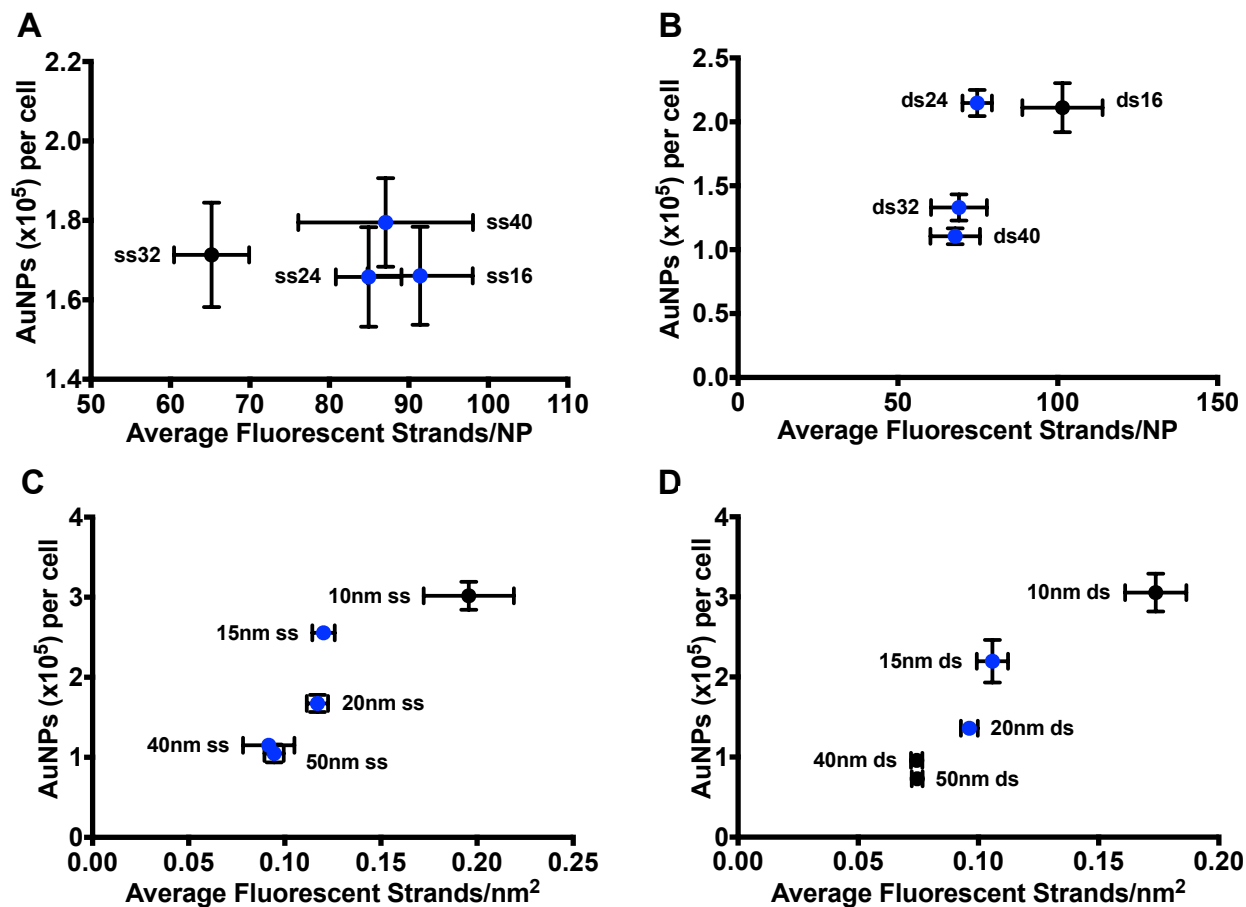
Supplemental Figure E.10. DNA density does not influence cellular uptake of some DNA-AuNPs. Blue circles: DNA-AuNPs that have statistically similar DNA ligand densities. Black circles: DNA-AuNPs with DNA densities that are significantly different from those of the blue circles. These data indicate that for some DNA-AuNPs, the density of DNA on the surface does not determine the extent of accumulation in cells. (A) For DNA-AuNPs conjugated to increasing lengths of ssDNA, those made with ss32-DNA have a significantly different DNA density than the other particles, but the cellular uptake levels are not significantly different for these four nanoparticles. (B) For DNA-AuNPs made with increasing lengths of dsDNA that have statistically similar DNA coverage, a difference in cellular AuNP accumulation is observed. (C – D) To compare between differently sized AuNP cores, the quantity of fluorescent DNA per AuNP was normalized by the surface area of each nanoparticle. Cells internalize decreasing quantities of DNA-AuNPs made with increasing core diameters even when they have statistically similar DNA densities. Taken together, these results show that DNA density cannot reliably predict cellular uptake and therefore, likely plays a minor role. Differences in DNA density do not always produce differences in cellular accumulation (A), but nanoparticles with the same DNA density can exhibit differences in accumulation (B – D).
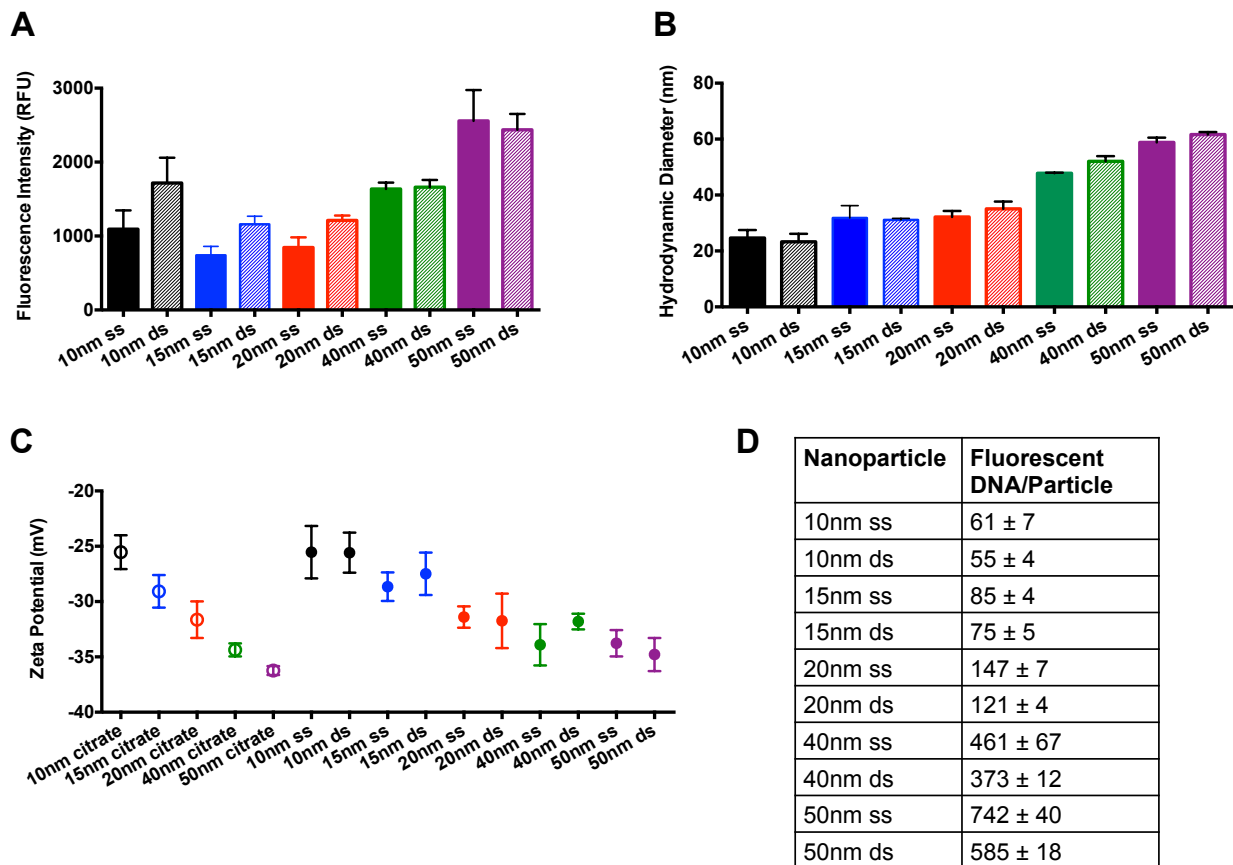
Supplemental Figure E.11. Characterization of 10, 15, 20, 40, and 50 nm AuNPs conjugated to Cy5 labeled ss- and dsDNA of 24 nucleotides in length. (A) Fluorescence and (B) hydrodynamic diameter measurements demonstrate that the DNA is conjugated to the AuNPs and that a range of sizes is obtained. (C) Zeta potential measurements result in a range of values from -25 to -35 mV. The zeta potential of citrate-stabilized AuNPs is also given and varies with core size in an identical manner to DNA capped AuNPs; therefore, differences in zeta potential are likely due to differences in the size of the AuNP core. (D) The average number of fluorescent DNA strands bound per particle is dependent on the size of the AuNP, with smaller AuNPs binding fewer DNA than larger AuNPs. Error bars denote standard deviation from three or more preparations of particles.
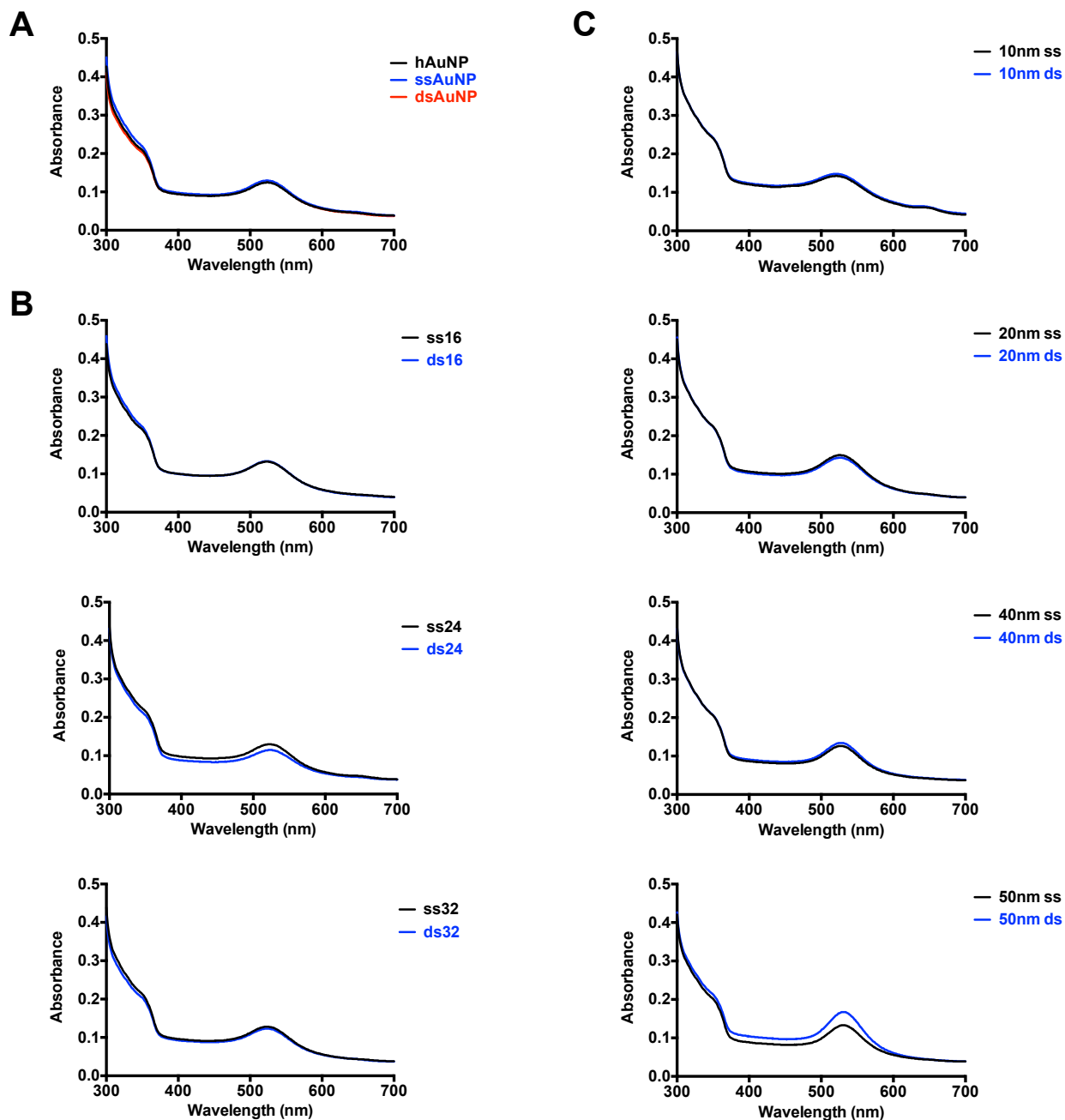
Supplemental Figure E.12. Absorbance spectra demonstrate that the DNA-AuNPs are monodisperse, maintaining a surface plasmon peak around 520 nm upon conjugation with DNA. Some DNA-AuNPs also have a small peak at 650 nm, which is characteristic of Cy5 absorption. (A) Absorbance spectra of hAuNPs, ssAuNPs, and dsAuNPs. (B) Absorbance spectra of 15 nm AuNPs conjugated to Cy5 labeled ss- and dsDNA that is 16, 24, or 32 nucleotides in length. (C) Absorbance spectra of 10, 15, 20, 40, and 50 nm AuNPs conjugated to Cy5 labeled ss- and dsDNA of 24 nucleotides in length. Note: In the naming schemes used throughout the paper, ssAuNPs and dsAuNPs are identical to ss40-AuNPs and ds40-AuNPs; ss24 and ds24 are identical to 15nm ss and 15nm ds.

156
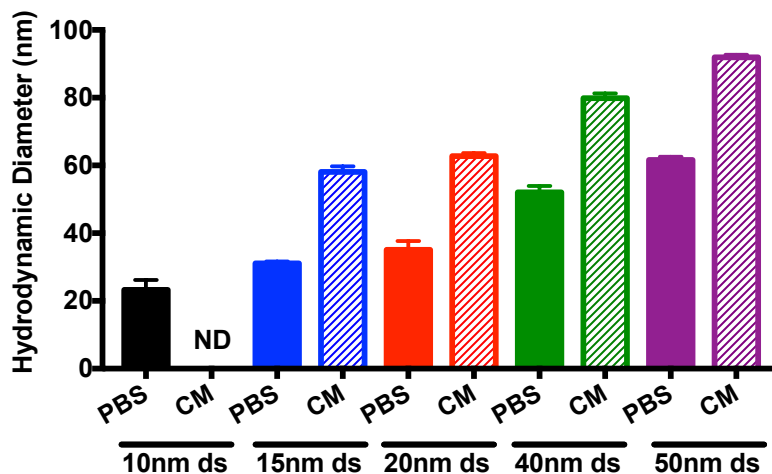
Supplemental Figure E.13. Formation of a protein corona does not change the size distribution of DNA-AuNPs. DNA-AuNPs were suspended in complete cell culture medium (CM) for 1 hour at 37°C with intermittent mixing. Complete medium contains 10% FBS. The hydrodynamic diameter was measured using DLS, and the same size distribution was achieved in PBS and CM. A value could not be determined (ND) for 10nm dsAuNPs in CM because the size distribution for these nanoparticles was identical to CM without any DNA-AuNPs added (Supplemental Figure E.14).
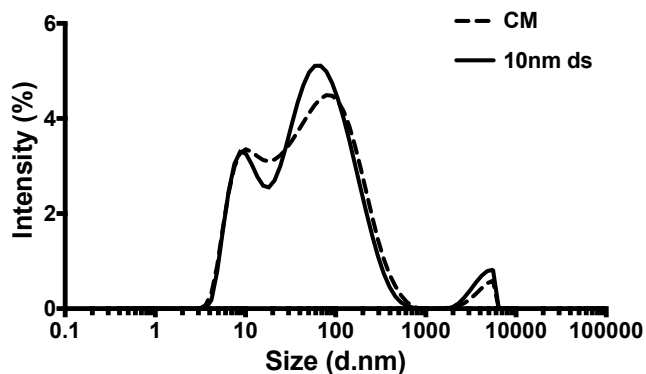
Supplemental Figure E.14. Complete medium and 10nm dsAuNPs give the same size distribution. 10nm dsAuNPs suspended in complete medium (CM) could not be distinguished from CM and were reported as not determined (ND) in Supplemental Figure E.13.

Supporting Information: Chapter IV

Analysis of ICP-OES Results for S2R+ Cell Supernatants

ICP-OES returns a µg/L measurement of the gold concentration for the 6 mL sample that was analyzed. This is converted to the concentration, in molarity, of gold nanoparticles in the original supernatant volume using Equation 1. The value of 1.04×10^5 atoms per nanoparticle is dependent on the size of the nanoparticle and was calculated using Equation 2, where ρ is the density of fcc gold (19.3 g cm^{-3}), D is the average diameter of the gold nanoparticle core (in cm), M is the atomic mass of gold (196.97 g/mol), and N_A is Avogadro's number (6.022×10^{23} nanoparticles/mol).

$$\frac{\mu g}{L} \times \frac{g}{10^6 \, \mu g} \times \frac{mol}{196.97g} \times \frac{6.022 \times 10^{23} \text{ atoms}}{mol} \times \frac{NP}{1.04 \times 10^5 \text{ atoms}} \times \frac{\text{Volume of ICP-OES sample}}{\text{Supernatant volume} * 6.022 \times 10^{23}} \qquad (1)$$

$$N_{Au/NP} = \frac{\pi}{6} \frac{\rho D^3}{M} N_A \qquad (2)$$
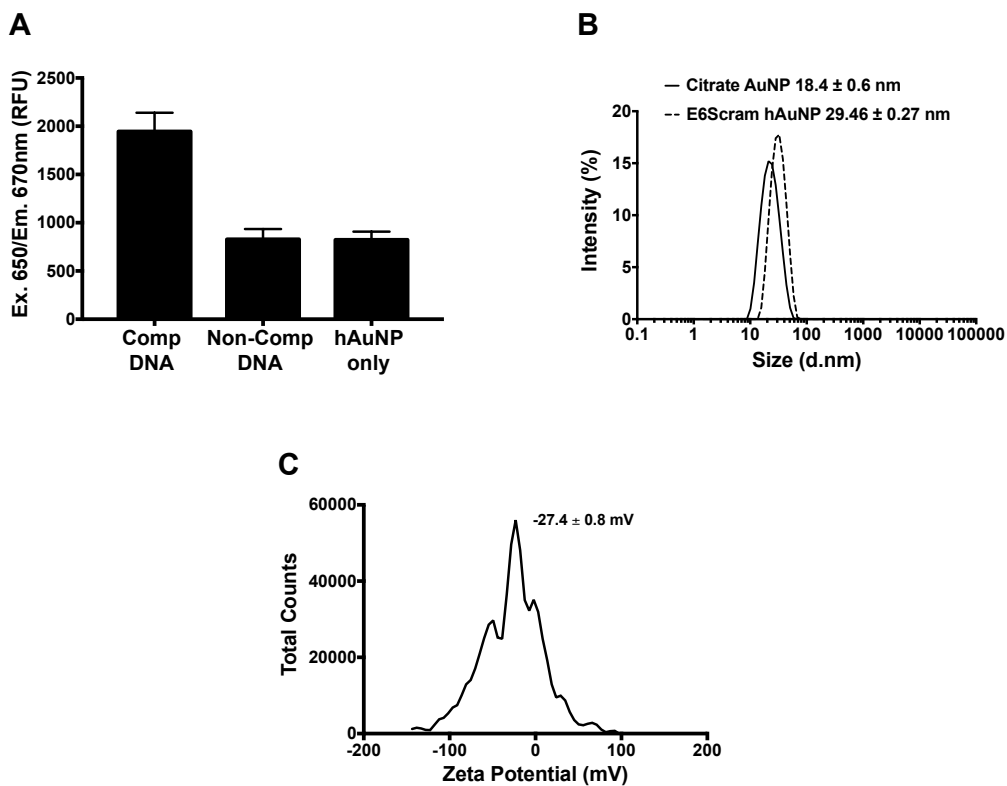
Supplemental Figure F.1. Characterization of hAuNPs. (A) Addition of DNA complementary to the hairpin loop results in an increase in fluorescence. Non-complementary DNA does not change the fluorescence relative to the hAuNP control. (B) The hydrodynamic diameter of hAuNPs increases relative to citrate AuNPs due to the conjugation of DNA on the gold surface. (C) hAuNPs have a negative zeta potential, as expected due to the negatively charged phosphodiester backbone of DNA. A value of 76 ± 5 hDNA strands per gold nanoparticle was measured.
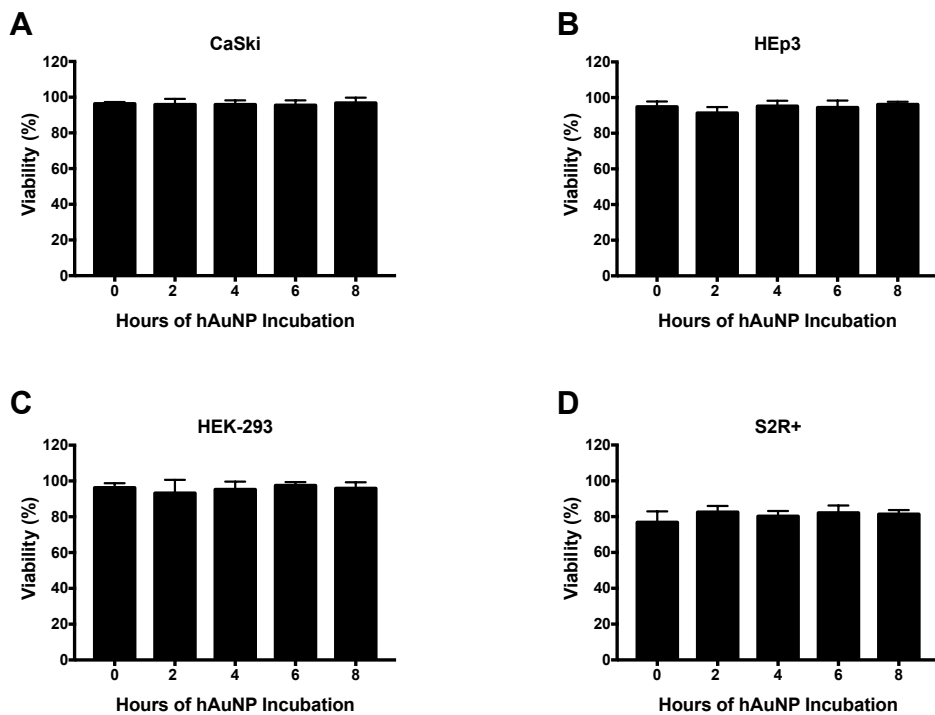
Supplemental Figure F.2. Cell viability of human and insect cells exposed to hAuNPs. hAuNP treatment does not affect the viability of (A) CaSki, (B) HEp3, (C) HEK-293, or (D) S2R+ cells. 0 hours is a control that represents cells that have not been exposed to nanoparticles.
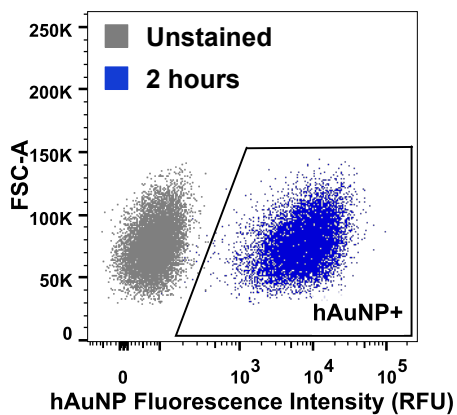
Supplemental Figure F.3. Setting the hAuNP positive gate to calculate transfection efficiency. The gate is drawn to encompass 1% of unstained cells and then applied to the remaining samples. The percentage of cells in the hAuNP positive gate represents the transfection efficiency. The cells act as a single population that shifts to greater fluorescence intensities as hAuNP exposure time increases.
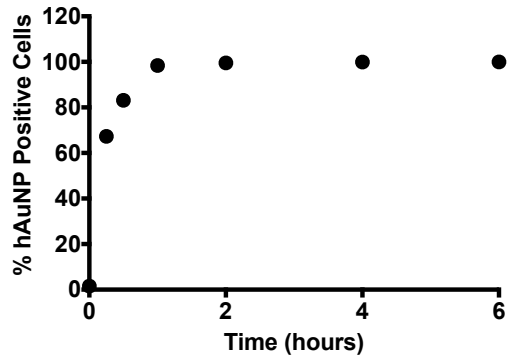
Supplemental Figure F.4. Transfection efficiency for CaSki cells over time. CaSki cells were treated with 0.25 nM hAuNPs and cell associated fluorescence was measured by flow cytometry. The percentage of hAuNP positive cells was determined as described above. CaSki cells quickly accumulate nanoparticles. After 15 minutes of hAuNP treatment, 67% of cells have detectable nanoparticle fluorescence. By 1 hour, > 98% of cells have been transfected. 0 hours is a control that represents cells that have not been exposed to nanoparticles.
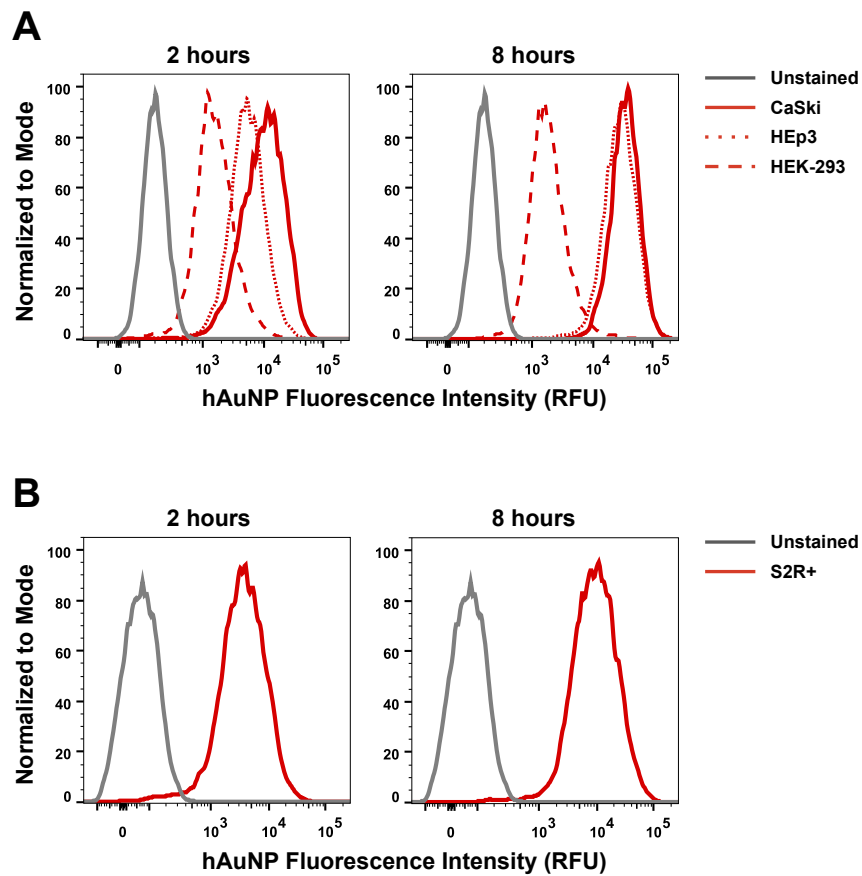
Supplemental Figure F.5. Flow cytometry histograms for the (A) human and (B) insect cell lines treated with hAuNPs for 2 and 8 hours. Fluorescence is distributed throughout the cell population, with some cells having high amounts of fluorescence and some having low amounts.

161
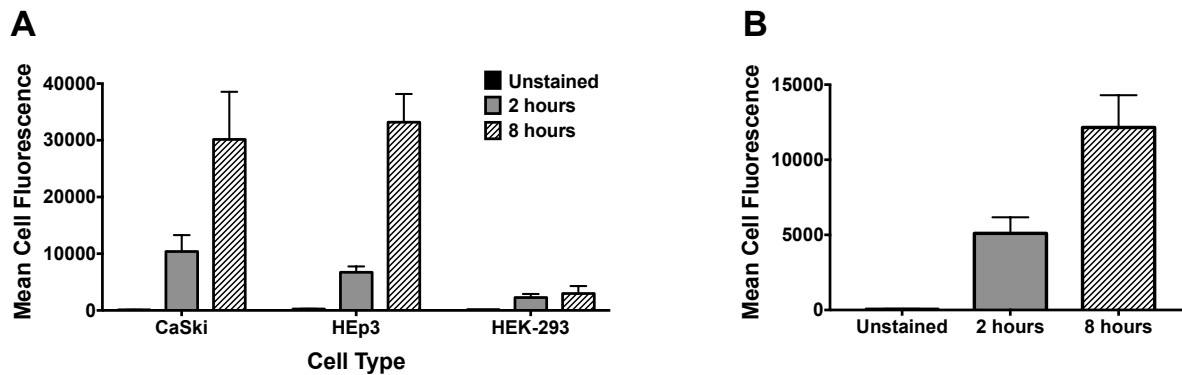
Supplemental Figure F.6. Mean cell fluorescence for human and insect cells. The fluorescence of (A) human and (B) insect cells treated with hAuNPs increases with longer hAuNP exposure times.
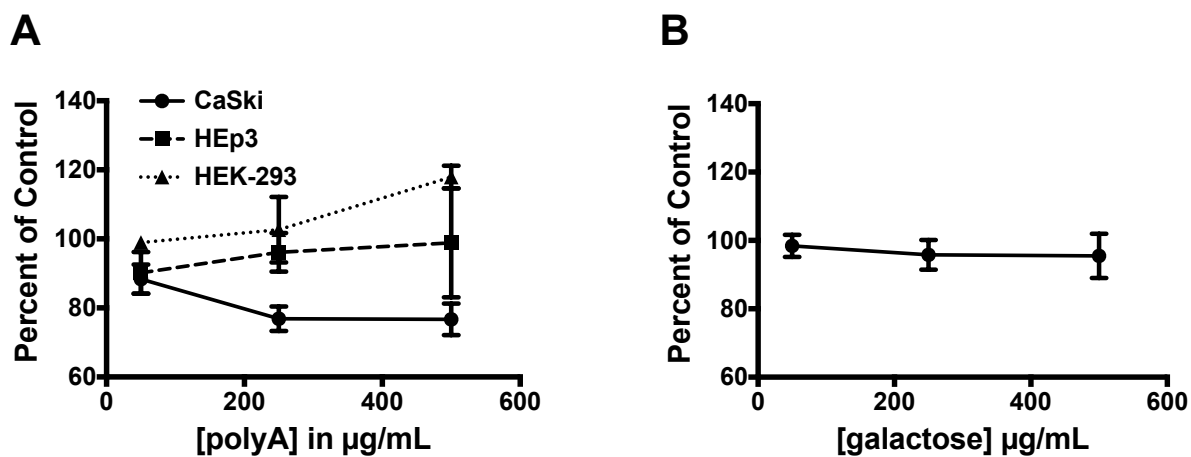
Supplemental Figure F.7. Cellular uptake is unaffected after treatment with negative control compounds. (A) polyA and does not affect hAuNP uptake into CaSki, HEp3, or HEK-293. (B) Galactose does not affect hAuNP uptake into S2R+ cells.
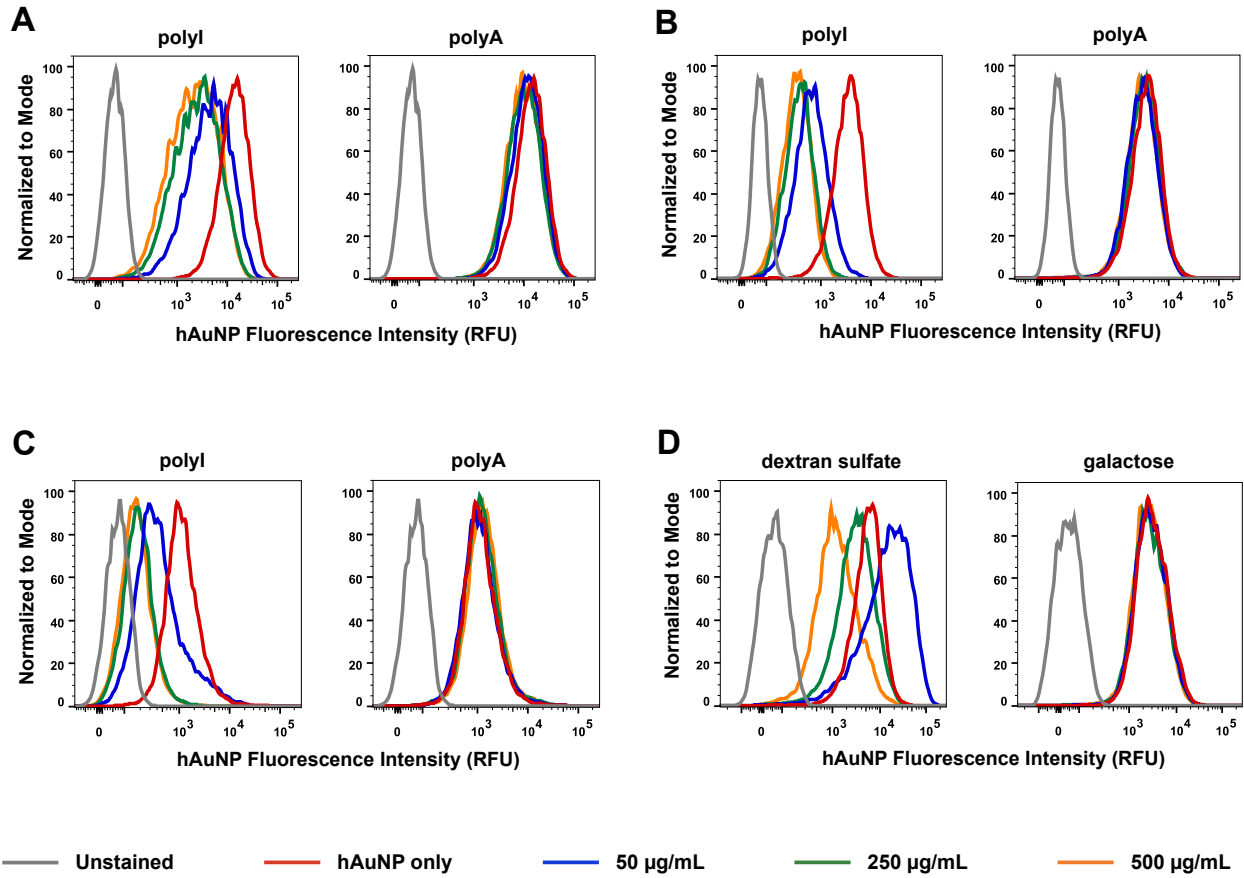
Supplemental Figure F.8. Flow cytometry histograms for (A) CaSki, (B) HEp3, (C) HEK-293, and (D) S2R+ treated with known scavenger receptor ligands (polyI and dextran sulfate) and negative control compounds (polyA and galactose). The cells shift to lower fluorescence intensities as the concentration of inhibitor increases. There is no significant change in fluorescence upon treatment with the control compounds.
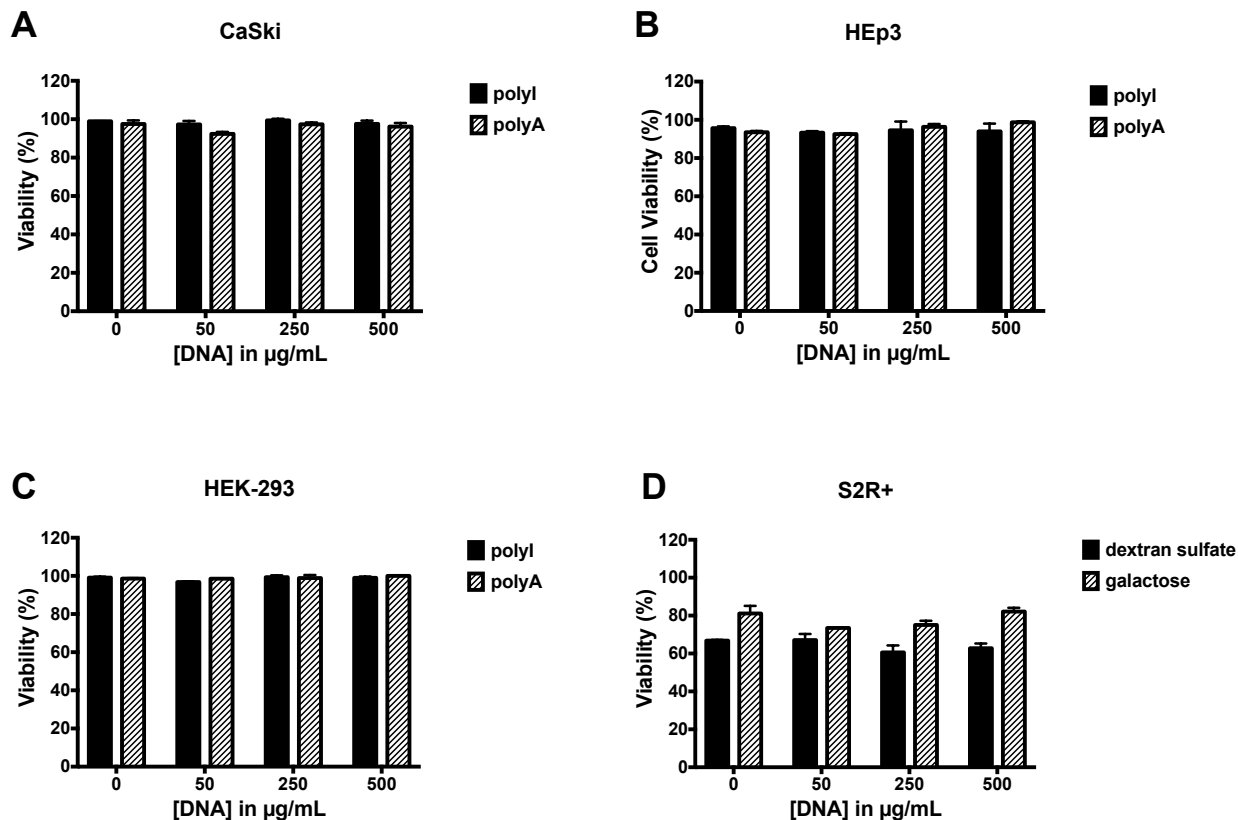
Supplemental Figure F.9. Cytotoxicity of the compounds used for the inhibition of scavenger receptor activity. PolyI and polyA do not affect the viability of (A) CaSki, (B) HEp3, and (C) HEK-293 cells. Dextran sulfate and galactose do not affect the viability of (D) S2R+ cells.
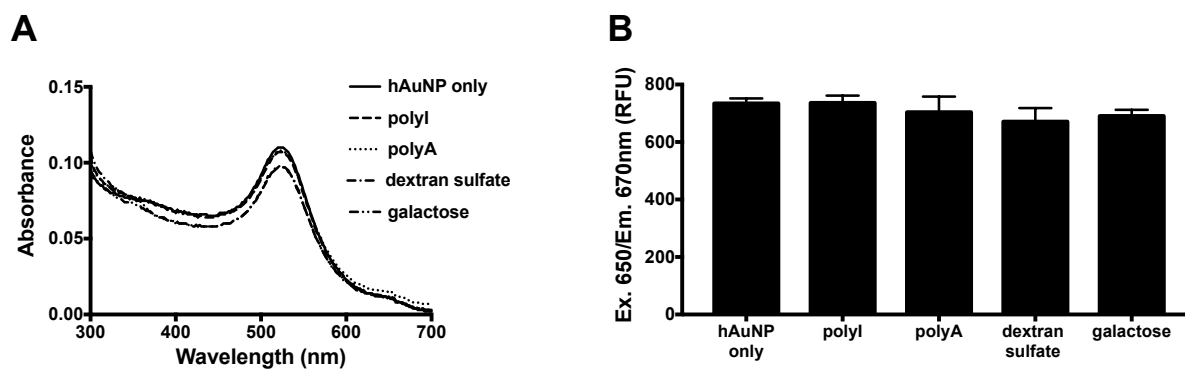
Supplemental Figure F.10. hAuNP stability in the presence of scavenger receptor ligands and the corresponding control compounds. The absorbance and fluorescence of 1 nM hAuNPs in 500 µg/mL of each compound in PBS was measured. (A) No shift in the SPR band indicates that the hAuNPs remain monodisperse. (B) hAuNP fluorescence is not significantly affected by inclusion of the compounds.
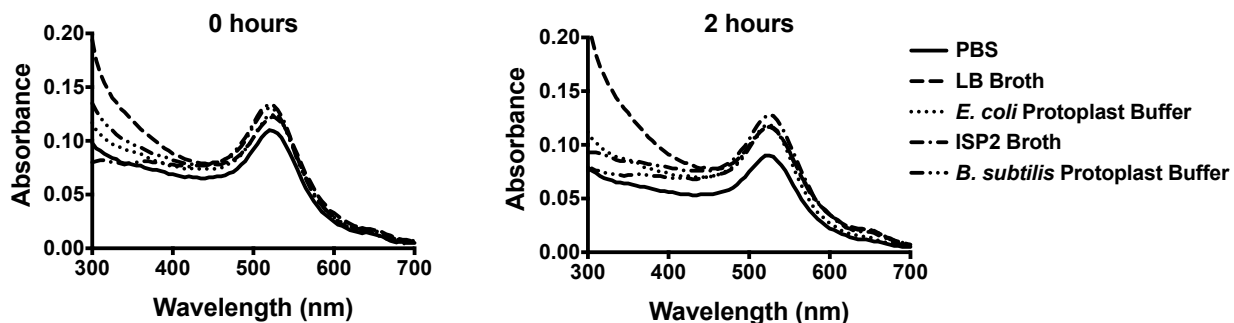
Supplemental Figure F.11. hAuNP stability in bacterial growth medias and protoplast buffers. The hAuNP absorbance was monitored by UV-vis spectrophotometry for 2 hours. No changes in the SPR peak (520 nm) occur, indicating that the nanoparticles do not undergo aggregation.
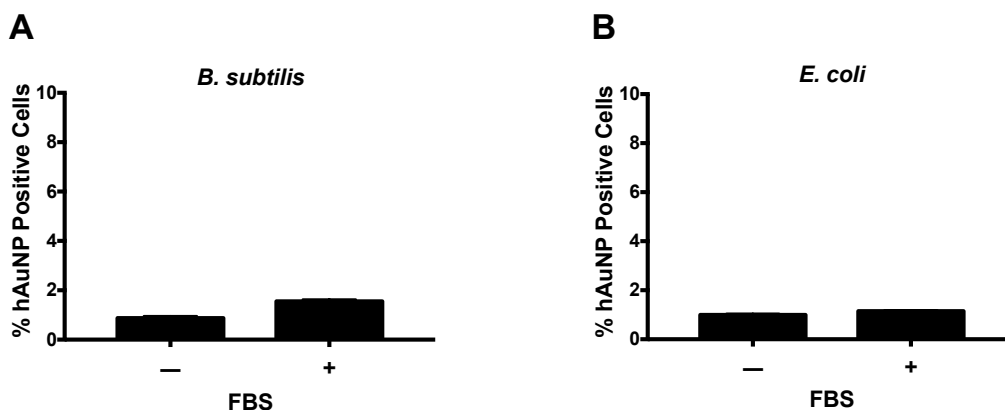
Supplemental Figure F.12. hAuNP treated *B. subtilis* and *E. coli* are not fluorescent. After being exposed to hAuNPs for 2 hours, neither species of bacteria exhibited any nanoparticle fluorescence. Under all conditions, ~1% of cells are present in the hAuNP positive gate, the same as the background level of the untreated control (not shown).
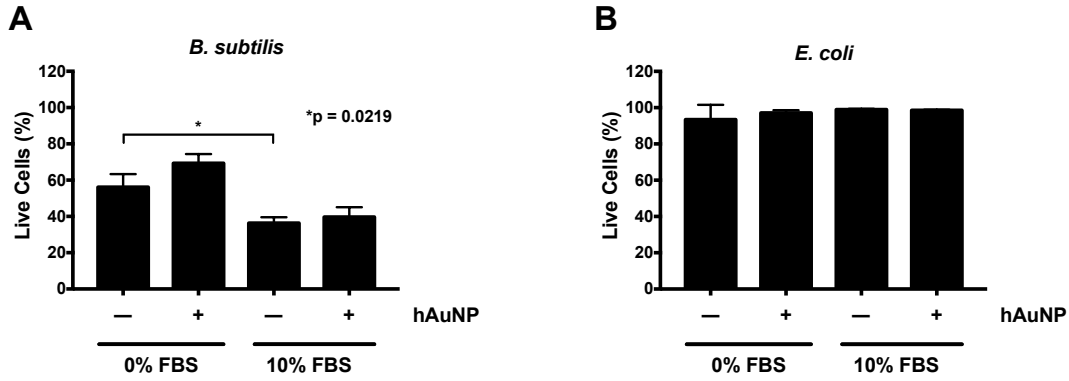
Supplemental Figure F.13. Viability of hAuNP treated *B. subtilis* and *E. coli.* (A) hAuNPs do not affect the viability of *B. subtilis,* but the presence of FBS causes a decrease in the amount of live cells. (B) *E. coli* viability is greater than 93% for all conditions.
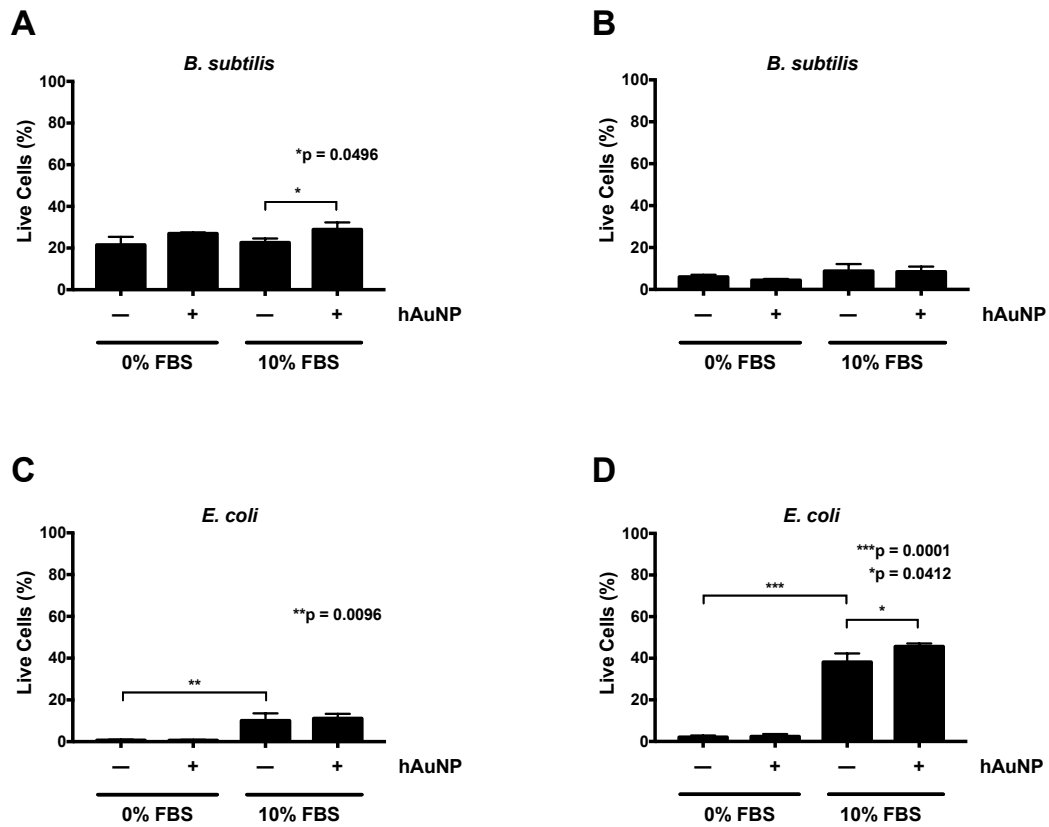
Supplemental Figure F.14. Viability of hAuNP treated *B. subtilis* and *E. coli* protoplasts. hAuNPs do not negatively impact the viability of *B. subtilis* after (A) 30 minutes or (B) 2 hours of treatment. The same is true for *E. coli* at (C) 30 minutes and (D) 2 hours of treatment.
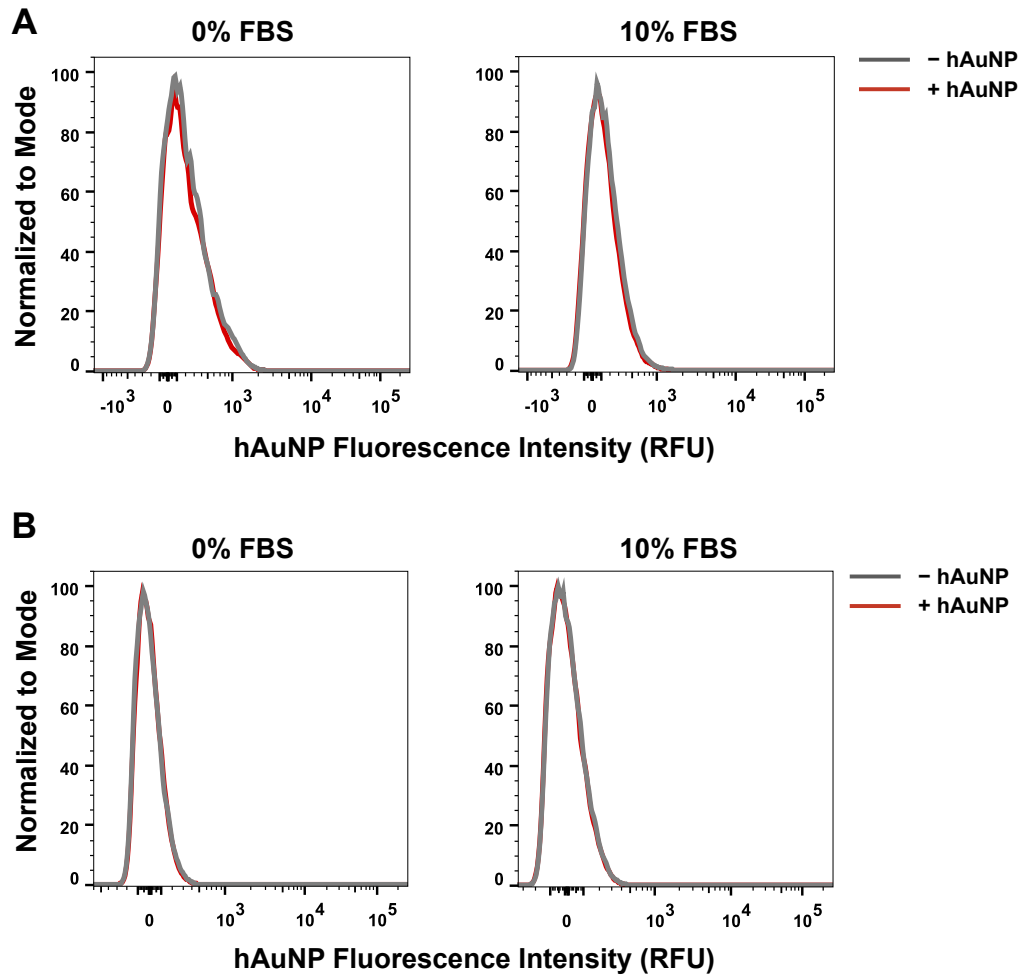
Supplemental Figure F.15. Flow cytometry histograms for hAuNP treated *B. subtilis* and *E. coli* in the presence and absence of FBS. (A) *B. subtilis*, 0% FBS and 10% FBS (B) *E. coli,* 0% FBS and 10% FBS
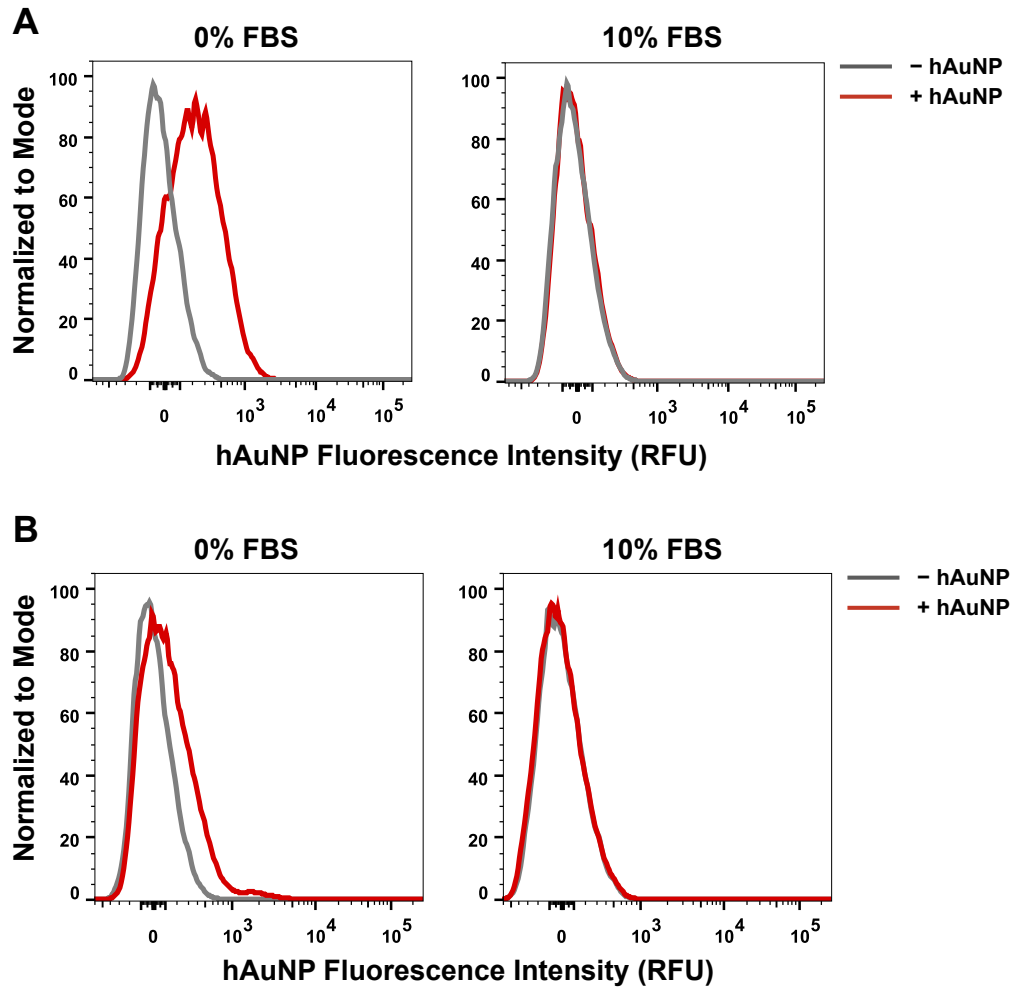
Supplemental Figure F.16. Flow cytometry histograms for hAuNP treated *B. subtilis* protoplasts in the presence and absence of FBS. (A) 30 minute hAuNP exposure, 0% FBS and 10% FBS (B) 2 hour hAuNP exposure, 0% FBS and 10% FBS
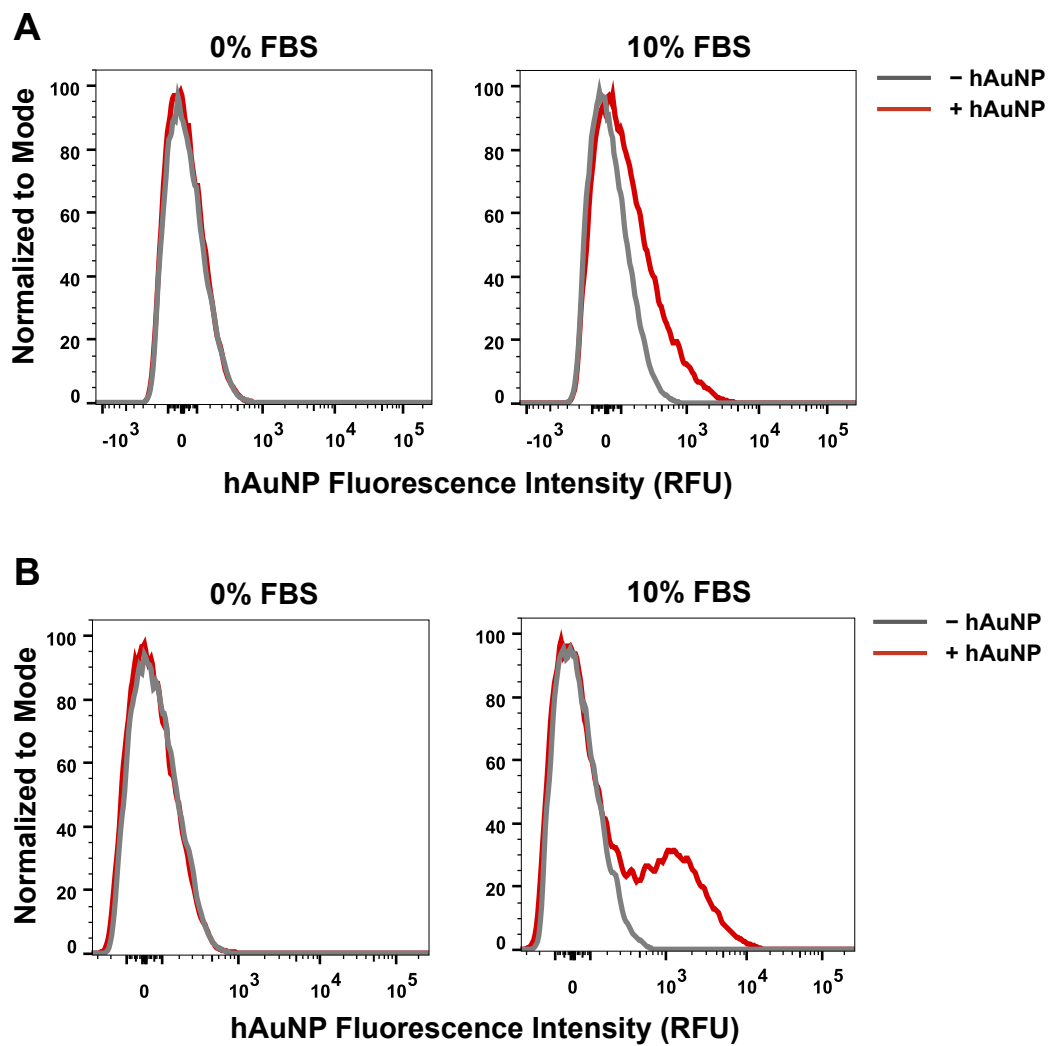
Supplemental Figure F.17. Flow cytometry histograms for hAuNP treated *E. coli* protoplasts in the presence and absence of FBS. (A) 30 minute hAuNP exposure, 0% FBS and 10% FBS (B) 2 hour hAuNP exposure, 0% FBS and 10% FBS
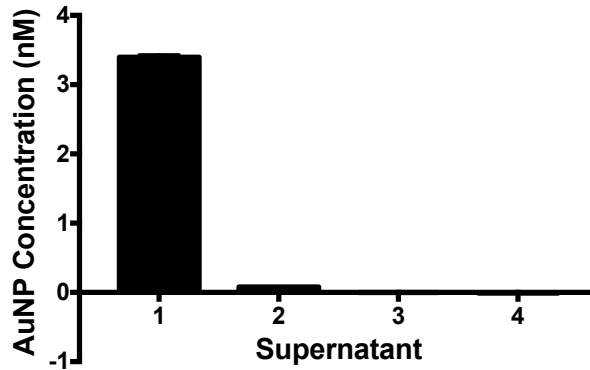
Supplemental Figure F.18. Washing a suspension of S2R+ cells by centrifugation and resuspension removes uninternalized hAuNPs. S2R+ cells were treated with excess hAuNPs (5 nM) for 16 hours. The cells were centrifuged three times at 1,500 g and washed in cell medium. The supernatants were analyzed for gold content by ICP-OES. After three washes (supernatant 3), no gold was detectable, indicating that this method was suitable for removing uninternalized hAuNPs from the insect cells.
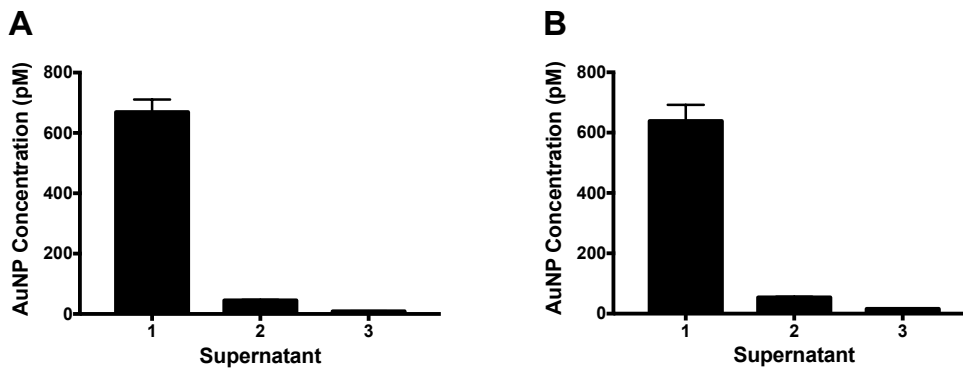
Supplemental Figure F.19. Washing bacteria by centrifugation and resuspension removes uninternalized hAuNPs. (A) *B. subtilis* and (B) *E. coli* were treated with 1 nM hAuNPs for 2 hours and washed by centrifugation at 1,500 g and resuspension with ISP2 or LB broth. The supernatants were analyzed for gold content by ICP-MS. After three washes, minimal levels of gold were detectable. This could be a result of the increased sensitivity of ICP-MS over ICP-OES, but could also be a consequence of the loss of small amounts of cells during supernatant removal.

REFERENCES

(1)   Yang, X.; Yang, M.; Pang, B.; Vara, M.; Xia, Y. Gold Nanomaterials at Work in Biomedicine. *Chem. Rev.* **2015**, *115* (19), 10410–10488.

(2)   Liang, R.; Wei, M.; Evans, D. G.; Duan, X. Inorganic nanomaterials for bioimaging, targeted drug delivery and therapeutics. *Chem. Commun.* **2014**, *50* (91), 14071–14081.

(3)   Dreaden, E. C.; Alkilany, A. M.; Huang, X.; Murphy, C. J.; El-Sayed, M. A. The golden age: gold nanoparticles for biomedicine. *Chem. Soc. Rev.* **2012**, *41* (7), 2740.

(4)   Mirkin, C. A.; Letsinger, R. L.; Mucic, R. C.; Storhoff, J. J. A DNA-based method for rationally assembling nanoparticles into macroscopic materials. *Nature* **1996**, *382* (6592), 607–609.

(5)   Alivisatos, A. P.; Johnsson, K. P.; Peng, X.; Wilson, T. E.; Loweth, C. J.; Bruchez Jr, M. P.; Schultz, P. G. Organization of "nanocrystal molecules" using DNA. *Nature* **1996**, *382*, 609–611.

(6)   Jayagopal, A.; Halfpenny, K. C.; Perez, J. W.; Wright, D. W. Hairpin DNA-functionalized gold colloids for the imaging of mRNA in live cells. *J. Am. Chem. Soc.* **2010**, *132* (28), 9789–9796.

(7)   Harry, S. R.; Hicks, D. J.; Amiri, K. I.; Wright, D. W. Hairpin DNA coated gold nanoparticles as intracellular mRNA probes for the detection of tyrosinase gene expression in melanoma cells. *Chem. Commun.* **2010**, *46* (30), 5557–5559.

(8)   Sita, T. L.; Kouri, F. M.; Hurley, L. A.; Merkel, T. J.; Chalastanis, A.; May, J. L.; Ghelfi, S. T.; Cole, L. E.; Cayton, T. C.; Barnaby, S. N.; et al. Dual bioluminescence and near-infrared fluorescence monitoring to evaluate spherical nucleic acid nanoconjugate activity in vivo. *Proc. Natl. Acad. Sci. U. S. A.* **2017**, *114* (16), 4129–4134.

(9)   Randeria, P. S.; Briley, W. E.; Chinen, A. B.; Guan, C. M.; Petrosko, S. H.; Mirkin, C. A. Nanoflares as Probes for Cancer Diagnostics; Springer International Publishing, 2015; pp 1–22.

(10)   Seferos, D. S.; Giljohann, D. a; Hill, H. D.; Prigodich, A. E.; Mirkin, C. a. Nano-flares: probes for transfection and mRNA detection in living cells. *J. Am. Chem. Soc.* **2007**, *129* (50), 15477–15479.

(11)   Jackson, S. R.; Wong, A. C.; Travis, A. R.; Catrina, I. E.; Bratu, D. P.; Wright, D. W.; Jayagopal, A. Applications of Hairpin DNA-Functionalized Gold Nanoparticles for Imaging mRNA in Living Cells. *Methods Enzymol.* **2016**, *572*, 87–103.

(12)   Zhang, S.; Gao, H.; Bao, G. Physical Principles of Nanoparticle Cellular Endocytosis. *ACS Nano*. 2015.

(13)   Zhao, F.; Zhao, Y.; Liu, Y.; Chang, X.; Chen, C.; Zhao, Y. Cellular uptake, intracellular trafficking, and cytotoxicity of nanomaterials. *Small* **2011**, *7* (10), 1322–1337.

(14) Duan, X.; Li, Y. Physicochemical characteristics of nanoparticles affect circulation, biodistribution, cellular internalization, and trafficking. *Small* **2013**, *9* (9–10), 1521–1532.

(15) Verderio, P.; Avvakumova, S.; Alessio, G.; Bellini, M.; Colombo, M.; Galbiati, E.; Mazzucchelli, S.; Avila, J. P.; Santini, B.; Prosperi, D. Delivering Colloidal Nanoparticles to Mammalian Cells: A Nano-Bio Interface Perspective. *Adv. Healthc. Mater.* **2014**, *3* (7), 957–976.

(16) Dykman, L. A.; Khlebtsov, N. G. Uptake of engineered gold nanoparticles into mammalian cells. *Chem. Rev.* **2014**, *114* (2), 1258–1288.

(17) Choi, C. H. J.; Hao, L.; Narayan, S. P.; Auyeung, E.; Mirkin, C. A. Mechanism for the endocytosis of spherical nucleic acid nanoparticle conjugates. *Proc. Natl. Acad. Sci. U. S. A.* **2013**, *110* (19), 7625–7630.

(18) Elbakry, A.; Wurster, E. C.; Zaky, A.; Liebl, R.; Schindler, E.; Bauer-Kreisel, P.; Blunk, T.; Rachel, R.; Goepferich, A.; Breunig, M. Layer-by-layer coated gold nanoparticles: Size-dependent delivery of DNA into cells. *Small* **2012**, *8* (24), 3847–3856.

(19) Zhang, C.; Hao, L.; Calabrese, C. M.; Zhou, Y.; Choi, C. H. J.; Xing, H.; Mirkin, C. A. Biodegradable DNA-Brush Block Copolymer Spherical Nucleic Acids Enable Transfection Agent-Free Intracellular Gene Regulation. *Small* **2015**, *11* (40), 5360–5368.

(20) Brodin, J. D.; Sprangers, A. J.; McMillan, J. R.; Mirkin, C. A. DNA-Mediated Cellular Delivery of Functional Enzymes. *J. Am. Chem. Soc.* **2015**, *137* (47), 14838–14841.

(21) Cutler, J. I.; Zhang, K.; Zheng, D.; Auyeung, E.; Prigodich, A. E.; Mirkin, C. A. Polyvalent Nucleic Acid Nanostructures. *J. Am. Chem. Soc.* **2011**, *133* (24), 9254–9257.

(22) Patel, P. C.; Giljohann, D. A.; Daniel, W. L.; Zheng, D.; Prigodich, A. E.; Mirkin, C. A. Scavenger Receptors Mediate Cellular Uptake of Polyvalent Oligonucleotide-Functionalized Gold Nanoparticles. *Bioconjug. Chem.* **2010**, *21* (12), 2250–2256.

(23) Witten, K. G.; Ruff, J.; Mohr, A.; Görtz, D.; Recker, T.; Rinis, N.; Rech, C.; Elling, L.; Müller-Newen, G.; Simon, U. Cellular uptake of fluorophore-labeled glyco-DNA-gold nanoparticles. *J. Nanoparticle Res.* **2013**, *15* (10).

(24) Fenz, S. F.; Sengupta, K. Giant vesicles as cell models. *Integr. Biol.* **2012**, *4* (9), 982–995.

(25) Treuel, L.; Jiang, X.; Nienhaus, G. U. New views on cellular uptake and trafficking of manufactured nanoparticles. *J. R. Soc. Interface* **2013**, *10* (82), 20120939.

(26) Wang, T.; Bai, J.; Jiang, X.; Nienhaus, G. U. Cellular uptake of nanoparticles by membrane penetration: A study combining confocal microscopy with FTIR spectroelectrochemistry. *ACS Nano* **2012**, *6* (2), 1251–1259.

(27) De Planque, M. R. R.; Aghdaei, S.; Roose, T.; Morgan, H. Electrophysiological characterization of membrane disruption by nanoparticles. *ACS Nano* **2011**, *5* (5), 3599–3606.

(28) Tahara, K.; Tadokoro, S.; Kawashima, Y.; Hirashima, N. Endocytosis-like Uptake of Surface-Modified Drug Nanocarriers into Giant Unilamellar Vesicles. *Langmuir* **2012**, *28*, 7114–7118.

(29) Montis, C.; Maiolo, D.; Alessandri, I.; Bergese, P.; Berti, D. Interaction of nanoparticles with lipid membranes: a multiscale perspective. *Nanoscale* **2014**, *6* (12), 6452–6457.

(30) Laurencin, M.; Georgelin, T.; Malezieux, B.; Siaugue, J. M.; Ménager, C. Interactions between giant unilamellar vesicles and charged core-shell magnetic nanoparticles. *Langmuir* **2010**, *26* (20), 16025–16030.

(31) Chan, Y. H. M.; Boxer, S. G. Model membrane systems and their applications. *Curr. Opin. Chem. Biol.* **2007**, *11* (6), 581–587.

(32) Ikonen, E. Cellular cholesterol trafficking and compartmentalization. *Nat. Rev. Mol. Cell Biol.* **2008**, *9* (2), 125–138.

(33) Lesniak, A.; Fenaroli, F.; Monopoli, M. P.; Åberg, C.; Dawson, K. A.; Salvati, A. Effects of the presence or absence of a protein corona on silica nanoparticle uptake and impact on cells. *ACS Nano* **2012**, *6* (7), 5845–5857.

(34) Zhu, Z. J.; Posati, T.; Moyano, D. F.; Tang, R.; Yan, B.; Vachet, R. W.; Rotello, V. M. The interplay of monolayer structure and serum protein interactions on the cellular uptake of gold nanoparticles. *Small* **2012**, *8* (17), 2659–2663.

(35) Chinen, A. B.; Guan, C. M.; Mirkin, C. A. Spherical nucleic acid nanoparticle conjugates enhance G-quadruplex formation and increase serum protein interactions. *Angew. Chemie - Int. Ed.* **2015**, *54* (2), 527–531.

(36) Chinen, A. B.; Guan, C. M.; Ko, C. H.; Mirkin, C. A. The Impact of Protein Corona Formation on the Macrophage Cellular Uptake and Biodistribution of Spherical Nucleic Acids. *Small* **2017**, *13* (16), 1603847.

(37) Manley, S.; Gordon, V. D. Making Giant Unilamellar Vesicles via Hydration of a Lipid Film. **2008**, 1–13.

(38) Nelson, D. L. (David L.; Nelson, D. L. (David L.; Lehninger, A. L.; Cox, M. M. *Lehninger principles of biochemistry*; W.H. Freeman, 2008.

(39) Membrane Protein Lipid Composition Atlas - Orientations of Proteins in Membranes (OPM) database http://opm.phar.umich.edu/atlas.php?membrane=Eukaryotic plasma membrane (accessed May 10, 2017).

(40) Van Meer, G. Lipids of the Golgi membrane. *Trends Cell Biol.* **1998**, *8* (1), 29–33.

(41) van Meer, G.; Voelker, D. R.; Feigenson, G. W. Membrane lipids: where they are and how they behave. *Nat. Rev. Mol. Cell Biol.* **2008**, *9* (2), 112–124.

(42) Gennis, R. B. Introduction: The Structure and Composition of Biomembranes; Springer New York, 1989; pp 1–35.

(43)   Betzer, O.; Meir, R.; Dreifuss, T.; Shamalov, K.; Motiei, M.; Shwartz, A.; Baranes, K.; Cohen, C. J.; Shraga-Heled, N.; Ofir, R.; et al. In-vitro Optimization of Nanoparticle-Cell Labeling Protocols for In-vivo Cell Tracking Applications. *Sci. Rep.* **2015**, *5*, 15400.

(44)   Chithrani, B. D.; Chan, W. C. W. Elucidating the mechanism of cellular uptake and removal of protein-coated gold nanoparticles of different sizes and shapes. *Nano Lett.* **2007**, *7* (6), 1542–1550.

(45)   Dykman, L.; Khlebtsov, N. Gold nanoparticles in biomedical applications: recent advances and perspectives. *Chem. Soc. Rev.* **2012**, *41* (6), 2256–2282.

(46)   Jans, H.; Huo, Q. Gold nanoparticle-enabled biological and chemical detection and analysis. *Chem. Soc. Rev.* **2012**, *41* (7), 2849–2866.

(47)   Jensen, S. A.; Day, E. S. E.; Ko, C. H. C.; Hurley, L. A.; Luciano, J. P.; Kouri, F. M.; Merkel, T. J.; Luthi, A. J.; Patel, P. C.; Cutler, J. I.; et al. Spherical nucleic acid nanoparticle conjugates as an RNAi-based therapy for glioblastoma. *Sci. Transl. Med.* **2013**, *5* (209), 209ra152.

(48)   Harry, S. R.; Hicks, D. J.; Amiri, K. I.; Wright, D. W. Hairpin DNA coated gold nanoparticles as intracellular mRNA probes for the detection of tyrosinase gene expression in melanoma cells. *Chem. Commun.* **2010**, *46* (30), 5557–5559.

(49)   Cheng, L.-C.; Jiang, X.; Wang, J.; Chen, C.; Liu, R.-S. Nano-bio effects: interaction of nanomaterials with cells. *Nanoscale* **2013**, *5* (9), 3547–3569.

(50)   Walkey, C. D.; Olsen, J. B.; Guo, H.; Emili, A.; Chan, W. C. W. Nanoparticle size and surface chemistry determine serum protein adsorption and macrophage uptake. *J. Am. Chem. Soc.* **2012**, *134* (4), 2139–2147.

(51)   Herd, H.; Daum, N.; Jones, A. T.; Huwer, H.; Ghandehari, H.; Lehr, C.; Drive, W.; City, S. L.; States, U.; Centre, H.; et al. Nanoparticle Geometry and Surface Orientation In fl uence Mode of Cellular Uptake. *ACS Nano* **2013**, *7* (3), 1961–1973.

(52)   Cho, E. C.; Au, L.; Zhang, Q.; Xia, Y. The effects of size, shape, and surface functional group of gold nanostructures on their adsorption and internalization by cells. *Small* **2010**, *6* (4), 517–522.

(53)   Mizuhara, T.; Saha, K.; Moyano, D. F.; Kim, C. S.; Yan, B.; Kim, Y. K.; Rotello, V. M. Acylsulfonamide-Functionalized zwitterionic gold nanoparticles for enhanced cellular uptake at tumor pH. *Angew. Chemie - Int. Ed.* **2015**, *54* (22), 6567–6570.

(54)   Liang, M.; Lin, I.-C.; Whittaker, M. R.; Minchin, R. F.; Monteiro, M. J.; Toth, I. Cellular uptake of densely packed polymer coatings on gold nanoparticles supporting info. *ACS Nano* **2010**, *4* (1), 403–413.

(55)   Pillai, P. P.; Huda, S.; Kowalczyk, B.; Grzybowski, B. A. Controlled pH stability and adjustable cellular uptake of mixed-charge nanoparticles. *J. Am. Chem. Soc.* **2013**, *135* (17), 6392–6395.

(56)   Hong, S.; Park, S.; Park, J.; Yi, J. Effect of end group modification of DNA-functionalized gold nanoparticles on cellular uptake in HepG2 cells. *Colloids Surfaces B Biointerfaces* **2013**, *112*, 415–420.

(57)   Giljohann, D. A.; Seferos, D. S.; Patel, P. C.; Millstone, J. E.; Rosi, N. L.; Mirkin, C. A. Oligonucleotide Loading Determines Cellular Uptake of DNA- Modified Gold Nanoparticles. *Nano Lett.* **2007**, *7* (12), 3818–3821.

(58)   Patel, P. C.; Giljohann, D. A.; Daniel, W. L.; Zheng, D.; Prigodich, A. E.; Mirkin, C. a. Scavenger receptors mediate cellular uptake of polyvalent oligonucleotide-functionalized gold nanoparticles. *Bioconjug. Chem.* **2010**, *21* (12), 2250–2256.

(59)   Rodriguez-Lorenzo, L.; Fytianos, K.; Blank, F.; Von Garnier, C.; Rothen-Rutishauser, B.; Petri-Fink, A. Fluorescence-encoded gold nanoparticles: Library design and modulation of cellular uptake into dendritic cells. *Small* **2014**, *10* (7), 1341–1350.

(60)   Narayan, S. P.; Choi, C. H. J.; Hao, L.; Calabrese, C. M.; Auyeung, E.; Zhang, C.; Goor, O. J. G. M.; Mirkin, C. A. The Sequence-Specific Cellular Uptake of Spherical Nucleic Acid Nanoparticle Conjugates. *Small* **2015**, *11* (33), 4173–4182.

(61)   Saha, K.; Kim, S. T.; Yan, B.; Miranda, O. R.; Alfonso, F. S.; Shlosman, D.; Rotello, V. M. Surface functionality of nanoparticles determines cellular uptake mechanisms in mammalian cells. *Small* **2013**, *9* (2), 300–305.

(62)   Zhang, Z.; Van Steendam, K.; Maji, S.; Balcaen, L.; Anoshkina, Y.; Zhang, Q.; Vanluchene, G.; De Rycke, R.; Van Haecke, F.; Deforce, D.; et al. Tailoring cellular uptake of gold nanoparticles via the hydrophilic-to-hydrophobic ratio of their (Co)polymer coating. *Adv. Funct. Mater.* **2015**, *25* (22), 3433–3439.

(63)   Jiang, Y.; Huo, S.; Mizuhara, T.; Das, R.; Lee, Y.; Hou, S.; Moyano, D. F.; Duncan, B.; Liang, X.; Rotello, V. M. The Interplay of Size and Surface Functionality on the Cellular Uptake. *ACS Nano* **2015**, *9* (10), 9986–9993.

(64)   Liu, X.; Huang, N.; Li, H.; Jin, Q.; Ji, J. Surface and size effects on cell interaction of gold nanoparticles with both phagocytic and non- phagocytic cells. *Langmuir* **2013**.

(65)   Jackson, S. R. DNA-functionalized Gold Nanoparticles for Enhanced Molecular Sensing, Vanderbilt Unversity, 2014.

(66)   GenScript. GenScript Sequence Scramble https://www.genscript.com/ssl-bin/app/scramble (accessed Dec 1, 2015).

(67)   NCBI. Standard Nucleotide BLAST https://blast.ncbi.nlm.nih.gov/Blast.cgi?PAGE_TYPE=BlastSearch (accessed Dec 1, 2015).

(68)   Wu, X. A.; Choi, C. H. J.; Zhang, C.; Hao, L.; Mirkin, C. A. Intracellular fate of spherical nucleic acid nanoparticle conjugates. *J. Am. Chem. Soc.* **2014**, *136* (21), 7726–7733.

(69)   Massich, M. D.; Giljohann, D. A.; Schmucker, A. L.; Patel, P. C.; Mirkin, C. A. Cellular

response of polyvalent oligonucleotide-gold nanoparticle conjugates. *ACS Nano* **2010**, *4* (10), 5641–5646.

(70)   Kim, J. A.; Åberg, C.; Salvati, A.; Dawson, K. A. Role of cell cycle on the cellular uptake and dilution of nanoparticles in a cell population. *Nat. Nanotechnol.* **2011**, *7* (1), 62–68.

(71)   Bartczak, D.; Nitti, S.; Millar, T. M.; Kanaras, A. G. Exocytosis of peptide functionalized gold nanoparticles in endothelial cells. *Nanoscale* **2012**, *4* (15), 4470–4472.

(72)   Kim, C. S.; Le, N. D. B.; Xing, Y.; Yan, B.; Tonga, G. Y.; Kim, C.; Vachet, R. W.; Rotello, V. M. The role of surface functionality in nanoparticle exocytosis. *Adv. Healthc. Mater.* **2014**, *3* (8), 1200–1202.

(73)   Weibull, C. Bacterial Protoplasts. *Annu. Rev. Microbiol.* **1958**, *12*, 1–26.

(74)   Weiss, R. L. Protoplast formation in Escherichia coli. *J. Bacteriol.* **1976**, *128* (2), 668–670.

(75)   Birdsell, D. C.; Cota-Robles, E. H. Production and ultrastructure of lysozyme and ethylenediaminetetraacetate-lysozyme spheroplasts of Escherichia coli. *J. Bacteriol.* **1967**, *93* (1), 427–437.

(76)   Zinder, N. D.; Arndt, W. F. Production of Protoplasts of Escherichia Coli By Lysozyme Treatment. *Proc. Natl. Acad. Sci. U. S. A.* **1956**, *42* (9), 586–590.

(77)   den Kamp, J. A. F. O.; Redai, I.; van Deenen, L. L. M. Phospholipid composition of Bacillus subtilis. *J Bacteriol* **1969**, *99* (1), 298–303.

(78)   Pattillo, R.; Hussa, R.; Story, M.; Ruckert, A.; Shalaby, M.; Mattingly, R. Tumor antigen and human chorionic gonadotropin in CaSki cells: a new epidermoid cervical cancer cell line. *Science (80-.).* **1977**, *196* (4297).

(79)   Toolan, H. W. Transplantable Human Neoplasms Maintained in Cortisone Treated Laboratory Animals: H.S. #1; H.Ep. #1; H.Ep. #2; H.Ep. #3; and H.Emb.Rh. #1. *Cancer Res.* **1954**, *14*, 660–666.

(80)   Graham, F. L.; Smileyt, J.; Russell, W. C.; Nairn, R. Characteristics of a Human Cell Line Transformed by DNA from Human Adenovirus Type 5. *J. gen. Virol* **2977**, *36*, 59–7.

(81)   Yanagawa, S.; Lee, J. S.; Ishimoto, A. Identification and characterization of a novel line of Drosophila Schneider S2 cells that respond to wingless signaling. *J. Biol. Chem.* **1998**, *273* (48), 32353–32359.

(82)   Canton, J.; Neculai, D.; Grinstein, S. Scavenger receptors in homeostasis and immunity. *Nat. Rev. Immunol.* **2013**, *13* (9), 621–634.

(83)   Shannahan, J. H.; Bai, W.; Brown, J. M. Implications of scavenger receptors in the safe development of nanotherapeutics. *Recept. Clin. Investig.* **2015**, *2* (3), e811.

(84)   Zhu, F. G.; Reich, C. F.; Pisetsky, D. S.; Pisetsky, D. S. The role of the macrophage scavenger receptor in immune stimulation by bacterial DNA and synthetic

oligonucleotides. *Immunology* **2001**, *103* (2), 226–234.

(85) Ulvila, J.; Parikka, M.; Kleino, A.; Sormunen, R.; Ezekowitz, R. A.; Kocks, C.; Rämet, M. Double-stranded RNA is internalized by scavenger receptor-mediated endocytosis in Drosophila S2 cells. *J. Biol. Chem.* **2006**, *281* (20), 14370–14375.

(86) Vlassov, V. V.; Laktionov, P. P.; Rykova, E. Y. Extracellular nucleic acids. *BioEssays* **2007**, *29* (7), 654–667.

(87) Takagi, T.; Hashiguchi, M.; Mahato, R. I.; Tokuda, H.; Takakura, Y.; Hashida, M. Involvement of Specific Mechanism in Plasmid DNA Uptake by Mouse Peritoneal Macrophages. *Biochem. Biophys. Res. Commun.* **1998**, *245* (3), 729–733.

(88) Orr, G. A.; Chrisler, W. B.; Cassens, K. J.; Tan, R.; Tarasevich, B. J.; Markillie, L. M.; Zangar, R. C.; Thrall, B. D. Cellular recognition and trafficking of amorphous silica nanoparticles by macrophage scavenger receptor A. *Nanotoxicology* **2011**, *5* (3), 296–311.

(89) Geninatti Crich, S.; Cadenazzi, M.; Lanzardo, S.; Conti, L.; Ruiu, R.; Alberti, D.; Cavallo, F.; Cutrin, J. C.; Aime, S. Targeting ferritin receptors for the selective delivery of imaging and therapeutic agents to breast cancer cells. *Nanoscale* **2015**, *7* (15), 6527–6533.

(90) Yamayoshi, S.; Yamashita, Y.; Li, J.; Hanagata, N.; Minowa, T.; Takemura, T.; Koike, S. Scavenger receptor B2 is a cellular receptor for enterovirus 71. *Nat. Med.* **2009**, *15* (7), 798–801.

(91) Danilo, C.; Gutierrez-Pajares, J. L.; Mainieri, M. A.; Mercier, I.; Lisanti, M. P.; Frank, P. G. Scavenger receptor class B type I regulates cellular cholesterol metabolism and cell signaling associated with breast cancer development. *Breast Cancer Res.* **2013**, *15*, R87.

(92) Pal, S.; Wu, L. Pattern recognition receptors in the fly : Lessons we can learn from the Drosophila melanogaster immune system. *Fly (Austin).* **2009**, *3* (2), 121–129.

(93) Pearson, A.; Lux, A.; Krieger, M. Expression cloning of dSR-CI, a class C macrophage-specific scavenger receptor from Drosophila melanogaster. *Proc. Natl. Acad. Sci. U. S. A.* **1995**, *92* (9), 4056–4060.

(94) Thelen, T.; Hao, Y.; Medeiros, A. I.; Curtis, J. L.; Serezani, C. H.; Kobzik, L.; Harris, L. H.; Aronoff, D. M. The Class A Scavenger Receptor, Macrophage Receptor with Collagenous Structure, Is the Major Phagocytic Receptor for Clostridium sordellii Expressed by Human Decidual Macrophages. *J. Immunol.* **2010**, *185* (7).

(95) Jayawardena, H. S. N.; Jayawardana, K. W.; Chen, X.; Yan, M. Maltoheptaose promotes nanoparticle internalization by Escherichia coli. *Chem. Commun.* **2013**, *49* (29), 3034.

(96) Kloepfer, J. A.; Mielke, R. E.; Nadeau, J. L. Uptake of CdSe and CdSe / ZnS Quantum Dots into Bacteria via Purine-Dependent Mechanisms Uptake of CdSe and CdSe / ZnS Quantum Dots into Bacteria via Purine-Dependent Mechanisms. *Appl. Environ. Microbiol.* **2005**, *71* (5), 2548–2557.

(97) Kumar, A.; Pandey, A. K.; Singh, S. S.; Shanker, R.; Dhawan, A. Cellular uptake and

mutagenic potential of metal oxide nanoparticles in bacterial cells. *Chemosphere* **2011**, *83* (8), 1124–1132.

(98)   Kumar, A.; Pandey, A. K.; Singh, S. S.; Shanker, R.; Dhawan, A. A flow cytometric method to assess nanoparticle uptake in bacteria. *Cytom. Part A* **2011**, *79 A* (9), 707–712.

(99)   Marslin, G.; Revina, A. M.; Khandelwal, V. K. M.; Balakumar, K.; Sheeba, C. J.; Franklin, G. PEGylated ofloxacin nanoparticles render strong antibacterial activity against many clinically important human pathogens. *Colloids Surfaces B Biointerfaces* **2015**, *132*, 62–70.

(100)   Butler, K. S.; Casey, B. J.; Garborcauskas, G. V. M.; Dair, B. J.; Elespuru, R. K. Assessment of titanium dioxide nanoparticle effects in bacteria : Association , uptake , mutagenicity , co-mutagenicity and DNA repair inhibition. *Mutat. Res. - Genet. Toxicol. Environ. Mutagen.* **2014**, *768*, 14–22.

(101)   Butler, K. S.; Peeler, D. J.; Casey, B. J.; Dair, B. J.; Elespuru, R. K. Silver nanoparticles : correlating nanoparticle size and cellular uptake with genotoxicity. *Mutagenesis* **2015**, *30*, 577–591.

(102)   Chowdhuri, A. R.; Tripathy, S.; Haldar, C.; Chandra, S.; Das, B.; Roy, S.; Sahu, S. K. Theoretical and experimental study of folic acid conjugated silver nanoparticles through electrostatic interaction for enhance antibacterial activity. *RSC Adv.* **2015**, *5*, 21515–21524.

(103)   Zhao, Y.; Tian, Y.; Cui, Y.; Liu, W.; Ma, W.; Jiang, X. Small Molecule-Capped Gold Nanoparticles as Potent Antibacterial Agents That Target Gram-Negative Bacteria. *J. Am. Chem. Soc.* **2010**, *142* (24), 12349–12356.

(104)   Abadeer, N. S.; Murphy, C. J. Recent Progress in Cancer Thermal Therapy Using Gold Nanoparticles.

(105)   Chernak, D. J.; Sisco, P. N.; Goldsmith, E. C.; Baxter, S. C.; Murphy, C. J. High-Aspect-Ratio Gold Nanorods: Their Synthesis and Application to Image Cell-Induced Strain Fields in Collagen Films. In *Nanobiotechnology Protocols*; Rosenthal, S. J., Wright, D. W., Eds.; 2013; Vol. 1026, pp 1–20.

(106)   Ruell, J. A.; Avdeef, A. Absorption Screening Using the PAMPA Approach. *Optim. Drug Discov.* **2004**, 37–64.

(107)   Kansy, M.; Avdeef, A.; Fischer, H. Advances in screening for membrane permeability: High-resolution PAMPA for medicinal chemists. *Drug Discov. Today Technol.* **2004**, *1* (4), 349–355.

(108)   Shanler, M.; Mason, A. K.; Crocker, R. M.; Vardaro, R.; Crespi, C. L.; Stresser, D. M.; Perloff, E. S. Automation of Pre-coated PAMPA Plates Improves Predictability, Reproducibility, and Efficiency. *Corning Appl. Note 475* **2008**, 1–4.

(109)   Avdeef, A. *Absorption and Drug Development: Solubility, Permeability, and Charge State*; John Wiley & Sons: Hoboken, NJ, 2003.

(110) Avdeef, A.; Bendels, S.; Di, L.; Faller, B.; Kansy, M.; Sugano, K.; Yamauchi, Y. PAMPA - Critical Factors for Better Predictions of Absorption. *J. Pharm. Sci.* **2007**, *96* (11), 2893–2909.

(111) Monnard, P. A.; Oberholzer, T.; Luisi, P. Entrapment of nucleic acids in liposomes. *Biochim. Biophys. Acta* **1997**, *1329*, 39–50.

(112) Gopal, A.; Zhou, Z. H.; Knobler, C. M.; Gelbart, W. M. Visualizing large RNA molecules in solution. *RNA* **2012**, *18* (2), 284–299.

(113) von Hippel, P. H.; Johnson, N. P.; Marcus, A. H. 50 years of DNA "Breathing": Reflections on old and new approaches. *Biopolymers* **2013**, *99* (12), 923–954.

(114) Fei, J.; Ha, T. Watching DNA breath one molecule at a time. *Proc. Natl. Acad. Sci. U. S. A.* **2013**, *110* (43), 17173–17174.

(115) Parroche, P.; Touka, M.; Mansour, M.; Bouvard, V.; Thépot, A.; Accardi, R.; Carreira, C.; Roblot, G. G.; Sylla, B. S.; Hasan, U.; et al. Human papillomavirus type 16 E6 inhibits p21WAF1 transcription independently of p53 by inactivating p150Sal2. *Virology* **2011**, *417* (2), 443–448.

(116) Mathews, D. H.; Mathews; H., D. RNA Secondary Structure Analysis Using RNAstructure. In *Current Protocols in Bioinformatics*; John Wiley & Sons, Inc.: Hoboken, NJ, USA, 2006; p 12.6.1-12.6.14.

(117) Love, J. C.; Estroff, L. A.; Kriebel, J. K.; Nuzzo, R. G.; Whitesides, G. M. Self-Assembled Monolayers of Thiolates on Metals as a Form of Nanotechnology. *Chem. Rev.* **2005**, *105*, 1103–1169.

(118) Templeton, A. C.; Wuelfing, W. P.; Murray, R. W. Monolayer-Protected Cluster Molecules Characterization of MPCs. **2000**, *33* (1), 27–36.

(119) Duff, D. G.; Baiker, A.; Edwards, P. P. A New Hydrosol of Gold Clusters. 1. Formation and Particle Size Variation. **1993**, *9*, 2301–2309.

(120) Duff, D. G.; Baiker, M.; Gameson, I.; Edwards, P. P. A New Hydrosol of Gold Clusters. 2. A Comparison of Some Different Measurement Techniques. *Langmuir* **1993**, *9*, 2310–2317.

(121) Westcott, S. L.; Oldenburg, S. J.; Lee, T. R.; Halas, N. J. Formation and Adsorption of Clusters of Gold Nanoparticles onto Functionalized Silica Nanoparticle Surfaces. *Langmuir* **1998**, *14* (19), 5396–5401.

(122) Pham, T.; Jackson, J. B.; Halas, N. J.; Lee, T. R. Preparation and Characterization of Gold Nanoshells Coated with Self-Assembled Monolayers. *Langmuir* **2002**, *18* (12), 4915–4920.

(123) Shi, W.; Sahoo, Y.; Swihart, M. T.; Prasad, P. N. Gold Nanoshells on Polystyrene Cores for Control of Surface Plasmon Resonance. *Langmuir* **2005**, *21* (4), 1610–1617.

(124) Piao, L.; Park, S.; Lee, H. B.; Kim, K.; Kim, J.; Chung, T. D. Single Gold Microshell Tailored to Sensitive Surface Enhanced Raman Scattering Probe. *Anal. Chem.* **2010**, *82* (1), 447–451.

(125) Gulka, C. P.; Swartz, J. D.; Trantum, J. R.; Davis, K. M.; Peak, C. M.; Denton, A. J.; Haselton, F. R.; Wright, D. W. Coffee Rings as Low-Resource Diagnostics: Detection of the Malaria Biomarker *Plasmodium falciparum* Histidine-Rich Protein-II Using a Surface-Coupled Ring of Ni(II)NTA Gold-Plated Polystyrene Particles. *ACS Appl. Mater. Interfaces* **2014**, *6* (9), 6257–6263.

(126) Han, X.; Goebl, J.; Lu, Z.; Yin, Y. Role of Salt in the Spontaneous Assembly of Charged Gold Nanoparticles in Ethanol. *Langmuir* **2011**, *27* (9), 5282–5289.

(127) Han, X.; Liu, Y.; Yin, Y. Colorimetric Stress Memory Sensor Based on Disassembly of Gold Nanoparticle Chains. *Nano Lett.* **2014**, *14* (5), 2466–2470.

(128) Liu, Y.; Han, X.; He, L.; Yin, Y. Thermoresponsive Assembly of Charged Gold Nanoparticles and Their Reversible Tuning of Plasmon Coupling. *Angew. Chemie Int. Ed.* **2012**, *51* (26), 6373–6377.

(129) Lim, S.; Song, J. E.; La, J. A.; Cho, E. C. Gold Nanospheres Assembled on Hydrogel Colloids Display a Wide Range of Thermoreversible Changes in Optical Bandwidth for Various Plasmonic-Based Color Switches. *Chem. Mater.* **2014**, *26* (10), 3272–3279.

(130) Xia, H.; Su, G.; Wang, D. Size-Dependent Electrostatic Chain Growth of pH-Sensitive Hairy Nanoparticles. *Angew. Chemie Int. Ed.* **2013**, *52* (13), 3726–3730.

(131) Zhang, H.; Fung, K.-H.; Hartmann, J.; Chan, C. T.; Wang, D. Controlled Chainlike Agglomeration of Charged Gold Nanoparticles via a Deliberate Interaction Balance. *J. Phys. Chem. C* **2008**, *112* (43), 16830–16839.

(132) Zhang, H.; Wang, D. Controlling the Growth of Charged-Nanoparticle Chains through Interparticle Electrostatic Repulsion. *Angew. Chemie Int. Ed.* **2008**, *47* (21), 3984–3987.

(133) Park, S.-J.; Lazarides, A. A.; Mirkin, C. A.; Letsinger, R. L. Directed Assembly of Periodic Materials from Protein and Oligonucleotide-Modified Nanoparticle Building Blocks. *Angew. Chemie Int. Ed.* **2001**, *40* (15), 2909–2912.

(134) Cho, E. C.; Choi, S.-W.; Camargo, P. H. C.; Xia, Y. Thiol-Induced Assembly of Au Nanoparticles into Chainlike Structures and Their Fixing by Encapsulation in Silica Shells or Gelatin Microspheres. *Langmuir* **2010**, *26* (12), 10005–10012.

(135) Lin, S.; Li, M.; Dujardin, E.; Girard, C.; Mann, S. One-Dimensional Plasmon Coupling by Facile Self-Assembly of Gold Nanoparticles into Branched Chain Networks. *Adv. Mater.* **2005**, *17* (21), 2553–2559.

(136) Lassiter, J. B.; Aizpurua, J.; Hernandez, L. I.; Brandl, D. W.; Romero, I.; Lal, S.; Hafner, J. H.; Nordlander, P.; Halas, N. J. Close Encounters between Two Nanoshells. *Nano Lett.* **2008**, *8* (4), 1212–1218.

(137) Hoffman, A. The Action of Hydrogen Phosphide on Formaldehyde. *J. Am. Chem. Soc.* **1921**, *43* (7), 1684–1688.

(138) Hoffman, A. The Action of Hydrogen Phosphide on Formaldehyde. II. *J. Am. Chem. Soc.* **1930**, *52* (7), 2995–2998.

(139) Grayson, M. Phosphonium Compounds. III. Mechanism of Hydroxide Cleavage of Tetrakis(hydroxymethyl)phosphonium Chloride. *J. Am. Chem. Soc.* **1963**, *85* (1), 79–83.

(140) Shao, S. X.; Jiang, L.; Li, Y.; Shi, K. Q. Effect of pH on the Phosphorous Components in Tetra-Hydroxymethyl Phosphonium Chloride Solution. *Adv. Mater. Res.* **2012**, *560–561*, 237–241.

(141) Shao, S.; Shi, K.; Li, Y.; Jiang, L.; Ma, C. Mechanism of Chrome-free Tanning with Tetra-hydroxymethyl Phosphonium Chloride. *Chinese J. Chem. Eng.* **2008**, *16* (3), 446–450.

(142) Doblas, S.; Pathuri, G.; Towner, R. A.; Gali, H. Feasibility Evaluation of Detecting Hydroxymethylphosphine Oxide In Vivo by (31)P-MRS. *Int. J. Biomed. Sci.* **2010**, *6* (3), 228–232.

(143) Ellzey, S. E.; Connick, W. J.; Boudreaux, G. J.; Klapper, H. Nuclear magnetic resonance study of the formaldehyde-induced exchange of methylol groups in tetrakis(hydroxymethyl)phosphonium chloride and tris(hydroxymethyl)phosphine. *J. Org. Chem.* **1972**, *37* (22), 3453–3457.

(144) Luo, K.; Schroeder, S. L. M.; Dryfe, R. A. W. Formation of Gold Nanocrystalline Films at the Liquid/Liquid Interface: Comparison of Direct Interfacial Reaction and Interfacial Assembly. *Chem. Mater* **2009**, *21*, 4172–4183.

(145) Dong, X.-Y.; Gao, Z.-W.; Yang, K.-F.; Zhang, W.-Q.; Xu, L.-W. Nanosilver as a new generation of silver catalysts in organic transformations for efficient synthesis of fine chemicals. *Catal. Sci. Technol.* **2015**, *5* (5), 2554–2574.

(146) Wang, D.; Cai, R.; Sharma, S.; Jirak, J.; Thummanapelli, S. K.; Akhmedov, N. G.; Zhang, H.; Liu, X.; Petersen, J. L.; Shi, X. "Silver Effect" in Gold(I) Catalysis: An Overlooked Important Factor. *J. Am. Chem. Soc.* **2012**, *134* (21), 9012–9019.

(147) Daniel J. Cline; Sarah E. Redding; Stephen G. Brohawn; James N. Psathas; Joel P. Schneider, A.; Thorpe, C. New Water-Soluble Phosphines as Reductants of Peptide and Protein Disulfide Bonds: Reactivity and Membrane Permeability. *Biochemistry* **2004**, *43* (48), 15195–15203.

CURRICULUM VITAE

Alexis C. Wong

512 Old Hickory Blvd. Apt 2721 • Nashville, TN 37209
(865) 384-4117 • alexis.c.wong@vanderbilt.edu

EDUCATION

Ph.D. in Chemistry, *Vanderbilt University*, Nashville, TN , August 2017 (Expected)
B.S. in Chemistry (*summa cum laude*), *Furman University*, Greenville, SC, May 2012

RESEARCH EXPERIENCE

NSF Fellow / Graduate Research Assistant, Vanderbilt University, 2012 – 2017
Dissertation: "Probing the Cellular Uptake of DNA Functionalized Gold Nanoparticles"
- Analyzed how the physical properties of DNA-coated gold nanoparticles affect uptake by human cell lines. Determined that cells take up higher amounts of small nanoparticles compared to large nanoparticles, and that the accumulation is controlled by nanoparticle size and concentration, as well as cell exposure time
- Developed a protein-free cell model using giant unilamellar vesicles (GUVs) to study the contribution of membrane lipids to DNA-coated gold nanoparticle uptake into cells. Established that fetal bovine serum, a common cell culture additive, increases the association of these nanoparticles with GUVs, and may facilitate the internalization process
- Showed that DNA-coated gold nanoparticles are internalized by a variety of human cell lines and an insect cell line. Gram-positive bacteria did not significantly internalize the nanoparticles, and final studies are planned with gram-negative bacteria and plant cells.
- Completed research enhances the fundamental understanding of how this class of nanoparticles interacts with cell membranes. This enables diagnostic and therapeutic applications by improving the design of nanoparticle sensors to increase transport into cells, reducing time-to-result and requiring less nanomaterial.

Senior Thesis, Furman University, Greenville, SC, 2012
- "Investigations of the Cellular Uptake of $[Cr(diimine)_2(DPPZ)]^{3+}$ Complexes by Transmission Electron Microscopy and Synchrotron Radiation-Fourier Transform Infrared Microspectroscopy"

Summer Undergraduate Research Fellow, Mayo Clinic, Rochester, MN, 2011
- Characterized RNA aptamers that bind and inhibit NF-κB transcription factors using electrophoretic gel mobility shift assays and explored strategies to express the aptamers in cells

Undergraduate Research Assistant, University of Wollongong, NSW, Australia, 2010
- Characterized structural changes in the DNA of cultured cells upon treatment with diimine Cr(III) complexes using synchrotron radiation-Fourier transform infrared microspectroscopy

HHMI Undergraduate Research Fellow, Furman University, Greenville, SC, 2009
- Using TEM, diimine Cr(III) complexes were putatively identified as interacting with the endoplasmic reticulum in breast cancer cells

PUBLICATIONS

- **Wong, A.C**.; Wright, D.W. Size-Dependent Cellular Uptake of DNA Functionalized Gold Nanoparticles. *Small*. **2016**. *12* (40), 5592-5600.
  *Selected to be featured as a frontispiece

- Jackson, S.R.; **Wong, A.C**.; Travis, A.R.; Catrina, I.E.; Bratu, D.P.; Wright, D.W.; Jayagopal, A. Applications of Hairpin DNA-Functionalized Gold Nanoparticles for Imaging mRNA in Living Cells. *Methods Enzymol.* **2016**, *572*, 87-103.

- Gulka, C.P.; **Wong, A.C**.; Wright, D.W. Spontaneous Self-Assembly and Disassembly of Colloidal Gold Nanoparticles Induced by Tetrakis(hydroxymethyl) Phosphonium Chloride. *Chem. Commun.* **2016**,*52*,1266.
- **Wong, A.C**.; Wright, D.W.; Conrad, J.A. Functionalized Gold Nanoparticles for Detection of Cancer Biomarkers. In *Biomarkers in Disease: Methods, Discoveries and Applications. General Methods in Biomarker Research and their Applications*; Preedy, V.R.; Patel, V.B., Eds.; Springer Netherlands, **2015**, 1143-1175.

MANUSCRIPTS IN PREPARATION

- **Wong, A.C**.; Wright, D.W. Differential Cellular Uptake of Hairpin DNA Functionalized Gold Nanoparticles is Driven by Scavenger Receptor Proteins.

LEADERSHIP AND SERVICE

Chemistry Forum Committee, Vanderbilt University, 2015 – 2016
- Served on inaugural committee
- Organized weekly chemistry department seminars for graduate students and postdoctoral fellows
- Topics included scientific research and professional development

Team Finalist, Phase 1, NIH Follow that Cell Challenge, Vanderbilt University, April 2015
- Team: Dr. Joseph Conrad, Alexis Wong, Dr. Andries Zijlstra, Dr. David Wright
- Wrote 85% of a theoretical solution proposing the use of DNA functionalized gold nanoparticles to analyze individual cell behavior and function over minutes, hours, and days, which could contribute to the understanding of disease progression and treatment
- Presented a poster of the progress and an outline of future work at the 2015 NIH Single Cell Analysis Investigators Meeting

Warren Lecture Committee, Vanderbilt University, 2014 – 2015
- Organized the14th Mitchum E. Warren, Jr. Lecture in Chemistry
  - Invited and hosted Prof. Jeremy Nicholson (Imperial College London, London, UK)
- Wrote and implemented a graduate student satisfaction survey about the Chemistry Ph.D. program. Analyzed, prepared, and presented the results to the faculty

SELECTED POSTER PRESENTATIONS

- **Metals in Medicine Gordon Research Conference**, Andover, NH, June 2016
  Hairpin DNA Functionalized Gold Nanoparticles as Molecular Probes for Disease

- **Southeastern Pediatric Research Innovation Conference**, Atlanta, GA, June 2016
  Applications of Hairpin DNA Functionalized Gold Nanoparticles For Molecular Identification of Disease
  Selected for a Rapid-Fire Talk

- **NIH Single Cell Analysis Investigators Meeting**, Bethesda, MD, April 2015
  Development, Optimization, and Enhancement of Fluorescent DNA-Hairpin Functionalized Gold Nanoparticles as Imaging Tools

- **Southeastern Regional Meeting of the American Chemical Society**, Nashville, TN, October 2014
  Optical Imaging Tools for Gene Expression Analysis in Cancer Cells

- **Vanderbilt Institute of Nanoscale Science and Engineering's 15th Annual Nanoscience/Nanotechnology Forum**, Vanderbilt University, November 2014
  Optical Imaging Tools for Gene Expression Analysis in Cancer Cells
  Third place poster

HONORS AND AWARDS

- **National Science Foundation Graduate Research Fellowship**, Vanderbilt University, 2013-2016

- **Third place poster**, Vanderbilt Institute of Nanoscale Science and Engineering's 15th Annual Nanoscience/Nanotechnology Forum, Vanderbilt University, November 2014
- **Vanderbilt Institute of Chemical Biology Fellowship,** Vanderbilt University, 2012-2013
- **Omicron Delta Kappa**, Furman University, 2012
- **Phi Beta Kappa**, Furman University, 2011
- **Goldwater Scholar**, Furman University, 2011

PROFESSIONAL AFFILIATIONS

- American Chemical Society

TECHNICAL SKILLS

- **Nanoparticle characterization:** Surface functionalization, TEM, DLS
- **Analytical techniques:** UV-visible absorbance, fluorescence, ICP-OES, infrared microspectroscopy
- **Molecular biology:** RTPCR, transfection and siRNA-based gene silencing, Western blotting, PAGE, electrophoretic mobility shift assay
- **Miscellaneous:** Flow cytometry, mammalian cell culture, insect cell culture, bacterial cell culture, confocal laser scanning microscopy, liposome and giant unilamellar vesicle preparation,
- **Software:** ImageJ, GraphPad Prism, MS Word, MS Excel, MS PowerPoint, FlowJo